UNIVERSITY OF NOTTINGHAM

DOCTORAL THESIS

Determining uncertainty in the functional quantities of fringe projection

Author:
George Gayton

Supervisors:
Mohammed Isa
Richard Leach

Submitted to the University of Nottingham for the degree of Doctor of Philosophy

March 2022

Determining uncertainty in the functional quantities of fringe projection

George Gayton

What makes a man turn neutral? Lust for gold? Power? Or were you just born with a heart full of neutrality?

-Zapp Brannigan, decorated hero

Abstract

Fringe projection systems can acquire a point-cloud of more than a million points in minutes while not needing to ever physically touch the measurement surface and can be assembled using relatively inexpensive off-the-shelf components. Fringe projection system can conduct measurements faster than their tactile counterparts and typically require less training to do so.

The disadvantage of using a fringe projection system is the measurements are less accurate than alternative tactile methods – and typical methods to obtain an uncertainty evaluation within fringe projection require a tactile system as a comparator. Anterior to any measurement, fringe projection systems undergo a calibration, whereby the set of functional quantities (defined in this thesis as the system parameters) are found that define the measurement (the point-cloud) from the indication (a set of images). The accuracy of the estimated parameters will define the accuracy of any measurements made by the system. The calibration process does not evaluate any uncertainty of the estimated system parameters – the accuracy of the estimation of the parameters remains unknown, as is their exact effect on the measurement result.

In this thesis, an investigation into the using the system parameters to evaluate the uncertainty of fringe projection measurements is made. Firstly, a method to localise the centre of ellipses in camera images with an uncertainty is given. This uncertainty is used to derive the uncertainty in the estimated system parameters. The uncertainty in the system parameters is tested by using the system parameters to measure known artefacts, a flatness artefact and two sphere-based artefacts, where the propagated uncertainty is tested against the measurement error. The accuracy of the system parameters are tested by comparing the measurement error of the measurements with measurements made on a commercial system, the GOM ATOS Core 300. In addition, an exhaustive study is undertaken on the calibration, including applying curvature, specificity and parameter stability tests on the non-linear regression used within calibration.

The sphere-based measurements were found to not be robust enough against measurement noise in fringe projection to be able to provide information on errors caused by the system parameters. This thesis raises questions as to the

appropriateness of using sphere-based measurements to represent the performance of a fringe projection system. The flatness measurements made using the estimated system parameters achieved an accuracy of approximately 30 µm across a 300 mm × 140 mm flatness artefact, which is similar to measurements made by the commercial system. However, the estimated uncertainty was unable to explain all measurement discrepancy between the fringe projection measurements and the tactile measurements. The result specificity test indicated poor specificity of the mathematical model of fringe projection, namely the camera pinhole model with Brown-Conrady distortion. It is concluded that the level of accuracy of the mathematical model has become a limiting factor in the accuracy of fringe projection measurements, instead of the accuracy of the inputs to the calibration. Therefore, the uncertainty of the system parameters cannot be used to evaluate an uncertainty of a measurement made using a fringe projection system.

Acknowledgements

I would like to thank, in no particular order:

Mohammed Isa for our technical discussions and Rong Su and Richard Leach for their constructive feedback.

Mum and Dad.

My housemates; Arthur, Dan, Siew, T-Bag and Fred-Lloyd, for being terrific housemates and a thank you to Charley for showing me what it's like to live with a barnyard animal.

Kieran Smith, Chris Strong, and Ifeanyi Echeta for being my friends, and especially Ifeanyi Echeta for creating the Word template used for this thesis.

Alexander Jackson-Crisp for all the technical support.

And finally, Microsoft Word, for showing me some things are exempt from following the rules of our universe.

Declaration

I, George Gayton, hereby declare that this thesis titled “Determining uncertainty in the functional quantities of fringe projection” is my own work from the time of my PhD at University of Nottingham under supervision of Professor Richard Leach and Dr Mohammed Isa, and that it has never been previously submitted for the award of any degree, diploma or any similar type of recognition.

Table of figures

Figure 1.1 Example of a fringe projection measurement. 29

Figure 2.1 The flow of data in fringe projection to define a measurement value, from image acquisition to the 3D point-cloud output. 34

Figure 2.2 The hardware along with the coordinate systems used in this thesis. 36

Figure 2.3 The pinhole camera model describing the projection of 3D points $\boldsymbol{x}$, first to a projective plane, and then to the camera image. 37

Figure 2.4 An arbitrarily rotated and translated camera defined as a direction sensor. 38

Figure 2.5 A projector in a fringe projection system projecting an image consisting of a single blue line. 39

Figure 2.6 Comparison of the model used here and Zhang's measurement model in terms of (a) maximum absolute difference between points and (b) computation time. 43

Figure 2.7 Distortion modelled using the Brown-Conrady model. 45

Figure 2.8 The maximum absolute error from the distortion-correction algorithm. 48

Figure 2.9 The "wrapped phase" defined from using three phase-shifted sinusoid images. 50

Figure 2.10 The modified heterodyne method. 51

Figure 2.11 Projector images (bottom) inferred from camera images (Top) 52

Figure 2.12 A DMD pixel projecting the intensity value 170 (10101010) as a series of off-on exposures. 53

Figure 2.13 Camera-projector response curves. 54

Figure 2.14 An expanded look into global point $\boldsymbol{x}$ as shown in Figure 2.5. 57

Figure 3.1 The optical resolution of the camera (purple) and the projector (orange and green) placing limits on the accuracy of a triangulation position (red). 60

Figure 3.2 A linear filter applied on a wave of exponentially increasing spatial frequency.....61

Figure 3.3 The limitation of optical resolution on the measurement result 63

Figure 3.4 Error in a phase map (right) caused by a contrast boundary and optical resolution when imaging the dot grid (left).....65

Figure 3.5 A medium of slightly different refractive index altering the path of a travelling ray of light.....66

Figure 4.1 The propagation of uncertainty using the Monte-Carlo method. ...72

Figure 5.1 A log plot giving the memory size of an optimized covariance matrix of a point cloud.....77

Figure 5.2 Spatial kriging of an arbitrary noisy function. The red line indicates the mean predicted outcome of the function, while the shaded area is a 95% confidence interval. 80

Figure 6.1 Calib.io dot grid used for the calibration throughout this thesis. ...86

Figure 6.2 The fitted circle (green) and the difference between the minimum and maximum fitted circles (red area).....87

Figure 6.3 The magnitude of the uncertainty in the x and y plane of each dot across the dot grid.....89

Figure 6.4 The deviation from flat across the dot grid board with the dots in black. 89

Figure 6.5 The outline of the algorithm to localise the centres of dots within the camera and projector images. 90

Figure 6.6 Gaussian filter used on the sinusoid images to reduce noise. 91

Figure 6.7 Rough estimation and extraction of an imaged ellipse from a dot grid artefact and its surrounding area. 93

Figure 6.8 Gradient image with radially expanding lines over which line-spread functions are interpolated over.....94

Figure 6.9 Linear interpolation scheme of a 2D image. The value A, B, C, D are the intensity values of the array at that location, u and v are the inter-array coordinates of range 0,1.....94

Figure 6.10 Gaussian function (red) fitted to the line-spread function (black). 95

Figure 6.11 The located sub-pixel boundary of an imaged ellipse. 98

Figure 6.12 Uncertainty of the imaged ellipses (a) boundary and (b) ellipse centre and perimeter at 95% confidence. 101

Figure 6.13 Comparison of the ellipse fitting methods for a full ellipse, three-quarter ellipse and half ellipse. 104

Figure 6.14 Image of ellipse annotated with the parameters used to define ellipses. 105

Figure 6.15 The distinction between "inside" an ellipse and "outside" an imaged ellipse. 106

Figure 6.16 The histograms (blue) and overlaid probability distribution functions (red) of the (a) internal pixels and (b) the external pixels. 107

Figure 6.17 The internal pixels that have been identified as specular reflections (red). 108

Figure 6.18 KDE of all parameters used to create a virtual ellipse, defined using the calibration dataset. 109

Figure 6.19 (a) Blurring kernels used in the creation of (b) virtual ellipses. (c) Four ellipses from the calibration dataset chosen at random. 110

Figure 6.20 Error in ellipse localisation from the Monte-Carlo test using each of the four blurring kernels. 110

Figure 6.21 The $\chi 2$ values for all ellipse localisation from the Monte-Carlo test of each blurring kernel. 111

Figure 6.22 Cropped region around the dot for the camera-to-projector mapping of the (a) u-axis and (b) v-axis. 112

Figure 6.23 Error in the camera-to-projector mapping of the (a) u-axis and (b) v-axis. 113

Figure 6.24 Eccentricity error caused by the circle centre not being projected onto the ellipse centre. 115

Figure 6.25 Distance from mean ellipse location taken of artefact in each position against the time of the first measurement. 117

Figure 6.26 (a-e) Position 1-5 of the board during repeatability test as seen by the camera. 118

Figure 6.27 Distance from initial ellipse location for the (a,c) camera and (b,d) projector against the time of the first measurement. 119

Figure 7.1 Graphical representation of the forward propagation algorithm in Algorithm 7. 132

Figure 7.2 Location of the 27 board locations and orientations used for the calibration.....134

Figure 7.3 Image points used in the calibration for the (a) camera and (b) projector. Upon any future measurement, any points within the black boundary will be discarded.....135

Figure 7.4 Correlation matrix of the parameter estimate from each calibration method.....137

Figure 7.5 The width of the Gaussian line-spread function in (a) 3D and (b) plotted against distance from the camera pinhole origin. The lateral distance is the distance in the XY plane to 0,0.....138

Figure 7.6 Comparison of the uncertainty contributed form the dot grid and the ellipse localisation in the camera image. 139

Figure 7.7 Comparison of the uncertainty contributed form the dot grid and the ellipse localisation in the projector image. 140

Figure 7.8 The Clarke curvatures Γ of the system parameters. 148

Figure 7.9 Comparison of the twenty-seven estimations of the transform between the camera and projector. 151

Figure 7.10 Histogram of the reprojection errors of the weighted serial and weighted parallel method across all 200 repeated regressions. 152

Figure 7.11 Parameter values of the camera and projector for all repeats of the non-linear regression in the weighted serial and weighted parallel methods. 154

Figure 8.1 Propagation of uncertainty to the final attribute of the point-cloud. 158

Figure 8.2 Information of the measurements of the flat plane used in the flatness measurements.....160

Figure 8.3 Relative locations of the flat plane in the GOM measurements. ...160

Figure 8.4 Flatness clustering algorithm used to remove phase error noise and lower the bandwidth of the measurement. 163

Figure 8.5 Box and whisker plot of the spread of deviations from the fitted plane.....164

Figure 8.6 Bar plot of the range of deviations from the from the fitted plane. 164

Figure 8.7 Box and whisker of the spread of the mean flatness deviations across all trials. 166

Figure 8.8 Mean deviation of each data point from the substitute best-fit plane across the flat plane from the Monte-Carlo trials. 167

Figure 8.9 Distribution of the standard deviations of the distances of the pseudo-points from the substitute best-fit plane. 168

Figure 8.10 Standard deviation of distance of each pseudo-point from the substitute best-fit plane. 169

Figure 8.11 Collective reduced $\chi 2$ test results of all pseudo-points. 170

Figure 8.12 Reduced $\chi 2$ test results of each pseudo-point across the plane. .171

Figure 8.13 Information on the sphere plate used in the sphere-based measurements. 174

Figure 8.14 The spheres used for the sphere-to-sphere distances. All sphere radii are 12.5 mm. 175

Figure 8.15 Information on the dumbbell measurements. 176

Figure 8.16 Relative positions of the dumbbell in the GOM measurements, with each position given a random colour to show pairs of spheres. 176

Figure 8.17 Sphere identification and cleaning algorithm used to prepare the sphere for the sphere fitting. 179

Figure 8.18 Random sphere cap made of N points. 180

Figure 8.19 Histogram of the errors of the sphere fitting test (blue), with an overlaid fitted Student's t distribution (red). 181

Figure 8.20 Error of the sphere radii measurements for the sphere plate. 182

Figure 8.21 Error of the sphere radii measurements for the sphere dumbbells. 183

Figure 8.22 Errors in the sphere-to-sphere length measurements of the sphere plate according to the configuration specified in Figure 8.14. 184

Figure 8.23 Errors in the sphere-to-sphere length measurements of the sphere dumbbell artefact. 185

Figure 8.24 Sphere radii error of each unique sphere using the sphere plate artefact along with a 95% confidence interval. 186

Figure 8.25 Sphere radii error of each unique sphere using the sphere dumbbell artefact along with a 95% confidence interval. 186

Figure 8.26 The mean sphere radii error obtained from the set of virtual point-clouds shown at its measurement location. 187

Figure 8.27 The mean sphere-to-sphere lengths of the sphere plate artefact using the configuration given in Figure 8.14. 188

Figure 8.28 The mean sphere-to-sphere lengths of the sphere dumbbell artefact. 188

Figure 8.29 The mean position of each sphere (red) in the sphere plate compared to the actual value (black) 189

Figure 8.30 The mean sphere-to-sphere length errors shown at the position of measurement. 190

Figure 9.1 Convergence of deviation from flatness values to their final value in each Monte-Carlo trial..... 221

Figure 9.2 Convergence of error of sphere radii values to their final value in each Monte-Carlo trial for (a) dumbbell and (b) sphere plate. 222

Figure 9.3 Convergence of error of sphere-to-sphere length values to their final value in each Monte-Carlo trial for (a) dumbbell and (b) sphere plate. 223

Table of tables

Table 2.1 Comparison of the number of operations per pixel between triangulation methods. 41

Table 2.2 Uniform distributions for testing Eq. (2.19) against Zhang's method. 42

Table 6.1 Ellipse quantities and the distributions they are drawn from. 102

Table 6.2 Virtual ellipse parameters. 105

Table 6.3 Repeatability test results of the camera and projector. 119

Table 7.1 Complete list of camera parameters required to triangulate a point. 122

Table 7.2 Complete list of projector parameters required to triangulate a point. 123

Table 7.3 Parameter estimations. 135

Table 7.4 Specificity test results for the weighted serial and weighted parallel method. 143

Table 7.5 Parameter-effects and intrinsic curvature measures for the parallel and serial methods. 148

Table 8.1 Distribution of the input values used for the Monte-Carlo testing of the sphere-fitting algorithm. 180

Table of definitions

Term	Definition
Calibration	The operation that, under specified conditions, in a first step, establishes a relation between the quantity values with measurement uncertainties provided by measurement standards and corresponding indications with associated measurement uncertainties and, in a second step, uses this information to establish a relation for obtaining a measurement result from an indication [1].
Calibration volume	Volume in 3D space that encompasses all points used during the calibration.
CCD	Charge-coupled device
Correlation	A statistical relationship between two random variables.
Correspondence decoding	The act of identifying correspondences.
Correspondences	The 2D points within the camera and projector image plane that correspond to the same 3D point in global space.
DMD	Digital micromirror device
Empirical model (in relation to uncertainty)	Uncertainty model based on variables chosen for their ease of use, requiring additional measurement evaluation to discern the relationship between uncertainty and chosen variables.
Feature artefact	An object that provides known dimensional quantities represented by recognisable features.

Feature localisation	The measurement of the location of the point of a feature.
Geometrical model (in relation to uncertainty)	Uncertainty model based on the fundamental geometrical parameters that define the fringe projection measurement model
Heteroscedasticity	The property of a random variable, wherein the standard deviations of the random variable are non-constant.
Influence factor	A quantity that, in a direct measurement, does not affect the quantity that is actually measured, but affects the relation between the indication and the measurement result [1].
Instrument resolution	The smallest discernible measurable interval of the system [1].
LCD	Liquid crystal display
Measurement model	Mathematical relation among all quantities known to be involved in a measurement [1].
Measurement process	Generic description of a logical organization of operations used to obtain a measurement [1].
MPE	The maximum permissible error - the maximum difference, permitted by specifications or regulations, between the instrument (reading) and the quantity being measured.
Optical resolution	The ability of the instrument to resolve detail.
Performance verification	Provision of objective evidence that a given item fulfils specified requirements [1].
Point-cloud	A set of data points in space.
Propagation of uncertainty	The calculation of uncertainty in the final product of a mathematical relation as a function of its inputs.
Reference measurement procedure	Measurement procedure accepted as providing measurement results fit for their intended use in assessing measurement trueness of measured

	quantity values obtained from other measurement procedures for quantities of the same kind, in calibration, or in characterizing reference materials [1].
Specificity	The appropriateness of a mathematical model to a particular dataset.
System parameters	The functional quantity values that related a measurement indication and a measurement result.
Triangulation	The process of determining the location of a point by forming triangles to the point from known points.
Uncertainty	(Also known as measurement uncertainty) non-negative parameter characterizing the dispersion of the quantity values being attributed to a measurand, based on the information used. [1]
Uncertainty model	Mathematical relation used to obtain uncertainty.
Virtual model (in relation to uncertainty)	Uncertainty model based on a comprehensive virtual recreation of the measurement.
Virtual parameters	Random parameters that are drawn from known distribution.
Virtual point-cloud	Point-cloud generated using the mathematical model of fringe projection, using virtual parameters.

Contents

Abstract ..... **v**

Acknowledgements ..... **vii**

Declaration ..... **ix**

Table of figures ..... **xi**

Table of tables ..... **xvii**

Table of definitions ..... **xix**

Chapter 1 – Introduction **27**

1.1 Coordinate metrology 27

1.2 Brief overview of fringe projection 28

1.3 Uncertainty evaluations in fringe projection 29

1.4 Thesis objectives 30

1.5 Thesis limitations 31

Chapter 2 – Measurement theory of fringe projection **33**

2.1 Measurement process overview 33

2.2 Experimental set-up 35

2.3 Measurement model 36

2.4 Correspondence decoding 48

2.5 Extension to over-determined systems 54

2.6 Frustrum model 55

2.7 Summary 57

Chapter 3 – Influence quantities in fringe projection **59**

3.1 Instrument resolution 60

3.2 Pixel-to-pixel non-linearity 63

3.3 Measurement Surface 64

3.4 Environment 65

3.5 Summary 67

Chapter 4 – General methods in uncertainty evaluation **69**

4.1 Uncertainty 69
4.2 Analytical 70
4.3 Monte-Carlo method 71
4.4 Reduced $\chi 2$ test 73
4.5 Summary 74
Chapter 5 – Methods of fringe projection uncertainty evaluation 75
5.1 Geometrical models 76
5.2 Empirical models 78
5.3 Virtual models 80
5.4 Summary 82
Chapter 6 – Feature localisation 83
6.1 Feature artefacts 83
6.2 Dot grid 85
6.3 Feature localisation overview 89
6.4 Image acquisition 91
6.5 Camera ellipse localisation 92
6.6 Camera ellipse localisation validation 101
6.7 Projector ellipses inference 111
6.8 Eccentricity correction 113
6.9 Repeatability test 115
6.10 Summary 119
Chapter 7 – Calibration of a fringe projection system 121
7.1 Overview of fringe projection calibration 121
7.2 Calibration method 124
7.3 Calibration outcome 134
7.4 Calibration validation 140
7.5 Summary 155
Chapter 8 – Validation 157
8.1 Propagation of uncertainty 157
8.2 Flatness artefact 158

8.3 Sphere-based artefacts 173
8.4 {Summary 192
Chapter 9 – Conclusion 193
9.1 Thesis summary 193
9.2 Problem summary 193
9.3 Thesis contributions 194
9.4 Thesis results 195
9.5 Future work 196
References 198
Appendix A – Gaussian fitting 215
Appendix B – Ellipse fitting 217
Appendix C – Rodrigues operator 219
Appendix D – Convergence 220

Chapter 1 – Introduction

This chapter introduces this thesis, including its objectives and novel contributions, and will provide context for proceeding chapters. First, Section 1.1 presents fringe projection systems and establishes the service that they perform. A brief overview of the basic working principles of fringe projection, as well as the advantages fringe projection offers over traditional measurement techniques is introduced in Section 1.2. Section 1.3 outlines the specific issue that is present in current fringe projection systems that this thesis will contribute towards solving. Section 1.4 will provide a summary of the objective of this thesis. Lastly Section 1.5 will detail limitations of this thesis that have been chosen to limit the scope.

1.1 Coordinate metrology

The complexity of manufactured goods has been increasing since the first Industrial Revolution, and continues to increase to this day with the "fourth Industrial Revolution" – smart automation and additive manufacturing [2]. As manufacturing processes increase in complexity, so too do metrological instruments designed to control the manufacturing processes [3].

When considering the manufacture of any part, given that all dimensions must be to specification, some aspects of dimension are more important than others. Geometric dimensioning and tolerancing (GD&T) enables control over the conformance of the part. GD&T encapsulates a broad range of possible dimensions - the full list is defined in the International Organisation for Standardisation (ISO) standard 1101 [4]. Form is one aspect of GD&T, and describes an object's shape, e.g. cylindricity, parallelism, flatness [5].

Coordinate measurement systems (CMSs) were developed in the 1970s, by manufacturing company Ferranti, to speed up inspection times which were lagging behind manufacturing times [6]. CMSs are versatile measurement tools for measuring an object's dimension and form [7]. CMSs provide data on the object's surface as a discrete set of coordinates in three-dimensional (3D) space, hereby called the point-cloud. The point-cloud can be analysed to give information on the form of the object being measured [8, 9].

CMSs can assume many different configurations but can be roughly categorised into two distinct types - tactile CMSs and optical CMSs. Tactile CMSs typically consist of a probe mounted onto a gantry system [7] (although this is not always the case [10]), with the probe tip registering each point within the point-cloud by physically touching the surface of the object. The gantry system simultaneously moves the probe tip and tracks its location. When the probe registers a pre-specified deflection, caused by the normal force of the object, the coordinate of the probe tip is recorded. Tactile CMSs are highly specialised, expensive systems that, depending on the size of the object being measured and the desired point-cloud density, can take many hours to acquire an accurate measurement.

1.2 Brief overview of fringe projection

Optical CMSs, instead of relying on the physical deflection of a probe, use the reflection of light to probe a surface. Fringe projection systems are a type of optical CMS, and, unlike tactile CMSs, fringe projection systems can be assembled using relatively inexpensive off-the-shelf components. Where a tactile CMS typically takes approximately thirty minutes to acquire roughly thousands of points, fringe projection systems take only minutes to acquire more than a million points over a similar measurement area. While tactile CMSs must physically touch a part to measure it, fringe projection systems do not.

Fringe projection system are well-suited for the measurement of simple and complicated forms [11-13]. A fringe projection system can measure manufactured parts autonomously in real-time [14-16] or be used to augment an operators vision with augmented reality [17]. Fringe projection systems are also well-suited for in-situ measurements on the production line, avoiding the need to relocate parts elsewhere for inspection [18]. The detection of early build faults busing fringe projection saves build material and time [19]. Fringe projection systems are one of the few measurement systems capable of providing in-situ topography measurements of the additive manufacturing process [20-22]. An example of a fringe projection measurement is shown in Figure 1.1.

Figure 1.1 Example of a fringe projection measurement. A measurement of a skull from the Zoology collection, School of Life Sciences, University of Nottingham, Thomas Hartman. Each dot is a single point within the point-cloud.

Fringe projection systems belong to a subset of optical CMS known as triangulation-based optical CMS – similar in operation to laser line scanners and photogrammetry [23]. A detailed overview of the measurement process is given in Chapter 2, a summary is given here. Triangulation-based optical CMS measure the surface of an object by recording the interaction of light with the object's surface, and using the principles of triangulation to record 3D points in the point-cloud. To complete a measurement, a projector first projects a pattern onto a measurement surface. A camera, offset from the projector, records the image of the projected pattern, which appears distorted due to surface geometry. The camera image is then decoded, to find corresponding two-dimensional (2D) locations between the camera and projector images, allowing 3D points to be triangulated.

1.3 Uncertainty evaluations in fringe projection

Measurement uncertainty is the quantification of the statistical dispersion of measurement values that can reasonably be attributed to the true value being measured [1]. The accepted method of evaluating uncertainty is detailed in the Guide to Uncertainty in Metrology (GUM) [24]. Measurement uncertainty allows the meaningful comparison of two measurements of the same object. Without uncertainty, the disparity in measurements cannot be accounted for, and it will remain unknown as to how to treat the disparity in measurements.

A fringe projection system goes through what is often referred to as a calibration, whereby a set of values (defined in this thesis as the system parameters) are found that define the measurement value (the point-cloud)

from the indication (a set of images). Typically, the calibration procedure provides an uncertainty associated with each value found, but in fringe projection this is typically not the case. According to The International Vocabulary of Metrology [1], this would therefore not qualify as a calibration. To remain congruent with current literature on fringe projection, the calibration procedure will remain known as calibration in this thesis.

Typically, to provide an uncertainty with a fringe projection measurement, a study must be completed by comparing a fringe projection measurement of an artefact that has been independently measured using a calibrated instrument. This must be completed for every unique measurement and can be resource intensive. It would be useful to only have to complete this process once during a set time period – like a tactile CMS. The series of standards ISO 15530 [25] details the determination of uncertainty in tactile CMS. Tactile CMS share some similarities to triangulation-based optical CMS, in that they both fulfil a similar measurement role. In 0, a comprehensive review of influence quantities in fringe projection is given, showing why fringe projection measurements are sensitive to surface characteristics, such as optical properties and topography, making ISO 15530 unsuitable for application to triangulation-based optical CMS.

In Chapter 3 and Chapter 4, a review of the current literature on methods of evaluating uncertainty in fringe projection measurements is given. Chapter 3 concludes that the evaluation of uncertainty in fringe projection is problematic even when ignoring the measurement surface in the evaluation of uncertainty. The light-surface interaction is a complex process, so producing a completely calibrated measurement from a fringe projection system is outside the scope of this thesis. Not all fringe projection measurements are highly sensitive to the measured surface; and for this category of measurements, it would be beneficial to have an uncertainty value derived from the system parameters (ignoring the surface problem).

1.4 Thesis objectives

The objective of this thesis is to provide an uncertainty on a fringe projection measurement derived only from the system parameters. The uncertainty on these parameters must be obtained during the calibration. The benefit of this approach is this will require no extra work from the operator of the system. The completion of this objective will require:

1. A novel method to obtain uncertainty from the reference measurement procedure – given in Chapter 6. A novel procedure is given that enables

the estimation of the centre of an ellipse along with an uncertainty – which is a key input to the calibration.

2. A novel method to obtain an uncertainty during the calibration of a fringe projection system – given in Chapter 7. It is popular to estimate the system parameters using a non-linear regression – which can provide an uncertainty estimate. Obtaining the uncertainty this way is a novel application within fringe projection.
    a. A method to quantify if the working conditions of the non-linear regression have not been violated – given in Chapter 7. The use of the tests used in this thesis is novel. The parameter stability test derived in this thesis is a novel test used to detect thermal instabilities during the calibration procedure.
3. A method to propagate the uncertainty in the system parameters to a measurement made using a fringe projection system – given in Chapter 8, using a novel triangulation method given in Chapter 2. The method used to propagate uncertainty from the system parameters in this thesis is necessary but is computationally expensive. The novel triangulation method given in Chapter 2 greatly reduces the computation time of the uncertainty propagation.
4. The validation of the evaluated uncertainties of the system parameters – given in Chapter 8.

1.5 Thesis limitations

To limit the scope of this thesis the following limits are given to the definition of fringe projection:

1. Fringe projection is defined as one camera and one projector only.
2. Fringe projection techniques are limited to full-field triangulation methods only.
3. Correspondence algorithms are limited to temporal correspondence algorithms only.
4. Computing power is limited to off-the-shelf components only.
5. Static fringe projection systems only are considered (i.e., static systems measuring static targets).

Chapter 2 – Measurement theory of fringe projection

This chapter outlines the basic theory required to understand a fringe projection system. The measurement process is described in detail, focussing on the implementations of methods that are specific to this thesis. An overview of the complete measurement process is given in Section 2.1. Section 2.2 gives a description of the experimental set-up used in this thesis.

Fringe projection systems are known as triangulation-based optical CMS – because the measurement model is based on triangulation. Triangulation is defined as the process of determining the location of a point by forming triangles from known positions [26]. In fringe projection, a camera and projector provide two angles within a triangle, system calibration provides a length, and the measurement surface is found as the final unknown corner of a triangle. The method of triangulation within the context of fringe projection is described in Section 2.3. Additionally, Section 2.3.2 defines a novel triangulation method that can be completed faster than comparable methods.

For a camera and a projector to provide an "angle" within the triangle, the location of the same point on the measurement surface must be localised within the camera and projector image. In this thesis, the act of correspondence refers to the decoding method that locates the two-dimensional (2D) sub-pixel location (image points) in both the camera and projector images that originate from the same point in three-dimensional (3D) space. The method of correspondence is described in Section 2.4.

For completeness, Section 2.5 defines the extension of the methods described in chapter to an over-determined system, i.e., where there are multiple cameras and projectors. Expanding on the model defined in Section 2.3, Section 2.6 defines the way in which uncertainties in fringe projection measurement are represented in this thesis.

2.1 Measurement process overview

This section will provide context on the following sections of this chapter by defining the entire measurement procedure. Prior to a measurement, a calibration step provides values that are used in the to generate measurements. Images are captured during the imaging stage. These images are then decoded in the correspondence

decoding. Camera and projector images typically contain some minor optical distortions, and so distortion correction is performed on the image points during the distortion correction stage (although distortion correction can instead be performed earlier, on the image itself, and projector distortion specifically can be corrected pre-imaging stage). Finally, each 3D point is realised in the triangulation stage using the quantities that define the fringe projection system. The entire measurement pipeline is represented graphically in Figure 2.1.

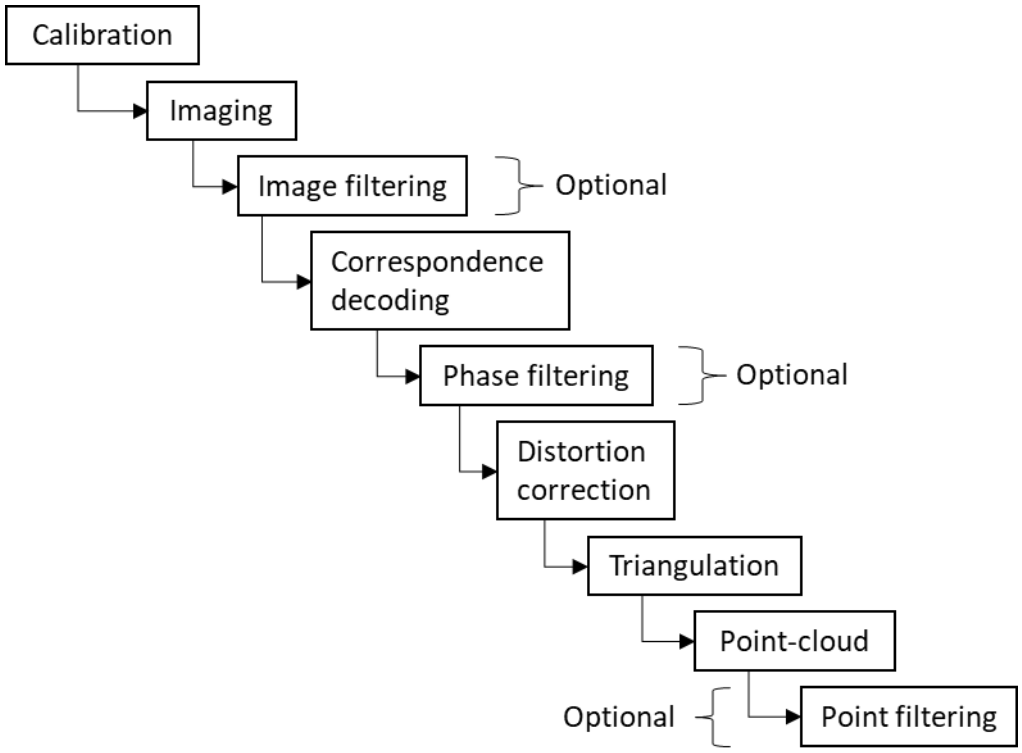

Figure 2.1 The flow of data in fringe projection to define a measurement value, from image acquisition to the 3D point-cloud output.

There are many optional filtering techniques that can be applied at various stages of the measurement process. Prior to the correspondence decoding stage, the raw camera images can be filtered of unnecessary pixels or saturated pixels. During the correspondence stage, a quality metric can be used to remove areas of an image where the correspondence algorithm has performed poorly [27]. In a final step, the output point-cloud itself can be filtered to remove various imperfections [28]. A review of fringe projection techniques can be found in Chen, Xu [29], Feng, Zuo [30] and Xu and Zhang [31]. Multiple cameras/projectors can be used in many different combinations [32]; this thesis will be limited to single camera-projector fringe projection systems to limit the scope.

2.2 Experimental set-up

This section will detail the experimental set-up used to conduct tests, calibrations, and measurements. The fringe projection components are mounted onto a static structure made of aluminium hex-bars, that are mounted to an optical mat. The fringe projection system sits in a semi-clean room with temperature kept between 20.5℃ and 21.5℃. It is assumed that the surrounding air is constant in temperature and the particulate content and humidity is negligible. The camera is a Prosilica GT5120 with an attached Soligor optic. The resolution of the camera is 5120×5120 and the focal length is $\sim$40 mm. The projector is a Texas Instruments 4500 Lightcrafter with a resolution of 912×1140 and a focal length of $\sim$20 mm. The projector and camera are synchronised using the 59 Hz signal from the High-Definition Multimedia Interface (HDMI). The working volume of the fringe projection system is approximately $300\,\text{mm} \times 200\,\text{mm} \times 200\,\text{mm}$.

> This thesis will establish some common coordinate systems. The two axes of images are given by (u, v), with any non-italic subscripts detailing what component the coordinates belong to, e.g., (u_c, v_c) are the image coordinates for the camera. Global coordinates are given by (x, y, z). The global coordinate system is aligned with the camera coordinate system, with the origin of the global coordinate system centered onto the camera coordinate system. The configuration of the fringe projection system as well as the coordinate systems used in this thesis are shown in

Figure 2.2.

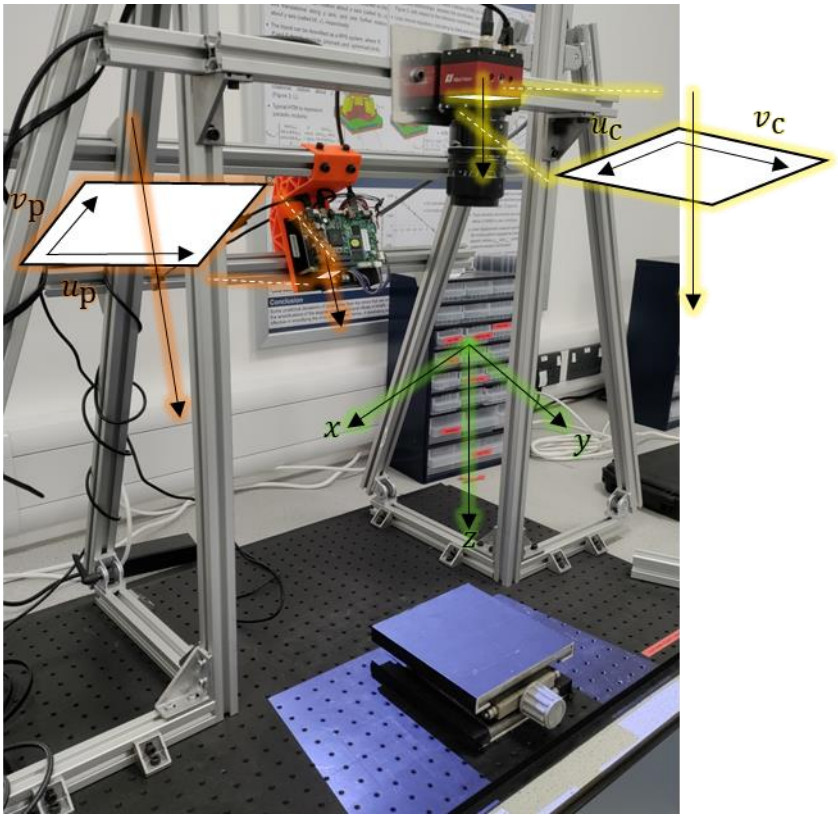

Figure 2.2 The hardware along with the coordinate systems used in this thesis. Camera coordinates are in yellow, projector coordinates are in orange and global coordinates are in green.

2.3 Measurement model

In this section, the fundamental mathematical model that defines fringe projection measurements from their indication, the triangulation model, is defined. In fringe projection, both cameras and projectors are described by the pinhole camera model, which will be defined in Section 2.3.1. The fringe projection measurement model is given in Section 2.3.2.

2.3.1 Pinhole camera model

The pinhole camera model describes the mathematical relationship between a 3D point and its corresponding 2D point projected onto the image plane. The pinhole model is given by

$$s\vec{\boldsymbol{u}} = \boldsymbol{K}\left(\boldsymbol{R}\vec{\boldsymbol{x}} + \vec{\boldsymbol{t}}\right), \tag{2.1}$$

where $\boldsymbol{R}$ and $\vec{\boldsymbol{t}}$ describe rotations and translations of the point $\vec{\boldsymbol{x}}$ from an arbitrary global coordinate system to the camera's own coordinate system. The matrix $\boldsymbol{K}$ is an upper triangular matrix that describes the scaling, skewing and translation operation of the camera on the point $\vec{\boldsymbol{x}}$. The scalar s is a scaling term, where every object has an

ambiguity of scale arising from mapping a 3D object onto a 2D plane. The transformations $\boldsymbol{K}$ and $\boldsymbol{R}$ and vector $\vec{\boldsymbol{t}}$ together define a projective transformation of the 3D point $\vec{\boldsymbol{x}}$ to the 2D image point $\vec{\boldsymbol{u}}$. A graphical representation of the pinhole camera model (eq. (2.1)) is given in Figure 2.3. In the pinhole model, it is common to show the projective plane as inverted and positions opposite the pinhole, as is physically realistic in pinhole cameras. In this thesis, the convention will be to show the image as non-inverted and positioned in front of the pinhole.

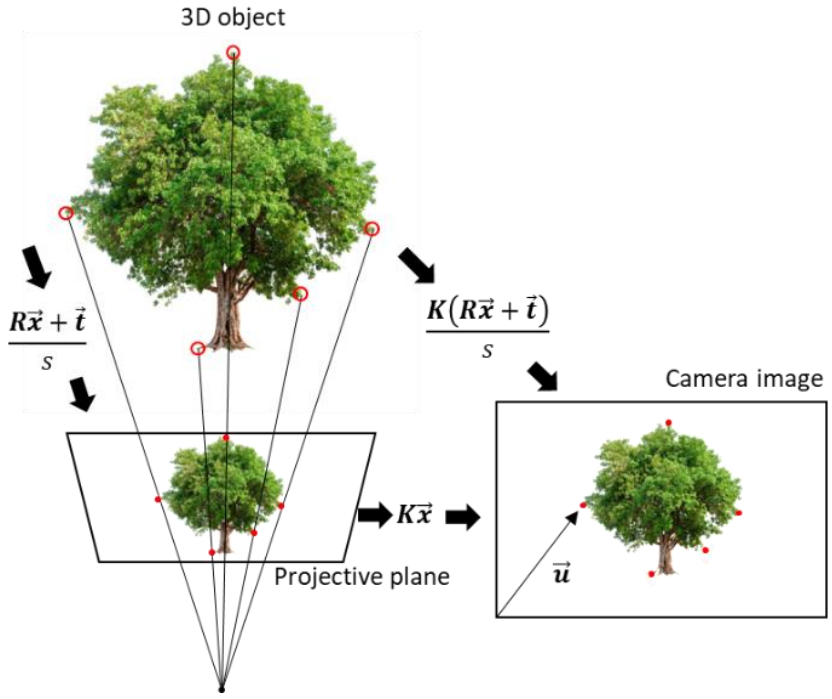

Figure 2.3 The pinhole camera model describing the projection of 3D points $\vec{\boldsymbol{x}}$, first to a projective plane, and then to the camera image.

The inverse of eq. (2.1) from an image point $\vec{\boldsymbol{u}}$ to a global point $\vec{\boldsymbol{x}}$ is given by

$$\vec{\boldsymbol{x}} = s\boldsymbol{R}^{-1}\boldsymbol{K}^{-1}\vec{\boldsymbol{u}} - \boldsymbol{R}^{-1}\vec{\boldsymbol{t}}, \tag{2.2}$$

or alternatively in the form

$$\vec{\boldsymbol{x}} = \vec{\boldsymbol{t}}' + s\vec{\boldsymbol{u}}'. \tag{2.3}$$

Given the parameters $\boldsymbol{K}$, $\boldsymbol{R}$ and $\vec{\boldsymbol{t}}$ are known, a single camera can define a global point $\vec{\boldsymbol{x}}$ to somewhere along a line in 3D space, given by the vector $\vec{\boldsymbol{u}}'$. This concept is shown in Figure 2.4, where the 3D object exists somewhere along the vectors defined by Eq. (2.3). The pinhole camera can define only in which direction global point $\vec{\boldsymbol{x}}$ exists, and not the depth along this direction. In other words, a pinhole camera can be considered as a direction sensor [33].

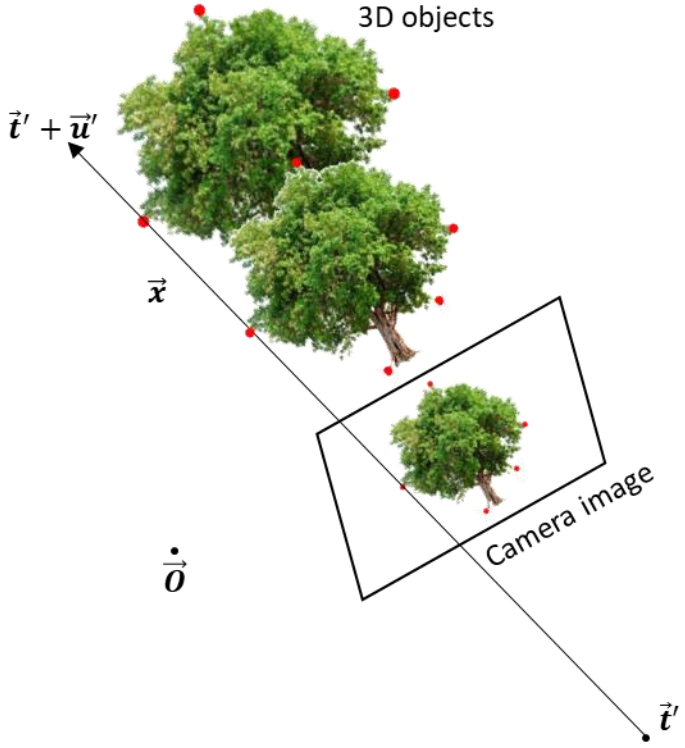

Figure 2.4 An arbitrarily rotated and translated camera defined as a direction sensor.

With two direction sensors, along with the known transformation between them, the original point $\vec{x}$ can be triangulated. Fringe projection systems triangulate 3D points by using both the camera and the projector as direction sensors, and therefore are known as triangulation-based optical CMSs.

2.3.2 Triangulation

This section will detail how to solve for the global position $\vec{x}$ using two direction sensors. This section will include a novel solution to the fringe projection measurement model that is simple to understand as well as faster than alternative solutions. In eq. (2.2) the parameter $\boldsymbol{K}$ is known and setting $\boldsymbol{R} = \mathbb{I}_3$ and $\vec{t} = \vec{0}$ without loss of generality, only the scalar s remains to be found. Consequently, only a single coordinate from a second direction sensor is required to fully realise the 3D point $\vec{x}$, provided the second direction sensor is sufficiently rotated and translated from the first. In fringe projection, a projector is modelled as a camera, so the camera and projector are both defined by two pinhole models given by

$$s_\mathrm{c}\vec{u}_\mathrm{c} = \boldsymbol{K}_\mathrm{c}\left(\boldsymbol{R}_\mathrm{c}\vec{x} + \vec{t}_\mathrm{c}\right) \tag{2.4}$$

$$s_\mathrm{p}\vec{u}_\mathrm{p} = \boldsymbol{K}_\mathrm{p}\left(\boldsymbol{R}_\mathrm{p}\vec{x} + \vec{t}_\mathrm{p}\right), \tag{2.5}$$

where the subscripts c an p distinguishes if the variable defines the camera or the projector. Defining the camera as a direction sensor gives

$$\vec{\boldsymbol{x}} = s_{\mathrm{c}}\boldsymbol{R}_{\mathrm{c}}^{-1}\boldsymbol{K}_{\mathrm{c}}^{-1}\vec{\boldsymbol{u}}_{\mathrm{c}} - \boldsymbol{R}_{\mathrm{c}}^{-1}\vec{\boldsymbol{t}}_{\mathrm{c}}. \tag{2.6}$$

The projection of a line in the projector's image space is shown in Figure 2.5.

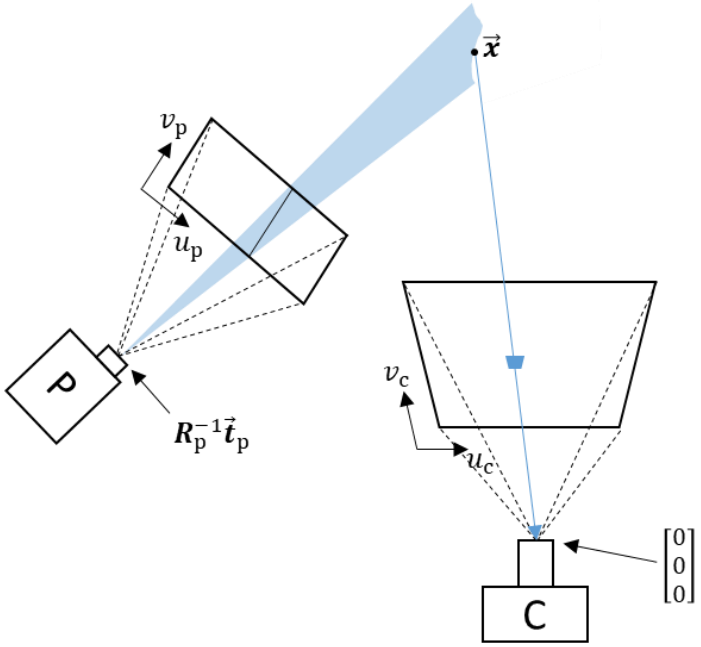

Figure 2.5 A projector in a fringe projection system projecting an image consisting of a single blue line.

The projection of a line in image space can be described as a plane in the global 3D coordinate system

$$\vec{\boldsymbol{n}} \cdot \left(\vec{\boldsymbol{x}} + \boldsymbol{R}_{\mathrm{p}}^{-1}\vec{\boldsymbol{t}}_{\mathrm{p}}\right) = 0, \tag{2.7}$$

where $\vec{\boldsymbol{n}}$ describes the plane normal of $\|\vec{\boldsymbol{n}}\| = 1$. The vector given by $-\boldsymbol{R}_{\mathrm{p}}^{-1}\vec{\boldsymbol{t}}_{\mathrm{p}}$ gives the origin of the projector coordinate system in a global coordinate system. Combining eq. (2.6) and eq. (2.7) gives

$$\left(-\boldsymbol{R}_{\mathrm{c}}^{-1}\vec{\boldsymbol{t}}_{\mathrm{c}} + s_{\mathrm{c}}\boldsymbol{R}_{\mathrm{c}}^{-1}\boldsymbol{K}_{\mathrm{c}}^{-1}\vec{\boldsymbol{u}}_{\mathrm{c}} + \boldsymbol{R}_{\mathrm{p}}^{-1}\vec{\boldsymbol{t}}_{\mathrm{p}}\right) \cdot \vec{\boldsymbol{n}} = 0, \tag{2.8}$$

and the unknown scalar s_{c} can be found using

$$s_{\mathrm{c}} = \frac{\left(\boldsymbol{R}_{\mathrm{c}}^{-1}\vec{\boldsymbol{t}}_{\mathrm{c}} - \boldsymbol{R}_{\mathrm{p}}^{-1}\vec{\boldsymbol{t}}_{\mathrm{p}}\right) \cdot \vec{\boldsymbol{n}}}{\boldsymbol{R}_{\mathrm{c}}^{-1}\boldsymbol{K}_{\mathrm{c}}^{-1}\vec{\boldsymbol{u}}_{\mathrm{c}} \cdot \vec{\boldsymbol{n}}}, \tag{2.9}$$

with the plane normal $\vec{\boldsymbol{n}}$ being a function of projector image coordinates. The plane normal $\vec{\boldsymbol{n}}$ is found using the cross-product of two vectors that exist on that plane. Defining the projector as a direction sensor,

$$\vec{\boldsymbol{x}} = -\boldsymbol{R}_{\mathrm{p}}^{-1}\vec{\boldsymbol{t}}_{\mathrm{p}} + s_{\mathrm{p}}\boldsymbol{R}_{\mathrm{p}}^{-1}\boldsymbol{K}_{\mathrm{p}}^{-1}\vec{\boldsymbol{u}}_{\mathrm{p}}, \tag{2.10}$$

and defining the two vectors on the plane to be $\vec{\boldsymbol{u}}_{\mathrm{p}}$ and $\vec{\boldsymbol{u}}_{\mathrm{p}} + \vec{\boldsymbol{\delta}}$, where $\vec{\boldsymbol{\delta}}$ is some vector that lies within the plane. Without loss of generality setting $s_{\mathrm{p}} = 1$, the plane normal is given by

$$\vec{\boldsymbol{n}} = \boldsymbol{R}_{\mathrm{p}}^{-1}\boldsymbol{K}_{\mathrm{p}}^{-1}\vec{\boldsymbol{u}}_{\mathrm{p}} \times \boldsymbol{R}_{\mathrm{p}}^{-1}\boldsymbol{K}_{\mathrm{p}}^{-1}\left(\vec{\boldsymbol{u}}_{\mathrm{p}} + \vec{\boldsymbol{\delta}}\right), \tag{2.11}$$

which is simplified to

$$\vec{\boldsymbol{n}} = \boldsymbol{R}_{\mathrm{p}}^{-1}\boldsymbol{K}_{\mathrm{p}}^{-1}\vec{\boldsymbol{u}}_{\mathrm{p}} \times \boldsymbol{R}_{\mathrm{p}}^{-1}\boldsymbol{K}_{\mathrm{p}}^{-1}\vec{\boldsymbol{\delta}}. \tag{2.12}$$

Under matrix transformations $\boldsymbol{R}_{\mathrm{p}}^{-1}\boldsymbol{K}_{\mathrm{p}}^{-1}$, the cross product is simplified to

$$\vec{\boldsymbol{n}} = \boldsymbol{R}_{\mathrm{p}}^{-1}\det\left(\boldsymbol{K}_{\mathrm{p}}^{-1}\right)\boldsymbol{K}_{\mathrm{p}}^{\mathrm{T}}\left(\vec{\boldsymbol{u}}_{\mathrm{p}} \times \vec{\boldsymbol{\delta}}\right). \tag{2.13}$$

The cross product $\vec{\boldsymbol{u}}_{\mathrm{p}} \times \vec{\boldsymbol{\delta}}$ can instead be represented as a linear mapping $\boldsymbol{A}\vec{\boldsymbol{u}}_{\mathrm{p}}$, where the linear encoding transform $\boldsymbol{A}$ defined explicitly by $\vec{\boldsymbol{\delta}}$, the vector parallel to the projected plane. For example, if the projected plane was projected along the x-axis, $\vec{\boldsymbol{\delta}} = [1 \quad 0 \quad 0]^{\mathrm{T}}$, then

$$\boldsymbol{A}_{\boldsymbol{x}} = \begin{bmatrix} 0 & 0 & 0 \\ 0 & 0 & 1 \\ 0 & -1 & 0 \end{bmatrix}. \tag{2.14}$$

If instead, the projected plane was along the y-axis, $\vec{\boldsymbol{\delta}} = [0 \quad 1 \quad 0]^{\mathrm{T}}$,

$$\boldsymbol{A}_{\boldsymbol{y}} = \begin{bmatrix} 0 & 0 & -1 \\ 0 & 0 & 0 \\ 1 & 0 & 0 \end{bmatrix}, \tag{2.15}$$

where subscripts have been used to differentiate the two transforms. The projected plane can be defined for any arbitrary direction. The final form for the plane normal is

$$\vec{\boldsymbol{n}} = \boldsymbol{R}_{\mathrm{p}}^{-1}\det\left(\boldsymbol{K}_{\mathrm{p}}^{-1}\right)\boldsymbol{K}_{\mathrm{p}}^{\mathrm{T}}\boldsymbol{A}\vec{\boldsymbol{u}}_{\mathrm{p}}. \tag{2.16}$$

Substituting eq. (2.16) into eq. (2.9) gives the final form to solve for s_{c}

$$s_{\mathrm{c}} = \frac{\left(\boldsymbol{R}_{\mathrm{c}}^{-1}\vec{\boldsymbol{t}}_{\mathrm{c}} - \boldsymbol{R}_{\mathrm{p}}^{-1}\vec{\boldsymbol{t}}_{\mathrm{p}}\right) \cdot \left(\boldsymbol{R}_{\mathrm{p}}^{-1}\boldsymbol{K}_{\mathrm{p}}^{\mathrm{T}}\boldsymbol{A}\vec{\boldsymbol{u}}_{\mathrm{p}}\right)}{\left(\boldsymbol{R}_{\mathrm{c}}^{-1}\boldsymbol{K}_{\mathrm{c}}^{-1}\vec{\boldsymbol{u}}_{\mathrm{c}}\right) \cdot \left(\boldsymbol{R}_{\mathrm{p}}^{-1}\boldsymbol{K}_{\mathrm{p}}^{\mathrm{T}}\boldsymbol{A}\vec{\boldsymbol{u}}_{\mathrm{p}}\right)}. \tag{2.17}$$

Setting the global coordinate system to be aligned with the camera for convenience, $\boldsymbol{R}_\mathrm{c} = \mathbb{I}_3$ and $\vec{\boldsymbol{t}}_\mathrm{c} = \vec{\boldsymbol{0}}$ gives

$$s_\mathrm{c} = \frac{\left(-\boldsymbol{R}_\mathrm{p}^{-1}\vec{\boldsymbol{t}}_\mathrm{p}\right)\cdot\left(\boldsymbol{R}_\mathrm{p}^{-1}\boldsymbol{K}_\mathrm{p}^{\mathrm{T}}\boldsymbol{A}\vec{\boldsymbol{u}}_\mathrm{p}\right)}{\left(\boldsymbol{K}_\mathrm{c}^{-1}\vec{\boldsymbol{u}}_\mathrm{c}\right)\cdot\left(\boldsymbol{R}_\mathrm{p}^{-1}\boldsymbol{K}_\mathrm{p}^{\mathrm{T}}\boldsymbol{A}\vec{\boldsymbol{u}}_\mathrm{p}\right)}. \tag{2.18}$$

Note, this is a novel approach to fringe projection triangulation compared to alternative methods [34, 35]. Eq. (2.18) solves for the unknown scale, s_c, allowing the full triangulation of a 3D point from the camera. The function inputs include the camera and projector 2D image coordinates, $\{\vec{\boldsymbol{u}}_\mathrm{c}, \vec{\boldsymbol{u}}_\mathrm{p}\}$, as well as a series of constants $\{\boldsymbol{K}_\mathrm{c}, \boldsymbol{K}_\mathrm{p}, \boldsymbol{R}_\mathrm{p}, \vec{\boldsymbol{t}}_\mathrm{p}\}$. The constants $\{\boldsymbol{K}_\mathrm{c}, \boldsymbol{K}_\mathrm{p}, \boldsymbol{R}_\mathrm{p}, \vec{\boldsymbol{t}}_\mathrm{p}\}$ are the system's quantity values that define the relation between 2D image coordinates $\{\vec{\boldsymbol{u}}_\mathrm{c}, \vec{\boldsymbol{u}}_\mathrm{p}\}$ to the final 3D point $\vec{\boldsymbol{x}}$, and will hereby be called the system parameters, and will be denoted using a single vector holding the component values of $\{\boldsymbol{K}_\mathrm{c}, \boldsymbol{K}_\mathrm{p}, \boldsymbol{R}_\mathrm{p}, \vec{\boldsymbol{t}}_\mathrm{p}\}$. For completeness, the full triangulation function is given as

$$f_\Delta\left(\vec{\boldsymbol{u}}_\mathrm{c}, \vec{\boldsymbol{u}}_\mathrm{p}, \vec{\boldsymbol{\theta}}\right) = \frac{\left(\boldsymbol{R}_\mathrm{p}^{-1}\vec{\boldsymbol{t}}_\mathrm{p}\right)\cdot\left(\boldsymbol{R}_\mathrm{p}^{-1}\boldsymbol{K}_\mathrm{p}^{\mathrm{T}}\boldsymbol{A}\vec{\boldsymbol{u}}_\mathrm{p}\right)}{\left(\boldsymbol{K}_\mathrm{c}^{-1}\vec{\boldsymbol{u}}_\mathrm{c}\right)\cdot\left(\boldsymbol{R}_\mathrm{p}^{-1}\boldsymbol{K}_\mathrm{p}^{\mathrm{T}}\boldsymbol{A}\vec{\boldsymbol{u}}_\mathrm{p}\right)}\boldsymbol{K}_\mathrm{c}^{-1}\vec{\boldsymbol{u}}_\mathrm{c}. \tag{2.19}$$

The assumption made here, is that both the camera and projector are accurately described by the pinhole camera model and the projected line from the projector is infinitely thin. However, both the camera and the projector are subject to optical distortions (see Section 2.3.3) and resolution limitation of the optics (a discussion is given in Section 2.3 and Section 3.1).

Alternative methods exist that range in simplicity, accuracy, and computational speed. A comparable method is Zhang's method [34], with both methods sharing the same assumptions. The method presented here, however, is faster and more memory-efficient compared to Zhang's method. The eq. (2.18) can be simplified to a single rational equation to allow rapid triangulation

$$s_\mathrm{c} = \frac{a\eta + b}{(c + du_\mathrm{c} + ev_\mathrm{c})\eta + f + gu_\mathrm{c} + hv_\mathrm{c}}, \tag{2.20}$$

where the encoding projector coordinates have been replaced by a single coordinate η. Eq. (2.19) is identical with Zhang's method up to numerical precision but has fewer operations per pixel required to define the final 3D point $\vec{\boldsymbol{x}}$ – a comparison is given in Table 2.1. The computational speed boost will be useful later for the method give in Section 8.1.

Table 2.1 Comparison of the number of operations per pixel between triangulation methods.

	Total number of operations (per pixel)	Number of stored variables (total)
Eq. (2.19)	32	13
Zhang	537	20

To compare the computation time and accuracy between the Zhang's method and Eq. (2.19), 300 random measurement scenarios were created by drawing values from uniform distributions defined in Table 2.2. The principle point was taken to be the centre of the image for both the camera and projector. The results can be found in Figure 2.6.

Table 2.2 Uniform distributions for testing Eq. (2.19) against Zhang's method.

	Input	Mean Value	Half-width
Camera	Focal length - x	1200	100
	Focal length - y	1200	100
	Resolution - x	1024	300
	Resolution - y	768	300
	Skew	0	0
Projector	Focal length - x	600	100
	Focal length - y	600	100
	Resolution - x	1024	300
	Resolution - y	768	300
	Skew	0	0
Extrinsics	Focus point - x	0	100
	Focus point - y	0	100
	Focus point – z	1000	100
	Translation – x	0	100
	Translation – y	0	100
	Translation – z	0	100
	Correspondence map	$\frac{1}{2}\times$Projector resolution - x	$\frac{1}{2}\times$Projector resolution - x

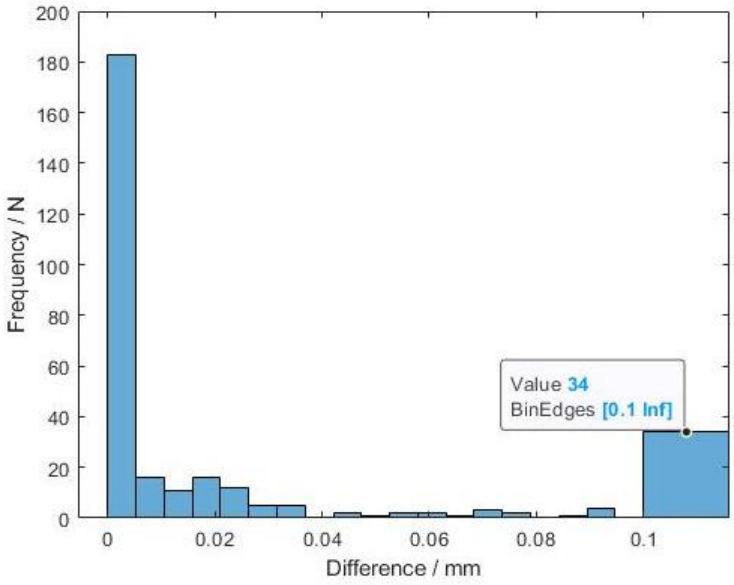

(a)

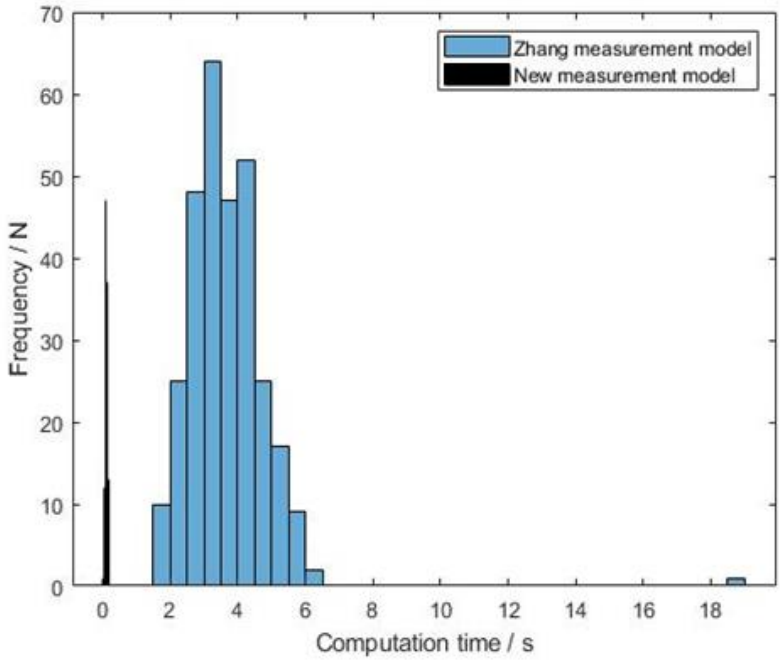

(b)

Figure 2.6 Comparison of the model used here and Zhang's measurement model in terms of (a) maximum absolute difference between points and (b) computation time.

The simple rational function given in eq. (2.19) is very similar to the alternative linear, polynomial and inverse models given in [30]. While some alternative methods can achieve comparable accuracy, the method described above is typically more robust when measuring objects outside of the volume that encompasses all the measured points used within the calibration, also known as the calibration volume.

A common issue of simpler models is that the linear assumptions used in these models are only valid for certain positions in the measurement volume [36]. The linear method only approximates the model well over a small measurement height and is subject to stricter geometric constraints. The inverse linear method captures more of the rational nature of the eq. (2.19), and is not subject to any such geometric constraints. Polynomial models are sometimes favoured for their simplicity as they effectively eliminate the need for distortion correction since the calibration is performed locally across the image [37] – but they are subject to over-fitting issues. More complex methods, such as the cross-ratio method [38], are effectively insensitive to common fringe projection problems, such as pixel-to-pixel non-linearity, but the disadvantage is that they require a precision motion stage during the calibration. Lately, using neural networks to perform the triangulation have become increased in popularity, but typically require a lot of training data, which is time-consuming to create [39], although this can be overcome with virtual training [40] or unsupervised learning techniques [41].

2.3.3 Distortion model

This section will detail the nonlinear extension to the pinhole camera model described in Section 2.3.1. The pinhole model described in Section 2.3.1 is an idealisation of the true nature of optical devices, being a geometrical interpretation of light propagation. In fact, an optical device will always exhibit geometric distortions and aberrations, due to imperfect optics and the wave nature of light. Therefore, additional nonlinear terms are included to model the distortion apparent in all cameras. The mathematical model used for this purpose is called the distortion model.

Several distortion models exist in literature, varying greatly in simplicity and accuracy [42]. Distortion correction is typically a trade-off between accuracy and numerical stability during the calibration procedure [42], with complexity varying from a couple of parameters [43] to many [44]. A common distortion model is the Brown-Conrady model [45], that splits the distortion into radial and tangential components, although other representations exist [46-48]. Despite the popularity of the Brown-Conrady model, there is ongoing debate about the importance of certain distortion coefficients with respect to accuracy. Although it is rarer to include the distortion centre as a parameter, Sun and Cooperstock [49] found that the distortion centre is an important parameter to include. Each optical system will have its own distortion that will lend itself to certain models [42]. It is worth noting that some triangulation methods, including the polynomial model, inherently correct for optical distortion, but still have the problem in deciding how many parameters is sufficient [50].

Due to the widely accepted use of the Brown-Conrady model [35, 51-53], it was chosen as the modelling function for this thesis. The distortion function is given by

$$f_{\mathrm{D}}(\vec{\boldsymbol{u}}, \vec{\boldsymbol{\tau}}) = \vec{\boldsymbol{u}}_{\mathrm{D}} \tag{2.21}$$

$$\begin{aligned}\vec{\boldsymbol{u}}_{\mathrm{D}} = (\vec{\boldsymbol{u}} - \vec{\boldsymbol{u}}_{\mathrm{DC}})(1 + k_1 r^2 + k_2 r^4 + k_3 r^6) \\ + \left(\begin{bmatrix} p_1 \\ p_2 \end{bmatrix} w + \begin{bmatrix} p_2 \\ p_1 \end{bmatrix} (r^2 + 2(\vec{\boldsymbol{u}} - \vec{\boldsymbol{u}}_{\mathrm{DC}})^2) \right) + \vec{\boldsymbol{u}}_{\mathrm{DC}}\end{aligned} \tag{2.22}$$

with distortion centre given by $\vec{\boldsymbol{u}}_{\mathrm{DC}} = [u_{\mathrm{DC}}, v_{\mathrm{DC}}]^{\mathrm{T}}$ and distortion coefficients given by $\vec{\boldsymbol{\tau}} = [k_1 \quad k_2 \quad k_3 \quad p_1 \quad p_2 \quad u_{\mathrm{DC}} \quad v_{\mathrm{DC}}]$. The quantities r and w are defined by

$$r^2 = (u - u_{\mathrm{DC}})^2 + (v - v_{\mathrm{DC}})^2 \tag{2.23}$$

$$w = (u - u_{\mathrm{DC}})(v - v_{\mathrm{DC}}). \tag{2.24}$$

The radial and tangential components of the Brown-Conrady model are shown in Figure 2.7.

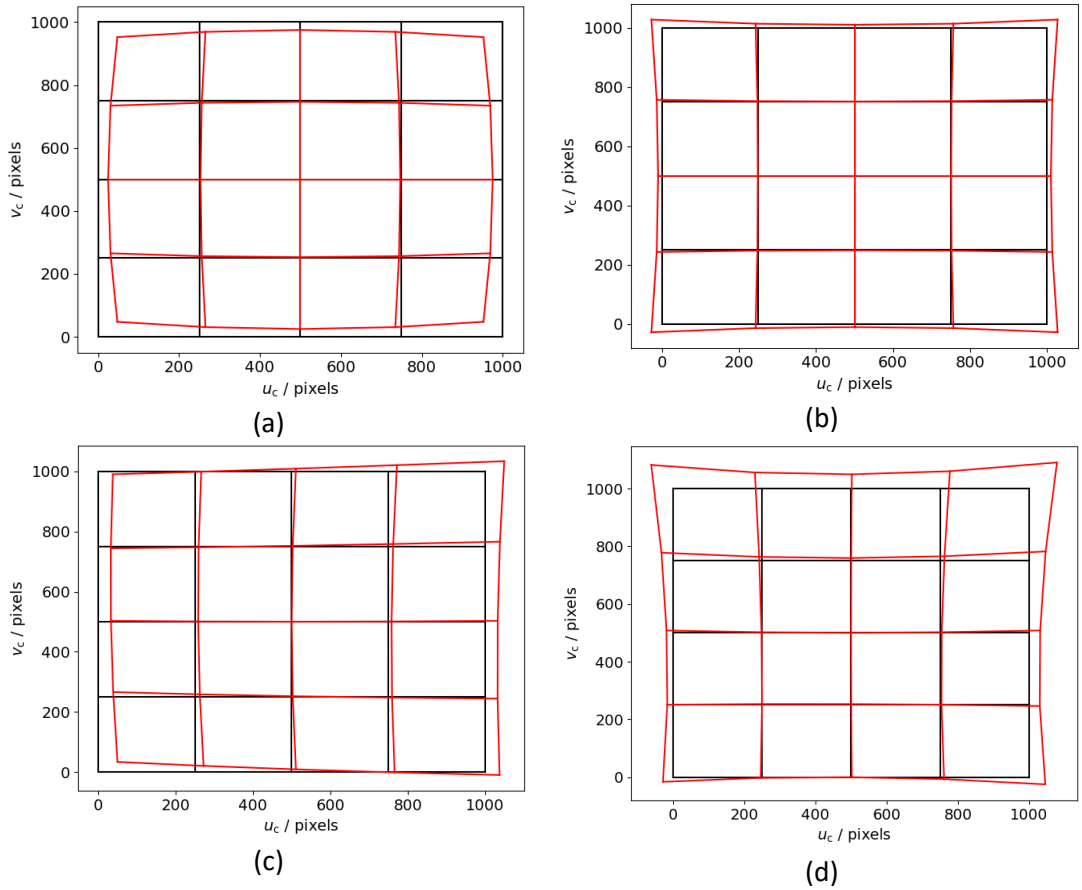

Figure 2.7 Distortion modelled using the Brown-Conrady model. Distortions shown are (a) radial "barrel" distortion, (b) radial "pincushion" distortion, (c) tangential distortion and (d) combined radial and tangential distortion.

The distortion function $f_{\mathrm{D}}(\vec{\boldsymbol{u}}, \vec{\boldsymbol{\tau}})$ is unique to each (u, v) image location, yet the projector only needs to resolve one dimension during the correspondence decoding

phase to fully triangulate a 3D point. If only one axis of the projector 2D image point is resolved during the correspondence stage, the projector point cannot immediately undergo a distortion correction. It is common therefore, to pre-distort the projector images prior to a measurement, so the distortion converts the image back to its ideal [51]. In this thesis, it was instead chosen to repeat the correspondence twice to resolve both axes of the 2D image point of the projector, i.e., projecting both horizontal and vertical fringes to fully define the projector image location.

2.3.4 Distortion correction

In Section 2.3.3, a model was given that described the typical nonlinear distortion found in all cameras. This model, in conjunction with the camera pinhole model, describes the propagation of light from an object to the charge-coupled device (CCD) in the camera (called "forward" propagation). However, the triangulation method given in Section 2.3.2, eq. (2.22), describes the inverse operation (called "backwards" propagation). However, eq. (2.22) has no analytical inverse. Some simple radial-only distortions can be analytically inverted [54], but most distortion models cannot. Most inverse distortions are computed numerically instead [55]. To enable a fast triangulation method, a simple, quick algorithm is needed, to estimate the pre-distorted coordinates given the distorted coordinates and distortion coefficients. The pre-distorted coordinates can be found with the following numerical algorithm, given in Algorithm 1, called fixed-point iteration, used by OpenCV 4.5.5 [56].

Algorithm 1 Fixed-point iteration method used as the inverse mapping operation.

Take estimate of undistorted point as the same as the distorted point $\vec{\boldsymbol{u}}_i = \vec{\boldsymbol{u}}_{\mathrm{DC}}$
While not converged:
    Compute distortion of estimated point $f_{\mathrm{D}}(\vec{\boldsymbol{u}}_i, \vec{\boldsymbol{\tau}}) = \hat{\boldsymbol{u}}_{\mathrm{DC},i}$
    Find difference between distorted estimate and actual point
        $\vec{\boldsymbol{u}}_i - \hat{\boldsymbol{u}}_{\mathrm{DC},i} = \vec{\boldsymbol{\delta}}_i$
    Update estimate with the difference $\vec{\boldsymbol{u}}_{i+1} = \vec{\boldsymbol{u}}_i + \vec{\boldsymbol{\delta}}_i$
    Iterate $i = i + 1$
    Compute the magnitude of the change during this iteration $\|\vec{\boldsymbol{\delta}}_i\|$
    If $\|\vec{\boldsymbol{\delta}}_i\| < \epsilon$:
        The method has converged.
    End If
End While

The fixed-point iteration method is only guaranteed to be converge to the correct answer under specific conditions. Using the above definitions, defining the function

$$g(\vec{\boldsymbol{u}}) = f_{\mathrm{D}}(\vec{\boldsymbol{u}}, \vec{\boldsymbol{\tau}}) - \vec{\boldsymbol{u}}_{\mathrm{D}}, \tag{2.25}$$

where $\vec{\boldsymbol{u}}_{\mathrm{D}}$ and $\vec{\boldsymbol{\tau}}$ are considered known constants, $g(\vec{\boldsymbol{u}}) = 0$ when $\vec{\boldsymbol{u}}$ correctly maps to $\vec{\boldsymbol{u}}_{\mathrm{D}}$, i.e., when the inverse is found. This mapping is only guaranteed to be found by the fixed-point iteration method in the case

$$0 < \frac{\mathrm{d}}{d\vec{\boldsymbol{u}}} g(\vec{\boldsymbol{u}}) \leq 1 \tag{2.26}$$

for all values of $\frac{\mathrm{d}}{d\vec{\boldsymbol{u}}} g(\vec{\boldsymbol{u}})$, i.e. the distortion function must be monotonically increasing. Typically, a camera's distortion function is monotonically increasing over the CCD area, a camera that fails this condition will not make a usable direction sensor given each pixel will not have a well-defined direction and will therefore invalidate the triangulation method.

Computing the derivatives is one method to test for convergence. An alternative simple method is to test the convergence using a set of predetermined values. Firstly, an estimation of the distortion coefficients, along with the camera matrix, is supplied by calibrating the camera using the method given in Chapter 7. Then, each distortion coefficient τ_i is sampled from a uniform distribution, $\mathcal{U}(0.5\tau_i, 1.5\tau_i)$. For alacrity, only 100×100 points are sampled across the CCD, sampled evenly in the range 0 to 5120 in both axes (see Section 2.2), to be distorted. The points are distorted using the analytical function eq. (2.22), and then corrected using the fixed-point iteration method, Algorithm 1. The original and the undistorted points are then analysed for their maximum absolute error. This is repeated 10,000 times and the results in Figure 2.8 show that the fixed-point iteration method converges as expected within the region of the estimation of the distortion coefficients provided by the camera calibration. The error of the fixed-point iteration method in this circumstance is less than 2×10^{-3} pixels and 0.5×10^{-3} pixels in the camera and projector respectively – and is therefore considered negligible.

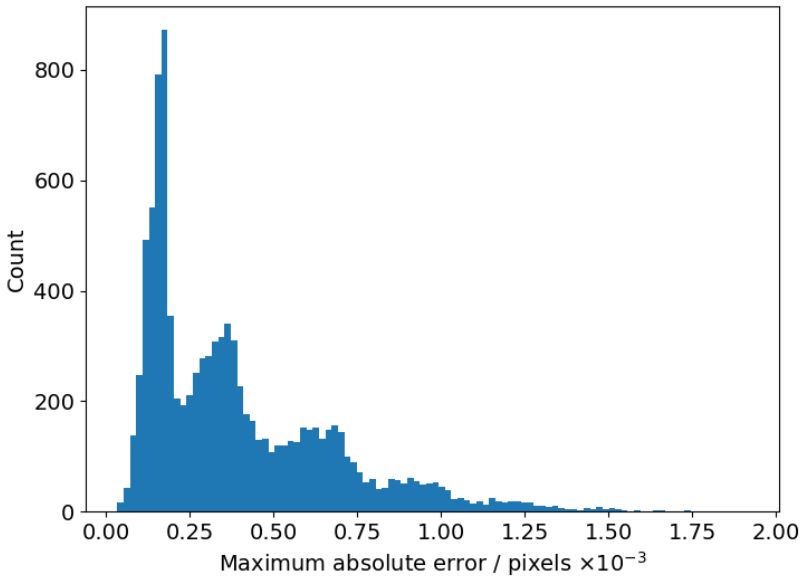

(a)

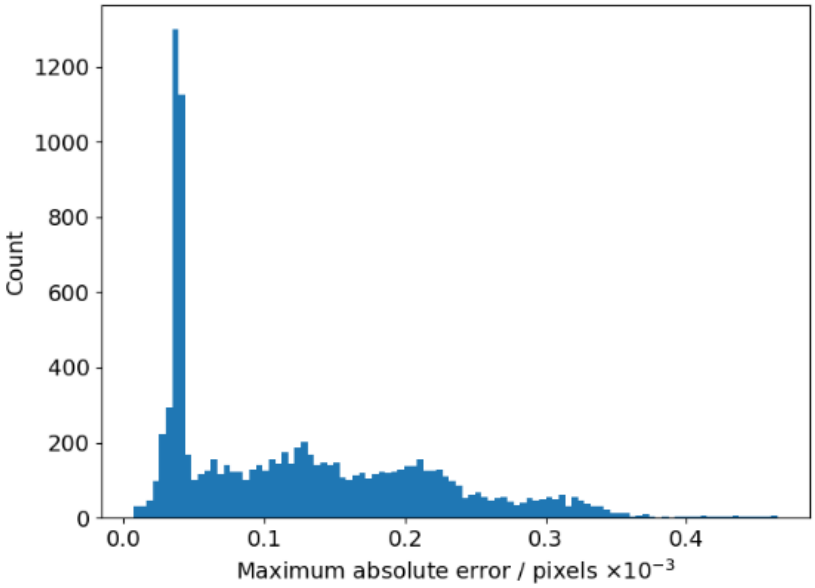

(b)

Figure 2.8 The maximum absolute error from the distortion-correction algorithm. Error is given for (a) the camera parameters and (b) the projector parameters.

2.4 Correspondence decoding

In this section, the method used to provide the 2D points within the camera and projector image plane that correspond to the same 3D point in global space is defined. 2D image points that originate from the same 3D points are "corresponding image points" will hereby be shortened to "correspondences".

In Section 2.3.2, it was demonstrated that only a single additional measurement dimension is necessary to encode information to fully-realise a 3D point. A simple algorithm, then, could project a series of individual lines from the projector. The problem with this approach is that, to obtain a full-field measurement, it would take a considerable amount of time. Instead, modern techniques utilise the full projector image and decode all pixels at once. The correspondence algorithm method can be seen as a communication problem, with each projector pixel as a transmitter and the camera pixels as receivers. The projection signal is subject to degradation and aberration from the optics of the projector and camera and the surface of the object being measured. The objective of the correspondence algorithm is to provide accurate correspondence information as robustly as possible, using as few images as possible.

Correspondence algorithms typically favour using low spatial-frequency content in the projection images. The optical resolution of the projector will limit the higher spatial-frequency content of projected images. This can be used, to a great effect, to remove higher spatial-frequency errors/noise from projected images [57, 58]. Correspondence algorithms therefore usually encode correspondence information in the phase of projected sinusoids [59] – although this is not always the case [60].

A common correspondence algorithm is the three-phase shift algorithm. A series of sinusoids are projected, each with a specific phase-shift, and the projector locations are encoded into the sinusoids phase. The underlying phase distribution can then be found. The intensity of a fringe pattern across k^{th} image I_k can be expressed as

$$I_k(u,v) = A\cos(\phi(u,v) + \delta_k) + B, \tag{2.27}$$

where $\phi(u,v)$ is the phase distribution, δ_k is the phase shift and coefficients A and B are the contrast and offset coefficients respectively. Using the phase shifts $\delta_k = \left\{-\frac{2\pi}{3}, 0, \frac{2\pi}{3}\right\}$, the "wrapped" phase distribution $\phi_{\text{w}}(u,v)$ is found along with a quality metric $\gamma(u,v)$ using

$$\phi_{\text{w}}(u,v) = \tan^{-1}\left(\frac{\sqrt{3}(I_0 - I_2)}{2I_1 - I_0 - I_2}\right) \tag{2.28}$$

$$\gamma(u,v) = \frac{A}{B} = \frac{\sqrt{3(I_0 - I_2)^2 + (2I_1 - I_0 - I_2)}}{I_0 + I_1 + I_2}. \tag{2.29}$$

While sinusoids avoid the spatial-frequency cut-off, they are periodic, and so certain pixels across the projector image will contain identical information. The obtained phase distribution $\phi_{\text{w}}(u,v)$ is said to be wrapped, since $\phi_{\text{w}}(u,v) = \text{mod}(\phi(u,v), 2\pi P)$, with P denoting the fringe pitch (wavelength of the projected fringes). The wrapped phase $\phi_{\text{w}}(u,v)$ is therefore defined within the range $[0, 2\pi P)$. A larger fringe pitch can be used at the expense of sensitivity [61]. The conversion of the wrapped phase to the

absolute (or "unwrapped" phase) is called unwrapping. The decoding via three-phase shifting is shown in Figure 2.9.

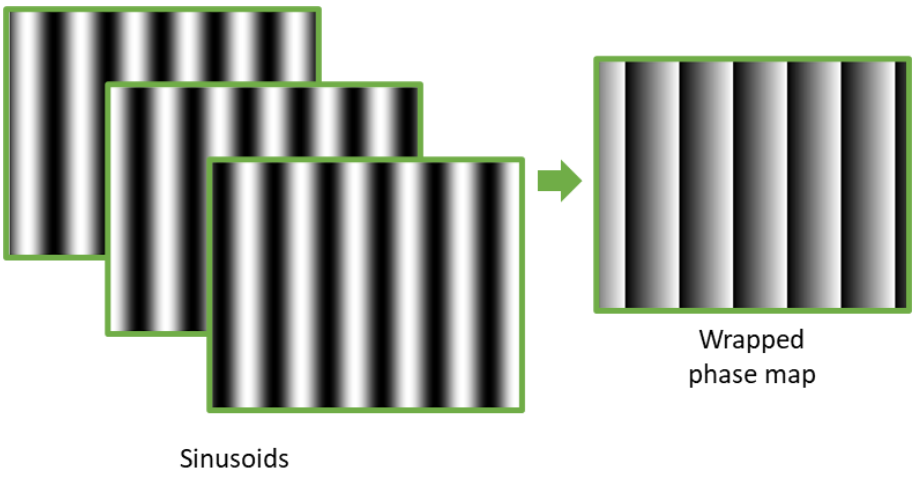

Figure 2.9 The "wrapped phase" defined from using three phase-shifted sinusoid images.

Correspondence algorithms can generally be classified into two different categories, spatial and temporal algorithms [35], although some newer algorithms combine the two as spatiotemporal algorithms [62]. Spatial algorithms decode the correspondence information across the captured image, or "spatially", so generally require fewer images. Since only one image is required, spatial correspondence algorithms have a lower acquisition time [63] and are favoured in high-speed situations.

Common spatial algorithms include the Fourier transform, windowed Fourier transform and the wavelet transform methods [64-66]. Other spatial algorithms include adding additional information to the projected image [67] or using parameter information [68, 69]. Temporal algorithms decode the correspondence information across multiple images of altering projections, or "temporally". Temporal algorithms are, in general, far more robust and accurate at the cost of higher acquisition time and are therefore favoured in metrological applications [70-72].

Popular temporal algorithms include heterodyne [73, 74], multi-frequency [75] and number-theoretical methods [76], and state-of-the-art systems have begun using neural networks to obtain the absolute phase map [77, 78]. The heterodyne method is considered accurate but prone to more unwrapping errors than other methods [71]. The general method behind the heterodyne method is to use the heterodyne principle to create artificially large fringe pitches that can be used to unwrap shorter fringes. The multi-frequency method projects larger fringe pitches (increasing fringe pitch P) to unwrap the shorter fringe pitches [79]. The number-theoretical method relies on fringe integers being co-prime throughout the image, therefore never sharing a common fringe jump.

For this thesis, it was decided that a modified heterodyne technique, given in Lai, Li [80], will be used for its simplicity and robustness against phase-unwrapping errors. The i^{th} phase map is made up of an integer order Φ_i and a fractional order $\Delta\phi_i$, $\phi_i = \Phi_i + \Delta\phi_i$. Fringe pitches are given by $P_1 < P_2 < P_3$. The integer order $\Phi_3 = 0$ because P_3 is chosen so that it spans the entire image. The phase maps can be successively unwrapped with

$$\Phi_2 = \text{round}\left(\frac{P_3\Delta\phi_3}{P_2} - \Delta\phi_2\right) \tag{2.30}$$

$$\Phi_1 = \text{round}\left(\frac{P_2(\Phi_2 + \Delta\phi_2)}{P_1} - \Delta\phi_1\right) \tag{2.31}$$

$$\phi_1 = \Phi_1 + \Delta\phi_1, \tag{2.32}$$

giving an absolute phase map. Three phase maps were used in this case, but this technique is not limited to three. The modified heterodyne method is shown graphically in Figure 2.10.

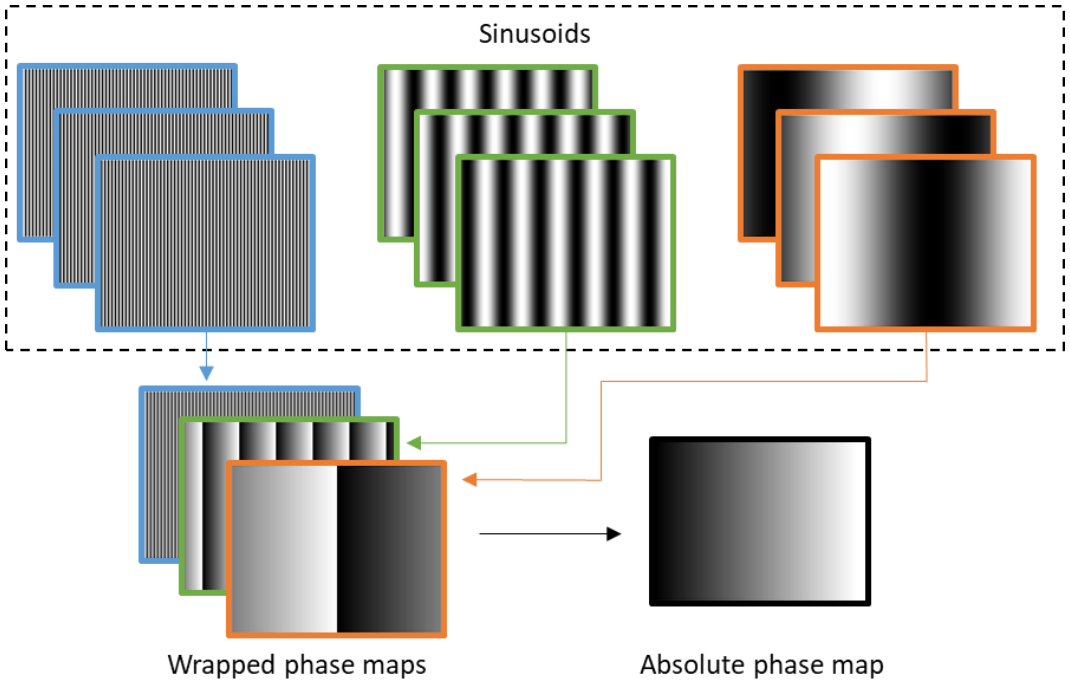

Figure 2.10 The modified heterodyne method. The largest wrapped phase map is used to unwrap the second largest phase map, which in turn is used to unwrap the final highest frequency phase map.

The correspondence decoding allows the indirect observation of the projector image, as if the projector is an equivalent camera. In Figure 2.11, the camera images are of a dot-grid artefact, and the modified heterodyne method above was then used to infer

what the projector was seeing by interpolating from the camera images. The borders were manually cropped, the images rescaled and noisy pixels were removed for clarity.

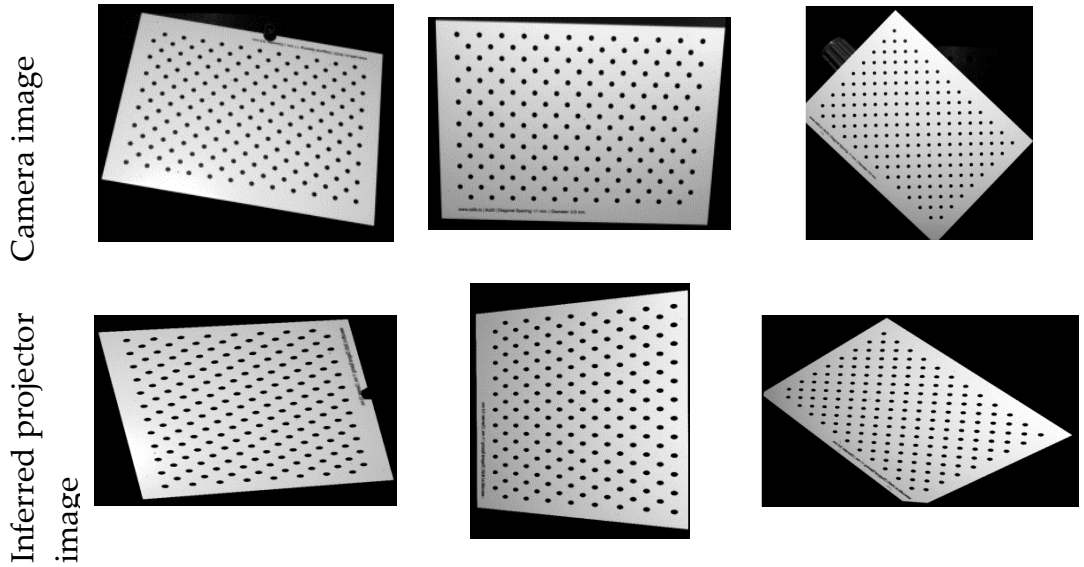

Figure 2.11 Projector images (bottom) inferred from camera images (Top)

2.4.1 Pixel-to-pixel calibration

In Section 2.4, it is assumed above that a projected sinusoid is recorded as a sinusoid within the camera. In other words, the projector output is related to the camera input with a single additive and multiplicative component

$$I_{\mathrm{c}} = A + BI_{\mathrm{p}}. \tag{2.33}$$

If this is not true, the sinusoid will become corrupted with higher-order components and cannot be modelled by eq. (2.27) giving a systematic error within the phase map [81]. Often, projectors are "corrected" for human vision by varying the output intensity exponentially instead of linearly. Correcting for this is called "gamma correction". This correction is completed by modelling the relationship $I_{\mathrm{c}} = f(I_{\mathrm{p}})$ and computing the inverse function f^{-1} so that eq. (2.27) is true.

A poor camera-projector response function will give a systematic error throughout the measurement volume. Like optical distortion, there are two main ways of compensating for this error: active and passive compensation. Active compensation alters the input projection image, so the image is pre-distorted, back to the original image. Passive compensation alters the camera image output instead. Active is recommended since it does not change with projector defocus [82]. Alternatively, modified phase-shifting methods can be used that will not produce an error when the system exhibits some form of gamma [83].

To perform a gamma correction, a series of images of a single intensity are projected, allowing the camera-projector response to be modelled. In a first step, the gamma correction measures the response curve of the camera input by gradually increasing the projector output. The basic gamma response curve model is given by

$$I_{\text{cam}} = aI_{\text{proj}}^{\gamma} + b. \tag{2.34}$$

It has been found that many projectors do not follow such a simple model and instead require a seventh order polynomial [35],

$$I_{\text{cam}} = \sum_{i=0}^{7} c_i I_{\text{proj}}^{i}. \tag{2.35}$$

Additionally, the camera and projector can suffer from synchronisation issues that can lead to nonlinear pixel-to-pixel response. A typical projector produces a specific intensity value by switching a micromirror on and off rapidly, creating an intensity value from a series of on/off switches. The array of micromirrors is called a digital micromirror device (DMD). Each image is projected as a series of 1-bit images sequentially over a specific time interval.

Consider a time interval split into 256 equal time periods, given that the projected image is an 8-bit image. Using the most significant bit first scheme, during the first 128 periods, the first bit is projected, and for the next 64 periods the second bit is projected, and so on. In this way, a specific intensity given as an 8-bit number is described over a specific time interval using 8 1-bit images, the diagram showing this is given in Figure 2.12.

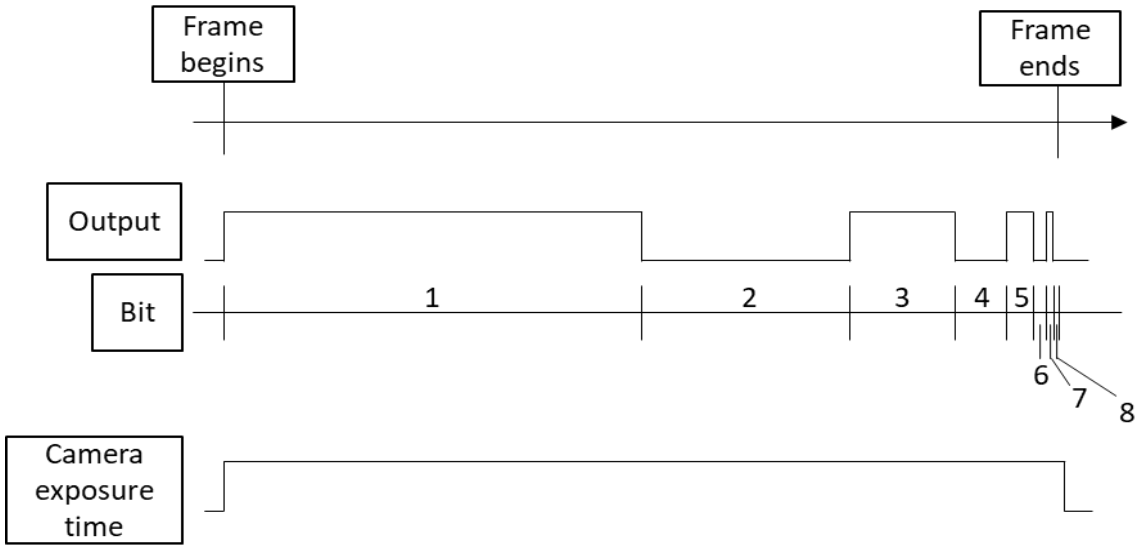

Figure 2.12 A DMD pixel projecting the intensity value 170 (10101010) as a series of off-on exposures.

To obtain a linear camera-projector response, it is very important for the camera to expose its charge-coupled device (CCD) for the duration of the on-off sequence. If the camera-projector pair are out of sync, there will be partial integrations of frames, leading to non-correctable, non-linear relationships. Projectors that use liquid crystal displays (LCD) or liquid crystal on silicon (LCoS) have far less stringent synchronisation requirements because they do not encode intensity temporally [84]. A camera-projector response curve considering gamma or asynchronisation is given in Figure 2.13.

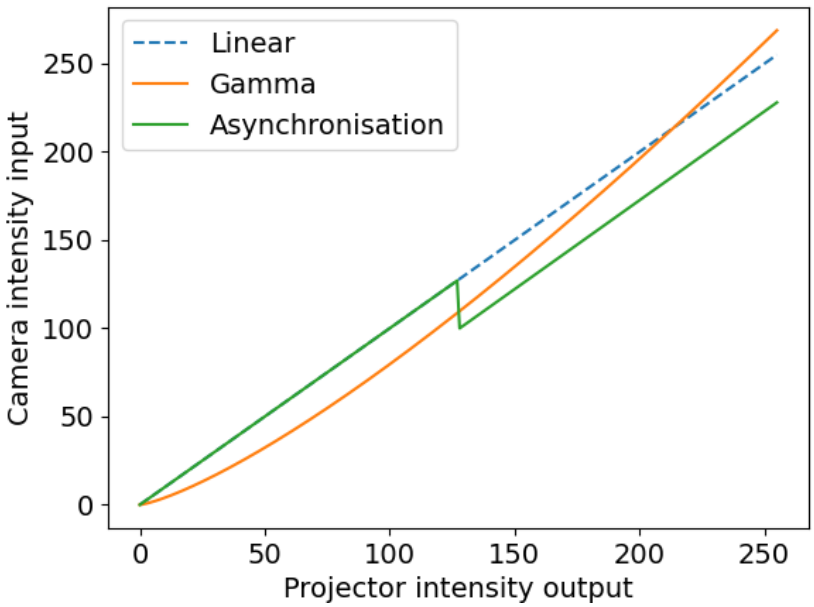

Figure 2.13 Camera-projector response curves. (blue dashed line) Linear response, (orange line) an uncorrected gamma response, and (green line) a non-linear response from an asynchronous camera-projector.

Synchronisation is usually achieved using an external signal. An external signal, sent to both the camera and projector simultaneously can trigger both to begin exposing the CCD and projecting images respectively. A projector could also send a trigger signal to indicate an image is currently being projected. The final step is to tune delays within the projector or camera to synchronise both to each other. Alternative methods include using software [85] or using field programmable gate arrays (FPGA) to handle the synchronisation of multiple cameras and projectors [86-88].

2.5 Extension to over-determined systems

The fringe projection techniques so far have been limited to single projector-camera systems that solve the triangulation exactly. This thesis is limited in scope to single camera/projector fringe projection systems, but for completeness, fringe projection methods that include additional cameras will be given here, where each 3D point is over-determined.

The triangulation method in Section 2.3.2 can be extended to over-determine each point with just one camera and projector by leveraging the two dimensions of the projector, instead of just one. Eq. (2.6) can be altered, and the subscript i will now differentiate M different camera sensors, instead of differentiating the camera and projector.

$$\vec{\boldsymbol{x}} = s_i \boldsymbol{R}_i^{-1} \boldsymbol{K}_i^{-1} \vec{\boldsymbol{u}}_i - \boldsymbol{R}_i^{-1} \vec{\boldsymbol{t}}_i, \tag{2.36}$$

$$\vec{\boldsymbol{x}} = \vec{\boldsymbol{t}}_i' + s_i \vec{\boldsymbol{u}}_i', \tag{2.37}$$

The problem now becomes finding the over-determined intersection of M lines; the solution can be found in Juarez-Salazar, Giron [33],

$$\vec{\boldsymbol{x}} = \left(\sum_{i=0}^{M} \boldsymbol{D}_i \right)^{-1} \left(\sum_{i=0}^{M} \boldsymbol{D}_i \vec{\boldsymbol{t}}_i' \right) \tag{2.38}$$

$$\boldsymbol{D}_i = \mathbb{I}_{3\times 3} - \frac{\vec{\boldsymbol{u}}_i' \vec{\boldsymbol{u}}_i'^{\mathsf{T}}}{\vec{\boldsymbol{u}}_i'^{\mathsf{T}} \vec{\boldsymbol{u}}_i'}. \tag{2.39}$$

Fringe projection systems with additional cameras have a unique advantage over single camera/projector systems – the measurement can be derived entirely from the two cameras. Instead of using the projector to solve for s_c in eq. (2.4), the projector exclusively provides correspondence points for the two cameras [32]. The realisation of projector pixel locations is guaranteed to be more error prone than the camera since pixel locations are inferred from the camera. Therefore, the advantage of this method is that measurement accuracy is no longer dependent on the projector and the realisation of its parameters.

This method will no longer provide an exact correspondence solution due to noise within the camera images, and so the phase maps within each camera must be correlated [89-91], which can be time consuming [92], rather than analytically solved. The extra correlation step adds complexity which was considered unnecessary for this thesis.

2.6 Frustrum model

This section will expand upon the concepts first defined in Section 2.3, to create a model that will give an intuitive framework to describe the concept of errors in fringe projection. The model created here will be used throughout this thesis. This section will be based on the concept of direction sensors, defined in Section 2.3.1, and how they can be used to recreate a 3D object, given in Section 2.3.2. In fringe projection, the projector acts only as an additional sensor to ascertain depth within the camera

coordinate system. Considering fringe projection in this way allows a simple interpretation of fringe projection using projective (also called homogeneous) coordinates. A point in Cartesian coordinates is represented in projective coordinates by

$$\begin{bmatrix} x/w \\ y/w \\ 1 \end{bmatrix}, \tag{2.40}$$

where the z coordinate has been replaced by depth coordinate w for clarity. Projective coordinates give an instinctive way to deal with direction sensors. By arbitrarily describing the camera coordinate system as aligned with the global coordinate system ($\boldsymbol{R} = \mathbb{I}_{3\times3}$, $\vec{\boldsymbol{t}} = \vec{\boldsymbol{0}}$), eq.(2.3) becomes

$$\vec{\boldsymbol{x}} = s\left(\boldsymbol{K}_\mathrm{p}, \vec{\boldsymbol{\tau}}_\mathrm{p}, \boldsymbol{R}_\mathrm{p}, \vec{\boldsymbol{t}}_\mathrm{p}\right)\begin{bmatrix} u_\mathrm{c}'(\boldsymbol{K}_c, \vec{\boldsymbol{\tau}}_\mathrm{c}) \\ v_\mathrm{c}'(\boldsymbol{K}_c, \vec{\boldsymbol{\tau}}_\mathrm{c}) \\ 1 \end{bmatrix}, \tag{2.41}$$

where the functional dependencies have been explicitly stated. Errors in the camera parameters will cause an error in the xy plane of a homogeneous coordinate system, errors in the projector parameters will cause an error in the depth w of a homogeneous coordinate system. Figure 2.5 is expanded to show this in Figure 2.14. The camera line, given some thickness shown by its cross-section on the camera image plane, intersects the projected projector planes, given as a maximum and minimum. The uncertainty in the camera line, denoted here as some ellipse, and the uncertainty in the projector plane location, given as maximum and minimum planes, has created a volume of uncertainty associated with the point $\vec{\boldsymbol{x}}$, shown in orange, that is similar in shape to a frustum. The uncertainty is shown as a hard boundary here for clarity but would in reality be some probability density. Although the two intersecting planes are not parallel, they are very close to parallel, and so this will be referred to in the rest of this thesis as the uncertainty frustum – this model being called the frustrum model.

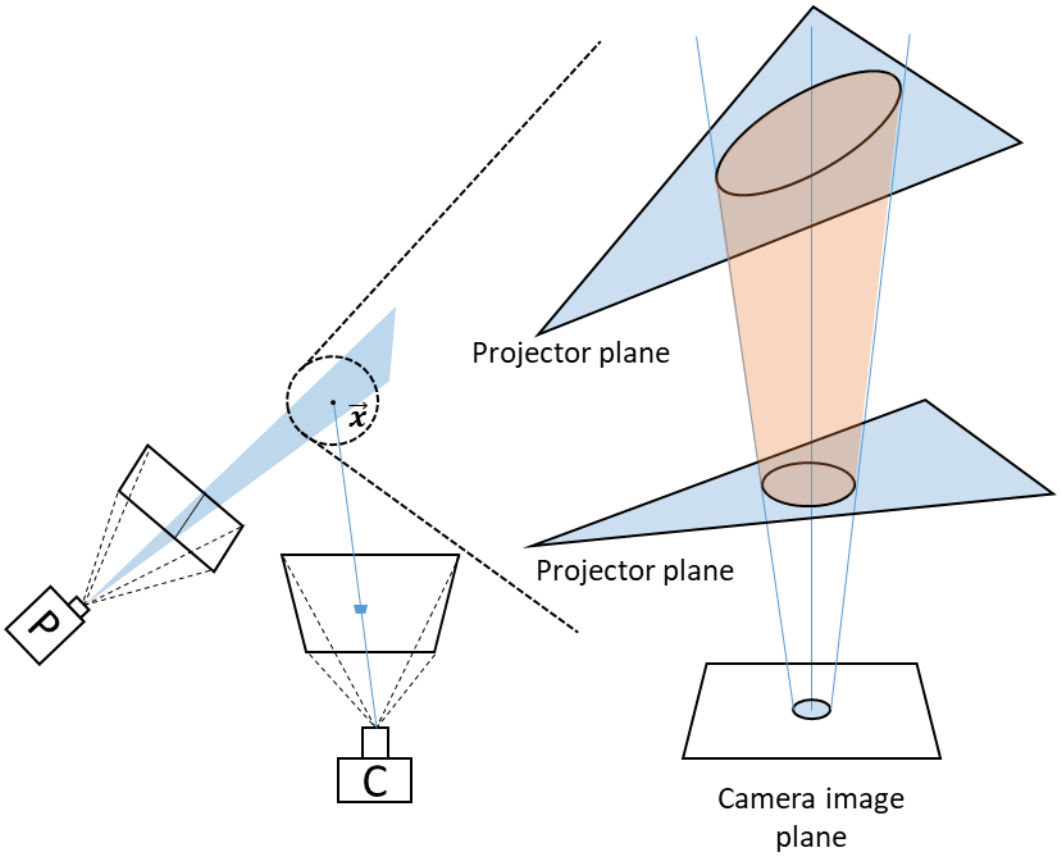

Figure 2.14 An expanded look into global point $\vec{x}$ as shown in Figure 2.5.

2.7 Summary

This chapter defines the entire measurement pipeline for a fringe projection system. Where necessary, methods have been chosen that are suitable for requirements of this thesis. Methods have been chosen based on the fewest limitations to working conditions, with the most robustness, with little concern for measurement speed. Only fringe projection systems consisting of a single camera and projector will considered in this thesis for simplicity.

In Section 2.3.2, a novel triangulation method has been defined that allows rapid triangulation of a measurement surface, that requires fewer mathematical operations than a similar, popular method. The lower computation time of the triangulation method will be useful for use within a Monte-Carlo simulation. In Section 2.4, a correspondence method is outlined that will provide high accuracy measurements during a reasonable measurement acquisition timeframe. In Section 2.5, an extension of the current method was given for overdetermined systems, where it was shown the additional complexity this configuration gives. Lastly, in Section 2.6, the frustum model was defined that will be used to define uncertainty in fringe projection throughout this thesis.

Chapter 3 – Influence quantities in fringe projection

This chapter explores the influence quantities that will affect a fringe projection measurement result. An influence quantity is a quantity that, in a direct measurement, does not affect the quantity that is actually measured, but affects the relation between the indication and the measurement result [1]. An example of an influence quantity is the internal temperature components within the fringe projection system, which will change the properties of the optical components in the measurement system thereby changing the measurement result. Another example is the camera's optics, which determine the quality of image formation. An influence quantity may originate externally, or it can be inherent within the system. There are many influence quantities in fringe projection, and together they can have a complicated causal relationship with the measurement result. In this chapter, it is shown that there are many factors that affect a fringe projection measurement result, and it is difficult to accurately determine their precise effect.

Each parameter included in the triangulation function eq. (2.19) (listed in Table 7.1) will determine the measurement and can be considered an influence quantity. However, there are also many influence quantities that are not inherently included in the triangulation function, which is problematic for any attempts to evaluate uncertainty, as each influence quantity must be controlled or accounted for. The pinhole camera model, and by extension fringe projection, is based on geometrical optics, i.e., light is treated as a ray. However, to obtain certain properties of the camera and projector associated with their optics, a wave optics approach is sometimes preferable, i.e., treating light as a wave to calculate the camera's or projector's optical resolution [93].

The rest of this chapter will be dedicated to defining a comprehensive list of influence quantities. The list of influence quantities can be summarised as: system parameters (found during the calibration step), spatial-frequency bandwidth limitation of the optics as well as the sampling resolution of the CCD and DMD, given in Section 3.1, pixel-to-pixel non-linearity given in Section 3.2, surface geometry and surface optical characteristics given in Section 3.3, and environmental factors given in Section 3.4.

3.1 Instrument resolution

Instrument resolution is defined as the smallest discernible measurable interval of the system. In fringe projection, instrument resolution is a function of optical resolution (the ability of the camera and projector to resolve detail) and the optical characteristics of the measurement surface. The optical resolution is a defined by both the focussing limitation of the optics and the sampling resolution of the CCD or DMD.

As direction sensor, the ability of the camera to resolve detail is directly related to the ability of the camera to resolve direction – and therefore will limit the accuracy of the triangulation measurement [94, 95]. Additionally, each sample point (pixel) within the CCD collects light over a finite area. This is known as sampling quantization, and is a limit to the accuracy of any optical sensor [96]. Considering the simple case of projecting only a single plane of light to obtain correspondence, the resolution can be well-defined using the frustrum model (see Section 2.6), shown in Figure 3.1. In this approximation, the effect of resolution is very similar to the limitation in accuracy of system parameters. The method to define the resolution limit values is an ongoing question.

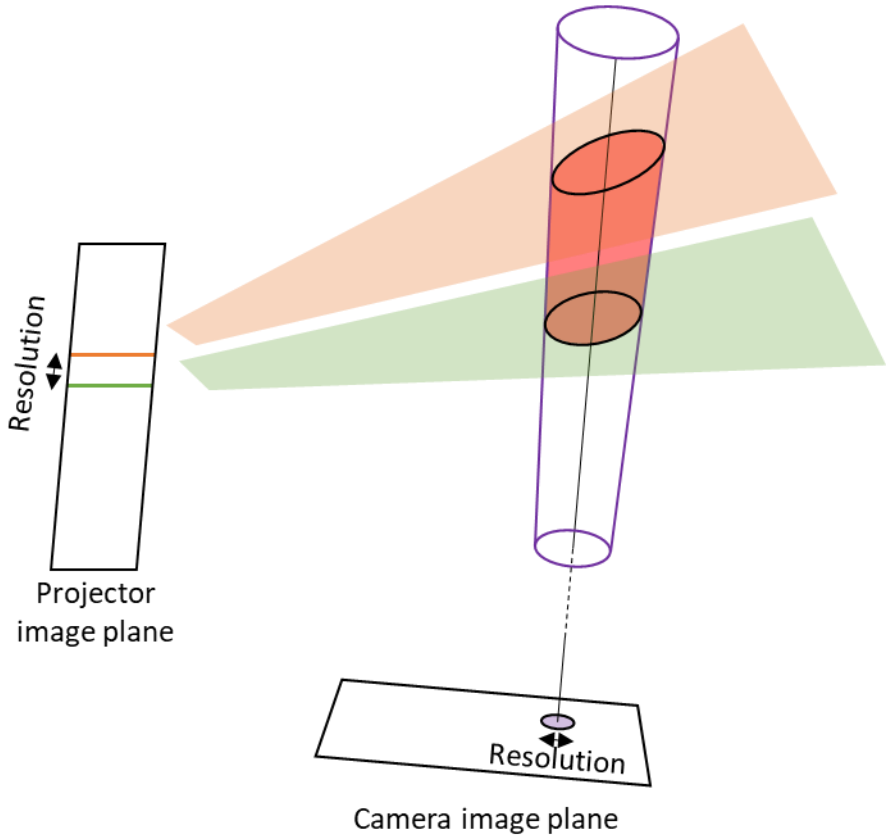

Figure 3.1 The optical resolution of the camera (purple) and the projector (orange and green) placing limits on the accuracy of a triangulation position (red).

Similar to a microscope, a camera can be modelled as applying a linear filter in spatial-frequency space [97]. The image acquired by the camera during a measurement will therefore be attenuated by the optics of the camera. The attenuation of the image is stronger at higher spatial frequencies of the image, compared to lower spatial frequencies, illustrated in Figure 3.2.

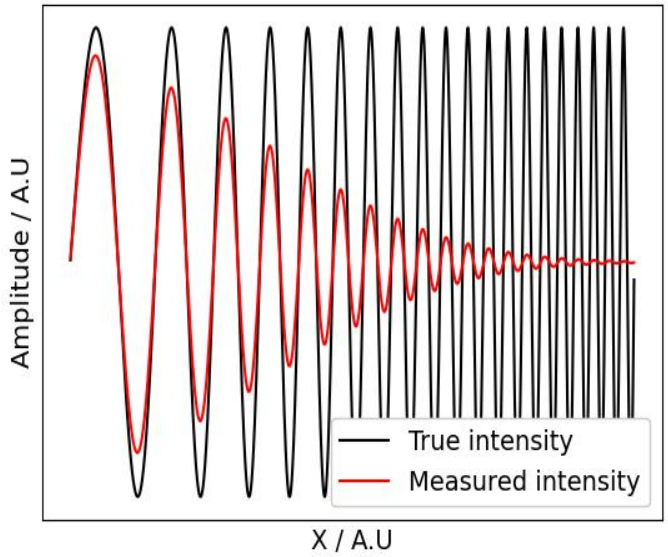

Figure 3.2 A linear filter applied on a wave of exponentially increasing spatial frequency.

The attenuation of higher spatial frequencies phenomenon is described by a linear filter. The instrument resolution can therefore be limited by this linear filter. However, the correspondence and triangulation algorithms are non-linear trigonometric and rational functions – the exact effect optical resolution will have on the measurement is unclear without extensive simplifications. It has been proposed that optical instruments can be described using an instrument transfer function (ITF) [98], i.e. the measured surface spatial frequencies are linearly related to the true surface spatial frequencies. The ITF is useful in determining the smallest discernible measurable interval of a measurement surface and, therefore, will be important in evaluating the measurement uncertainty. The validity of the ITF approach to fringe projection systems is given in Zhang, Davies [99], who also define the limits to that validity.

Unfortunately, the ITF is only applicable to fringe projection under strict linear assumptions, and the limits are broken when considering significant range of depth values within the measurement. The ITF approach is further complicated when considering that measurement sensitivity is dependent on position within the measurement volume. Any consistent ITF must consider spatial

variance [100], yet the ITF is typically considered spatially-invariant for simplicity. Additionally, in fringe projection, the ITF is a function of the measurement surface [101] as well as the optics, and is discussed further in Section 3.3. A alternative method to calculate instrument resolution is given in Guidi, Russo [102] who consider the instrument resolution within the xy plane and the z-axis as two separate independent quantities.

There is no generic method for evaluating the effect of optical resolution on the point-cloud. Neighbouring pixels (and by extension, neighbouring points in the point-cloud), will be innately linked by the spatial frequency limitation of the optics and the sampling quantisation of the CCD. While this effect is generally local, overall, it will make a sizeable contribution uncertainty evaluation complexity, since each point-point relationship must be accounted for.

Sampling resolution limits in the projector can be problematic due to the perceived edges of each micromirror. Fringe projection systems that have highly mismatched CCD/DMD sampling resolution will suffer reduced accuracy [103]. The projector relies upon the finite optical resolution of its own optics to remove the quantization effects of the DMD, and will not adversely affect the measurement result [101, 104] – the projector is often purposefully blurred to produce higher quality fringes and measurements [57, 58, 104, 105].

The resolution model given in Figure 3.1 therefore does not apply to full-field projection images – since an optical resolution limit is limiting the spatial-frequency content of the projection, and projections are typically chosen to be absent of high spatial-frequencies. In the phase-retrieval regime, the projector optical resolution will limit the frequency of the projected fringes, limiting the robustness of the measurement against noise. Figure 3.1 can be updated to reflect the phase-retrieval regime, shown in Figure 3.3. Instead, a sinusoid is projected that is limited in frequency by the optical resolution of the projector. The camera can resolve the sinusoid to a limited accuracy – a higher frequency sinusoid will be far less sensitive to errors in resolving the sinusoid. Additionally, in some cases, the camera resolution invalidate

$$I_k(u,v) = A\cos(\phi(u,v) + \delta_k) + B. \tag{2.27}$$

This is explored in more detail given in Section 3.3 given it is fundamentally a measurement surface quantity.

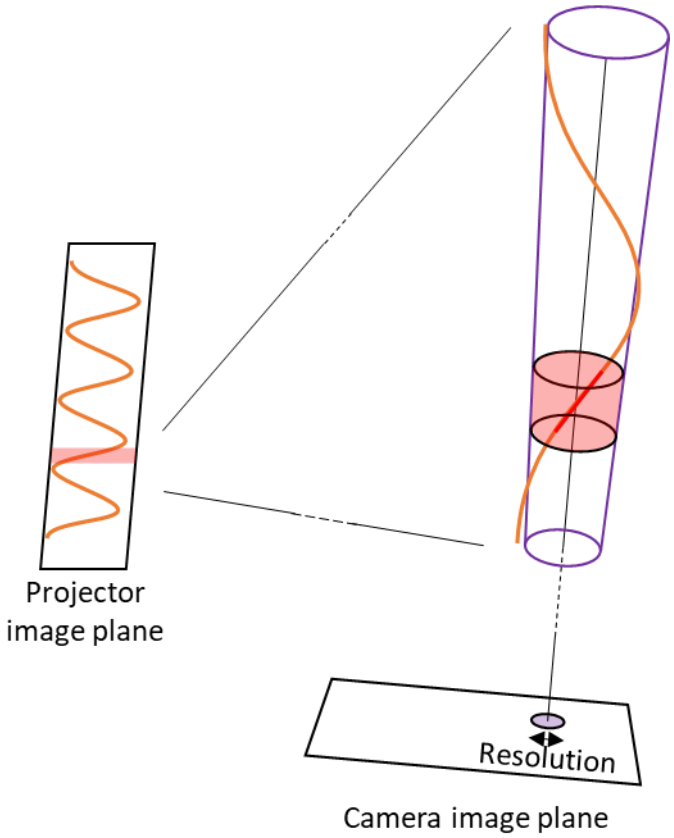

Figure 3.3 The limitation of optical resolution on the measurement result

3.2 Pixel-to-pixel non-linearity

The section will explore the relationship between DMD micromirror output and CCD pixel input. Pixel-to-pixel non-linearity is defined as deviation from the ideal case where CCD pixel measurements are linearly dependent on DMD micromirror output. The correspondence (see Section 2.4) is found pixel-by-pixel, with each DMD micromirror projecting its own time-varying sinusoidal signal The DMD image is described by a sinusoidal function, using two coefficients for the contrast A and the offset B. If the correspondence obeys any model but this contrast-offset model, a sinusoid as output b the projector will not be measured as sinusoidal by the camera, so there will be some systematic error in the measurement. However, there is rarely an ideal linear relationship between projector irradiance output and camera irradiance input [106]. The correction for non-linear mapping between projection irradiance output and camera irradiance input is called pixel-to-pixel, detailed in Section 2.4.1.

Crosstalk is problematic when colour is used to encode information, and must be corrected [83, 107, 108]. Properties of the camera and projector optics are also wavelength dependent, and can cause chromatic aberrations that are often

corrected [109]. These issues can be ignored when using monochromatic encoding for the correspondence algorithm. Both the camera and the projector are limited to recording/projecting a select range of values. Exceeding the camera pixel's maximum value is called "saturating" the pixel, and is problematic for the correspondence algorithm [110, 111].

Camera-projector asynchronisation is another problem that can affect the linearity of the camera-projector relationship. Unlike the camera CCD, the projector DMD defines an output intensity by the physical switching of a mirror – a binary output. A single camera image acquisition must therefore integrate over time the binary outputs that equate to an eight-bit integer. This is known as camera-projector synchronisation, and a high degree of synchronisation must be attained before errors can be removed [85]. All projectors suffer from "jitter" – uncertainty in the projection image start time and duration, which can be seen as a contributor to DMD noise [112]. The CCD will also exhibit its own form of noise, a combination of photon shot noise, dark current, amplification noise and digitisation noise, with different noise sources dominating in specific circumstances [113, 114].

3.3 Measurement Surface

This section shall explore measurement surface characteristics as an influence quantity. The measurement surface is a significant influence quantity and should be taken into account when performing a measurement [115] When finding matching correspondences, each CCD pixel can be considered as a detector receiving a signal emitted by a DMD micromirror, with the measurement surface acting as a perturbator of the signal. Certain surface effects, such as measurement surface angle and sub-surface scattering, produce predictable errors. The angle of the surface will dictate the level of light returned to the sensor, reducing the measurement signal-to-noise ratio at high angles [116]. Sub-surface scattering can be seen as a linear filter that attenuates the high-spatial frequency content of images [101, 117].

When considering changes of contrast on the surface, or measurement surface discontinuities, limitations of optical resolution may produce erroneous points [101]. If the measurement surface has a highly non-smooth reflectivity, the contrast will corrupt neighbouring pixels and cause a systematic error [118, 119], illustrated in Figure 3.4.

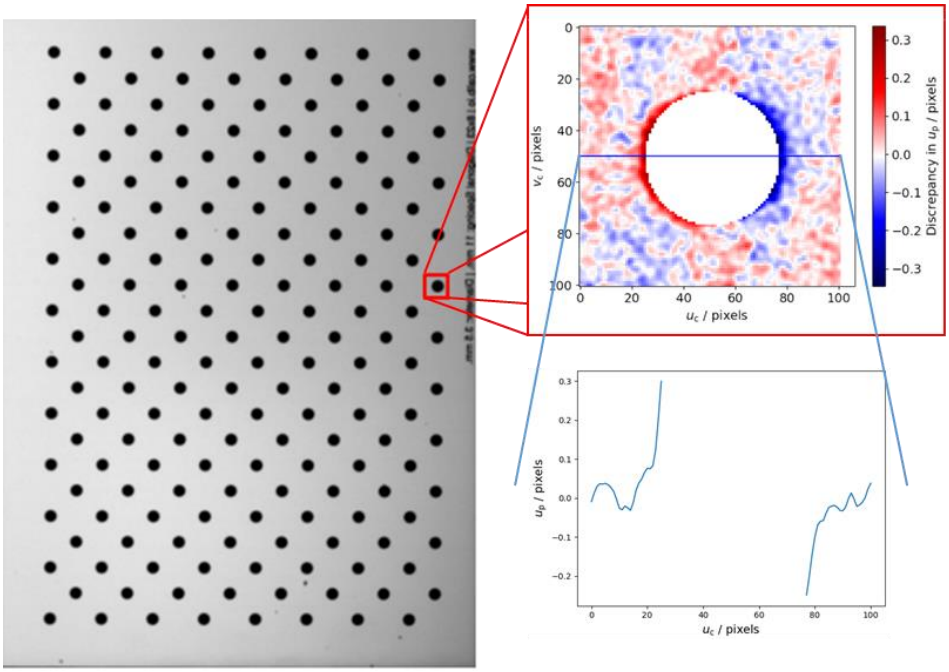

Figure 3.4 Error in a phase map (right) caused by a contrast boundary and optical resolution when imaging the dot grid (left).

Another assumption inherent in the correspondence decoding, given in Section 2.4, is that each camera pixel is dependent on a set of localised projector pixels, i.e., that each pixel is related by a projective transformation, along with a filtering operation. But this assumption fails in the event of multiple reflection, which occurs when a photon reflects twice off the measurement surface before travelling to the CCD [120]. This measurement error is particularly difficult to identify, since it requires information on the geometry of the surface being measured [121].

It is unclear how to account for the effect of non-smooth reflectivity and multiple reflections on the measurement result – there is no analytical solution. Both effects are dependent on the measurement object, and the effect of non-smooth reflectivity is additionally dependent on camera optical characteristics and parameters. Unlike optical resolution, multiple reflections have no limit on their range, and could in theory link any pixel to any other [121], making it difficult to evaluate their contribution to data-density, since it would always be highly object-dependent.

3.4 Environment

This section will identify how the environment can affect and fringe projection measurement result. Temperature is a significant influence factor in fringe projection. The expansion of materials due to temperature will affect optical

housing and optical components, which is critical to their performance. Temperature will therefore modify both the intrinsic [122] and extrinsic [123] parameters of fringe projection systems, and can in principle be corrected [124]. However, while the change in focal length and the principal point of the optic resulting from thermal expansion can be compensated, the distortion parameters tend to vary unpredictably [125].

It is assumed that light propagates in a straight line from the object to the optic. However, the medium in which the light propagates is never fully homogenous, which can induce significant errors in optical systems [126]. In Figure 3.5 shows the effect of an inhomogeneous medium on the fringe projection model, shown in Figure 2.5. A ray of light propagating to a camera pixel encounters a medium of different refractive index that bends the path slightly, and the camera incorrectly perceives the light as coming from a different source.

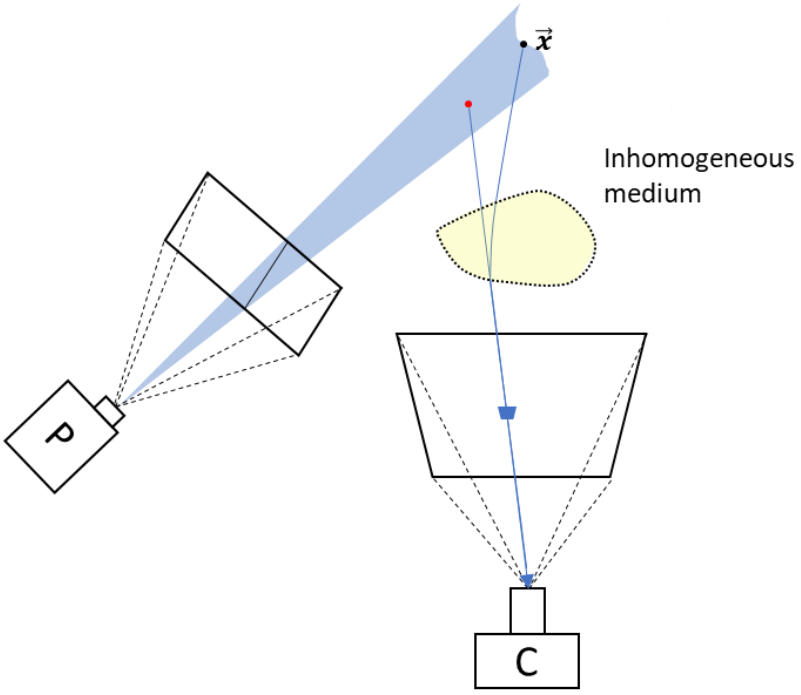

Figure 3.5 A medium of slightly different refractive index altering the path of a travelling ray of light.

Vibration is another influence factor [127], and methods exist to reduce noise and vibration [128]. The ambient light condition can break many correspondence algorithm assumptions; fringe projection systems can be made more robust by using the correct correspondence algorithms [110, 111, 129]. In Section 2.4, the ambient light coefficient is estimated from several images taken over time, and if the ambient light is temporally varying, this assumption will

be rendered incorrect. This assumption is commonly broken in environments with overhead lights synchronized with mains electricity, varying at 50 Hz.

3.5 Summary

This chapter outlines the influence quantities that affect fringe projection systems, many of which are not inherently included in the current fringe projection measurement model. Defining the exact affect each influence quantity has on the measurement outcome can be complicated. For example, the optical resolution limit of the camera optics will only affect the measurement of surfaces with sufficiently high spatial-frequencies in contrast or height. However, many influence quantities can become negligible in certain circumstances. Measuring the correct artefact in the right conditions will allow the measurement result accuracy to be limited only by the accuracy of the system parameters and model used to generate the result. This will allow a method for which to validate any uncertainty estimation in the measurement result propagated from the uncertainty in the system parameters.

Chapter 4 – General methods in uncertainty evaluation

This chapter will provide a background to general methods in uncertainty evaluation that are relevant to this thesis. This section is split into four parts. Section 4.1 gives a definition of uncertainty. Section 4.2 defines an analytical method to propagate uncertainty and Section 4.3 defines a numerical method to propagate uncertainty – both of which will be useful in determining the uncertainty in a measurement caused by the system parameters. Section 4.4 describes a method to determine the validity of an uncertainty evaluation.

4.1 Uncertainty

No measurement can be made with absolute certainty, and therefore every measurement should be expressed with along with a quantity defining the dispersion of values that are reasonably attributed to the measurand. Uncertainty is the quantification of that statistical dispersion [1]. A measurement with uncertainty is written as

$$a \pm b(\text{units}) \text{ @ } k\% \text{ confidence}$$

and is incomplete without all the above components. In this thesis, unless otherwise stated, the uncertainty will be stated at a confidence will be at 95%. The central limit theorem states that the summation of many independent random variables tends towards a normal distribution, including the case where the independent variables being summed are, themselves, not normally distributed. It is common to assign the normal distribution as a variable's probability distribution function (PDF).

The GUM gives two methods to obtain the uncertainty (both quantities b and k), named type A and type B. A type A evaluation of uncertainty is completed by repeating the measurement. This is method will reveal the distribution of quantities associated with a particular measurement, but not any information on how accurate the expected value of such a distribution is. A type B uncertainty evaluation is any method not following a type A uncertainty evaluation. The analytical and Monte-Carlo method given in Section 4.2 and Section 4.3 respectively are both type B methods.

4.2 Analytical

The standardised analytical evaluation of uncertainty is set out in the GUM (2008), a brief overview of which is given here. For an introduction to the basic mathematical approach to uncertainty evaluation, see [130] and [131]. Consider a measurement model that acts on inputs $\vec{\boldsymbol{x}}$ with influence quantities $\vec{\boldsymbol{\Theta}}$ to output measurement $\vec{\boldsymbol{y}}$

$$\vec{\boldsymbol{y}} = f\left(\vec{\boldsymbol{x}}, \vec{\boldsymbol{\Theta}}\right). \tag{4.1}$$

Note that the system parameters are a subset of the complete list of influence quantities $\vec{\boldsymbol{\theta}} \subset \vec{\boldsymbol{\Theta}}$. Given a small perturbation on the influence quantities $\vec{\boldsymbol{\Theta}}$, the measurement outcome will similarly undergo a small perturbation

$$\vec{\boldsymbol{y}} + \delta\vec{\boldsymbol{y}} = f\left(\vec{\boldsymbol{x}}, \vec{\boldsymbol{\Theta}} + \delta\vec{\boldsymbol{\Theta}}\right). \tag{4.2}$$

None of the function inputs or outputs need to be in vector form but doing so simplifies the following. Given the function f is not at all guaranteed to be linear, a Taylor expansion of eq. (4.2) around $\vec{\boldsymbol{\Theta}}$ is given by

$$f\left(\vec{\boldsymbol{x}}, \vec{\boldsymbol{\Theta}} + \delta\vec{\boldsymbol{\Theta}}\right) = \sum_{j=0}^{\infty} \frac{1}{j!} \left(\delta\vec{\boldsymbol{\Theta}} \cdot \nabla\right)^j f\left(\vec{\boldsymbol{x}}, \vec{\boldsymbol{\Theta}}\right). \tag{4.3}$$

Limiting eq. (4.3) to the first order terms only gives

$$f\left(\vec{\boldsymbol{x}}, \vec{\boldsymbol{\Theta}} + \delta\vec{\boldsymbol{\Theta}}\right) = f\left(\vec{\boldsymbol{x}}, \vec{\boldsymbol{\Theta}}\right) + \left(\delta\vec{\boldsymbol{\Theta}} \cdot \nabla\right) f\left(\vec{\boldsymbol{x}}, \vec{\boldsymbol{\Theta}}\right), \tag{4.4}$$

with

$$\nabla = \left[\frac{\partial}{\partial\Theta_1} \quad \frac{\partial}{\partial\Theta_2} \quad \cdots \quad \frac{\partial}{\partial\Theta_n}\right]. \tag{4.5}$$

Assuming $\delta\vec{\boldsymbol{\Theta}}$ is small, higher order contributions of the Taylor series can be neglected. Given that the mean and covariance of the input quantities is known, the covariance of the output quantities can be found by

$$
\begin{aligned}
\boldsymbol{\Sigma}_y &= \mathbb{E}\left[\left(f(\vec{\boldsymbol{x}},\vec{\boldsymbol{\Theta}}) - f(\vec{\boldsymbol{x}},\vec{\boldsymbol{\Theta}}+\delta\vec{\boldsymbol{\Theta}})\right)^2\right] \\
&= \mathbb{E}\left[\left(f(\vec{\boldsymbol{x}},\vec{\boldsymbol{\Theta}}) - f(\vec{\boldsymbol{x}},\vec{\boldsymbol{\Theta}}) - (\delta\vec{\boldsymbol{\Theta}}\cdot\nabla)f(\vec{\boldsymbol{x}},\vec{\boldsymbol{\Theta}})\right)^2\right] \\
&= \mathbb{E}\left[\left((\delta\vec{\boldsymbol{\Theta}}\cdot\nabla)f(\vec{\boldsymbol{x}},\vec{\boldsymbol{\Theta}})\right)^2\right] \\
&= \mathbb{E}\left[\left((\delta\vec{\boldsymbol{\Theta}}\cdot\nabla)f(\vec{\boldsymbol{x}},\vec{\boldsymbol{\Theta}})\right)^{\mathrm{T}}\left((\delta\vec{\boldsymbol{\Theta}}\cdot\nabla)f(\vec{\boldsymbol{x}},\vec{\boldsymbol{\Theta}})\right)\right] \\
&= \mathbb{E}\left[\nabla f(\vec{\boldsymbol{x}},\vec{\boldsymbol{\Theta}})\delta\vec{\boldsymbol{\Theta}}\delta\vec{\boldsymbol{\Theta}}^{\mathrm{T}}\nabla f(\vec{\boldsymbol{x}},\vec{\boldsymbol{\Theta}})^{\mathrm{T}}\right] \\
&= \nabla f(\vec{\boldsymbol{x}},\vec{\boldsymbol{\Theta}})\mathbb{E}\left[\delta\vec{\boldsymbol{\Theta}}\delta\vec{\boldsymbol{\Theta}}^{\mathrm{T}}\right]\nabla f(\vec{\boldsymbol{x}},\vec{\boldsymbol{\Theta}})^{\mathrm{T}} \\
&= \boldsymbol{\mathcal{J}}\boldsymbol{V}(\vec{\boldsymbol{x}},\vec{\boldsymbol{\Theta}})\boldsymbol{\mathcal{J}}^{\mathrm{T}}
\end{aligned}
\tag{4.6}
$$

where $\mathbb{E}[\ldots]$ is the expected value operator. The multi-variate derivative is defined as the Jacobian $\nabla f(\vec{\boldsymbol{x}},\vec{\boldsymbol{\Theta}}) = \boldsymbol{\mathcal{J}}$, and is also known as the sensitivity matrix. The covariance between the outputs is given by $\boldsymbol{V}(\vec{\boldsymbol{\Theta}},\vec{\boldsymbol{\Theta}})$.

There are number of assumptions made for this analytical method to work. The conditions for the GUM uncertainty framework are given below [132]:

1. Measurement model must be approximately linear under small perturbations. If higher-order terms in the Taylor expansion become non-negligible, the approximation is no longer valid.
2. The central limit theorem must apply.
3. Uncertainty sources must be quantifiable.
4. Measurement model must be differentiable. If this is not the case, then the sensitivity coefficient must be able to be found empirically.
5. The Welch-Satterthwaite formula for calculating effective degrees of freedom must apply.

If the off-diagonal components of $\boldsymbol{V}(\vec{\boldsymbol{\Theta}},\vec{\boldsymbol{\Theta}})$ are zero, i.e. the influence quantities are completely uncorrelated, then eq.(4.6) can be simplified to

$$
\sigma_y^2 = \left(\frac{\partial y}{\partial \Theta_1}\right)^2 {\sigma_{\Theta_1}}^2 + \left(\frac{\partial y}{\partial \Theta_2}\right)^2 {\sigma_{\Theta_2}}^2 + \cdots. \tag{4.7}
$$

From eq. (4.7) it can be seen how the central limit theorem applies to many cases of measurement uncertainty when considering first-order expansions only.

4.3 Monte-Carlo method

Another method of propagating uncertainty is the Monte-Carlo method. Information on how to apply the Monte-Carlo method to a measurement system is found in supplement 1 to the GUM (2008). ISO 15530 part 4 concerns the use of Monte-Carlo method regarding tactile CMSs. The Monte-Carlo

algorithm is outlined Algorithm 2, with a graphical representation given in Figure 4.1.

Algorithm 2 Monte-Carlo method to establishing a confidence interval.

Define the virtual process $f(\dots)$ that is under investigation.
Define the arbitrary PDF, $Q(\dots)$, of each input vector $\vec{\boldsymbol{x}}_i$, that is fed into the virtual process.
For 10^6 repetitions:
Sample a random number $\tilde{\boldsymbol{x}}_i$ from $Q(\dots)$ for all input vectors.
Find virtual output $\tilde{\boldsymbol{y}}_n = f(\dots)$ using the samples $\tilde{\boldsymbol{x}}_i$.
End For
Define a PDF of the virtual outputs $\tilde{\boldsymbol{y}}_n$.
Generate a confidence interval $\vec{\boldsymbol{\sigma}}_{\boldsymbol{y}}$.

For more computational expensive processes, the algorithm can be repeated until convergence instead [133]. Random number sampling can be found in Von Neumann [134].

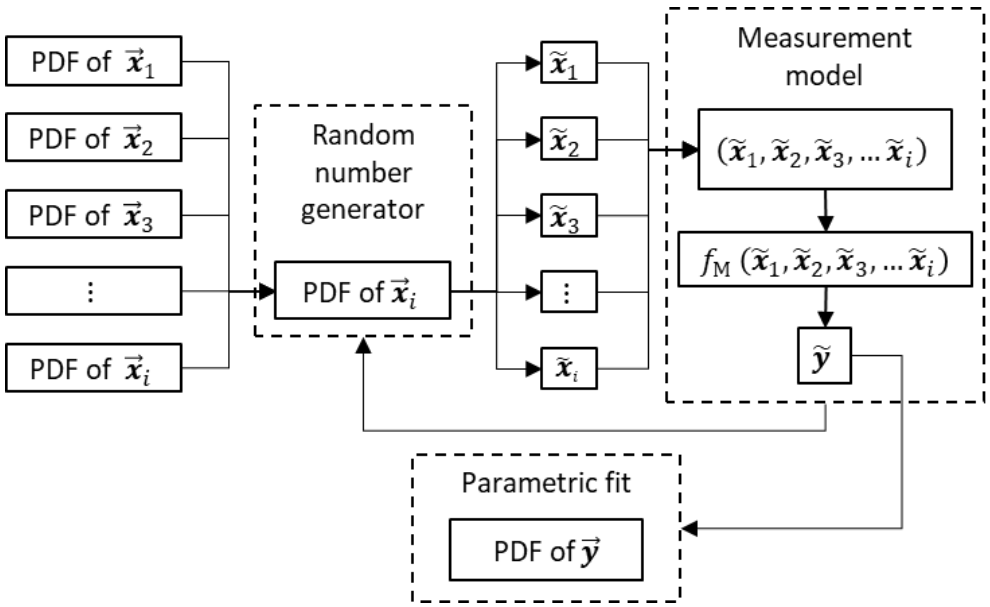

Figure 4.1 The propagation of uncertainty using the Monte-Carlo method.

The Monte-Carlo method is effective when the analytical method is not applicable due to the stated assumptions being broken, if the covariance matrix $\boldsymbol{V}$ is too large to handle (the covariance matrix size scales to the power of 2), or if a function has no analytically derivable sensitivity coefficients.

4.4 Reduced χ^2 test

This subsection will define the χ^2 test that will be used in this thesis to conduct tests on uncertainties. Traditionally, a χ^2 test is used to determine if two quantities are significantly different given their distribution is known. The sum of a squared set of k quantities, drawn from normal distribution of mean 0 and variance 1, $x_i \sim \mathcal{N}(0,1)$, will follow a χ^2_k distribution, with k determining the degrees of freedom,

$$\sum_{i=0}^{k} x_i^2 = y \sim \chi_k^2. \tag{4.8}$$

A quantity drawn from an arbitrary normal distribution $\mathcal{N}(\mu, \sigma)$ can be transformed into a quantity drawn from $\mathcal{N}(0,1)$ by

$$\frac{x_i - \mu}{\sigma} = x_i' \sim \mathcal{N}(0,1). \tag{4.9}$$

The transform can also be generalised to N dimensions where $\vec{\boldsymbol{x}}_i \sim \mathcal{N}(\vec{\boldsymbol{\mu}}, \boldsymbol{V})$. Because the covariance matrix is—by definition—a Hermitian positive semi-definite matrix, it can be decomposed

$$\boldsymbol{C}\boldsymbol{C}^{\mathrm{T}} = \boldsymbol{V}, \tag{4.10}$$

using a Cholesky decomposition [135]. A set of random uncorrelated variables drawn from $\mathcal{N}\left(\vec{\boldsymbol{0}}, \mathbb{I}_{\mathrm{N}\times\mathrm{N}}\right)$ can be given arbitrary correlations by applying the linear transform $\boldsymbol{C}$, and can therefore be uncorrelated with

$$\boldsymbol{C}^{-1}(\vec{\boldsymbol{x}}_i - \vec{\boldsymbol{\mu}}) = x_i' \sim \mathcal{N}\left(\vec{\boldsymbol{0}}, \mathbb{I}_{N\times N}\right). \tag{4.11}$$

Given k samples of vector $\vec{\boldsymbol{x}}_i$ of size N, the appropriate χ^2 test is given by

$$\sum_{i=0}^{k} (\vec{\boldsymbol{x}}_i - \vec{\boldsymbol{\mu}})^{\mathrm{T}} \boldsymbol{V}^{-1} (\vec{\boldsymbol{x}}_i - \vec{\boldsymbol{\mu}}) = y \sim \chi^2_{k\times N}, \tag{4.12}$$

where y is checked against a critical value of the $\chi^2_{k\times N}$, which here is a value at which only 5% of values drawn from $\chi^2_{k\times N}$ are expected to be higher. For simplicity, a reduced χ^2 test is

$$\frac{1}{kN} \sum_{i=0}^{k} (\vec{\boldsymbol{x}}_i - \vec{\boldsymbol{\mu}})^{\mathrm{T}} \boldsymbol{V}^{-1} (\vec{\boldsymbol{x}}_i - \vec{\boldsymbol{\mu}}) = 1, \tag{4.13}$$

And is typically used for testing an uncertainty interval. A test result of $\gg 1$ means either $\vec{\boldsymbol{\mu}}$ or $\boldsymbol{V}$ or both are invalid. A test result or $\ll 1$ means the covariance matrix $\boldsymbol{V}$ is too large. A test result ≈ 1 indicates success.

4.5 Summary

This chapter has provided relevant background methods in determining uncertainty for a fringe projection measurement. The methods included here are a general analytical method and a numerical method, namely the Monte-Carlo method, to propagate uncertainty. Finally, a test is given that can be used to evaluate the validity of a proposed uncertainty value for a measurement.

Chapter 5 – Methods of fringe projection uncertainty evaluation

In this chapter, the current state of the art in uncertainty evaluation in fringe projection is reviewed. Several factors have hindered the development of uncertainty within fringe projection; a lack of independent traceable realisations of system parameters, significant uncertainty evaluation complexity, domination of errors related to the measurement surface and difficulty in verifying uncertainty conditions.

Given a valid method to propagate uncertainty to the final measurement, an independent realisation of the system parameters would allow an evaluation of uncertainty of the measurement independent of the measurement surface. However, there are limited methods to independently measure the focal length of a camera [136], and no accepted way to independently measure the origin of the camera and projector pinhole models [137]. No direct measurements of these parameters can be made with traceable instruments, instead novel methods must be used.

The following sections will cover the current state of literature evaluating uncertainty in fringe projection systems. Uncertainty models can generally be categorised into three groups: geometrical, empirical, and virtual models. Geometrical models typically define uncertainty using parameters taken from the fringe projection measurement model. The advantage of this method is that each model is based on a real physical attribute, which can provide information on improvements to be made to the system. Empirical models do not base parameters on physical attributes of the system. The advantage of an empirical model is its simplicity – but that same simplicity may prevent the model from representing more complex aspects of a fringe projection system. Virtual models aim to recreate the measurement virtually, using a full description of the measurement scenario. The virtual technique is the most complicated, but it has the advantage of being constrained by fewer working assumptions than either geometrical or empirical models. This section will cover geometrical models in Section 5.1, empirical models in Section 5.2 and virtual models in Section 5.3.

5.1 Geometrical models

With fringe projection primarily based on geometrical optics, many uncertainty evaluations have been based on using the parameters that derive from the pinhole camera model. Generally, this works best when describing phenomena that are well-described by geometrical optics but can fail when considering phenomena that are less well-described, such as resolution.

Due to the simplicity of alternative triangulation methods (see Section 2.3.2), it is common to create an uncertainty model based on these methods [138-140]. Such uncertainty models would similarly be subject to limited working constraints and simplifications. Certain extensions on the alternative models allow for a more comprehensive uncertainty evaluation on the parameters [141]. Existing uncertainty models based on Zhang's method are highly simplified [114, 142], but highlight the difficulty in quantifying the uncertainty of fringe projection – that there will be significant correlation between calibration parameters and world coordinates used in the calibration step.

Geometrical models based on the analytical method have problems dealing with the high data-density. Each point within the point-cloud is derived from a common set of parameters that define the fringe projection system, see Section 2.3.2. The error of every point will therefore be highly correlated with the error of every other point. For n points there will exist a covariance matrix of size $n \times n$. One simplification is to assume homoscedasticity, i.e., the error of each point is independent and identically distributed, allowing uncertainty to be represented by a single quantity. Another simplification is to assume the errors are heteroscedastic, but uncorrelated, allowing uncertainty to be represented by just n terms. However, since every point is derived from the same set of uncertain parameters, both assumptions of homoscedasticity and uncorrelated heteroscedasticity fail.

Each point within a point-cloud is only known by its relative position, i.e., its position in relation to every other point. The fitting of prismatic shapes is generally insensitive to measurement noise that is uncorrelated using the correct fitting algorithms [143]. Evaluating uncertainty using only heteroscedastic, uncorrelated terms neglects local effects on the measurement point-cloud that is the result of uncertainty in system parameters. The off-diagonal terms within the covariance matrix cannot be ignored and must be accounted for.

Computational complexity can be quantified using big O notation. Big O notation defines how a function behaves when its argument tends to infinity

and is given by some function f, written as $O(f(n))$, with n being the size of the function argument. Using a multivariate Gaussian to model the distribution of quantities for each point in a point-cloud of n points uses $n \times n$ coefficients. Therefore, the computation cost scales by $O(n^2)$, but given there are only $\sum_{i=1}^{n} i$ unique coefficients, the memory scales by $O\left(\frac{n(n+1)}{2}\right)$. The benefit of fringe projection is the increased data density – a typical measurement is upwards of a million points. Fringe projection's high data-density is problematic for geometrical models. In Figure 5.1, the approximate memory size of the relationship coefficient when measuring two spheres or a flat plane is shown.

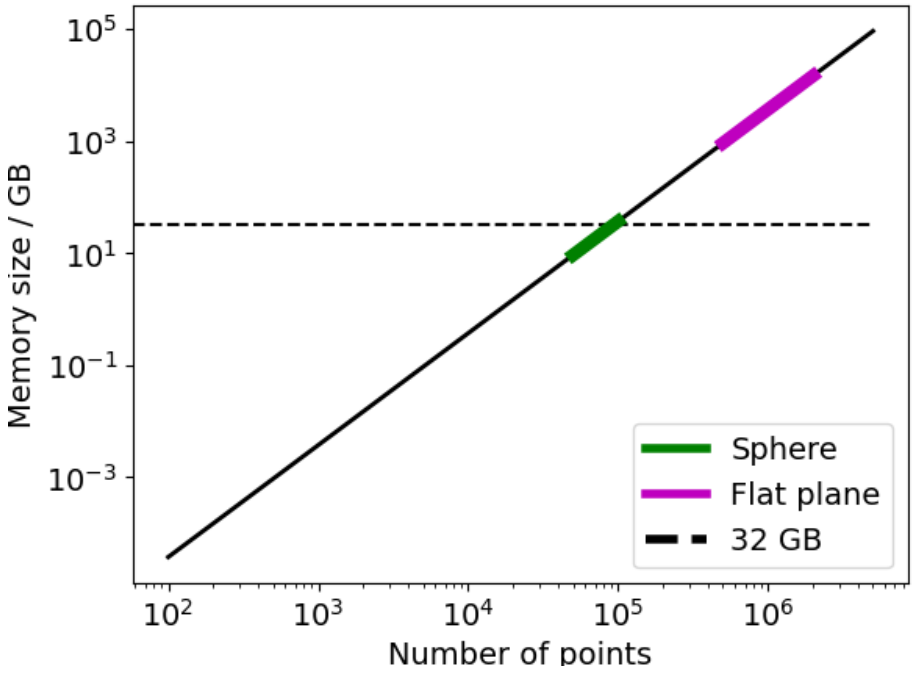

Figure 5.1 A log plot giving the memory size of an optimized covariance matrix of a point cloud. It is assumed here each value is stored as a 64-bit float. Typical off-the shelf memory is taken at 32 GB. A sphere is approximated to have between 4×10^4 to 1.4×10^5 points. A typical flat plane measurement is approximated to have between 5×10^5 to 2×10^6 points.

Common simplifications are to ignore uncertainty in the distortion coefficients [138, 139] or only focus on single influence quantities such as pixel quantization [144]. The problem with considering only one influence factor at a time is the lack of consideration for interactions between influence quantities. More rigorous models that do include distortion, find that the measurement result is highly-sensitive to distortion parameters and should not be ignored [145].

Other uncertainty models can derive effective uncertainties in common intrinsic parameters from gauge blocks [146], but still neglect distortion parameters [147, 148]. Additionally, many methods will neglect the

contribution of the correspondence algorithm to the uncertainty – this is known as "phase error", which is a significant component of the error with fringe projection [149].

Monte-Carlo methods allow for a reduction in analytical complexity at the cost of computation time [150], which is useful when propagation uncertainty in both triangulation methods [149] and correspondence methods [151]. The Monte-Carlo method is also able to propagate uncertainty in numerical calculations, such as those used in camera calibration [152, 153], although this method has yet to be applied to fringe projection.

5.2 Empirical models

Empirical models do not base their parameters on the pinhole model and are instead based on variables chosen for their ease of use. Variables may be derived from some theoretical foundation. Empirical models will require their own evaluation, i.e. an additional round of measurements to discern the relationship between uncertainty and the chosen variables. An example of this is a simple model evaluating uncertainty purely as a function of position and orientation of an object within the measurement volume [154]. The advantage of these models is that the parameters used are significantly lower in number and easier to determine. The benefit of using an empirical model, such as the model given in Sankowski, Włodarczyk [154], is that the simplicity allows measurement performance to be tracked day-by-day, with certain conditions triggering a re-calibration. An empirical model can also be used to optimise camera calibration in terms of select parameters such as the number of targets used [155].

Performance verification is an example of an empirical model. A performance verification test relates measurement length and size to a maximum permissible error (MPE), which is like an uncertainty. Performance verification test will be included here for completeness. ISO 10360-13 [156] is a new standard dealing with performance verification in optical CMS such as fringe projection. VDI/VDE 2634-3 [157] also deals with performance verification in the same manner. The two performance verification methodologies use measurements provided by artefact features, such as sphere-to-sphere distance or flatness. The measured features are compared against the same traceable "true" features. Performance verification can be a useful tool to compare competing fringe projection systems. However, such a performance verification only demonstrates that the machine meets its specification for measuring simple features. Performance verification does not give an

uncertainty value. To obtain a more generic uncertainty would require "sampling" the measurement volume at many different locations. Even then the uncertainty evaluation would only be valid for measuring surfaces that have the same optical characteristics [115, 158]. The current performance verification tests given in ISO 10360-13 do not accurately reflect the true nature of the measurement error [159].

Spatial kriging, otherwise known as Gaussian process regression, is a powerful tool allowing the full estimation of a continuous field from a few discrete sampling points, along with an uncertainty, and lends itself well to point-clouds [160]. Spatial kriging can estimate the uncertainty that comes with interpolating between discrete measurement points by estimating the range of interaction within the dataset. A typical 1D example of spatial kriging is illustrated in Figure 5.2. Kriging has recently been used to estimate fringe projection uncertainty with respect to position within the measurement volume [161]. Kriging can also be used to estimate camera distortion [162], and can be adapted for use in a projector [51] to allow for distortion estimation [163].

The downside to spatial kriging is the expensive computational cost of interpolating points. Spatial kriging is an $O(n^3)$ problem [164], and it is common to use hardware acceleration, such as the GPFlow library that runs on TensorFlow [165, 166], to improve computation time. By approximating the dataset with m latent variables, instead of using all n datapoints, sparse kriging can reduce the complexity of interpolation form $O(n^3)$ to $O(nm^2)$ [167]. Kriging has only recently been introduced to fringe projection; further research is required to optimise this approach.

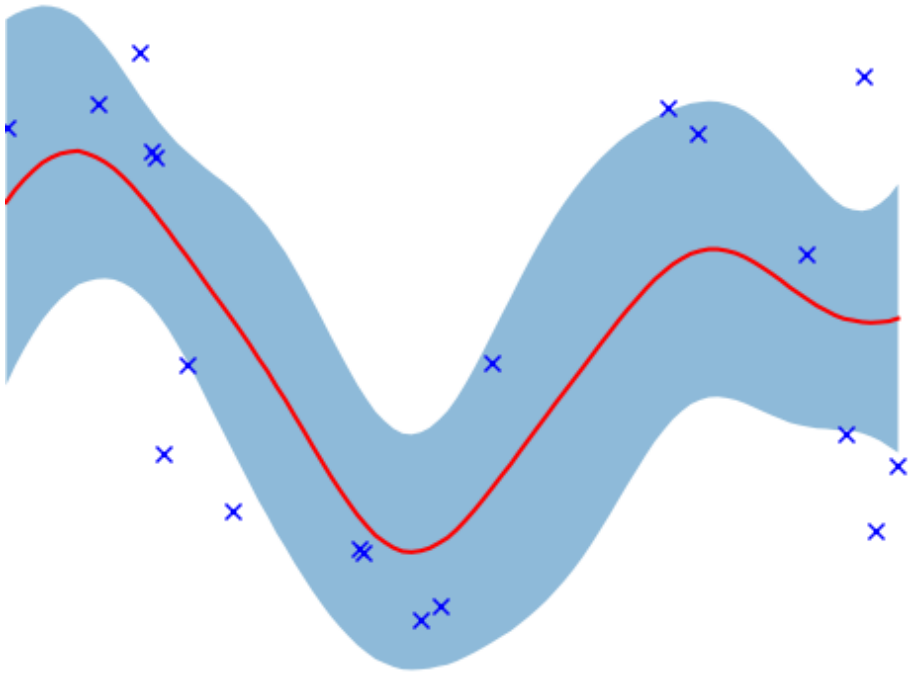

Figure 5.2 Spatial kriging of an arbitrary noisy function. The red line indicates the mean predicted outcome of the function, while the shaded area is a 95% confidence interval.

Since an empirical model chooses parameters based on simplicity over physical reality, it is difficult to know exactly when an empirical model is valid. The measurement artefacts used to characterise parameters in an empirical model must be chosen carefully, otherwise the empirical uncertainty will be intrinsically linked to the specific measurement object.

5.3 Virtual models

Complexity can make more traditional analysis methods ineffective. If a complete, rigorous model is available that describes a physical process, then that model can be used to create a "digital twin" of the process in question. Digital twins are used to faithfully recreate a physical process, when that physical process is too costly to run, such as modelling airplane component degradation [168] or city-planning [169]. A digital twin is built from first principles, e.g., the propagation of light (as either a ray or a wave). In this way, the digital twin can model arbitrary processes by recreating the measurement indication, in the case of fringe projection a camera image. The camera image would subsequently be input to the measurement process to create a final measurement result, a point-cloud. Using the Monte-Carlo method (see Section 4.3), a set of measurement results can be built up using random sampling, and an uncertainty obtained. Virtual models are well-suited to handle the complex interrelationships between influence quantities, such as camera optical

resolution and surface reflectivity, since they are inherently modelled by the digital twin.

The concept of the digital twin is a significant part of Industry 4.0 [170], and can be used to automate measurement strategies in tactile CMS [171-173]. Digital twin guides can be found in GUM supplement 1 [150] and NPL [174]. Digital twins have been used extensively in tactile CMS [175, 176] and can be used in non-ideal industrial conditions [177]. Digital twins for optical CMS exist [178] but are typically limited.

Digital twins produce results that are only as accurate as the model used to create the twin. Trust in the twin requires validation and verification [179]. In theory, a virtual model should have comparable physics, be accurate and low computation times, but in practice, there is often a trade-off. Choosing the correct model can raise difficult questions [180]. It remains an open question as to whether a virtual instrument can be applied to fringe projection.

Current virtual models of fringe projection vary in complexity. Some models only vary the phase in the correspondence algorithm [181, 182], being only applicable to simple linear triangulation methods, see Section 2.3.2. More sophisticated methods may use ray tracing. Ray tracing is a widely-used method that can simulate the propagation of light, based on geometrical optics [183].

Fringe projection models based on ray tracing vary in complexity. Basic models assume negligible distortion and Lambertian reflectivity [40, 184-186]. More advanced models can include surface scattering, modelled using a measured bidirectional reflectance distribution function (BRDF) representation of the measurement surface optical characteristics [187, 188]. Ray tracing models can be even more comprehensive and consider the effects of multiple-scattering [189-191].

While virtual models are adept at handling complex influence quantities and their interrelationships, it can be difficult to verify the virtual model is functioning correctly. A fringe projection system measurement provides a very complicated scene to render with ray tracing. The influence factors and their interrelationships (see Chapter 3), such as the relationship between surface contrast discontinuities and optical resolution of the camera, show that common approximations for multiple scattering, surface reflectivity and resolution will invalidate the virtual model in some way. The magnitude of the errors introduced by such approximations is unknown. It remains an open

question exactly how accurate a digital twin is required to be, in the trade-off between accuracy and computation time, to faithfully model fringe projection.

5.4 Summary

This chapter categorises three distinct models available in literature to evaluate uncertainty in fringe projection. Models are categorised into geometrical, empirical, and virtual models. In addition to categorisation, the limitations, and advantages of each model have been discussed. Each model has currently failed to evaluate uncertainty in fringe projection. Geometrical models become too complex when considering complex phenomena such as resolution. Empirical models add extra work while their validity across different measurements is generally poor. Virtual models are currently beyond capabilities to validate the model.

Chapter 6 – Feature localisation

The aim of this chapter is to develop a method of localising features within images that are both accurate and provides a reasonable evaluation of uncertainty. Calibration requires known quantities and a measurement of those same known quantities, as well as a method to compare the two. The calibration method used in this thesis is defined in Chapter 7. In fringe projection, the measurement of a known quantity is typically completed using an artefact with features of known position that can be localised within the camera image. The act of identifying and accurately localising all sets of features is called feature localisation in this thesis. The feature localisation method defined here must provide both the position of each feature as well as an uncertainty evaluation. The calibration will then provide a parameter estimation with an uncertainty that can be propagated through to the final measurement. Failures in the feature localisation will also propagate to the final measurement and provide a poor measurement or uncertainty evaluation.

In Section 6.1, the choice of feature artefact is discussed, and a dot grid artefact is chosen as the calibration artefact. Section 6.2 provides information on the dot grid as well as independent measurements of the dot grid and its features. An overview of the feature localisation method is given in Section 6.3, and Sections 6.4, 6.5, 6.7 and 6.8 all define specific sections of feature localisation. Section 6.6 provides validation on certain sections of feature localisation. A repeatability test in Section 6.9 is used to provide information on the warm-up time of the fringe projection system.

6.1 Feature artefacts

This section will discuss feature artefacts used in the calibration of fringe projection systems. A feature artefact provides a set of identifiable marks, called fiducials, that provide a known reference quantity – the relative positions of all fiducials on the artefact. Typically, the same artefact is imaged multiple times in different positions and orientations, each unique image of an artefact is called a pose. An ideal feature artefact is chosen for its information content, and the accuracy and precision to which its features can be localised.

Feature artefacts are split into two categories, active and passive artefacts. An active artefact dynamically generates its fiducials providing much higher information content. The feature localisation work is entirely completed by the active target. Active targets work by typically following an algorithm such as those referenced in Section 2.4, such as binary patterns [192], through the use of a liquid crystal display (LCD). Active targets generally provide higher accuracy at lower spatial frequencies than passive targets, so are useful when performing feature localisation on defocused systems [193, 194]. Active artefacts require some pre-processing to increase the accuracy of the feature localisation due to pixel-quantization and refraction effects [193, 195]. Obtaining an uncertainty in a localised feature on an active artefact is far more complex compared to the passive artefact given its more complex nature. To reduce complexity in an uncertainty evaluation on the feature localisation, active targets will not be chosen.

Passive artefacts have fixed fiducials and are generally more widely used than active artefacts given their availability and well-established use in calibrations. Typically, a passive target is limited by its original manufacturing accuracy, but this can be improved by including the target in the optimisation [196, 197]. The accuracy of the feature artefact can be problematic, but more sophisticated calibration algorithms can alleviate some of the problems [198]. There are many choices of passive artefacts, the only limitation is the ability of the artefact to provide enough easily recognisable fiducials to estimate all parameters of the system, given that every pose of the feature artefact adds 6 parameters to be estimated [199]. The calibration of a fringe projection system adds another constraint to the choice of feature artefact: to obtain the fiducial locations in the projector image, the artefact must not hinder the correspondence decoding process. Many fiducials are provided as a coloured pattern on the surface of the artefact. It is well-known that the measurement surface, and in particular contrast discontinuities, greatly affect the measurement result (see Section 3.3). The choice of fiducial, as well as the choice of surface material will greatly affect the inference of projector points.

The most popular pattern in camera calibration is the checkerboard [200, 201], with every corner providing a fiduciary marker. Feature localisation is completed by either calculating saddle points or by projecting lines across the artefact's surface [202]. However, the sharp discontinuities in contrast across the surface degrade make it difficult to accurately infer the projector pixel location at the corners [203]. Additionally, determination of checkerboard corners is greatly influenced by the exposure levels of the camera, which must be finely tuned so as to avoid underexposure or overexposure [204] – which is

particularly difficult when considering fringe projection. Checkerboards can be coloured so as not to interfere with the colour used by the projector during correspondence decoding, but this method is not perfect.

An alternative common pattern is the dot grid [205]. Although the dot grid also contains contrast discontinuities, they are symmetrical about the point of interest, which greatly simplifies the inference of the projector points. Therefore, the dot grid is generally favoured for fringe projection calibration [206]. However, a disadvantage of the dot grid is there is an extra processing step to correct for eccentricity [44, 207-210], see Section 6.8.

Traditionally, the pattern of dots is uniform, but can be random. Random dot patterns provide similar benefits of using a traditional dot pattern in fringe projection, but offer slightly higher information content [211]. Instead of well-defined features, noise-like patterns can be used to provide even more information content [212]. However, the processing step in the noise-like patterns is far more complicated, and the pattern will suffer from the contrast discontinuity problem that also plagues checkerboards.

Dot grids provide the simplest fiducials while also maintaining good levels of accuracy and being easily obtainable. The errors caused by contrast discontinuities as fiducials can be easily managed by a dot grid given its symmetry, making the inference of the projector dot centre simple and accurate as opposed to a checkerboard. Therefore, the dot grid is chosen as the feature artefact for use in this thesis.

6.2 Dot grid

This section will define the dot grid to be used in the proceeding work. The dot grid used in this work, obtained from Calib.io, is shown in Figure 6.1.

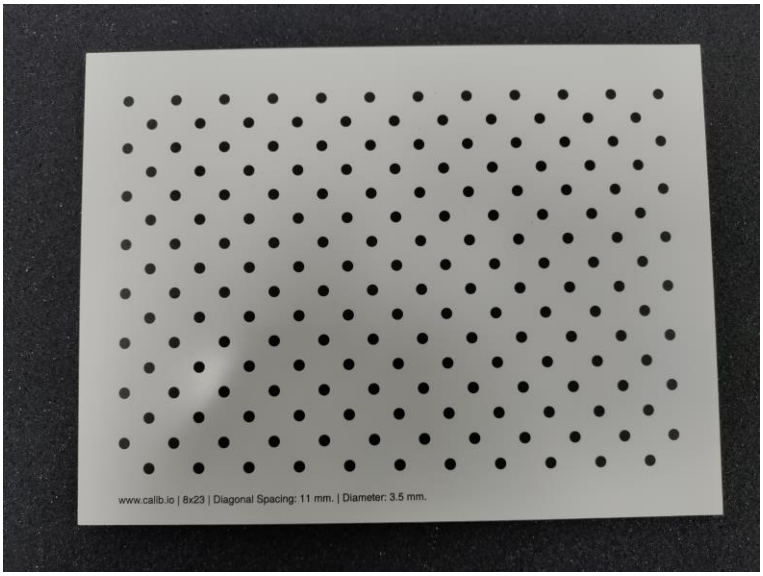

Figure 6.1 Calib.io dot grid used for the calibration throughout this thesis.

The position and quality of the dots were measured by Veras metrology using an optical CMS. The optical CMS has a maximum permissible error (MPE) of $MPE_L = 2.5\ \mu m + \frac{L}{1000}\ \mu m$, where L is a length in mm. The MPE shall be treated as a uniform distribution of half length MPE_L. The MPE can be related to an uncertainty given as σ_{MPE}^2 by

$$\sigma_{MPE}^2 = \frac{2 \times MPE_L^2}{12}. \tag{6.1}$$

Each dot has an inherent error of non-circularity given by the quantity circularity. The circularity is defined as the difference in diameter between the largest circle that can be drawn inside the section and the smallest circle that can be drawn outside the section, while maintaining concentricity between the two circles. This concept is shown in Figure 6.2. The circularity shall be treated as a non-uniform distribution

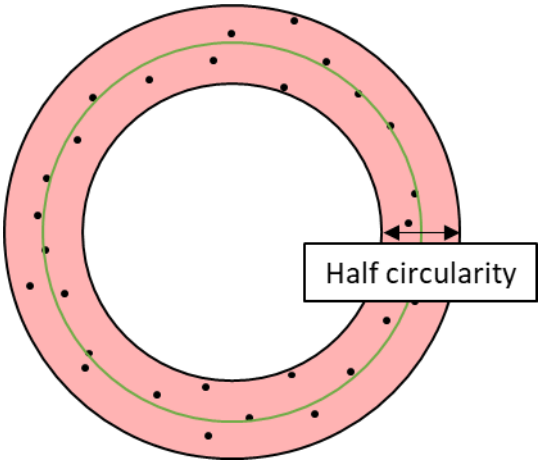

Figure 6.2 The fitted circle (green) and the difference between the minimum and maximum fitted circles (red area).

The final uncertainty on the position of the dot centre can be found by propagating the uncertainty of the circularity through a circle fitting function

$$\boldsymbol{X}\vec{\boldsymbol{\beta}} = \boldsymbol{y}, \tag{6.2}$$

$$\begin{bmatrix} x_1 & y_1 & 1 \\ \vdots & & \end{bmatrix} \begin{bmatrix} 2x_\mathrm{c} \\ 2y_\mathrm{c} \\ r^2 - x_\mathrm{c}^2 - y_\mathrm{c}^2 \end{bmatrix} = \begin{bmatrix} x_1^2 + y_1^2 \\ \vdots \end{bmatrix}. \tag{6.3}$$

The uncertainty, defined by the circularity and treated as a uniform distribution, can be transformed to a normal distribution width σ_{CIRC} using eq. (6) from the GUM

$$\sigma_{\mathrm{CIRC}}^2(x^2 + y^2) = \left(\frac{\varepsilon_{\mathrm{CIRC}}}{2}\right)^2 \times \frac{1}{12}, \tag{6.4}$$

where $\varepsilon_{\mathrm{CIRC}}$ is the form error value. Although strictly there are errors in both the regressors $\boldsymbol{X}$ and dependent variable $\vec{\boldsymbol{y}}$, it is approximated that errors only appear in the dependent variable which will greatly simplify the following analysis. The approximations $\sigma_{\mathrm{CIRC}}^2(x_\mathrm{c}) = \sigma_{\mathrm{CIRC}}^2(y_\mathrm{c})$ and $\sigma_{\mathrm{CIRC}}^2(x_\mathrm{c}, y_\mathrm{c}) = 0$ are also used for simplicity. There will some covariance and heteroscedasticity between the axes x and y from the printing process, but this can be expected to be negligible. The errors can therefore be found by

$$\sigma_{\mathrm{CIRC}}^2 = \sigma^2(x^2 + y^2)\frac{1}{\sum_{i=1}^{N} x_i^2}. \tag{6.5}$$

where N is the number of points used in the regression. The expectation of the square is given as

$$\mathbb{E}(x_i^2) = \frac{1}{N}\sum_{i=1}^{N} x_i^2 = \frac{r^2}{2}, \tag{6.6}$$

and therefore the eq. (6.5) can written as

$$\sigma_{\text{CIRC}}^2 = \frac{2}{Nr^2}\sigma^2(x^2 + y^2). \tag{6.7}$$

The uncertainty in position due to non-circularity is related to the circularity quantity by

$$\sigma_{\text{CIRC}}^2 = \frac{\varepsilon_{\text{CIRC}}^2}{24Nr^2}. \tag{6.8}$$

The highest measured circularity on the got grid is 100 µm. For dot of size 3.6 mm measured using 50 points, the resulting uncertainty in position is approximately 0.2 µm. The lowest uncertainty resulting from the MPE is approximately 1.5 µm – the circularity will have a small, almost negligible effect on the overall uncertainty. The uncertainty in x and y of each point is found by

$$\sigma^2(x) = \sigma^2(y) = \sigma_{\text{CIRC}}^2 + \sigma_{\text{MPE}}^2. \tag{6.9}$$

The dot grid was also measured for its flatness. The deviation of the dot grid was found by measuring the dot grid on a tactile CMS, given an MPE of 2.5 µm. The flatness deviation was found to be approximately 40 µm. The dot grid is assumed to be perfectly stiff, and not bend during the calibration. There will however be some bending in the calibration board, but it is assumed to be negligible. Similarly treating the MPE as a uniform distribution, a transform to a normal distribution gives

$$\sigma^2(z) = \frac{5^2}{12} \cong 3 \text{ µm}. \tag{6.10}$$

The magnitude of the uncertainty $\sqrt{\sigma^2(x) + \sigma^2(y)}$ for every dot on the dot grid is shown in Figure 6.3. The deviation from flat measured across the dot grid is given in Figure 6.4.

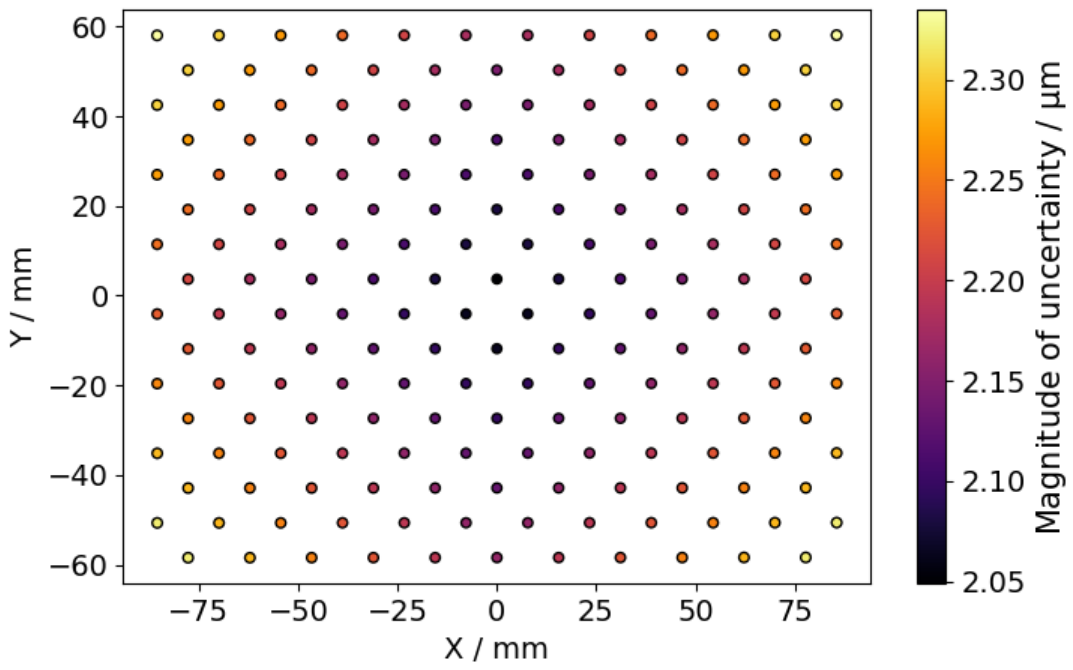

Figure 6.3 The magnitude of the uncertainty in the x and y plane of each dot across the dot grid.

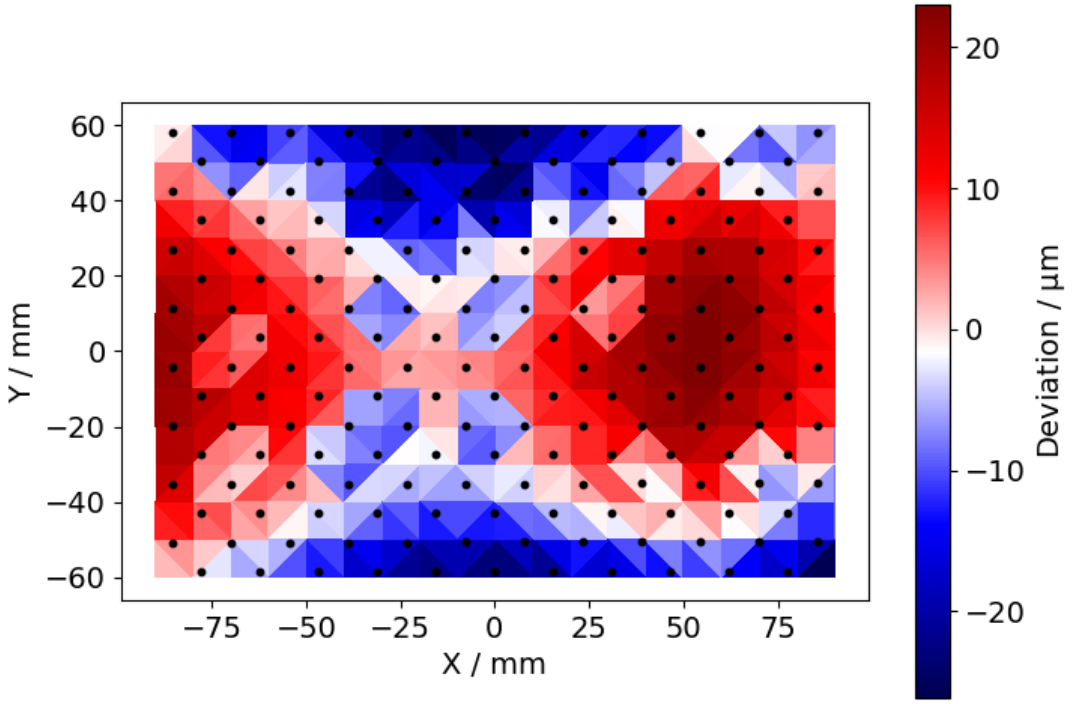

Figure 6.4 The deviation from flat across the dot grid board with the dots in black.

6.3 Feature localisation overview

This section will give an overview of the feature localisation method used in this thesis. Given the circular fiducials of the dot grid are imaged as an

approximately elliptical shape, this feature localisation method is named the ellipse localisation method. Dots refer specifically to the artefact fiducials, while ellipses refer specifically to the image of the dots, i.e., their projective transform to the image plane. Alternative dot localisation techniques can be found in [44, 207, 208]. The feature acquisition method must go through several steps, to produce a fully localised point within both the camera and projector images. An overview of the process is given in Figure 6.5.

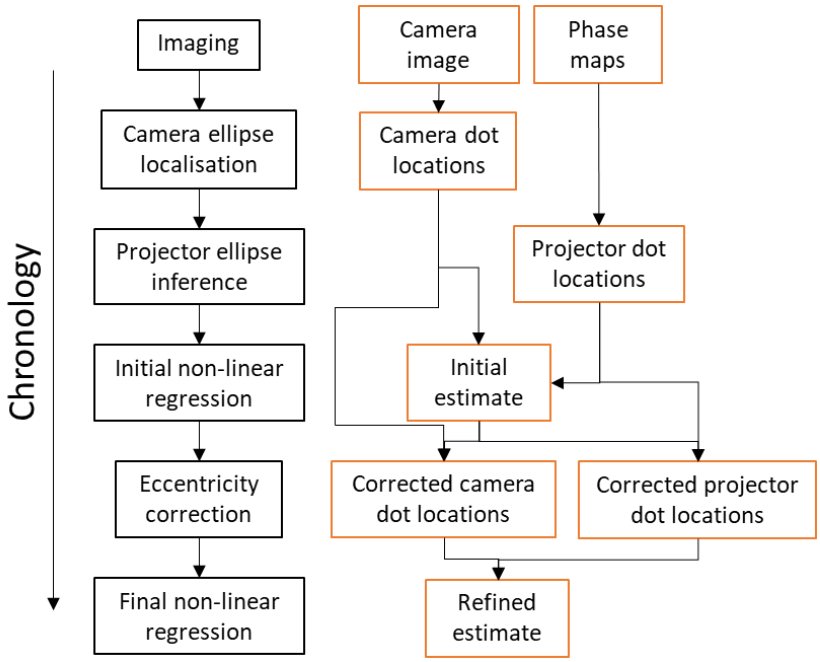

Figure 6.5 The outline of the algorithm to localise the centres of dots within the camera and projector images.

Prior to any measurements taking place, a start-up procedure is completed to allow thermal equilibrium within the camera and projector to be reached. For each pose, a single, well-illuminated image is taken followed by a series of images of projected sinusoids following the method given in Section 2.4. The camera ellipse locations are found in the single well-illuminated camera image. The method of obtaining the camera images used for the ellipse localisation is given in Section 6.4. The method to localise the ellipse centres in the camera image is given in Section 6.5. The images of projected sinusoids are decoded, to give a one-to-one correspondence map of camera pixels to projector pixels, called the phase map, using the method given in Section 2.4. The inside of the ellipses (the fiducial) provides poor phase measurements, so the surrounding local phase is used to estimate the phase map at the centre of the ellipse, and therefore convert the ellipse centre from camera coordinates to projector coordinates. The camera to projector coordinate transformation method is

given in Section 6.7. Given the centre of the dot does not map to the centre of the ellipse, Section 6.8 gives a correction method called eccentricity correction.

6.4 Image acquisition

This subsection details the imaging process used exclusively within the calibration. The aim of this subsection is to acquire images of the dot grid as accurately as possible. During the imaging step, a single, globally-illuminated image is taken of the dot grid, from which the camera ellipses are extracted in Section 6.5. Following this, a series of sinusoids are projected and captured, referred to as the "sinusoid images", that form the images of the modified heterodyne correspondence algorithm defined in Section 2.4. The sinusoid images will be decoded to give the projector mapping, from which the projector ellipse locations are inferred in Section 6.7.

Since the dot grid is on a flat plane, images of the dot grid can be expected to be absent of high-frequency components – except at the ellipse boundaries. However, the boundaries are not used in the inference of projector pixels. To reduce the impact that noise has on the phase map, sinusoid images can be filtered to remove high spatial-frequency components from the image. The cut-off frequency choice is a trade-off between removing high spatial frequency noise and corrupting the surrounding phase map with the ellipse boundary. The filter is chosen to be a Gaussian filter with width $\sigma = 0.28$, shown in Figure 6.6.

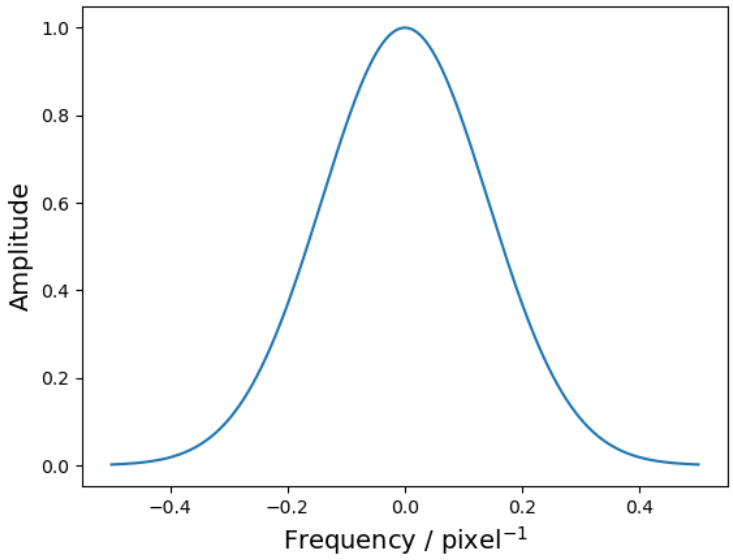

Figure 6.6 Gaussian filter used on the sinusoid images to reduce noise.

It was noted by Smith and Cope [125] that calibration should always be undertaken in the same conditions that a typical measurement will be carried out in. Changes in the system temperature affect optics, the CCD and the DMD, while temperature of the surrounding medium can alter the optical path of light rays. The temperature is a significant influence factor when considering the accuracy of the calibration, see Section 3.4.

Although a temperature compensation method can be used to alleviate change in focal length, the distortion parameters vary unpredictably, see Section 3.4. For this thesis, it was chosen not to use temperature compensation methods, to reduce complexity. Instead, it was assumed the fringe projection system reaches an equilibrium temperature after some time period. It is common to implement a warm-up period in fringe projection systems, for example in the GOM ATOS Core 300. The time period for this fringe projection system was found to be 45 mins, the result of which is taken from the repeatability test given in Section 6.9.

Secondly, pixels can be identified as saturated using the globally illuminated image. Any pixels values at 1023 are considered saturated. By streaming the camera image to the user while calibrating, the number of saturated pixels can be minimised by highlighting them to the user, to avoid positions of the board that are problematic.

6.5 Camera ellipse localisation

This section will detail how the centres of the ellipses are localised within camera images. This section will also evaluate the uncertainty on the localised ellipse centres. To localise the ellipses, gradient methods have been found to be a robust method [213], and therefore will form the basis of the method used in this thesis. Ellipse centres are localised using an estimation of the ellipse boundary, located at gradient peaks within the image. The sub-pixel gradient peaks are found using a series of line-spread functions. A rough ellipse centre location is found using the method findCirclesGrid in OpenCV 4.5.5. Ellipse boundary estimation outliers are removed using a RANSAC algorithm. Finally an ellipse is fit to the remaining points using a weighted total least-squares algorithm. A typical measurement is given in Figure 6.7 where a poorly imaged ellipse has been highlighted. There are several obvious issues with this particular dot: there is some specular reflection corrupting the edge pixels; there is some significant specular reflections inside the dot; and the projector pixels (providing the global illumination) are somewhat visible. The dot localisation algorithm must be robust against these specific issues.

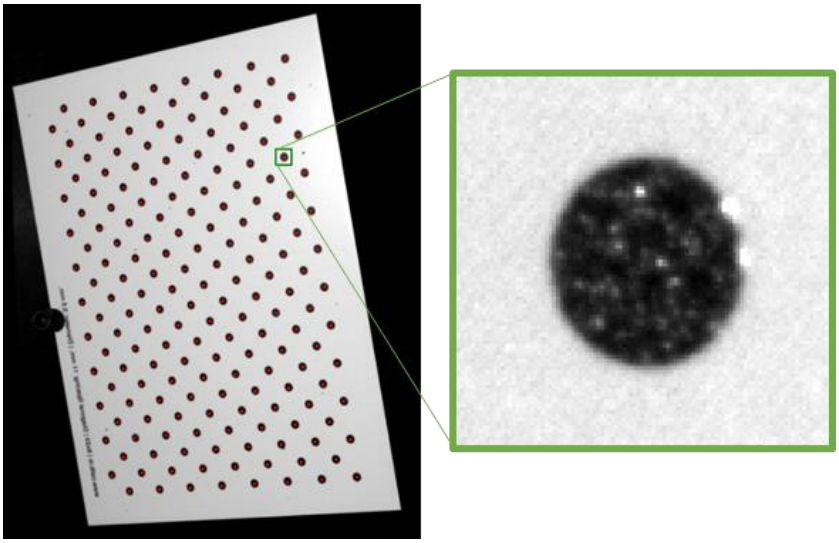

Figure 6.7 Rough estimation and extraction of an imaged ellipse from a dot grid artefact and its surrounding area.

6.5.1 Gradient image

To obtain the gradient image, a 101 × 101 pixel region of the image centred on the estimated dot location rounded to the nearest integer is extracted. The gradient image $\boldsymbol{I}_{\mathrm{G}}$ is found using convolution of the image with the Sobel kernels $\boldsymbol{S}_x$ and $\boldsymbol{S}_y$

$$\boldsymbol{S}_x = \begin{bmatrix} -1 & 0 & 1 \\ -2 & 0 & 2 \\ -1 & 0 & 1 \end{bmatrix} \tag{6.11}$$

$$\boldsymbol{S}_y = \begin{bmatrix} 1 & 2 & 1 \\ 0 & 0 & 0 \\ -1 & -2 & -1 \end{bmatrix}, \tag{6.12}$$

$$\boldsymbol{I}_{\mathrm{G}} = (\boldsymbol{S}_x \circledast \boldsymbol{I}_{\mathrm{D}})^2 + \left(\boldsymbol{S}_y \circledast \boldsymbol{I}_{\mathrm{D}}\right)^2 \tag{6.13}$$

with $\circledast$ defining a convolution.

6.5.2 Line-spread function

To find the sub-pixel location of the gradient peak, a series of line-spread functions are taken of the gradient image that expand radially from the estimated centre of the ellipse. It is assumed that the initial ellipse estimation is within ± 1 pixels. The number of line-spread functions are chosen to be the maximum number possible while remaining somewhat independent of each other at the ellipse boundary. The extracted gradient image is given in Figure 6.8. Each white line constitutes a line over which a line-spread function will be interpolated from.

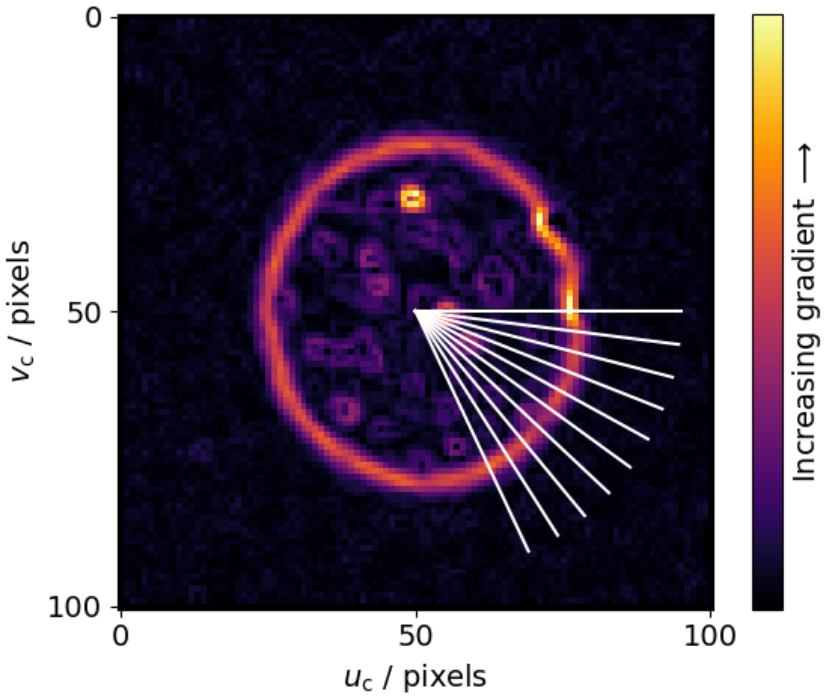

Figure 6.8 Gradient image with radially expanding lines over which line-spread functions are interpolated over.

The line-spread function is interpolated from the gradient image using a bilinear interpolation given by

$$y = A(u - uv) + Buv + C(1 - u - v + uv) + D(v - uv), \qquad (6.14)$$

where A, B, C, D represent the four closest pixel values, and u, v are the sub-pixel lengths denoting the position of the new value between pixels A, B, C, D. A diagram of the bilinear interpolation is given in Figure 7.

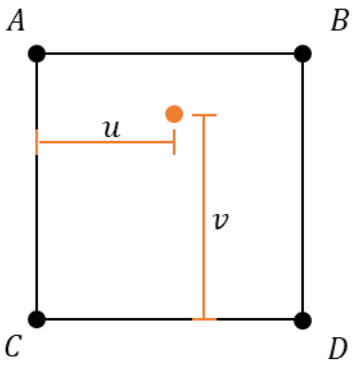

Figure 6.9 Linear interpolation scheme of a 2D image. The value A, B, C, D are the intensity values of the array at that location, u and v are the inter-array coordinates of range [0,1).

6.5.3 Peak determination

The ellipse boundary is estimated to be at the peak of each line-spread function. All line-spread functions are refined together during a single non-linear regression using the Levenberg-Marquardt algorithm. Each line-spread function is fitted with a Gaussian function, given by:

$$y = g(x, A, \mu, \sigma) = Ae^{-\frac{(x-\mu)^2}{2\sigma^2}}. \tag{6.15}$$

The parameters A, μ, σ are the peak height, peak centre and peak width to be found during the fitting. The fitting process is detailed explicitly in Appendix A. The peak height A and the peak centre μ are line-specific parameters. The peak width σ is a dot-specific parameter that is shared by all line-spread functions – reducing the degrees of freedom of the overall problem which will increase the accuracy and robustness.

The Gaussian function is chosen for this method because it is assumed that the line-spread function follows a similar function to a Gaussian function and because the tails of the Gaussian function quickly approaches zero. This is advantageous, since there is a lot of noise on either side of the peak, and this noise will have no effect on the Gaussian fitting. This allows the Gaussian function to effectively filter noisy false peaks on either side of the main contrast peak. The disadvantage is that a poor initial estimation will lead to the Gaussian function fitting to the wrong peak. A Gaussian function fitted to a line-spread function shown in Figure 6.8 is given in Figure 6.10.

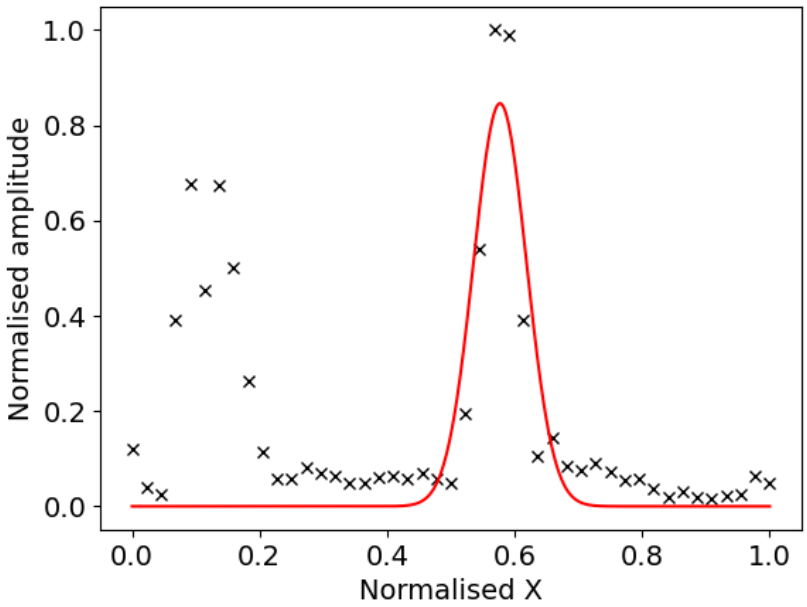

Figure 6.10 Gaussian function (red) fitted to the line-spread function (black).

The Levenberg-Marquardt algorithm requires an estimate, which is found by assuming that the semi-major and semi-minor axes of each ellipse do not greatly vary, and therefore the peak should occur in roughly the same place. The peak estimate is then found by finding the maximum value of the sum of all line-spread functions. Since the start of all line-spread functions begin in the same pixel, any specular reflection here will appear in all line-spread functions and could dominate the sum. An example of this can be seen at around $X \approx 0.1$ in Figure 6.10. Given the dot-grid artefact is never far enough away that the ellipse will spear small in the camera image, the first 20% of the line-spread function is discarded during the initial estimate so there can be no dominating effects from specular reflections. If the true Gaussian peak is not within the estimated Gaussian curve, the Jacobian could be zero at the true Gaussian peak location, and therefore the Levenberg-Marquardt algorithm will fail to converge to this location. Therefore, an initial estimate of the Gaussian curve is provided that is large enough to always encompass the true Gaussian peak location – avoiding this issue. Significant specular reflection close the ellipse boundary can lead to fitting to the wrong peak, seen in Figure 6.11.

6.5.4 Outlier removal

There is no guarantee that the Gaussian peaks fitted in Section 6.5.3 have converged to the correct peak – the outliers in the peak centre estimation data must be removed as they do not conform to a normal distribution of errors. A random sample consensus (RANSAC) algorithm is used to determine if any line-spread functions have fitted to the wrong peak. The ellipse RANSAC cleaning algorithm is given in Algorithm 3 below. A series of ellipses are defined from a randomly subsampled set of five ellipse boundary points. For each randomly defined ellipse, the distance of each point to the ellipse boundary is found. The point-to-boundary distance is used to judge the viability of the ellipse, where the best ellipse has the lowest collective point-to-boundary distance. Points are discarded based on the collection of point-to-boundary distances.

Algorithm 3 Ellipse RANSAC algorithm used to identify and remove erroneous boundary estimations of ellipses.

Set N_{best} to 0
Set maximum distance $d_{\max}$
For number of iterations:
    Randomly sample 5 points without replacement from the total dataset.
    Fit ellipse to sampled points using the least-squares regression,
        described in Appendix B
    Calculate the smallest distance, d from each point to the ellipse
        perimeter.
    Calculate $N = \sum(d < d_{\max})$.
    If $N > N_{\text{best}}$:
        $N = N_{\text{best}}$.
        Store ellipse coefficients.
    End If
End For

The calculation of point-to-ellipse perimeter distance is given in Chou [214]. The extracted dot in Figure 6.7 has some significant specular reflections that have corrupted the boundary of the ellipse and have the potential for the Gaussian to fit to false peaks within the ellipse. A single false peak and several poor edge points can be found in the located sub-pixel boundary points given in Figure 6.11. The RANSAC algorithm is subsequently able to differentiate these corrupted points, denoted as red in the figure. It should be noted that the method given in Chou [214] can suffer from numerical inaccuracies – particularly oblique ellipses may produce invalid results. Any invalid results will be reflected in the uncertainty estimation and will be essentially removed from the calibration using the weighting matrix. All ellipses used in this calibration were far from this condition.

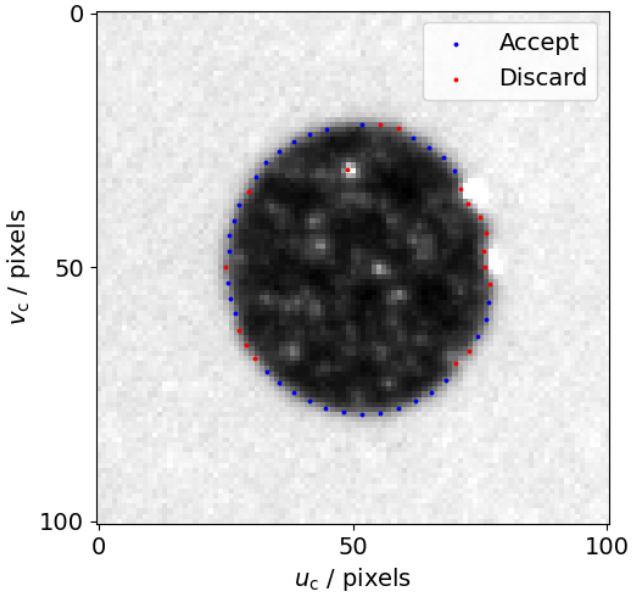

Figure 6.11 The located sub-pixel boundary of an imaged ellipse. Points that have been found to be erroneous are coloured red, remaining points are coloured blue.

6.5.5 Ellipse fitting

The ellipse centre can now be localised using the estimated ellipse boundary points. An ellipse is defined as ellipse function f_e,

$$\begin{aligned} f_e(x, y, x_0, y_0, a, b, \phi) \\ &= \left(\frac{(x - x_0)\cos\phi + (y - y_0)\sin\phi}{a}\right)^2 \\ &+ \left(\frac{-(x - x_0)\sin\phi + (y - y_0)\cos\phi}{b}\right)^2 = 1, \end{aligned} \tag{6.16}$$

where (x_0, y_0) is the ellipse centre, a and b are the semi-major and semi-minor axes respectively and ϕ is an arbitrary rotation. Eq. (6.17) can be compactly written with the implicit matrix equation

$$\begin{bmatrix} x \\ y \\ 1 \end{bmatrix}^{\mathrm{T}} \begin{bmatrix} A & \frac{B}{2} & \frac{D}{2} \\ \frac{B}{2} & C & \frac{E}{2} \\ \frac{D}{2} & \frac{E}{2} & F \end{bmatrix} \begin{bmatrix} x \\ y \\ 1 \end{bmatrix} = 0 \tag{6.17}$$

$$\vec{\boldsymbol{x}}^{\mathrm{T}} \boldsymbol{M} \vec{\boldsymbol{x}} = 0. \tag{6.18}$$

The ellipse fitting algorithm is needed to find coefficients $\vec{\boldsymbol{m}} = \{A, B, C, D, E, F\}$ with robustness and accuracy. Given the magnitude $\|\boldsymbol{M}\|$ is arbitrary, the ellipse coefficients are often shortened to $\vec{\boldsymbol{m}}' = \{A', B', C', D', E'\}$ to remove this

degree of freedom. For information on ellipse fitting algorithms, see Appendix B .

An ordinary least-squares estimation will neglect any error in the regressors. Weighted total least-squares will consider the error of the regressors in determining the outputs. The weighted total least-squares method given here is taken from Amiri-Simkooei and Jazaeri [215] and adapted to the least-squares method used in Fitzgibbon, Pilu [216]. The weighted total least-squares method given in Amiri-Simkooei and Jazaeri [215] is a natural extension to the iteratively reweighted least-squares method, described in Appendix B. The method given below allows the propagation of uncertainty from ellipse points to the ellipse coefficients.

At each iteration, instead of estimating the error in the observation vector $\vec{\boldsymbol{y}}$ as a parameter during the regression, the error can be estimated from propagating the error in the regressor matrix to the dependent variable. The dependent variable in this case is given by $\vec{\boldsymbol{y}} = \vec{\mathbf{1}}$. The uncertainty in $\vec{\boldsymbol{y}}$ is given by $\boldsymbol{V}_y$. The uncertainty in the regressor matrix $\boldsymbol{A}$ is given by $\boldsymbol{V}_A$. The notation convention is transposed to that supplied in Amiri-Simkooei and Jazaeri [215] to maintain consistency with the matrix notation used within this thesis. The ellipse $\overrightarrow{\boldsymbol{m}}'$ is found as the solution to

$$\vec{\boldsymbol{y}} = \boldsymbol{A}\vec{\boldsymbol{x}} = \begin{bmatrix} A_{11} & A_{12} & \cdots \\ A_{21} & \ddots & \ddots \\ \vdots & \ddots & \ddots \end{bmatrix} \overrightarrow{\boldsymbol{m}}'. \tag{6.19}$$

The regressor uncertainty, $\boldsymbol{V_A}$, is given in row-leading format (as opposed to column-leading in Amiri-Simkooei and Jazaeri [215]). For an ellipse containing N points, the columns and rows of $\boldsymbol{V_A}$ are covariances of

$$[A_{11} \quad \ldots \quad A_{1N} \quad A_{21} \quad \ldots]. \tag{6.20}$$

It is noted in Amiri-Simkooei, Zangeneh-Nejad [217], that both $\boldsymbol{V}_{\hat{y}}$ and $\boldsymbol{E_A}$ exhibit some randomness and the weighted total least-squares is only a linear approximation. Therefore, when estimating the final uncertainty, a loss function is used to estimate the impact of the estimation of $\overrightarrow{\boldsymbol{m}}'$, assuming $\boldsymbol{V}_y$ to be correct, given as

$$\sigma^2 = \max\left(1, \left(\hat{\boldsymbol{y}} - \hat{\boldsymbol{A}}\overrightarrow{\boldsymbol{m}}'_{i+1}\right)^{\mathrm{T}} \boldsymbol{V}_{\hat{y}}^{-1} \left(\hat{\boldsymbol{y}} - \hat{\boldsymbol{A}}\overrightarrow{\boldsymbol{m}}'_{i+1}\right)\right). \tag{6.21}$$

The total weighted least-square method to fit ellipses is defined in Algorithm 4 below.

Algorithm 4 Weighted total least-squares ellipse estimation.

Obtain least squares estimation of the ellipse, $\vec{\boldsymbol{m}}'_{i=0} = (\boldsymbol{A}^{\mathrm{T}}\boldsymbol{A})\boldsymbol{A}^{\mathrm{T}}\vec{\boldsymbol{y}}$
Set $i = 0$
While not converged:
    Estimate updated covariance matrix $\boldsymbol{V}_{\hat{y}} = \boldsymbol{V}_{y} + (\mathbb{I} \otimes \vec{\boldsymbol{m}}'_i)^{\mathrm{T}}\boldsymbol{V}_{A}(\mathbb{I} \otimes \vec{\boldsymbol{m}}'_i)$
    Estimate errors $\vec{\boldsymbol{e}}_{\boldsymbol{A}} - \boldsymbol{V}_{\boldsymbol{A}}(\mathbb{I} \otimes \vec{\boldsymbol{m}}')\boldsymbol{V}_{\hat{y}}^{-1}(\vec{\boldsymbol{y}} - \boldsymbol{A}\vec{\boldsymbol{m}}'_i)$
    Convert to matrix $\boldsymbol{E}_{\boldsymbol{A}} = \mathrm{vec}^{-1}(\vec{\boldsymbol{e}}_{\boldsymbol{A}})$
    Estimate updated regressor matrix $\hat{\boldsymbol{A}} = \boldsymbol{A} - \boldsymbol{E}_{\boldsymbol{A}}$
    Estimate update observation vector $\hat{\boldsymbol{y}} = \vec{\boldsymbol{y}} - \boldsymbol{E}_{\boldsymbol{A}}\vec{\boldsymbol{m}}'_i$
    Solve for the ellipse using weighted least – squares
        $\vec{\boldsymbol{m}}'_{i+1} = \left(\hat{\boldsymbol{A}}^{\mathrm{T}}V_{\hat{y}}^{-1}\hat{\boldsymbol{A}}\right)\hat{\boldsymbol{A}}^{\mathrm{T}}V_{\hat{y}}^{-1}\hat{\boldsymbol{y}}$
    If $\|\vec{\boldsymbol{m}}'_{i+1} - \vec{\boldsymbol{m}}'_i\| < 1 \times 10^{-10}$:
        Break While loop, the algorithm has converged
    End If
    Iterate $i = i + 1$
End While
Estimate error using the loss function:
    $\sigma^2 = \max\left(1, \left(\hat{\boldsymbol{y}} - \hat{\boldsymbol{A}}\vec{\boldsymbol{m}}'_{i+1}\right)^{\mathrm{T}}\boldsymbol{V}_{\hat{y}}^{-1}\left(\hat{\boldsymbol{y}} - \hat{\boldsymbol{A}}\vec{\boldsymbol{m}}'_{i+1}\right)\right)$
Estimate uncertainty using $\sigma^2\left(\hat{\boldsymbol{A}}^{\mathrm{T}}V_{\hat{y}}^{-1}\hat{\boldsymbol{A}}\right)$

In the algorithm above, $\otimes$ is the Kronecker product. The vec operator transforms a matrix into a vector, and its inverse, vec^{-1}, transforms a vector into a matrix

The weighted total least-squares algorithm allows the uncertainty in the ellipse boundary points found above to be propagated to uncertainty in the ellipse coefficients. An alternative unweighted total least-squares method to estimate ellipses is found in Fang, Wang [218]. The novelty here is this is the first time a weighted total least-squares method is applied to ellipses for the application of calibration of a fringe projection system. The weight total least-squares method is tested against other ellipse methods, as well the uncertainty, in Section 6.6.1. The image ellipse localisation algorithm is tested in Section 6.6.2. The uncertainty in boundary points is shown in Figure 6.12(a), and the uncertainty of the ellipse is shown Figure 6.12(b).

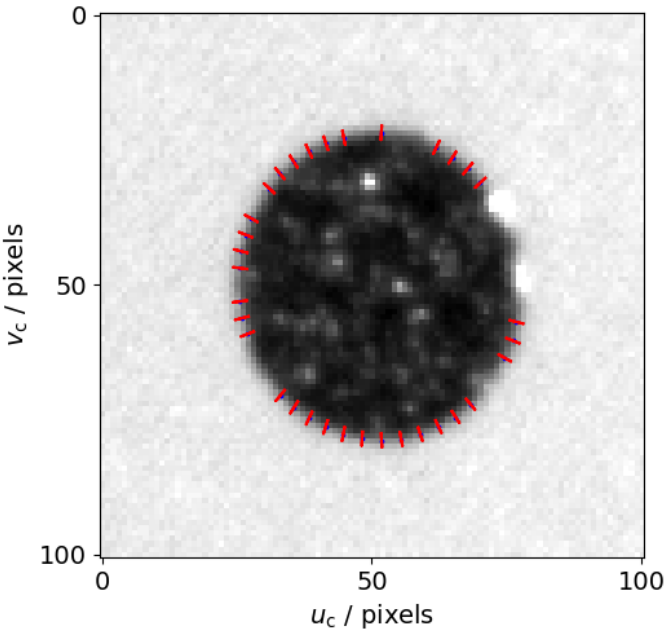

(a)

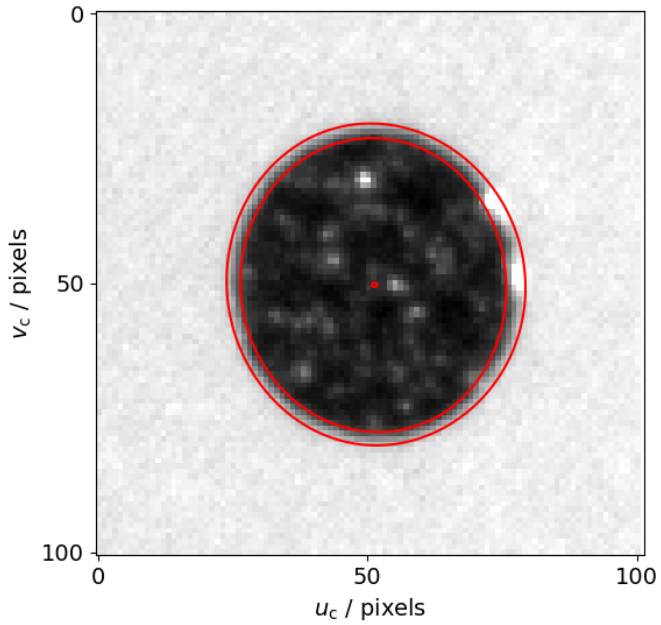

(b)

Figure 6.12 Uncertainty of the imaged ellipses (a) boundary and (b) ellipse centre and perimeter at 95% confidence.

6.6 Camera ellipse localisation validation

In this section, a series of tests are performed on the methods developed in Section 6.5 to validate their performance. In Section 6.6.1, the accuracy of different ellipse fitting algorithms are tested against each other. Additionally,

the weighted total least-squares method defined in Section 6.5.5 will be tested for validity. In Section 6.6.2, the ellipse localisation method defined in Section 6.5 will be tested for validity using virtual ellipses.

6.6.1 Ellipse fitting algorithm test

In this section, existing ellipse fitting algorithms are compared against each other to test how accurately they localise the centre of an ellipse given the boundary point estimations. The following ellipse fitting methods will be tested: least-squares, iteratively-reweighted least-squares, weighted total least-squares, Taubin and hyper-renormalisation. The methods least-squares and iteratively-reweighted least-squares are defined in Appendix B, weighted total least-squares is defined in Section 6.5.5, and Taubin and hyper-renormalisation methods are not defined in this thesis but can be found in Kanatani, Sugaya [219]. The covariance matrix estimated using the weighted total least-squares method defined in Section 6.5.5 will be tested using the reduced χ^2 condition.

Each algorithm is tested on a set of randomly generated ellipse points, where the set of ellipse points will be designated the term virtual ellipse. Four tests were conducted using varying correlation between points and a set lengths of arc of the ellipse. For each virtual ellipse, a random covariance matrix was created that would be used to randomly perturb 50 points of an ellipse. To simulate the RANSAC algorithm in Section 6.5.4, each point has a 40% chance of being discarded. Each ellipse fitting method is tested with 10000 virtual ellipses. The distribution of the virtual ellipse parameters are given in Table 6.1. Each distribution was chosen to be representative of the conditions the fitting algorithms are to perform in.

Table 6.1 Ellipse quantities and the distributions they are drawn from.

Quantity	Distribution
Centre of ellipse, $\begin{bmatrix} x_0 \\ y_0 \end{bmatrix}$	$\mathcal{N}\left(\begin{bmatrix} 0 \\ 0 \end{bmatrix}, 0.1 \times \mathbb{I}_{2\times 2}\right)$
Ellipse axes, $\begin{bmatrix} A \\ B \end{bmatrix}$	$\mathcal{N}\left(\begin{bmatrix} 25 \\ 25 \end{bmatrix}, \mathbb{I}_{2\times 2}\right)$
Rotation of ellipse, ϕ	$\mathcal{U}(0, 2\pi)$
Point error, σ	$\mathcal{N}(0,0.5)$
Correlation, ρ	$\mathcal{U}(0, 1)$

Each generated ellipse point was perturbed using a Gaussian error defined by $\mathcal{N}\left(\begin{bmatrix} 0 \\ 0 \end{bmatrix}, \boldsymbol{V}_{\mathrm{R}}\right)$, where $\boldsymbol{V}_{\mathrm{R}}$ is a covariance matrix generated using correlation coefficient ρ

$$\boldsymbol{V}_R = \mathbb{I}_{2\times 2}\sigma_R + \begin{bmatrix} 0 & \rho \\ \rho & 0 \end{bmatrix}\sigma^2. \tag{6.22}$$

The algorithm used to define each ellipse is given in Algorithm 5.

Algorithm 5 Monte-Carlo test of ellipse fitting functions

For 10000 repetitions:
    Create random covariance matrix $\boldsymbol{V}_{\mathrm{R}}$
    Find Cholesky decomposition of $\boldsymbol{V}_{\mathrm{R}} = \boldsymbol{C}\boldsymbol{C}^{\mathrm{T}}$
    Create random ellipse $\vec{\boldsymbol{x}}$ edge points
    Generate vector of independently and identically distributed random variables, sampled from $\vec{\boldsymbol{\xi}} \sim \mathcal{N}(0, 1)$
    Apply correlation to the random variables with $\boldsymbol{C}\vec{\boldsymbol{\xi}}$
    Perturb ellipse edge points $\tilde{\boldsymbol{x}} = \vec{\boldsymbol{x}} + \vec{\boldsymbol{\xi}}$
    Randomly discard roughly 40% of boundary points
    Fit ellipse to boundary points $\tilde{\boldsymbol{x}}$
End For

The results of the full Monte-Carlo test for the five ellipse fitting methods are given in Figure 6.13. The ellipse fitting techniques show very similar across all scenarios and are all ill-conditioned in the half-ellipse scenario. It is to be expected therefore that ellipses in the dot-localisation algorithm that have a significant portion of the ellipse boundary corrupted with noise will have significantly higher errors in the ellipse fitting.

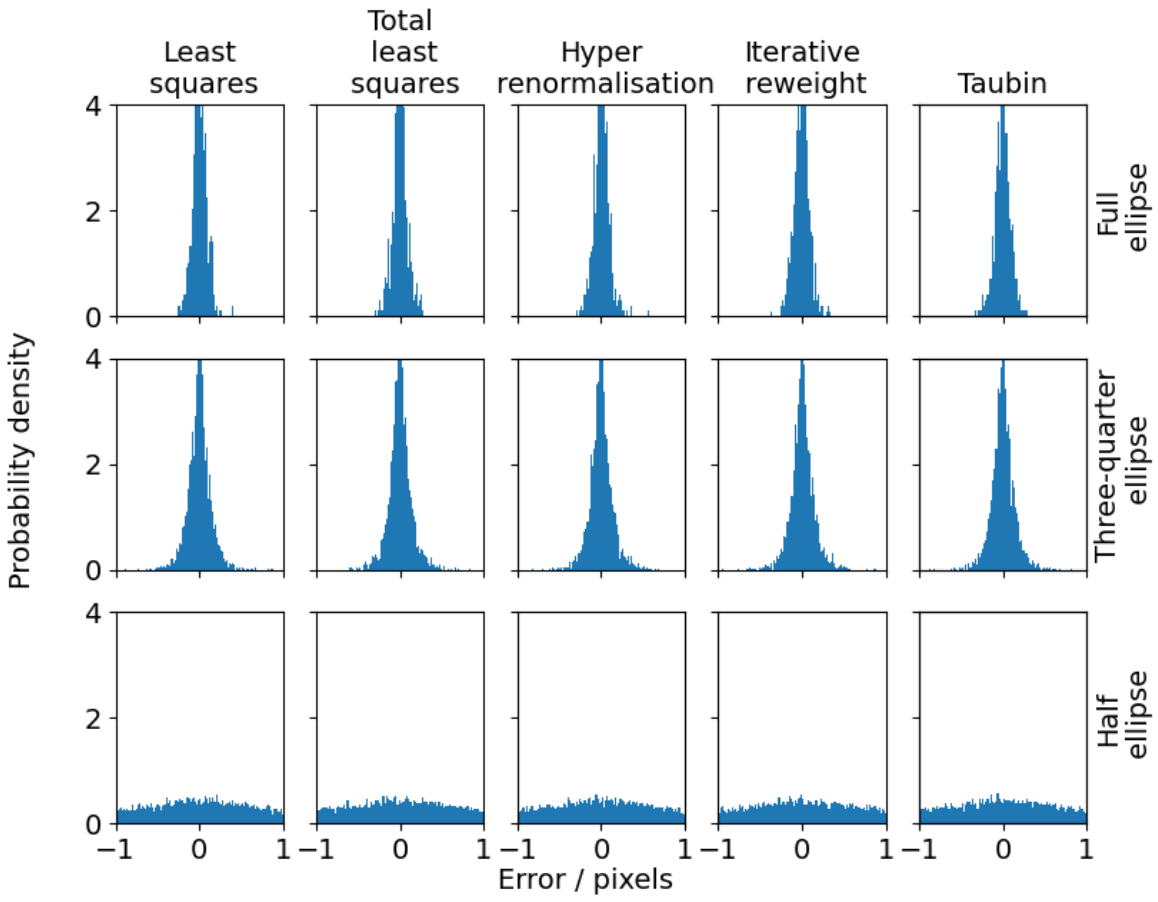

Figure 6.13 Comparison of the ellipse fitting methods for a full ellipse, three-quarter ellipse and half ellipse.

Additionally, the uncertainty evaluation of the fitting process from the weighted total least-squares fitting for the centre of the ellipses is tested using the reduced χ^2 test, see Section 4.4. Since each ellipse fitting can be solved with at least four ellipse solutions (given the four-way symmetry of an ellipse), only the ellipse centre is tested. Regardless, it is only the ellipse centre information that is important in the ellipse localisation algorithm. The reduced χ^2 test results of the weight total least-squares method for each ellipse fitting test was 0.86, 0.87 and 0.87 for the full ellipse, three-quarter ellipse and half ellipse tests respectively. This result shows that the weighted total least-squares function, provided with the correct weighting matrix, adequately provides an accurate estimation of the ellipse centre rivalling most fitting methods, as well as a reasonable estimate of the uncertainty in the ellipse centre.

6.6.2 Ellipse localisation test

In this section, the complete camera ellipse localisation method defined throughout Section 6.5 will be tested using a series of virtual ellipse. A virtual ellipse in this section is defined as a virtual image, unlike the previous section.

To ensure the generated virtual ellipses are consistent with measured ellipse, the virtual ellipses will be generated using parameters sampled from real measured ellipses. The ellipses are defined using the following parameters given in Table 6.2. The parameters are shown in Figure 6.14. The internal distribution defines the distribution of intensity values inside the ellipse, while the external distribution defines the distribution of intensity values outside the ellipse. Specular components within the ellipse are defined as intensity values that do not conform to the internal intensity distribution. The blurring kernel defines the blur of the image of the ellipse.

Table 6.2 Virtual ellipse parameters.

Definition	Unit
Ellipse position X axis	pixels
Ellipse position Y axis	pixels
Ellipse semi-major axis	pixels
Ellipse semi-minor axis	pixels
Internal pixel distribution mean	unitless
Internal pixel distribution scale	unitless
External pixel distribution mean	unitless
External pixel distribution scale	unitless
Specular volume	unitless
Specular max	unitless
Blurring kernel width	pixels

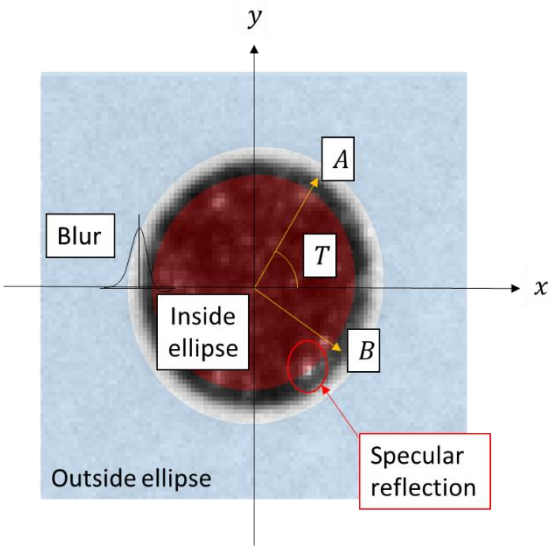

Figure 6.14 Image of ellipse annotated with the parameters used to define ellipses.

The distributions of the ellipse parameters given above are defined from the current dataset of ellipses found during the calibration. This way, the virtual dataset will accurately represent the real dataset. To define each parameter distribution, each ellipse is first extracted. The internal intensity values are defined as all pixels within a perimeter offset −5 pixels from the estimated ellipse boundary. The external values are defined as all pixels outside the ellipse defined by a perimeter offset +5 pixels from the estimated ellipse boundary, so as not to include any pixels corrupted by the contrast boundary, shown in Figure 6.15.

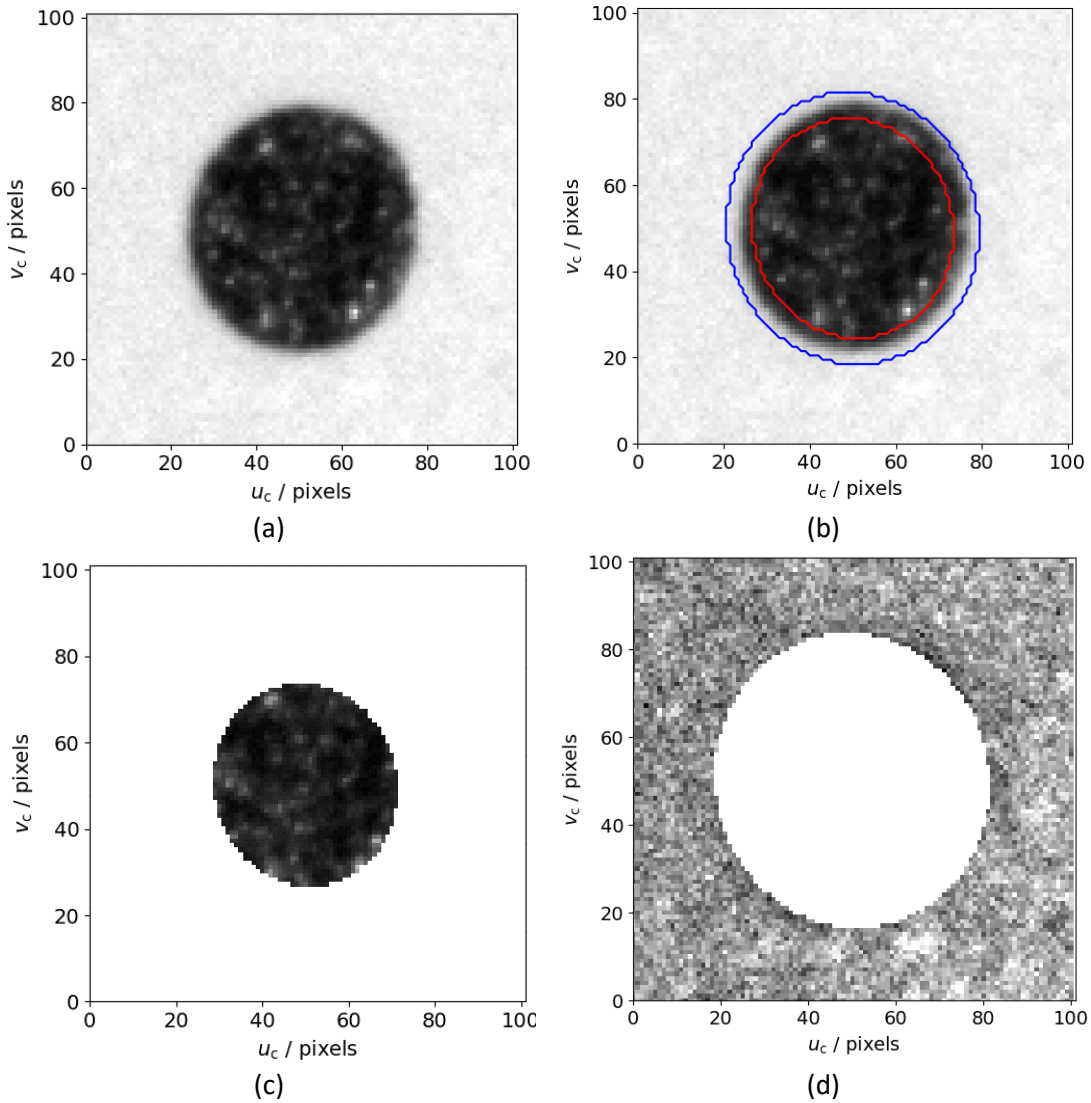

Figure 6.15 The distinction between "inside" an ellipse and "outside" an imaged ellipse. (a) The extracted ellipse. (b) The offset perimeters from the estimated ellipse used to define the boundary between the inside and outside of the ellipse. (c) The internal pixels and (d) the external pixels.

The internal and external histogram plots of the internal and external pixels, along with a fitted log-normal distribution, shown in Figure 6.16. It should be noted that several pixel values are missing – this is possibly due to the camera outputting 8-bit numbers, and interpolates pixel values to 10-bit. The error this causes is about 0.1% error, negligible compared to the phase error values.

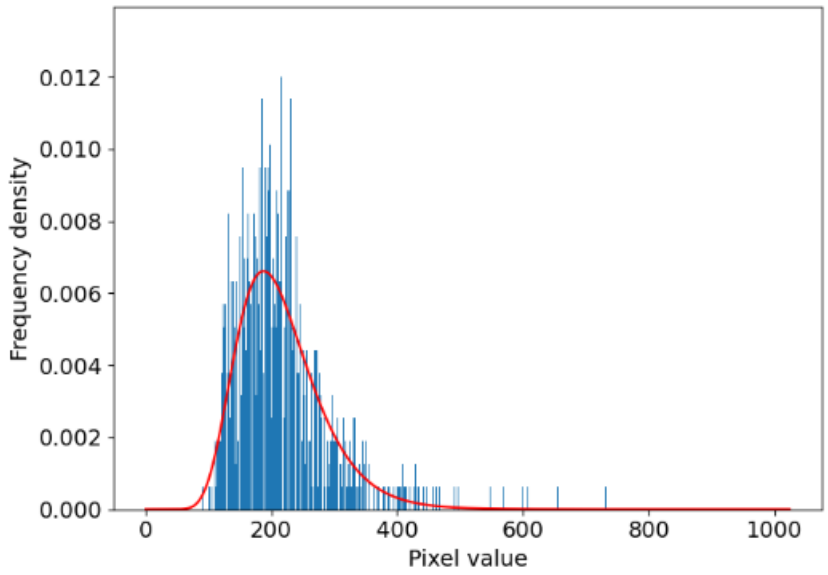

(a)

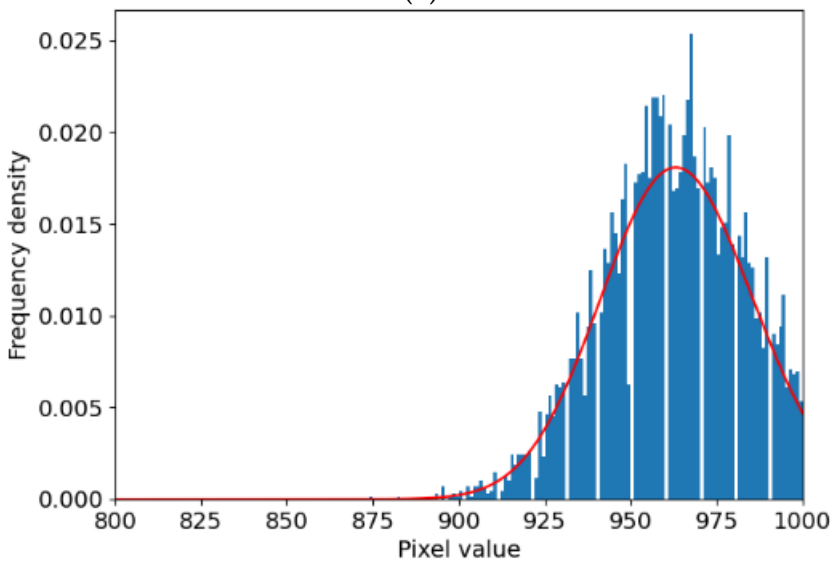

(b)

Figure 6.16 The histograms (blue) and overlaid probability distribution functions (red) of the (a) internal pixels and (b) the external pixels.

The specular components are isolated by identifying pixels that are higher 99% of other pixels within the internal region, shown in Figure 6.17. Specular components are defined by two parameters, specular volume that defines the extent of speckle in the ellipse, and speckle max

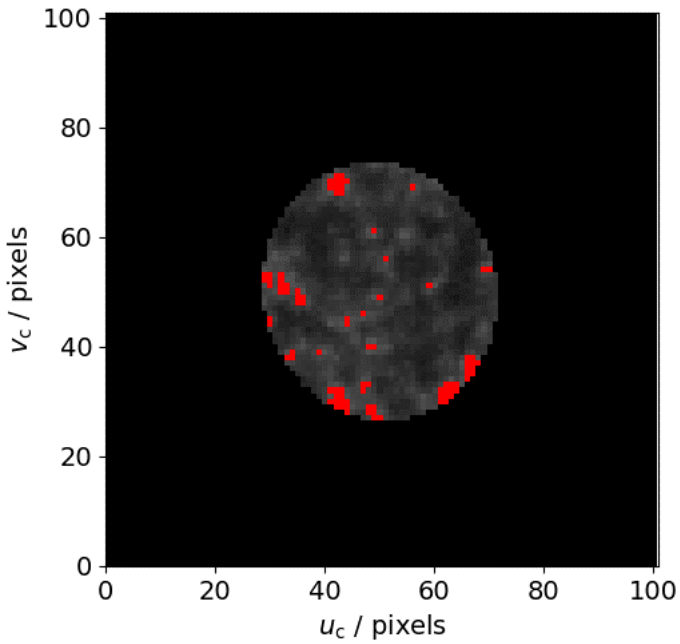

Figure 6.17 The internal pixels that have been identified as specular reflections (red).

Repeating this for every dot in the calibration gives a distribution of all ellipse parameters. The distributions are generally not well-defined by a parametric distribution. Kernel density estimation (KDE) is a non-parametric way to estimate a variables probability distribution function [220]. The theory of KDE and the practical application is outside the scope of this thesis and only a basic overview is given here. The KDEpy library is used in this thesis for any KDE computations. A kernel density estimate is very similar to a histogram but can be endowed with properties such as smoothness or continuity by using a suitable kernel. The choice of kernel, i.e., the level of smoothing, and can be optimally chosen from the data. Resampling data from the fitted KDE is equivalent to (1) first resampling the original data (with replacement), then (2) adding noise drawn from the same probability density as the kernel function in the KDE. The resampling method can be extended to arbitrary extra dimensions. Some consideration must be taken for the correlation between some variables. For example, a poor contrast will give a poor ellipse localisation. Therefore, the input and output distribution parameters are treated in a single 4D KDE. The histograms of each parameter, along with a fitted KDE, is give in Figure 6.18.

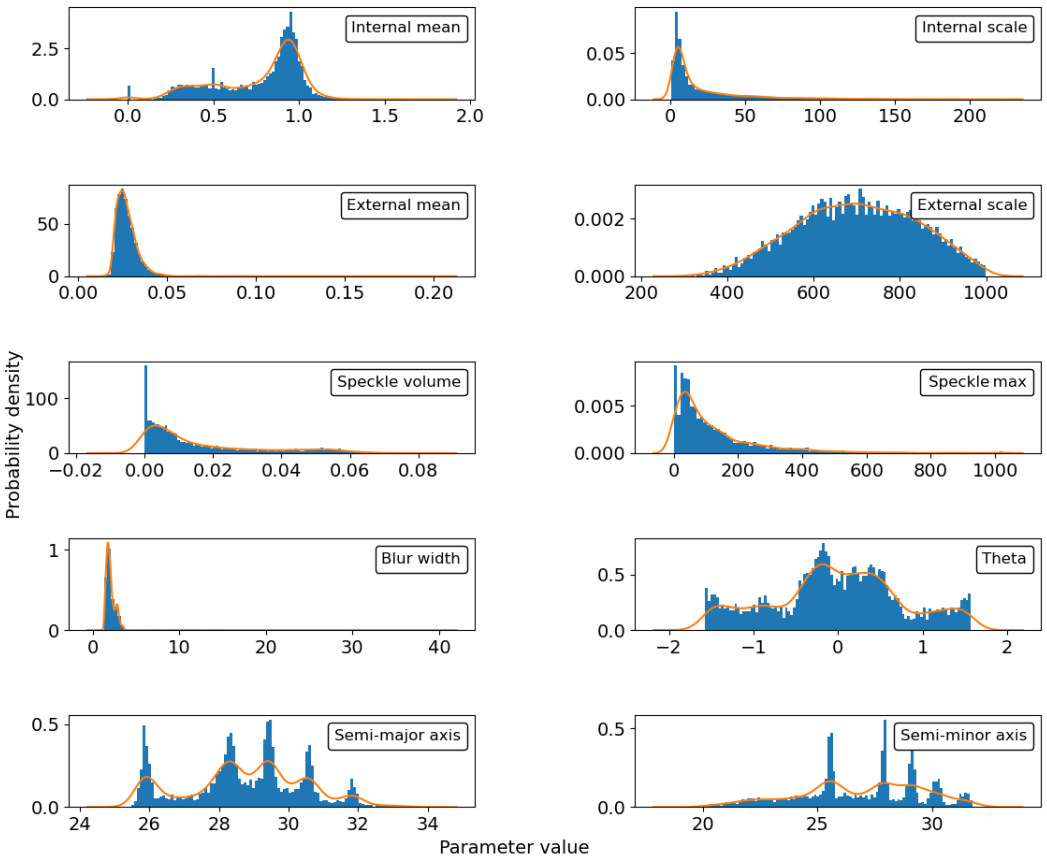

Figure 6.18 KDE of all parameters used to create a virtual ellipse, defined using the calibration dataset.

Some sampled KDEs can produce invalid samples, such as a negative internal scale value. In the case an invalid value is drawn, the value is redrawn. The true blurring kernel is unknown, and so the test will be repeated with four different blurring kernels. The virtual ellipses along with the blur kernels is shown in Figure 6.19.

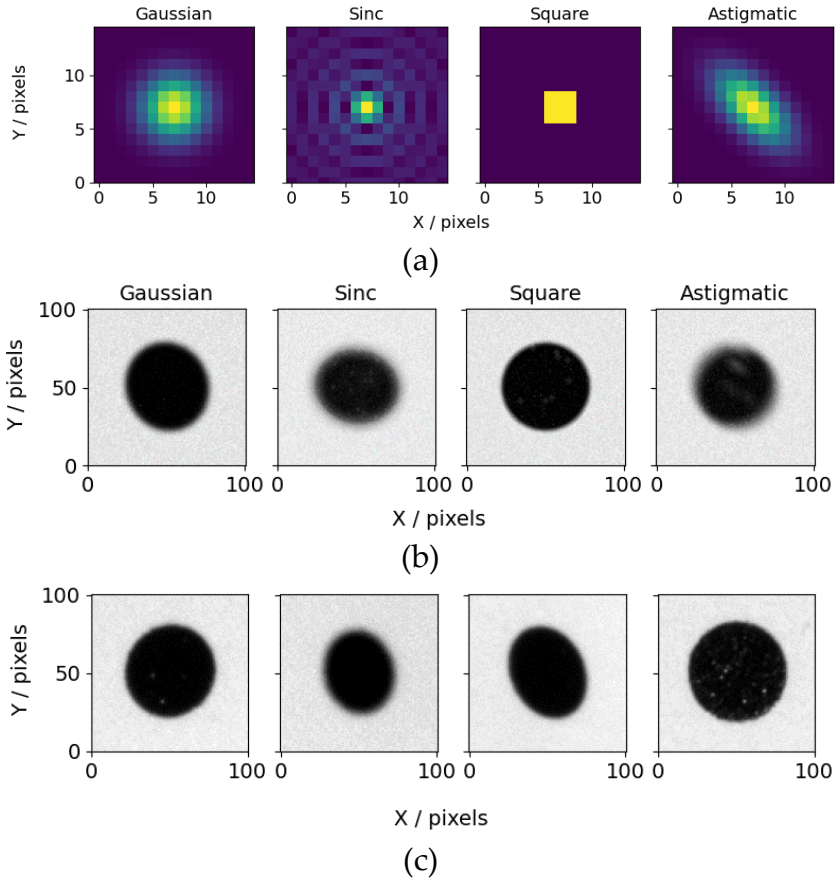

Figure 6.19 (a) Blurring kernels used in the creation of (b) virtual ellipses. (c) Four ellipses from the calibration dataset chosen at random.

The results of the ellipse localisation algorithm are given in Figure 6.20, and the χ^2 values are given in Figure 6.21. The ellipse localisation performs well with all blurring kernels, with the best performance with the square blur kernel. Some significant outliers exist where the simulated data has a substantial portion of the ellipse boundary corrupted. The χ^2 test values show that the uncertainty evaluation of the ellipse localisation consistently over-estimates the uncertainty in the ellipse locations.

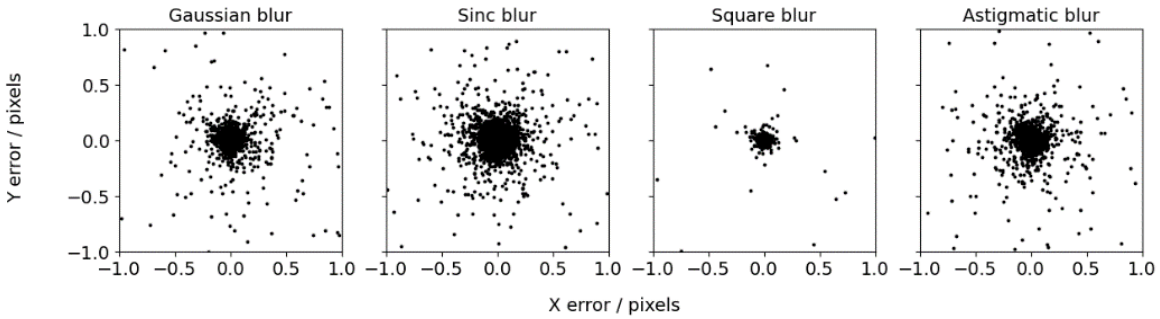

Figure 6.20 Error in ellipse localisation from the Monte-Carlo test using each of the four blurring kernels.

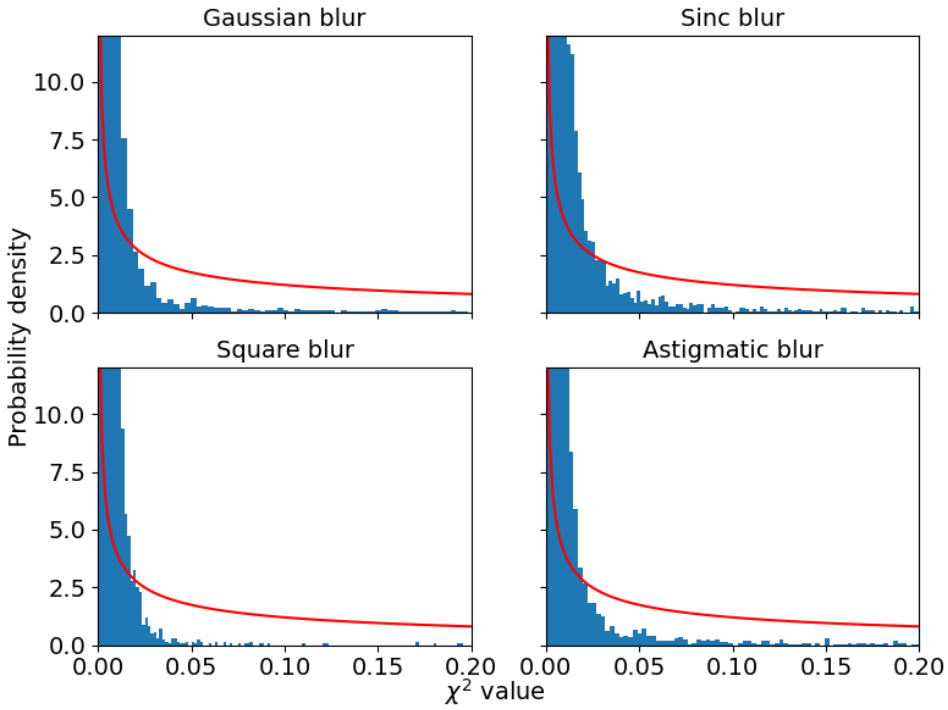

Figure 6.21 The χ^2 values for all ellipse localisation from the Monte-Carlo test of each blurring kernel.

6.7 Projector ellipses inference

This section describes the method used to infer the projector ellipse centre, using the camera ellipse centres found using the method in Section 6.5, and the decoded mapping images captured and decoded using the method given in Section 2.4. Inference is given in three steps, mapping region extraction, transform estimation and finally transform application.

As with the camera, a 101×101 region around the ellipse centre is extracted, so that the ellipse exists in the centre of the image. The ellipse centre and its boundary will not give accurate mapping data and must be discarded. The discarded area is found by expanding both the semi-major and semi-minor axes by 8 pixels. Pixels located within the expanded ellipse are discarded, leaving only the surrounding mapping region that is uncorrupted by a contrast boundary or poor contrast, shown in Figure 6.22.

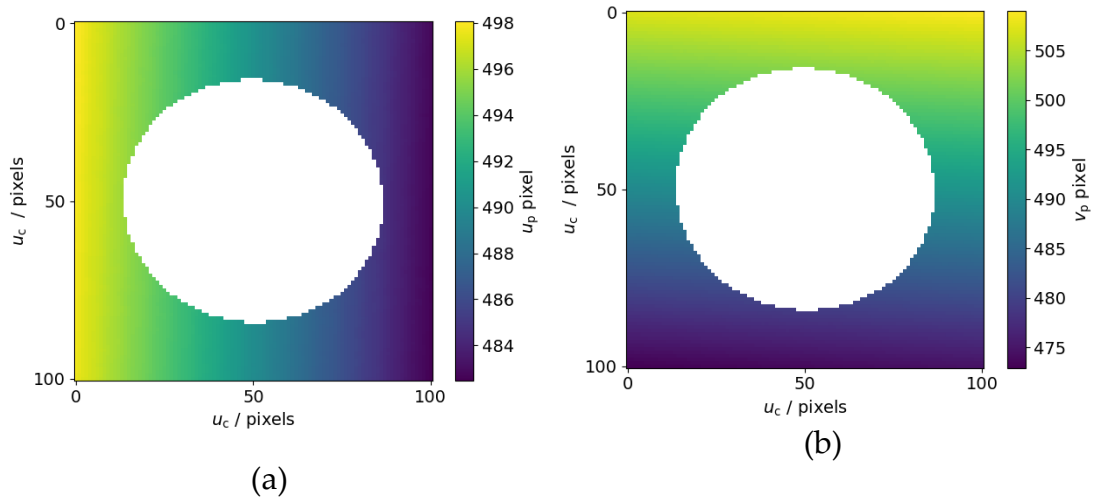

Figure 6.22 Cropped region around the dot for the camera-to-projector mapping of the (a) u-axis and (b) v-axis.

The dot grid is located on a flat plane, so the mapping is given by a rational function. However, locally, the mapping can be considered linear and is given by

$$\begin{bmatrix} u_\mathrm{p} \\ v_\mathrm{p} \end{bmatrix} = \begin{bmatrix} A & B & C \\ D & E & F \end{bmatrix} \begin{bmatrix} u_\mathrm{c} \\ v_\mathrm{c} \\ 1 \end{bmatrix}. \tag{6.23}$$

The coefficients $\vec{\boldsymbol{X}} = \{A, B, C, D, E, F\}$ can be found using the linear regression $\vec{\boldsymbol{u}}_\mathrm{p} = \hat{\boldsymbol{u}}_\mathrm{c}\vec{\boldsymbol{X}}$ (note that $\hat{\boldsymbol{u}} \neq \vec{\boldsymbol{u}}$),

$$\begin{bmatrix} u_\mathrm{p} \\ v_\mathrm{p} \end{bmatrix} = \begin{bmatrix} u_\mathrm{c} & v_\mathrm{c} & 1 & 0 & 0 & 0 \\ 0 & 0 & 0 & u_\mathrm{c} & v_\mathrm{c} & 1 \end{bmatrix} \begin{bmatrix} A \\ B \\ C \\ D \\ E \\ F \end{bmatrix}, \tag{6.24}$$

and the uncertainty can be found with

$$\boldsymbol{V}_{\vec{\boldsymbol{X}}} = \epsilon^2 (\hat{\boldsymbol{u}}_c^\mathrm{T} \hat{\boldsymbol{u}}_c)^{-1}. \tag{6.25}$$

The errors in $[u_\mathrm{p} \quad v_\mathrm{p}]^\mathrm{T}$ are heteroscedastic, the error in u_p or v_p will be larger depending on the board orientation and the orientation of the projector with respect to the camera. However, the two mappings $[u_\mathrm{c} \quad v_\mathrm{c} \quad 1] \rightarrow u_\mathrm{p}$ and $[u_\mathrm{c} \quad v_\mathrm{c} \quad 1] \rightarrow v_\mathrm{p}$ are both independent (there are no off-diagonal terms in $(\hat{\boldsymbol{u}}_\mathrm{c}^\mathrm{T} \hat{\boldsymbol{u}}_\mathrm{c})^{-1}$ defining their interaction). The estimate therefore can be found independently using

$$\epsilon_x^2 = \sum_{i=1}^{N} \left(u_{\mathrm{p}i} - [A \quad B \quad C] \begin{bmatrix} u_{\mathrm{c}i} \\ v_{\mathrm{c}i} \\ 1 \end{bmatrix} \right)^2 \tag{6.26}$$

$$\epsilon_y^2 = \sum_{i=1}^{N} \left(v_{\mathrm{p}i} - [D \quad E \quad F] \begin{bmatrix} u_{\mathrm{c}i} \\ v_{\mathrm{c}i} \\ 1 \end{bmatrix} \right)^2 . \tag{6.27}$$

The error in projector dimensions u_c and v_c are given in Figure 6.23 (a) and (b) respectively. It is also noted that the errors in $[u_\mathrm{p} \quad v_\mathrm{p}]^\mathrm{T}$ will both present autocorrelation, but since the number of observations are high, the errors are assumed to asymptotically follow a normal distribution.

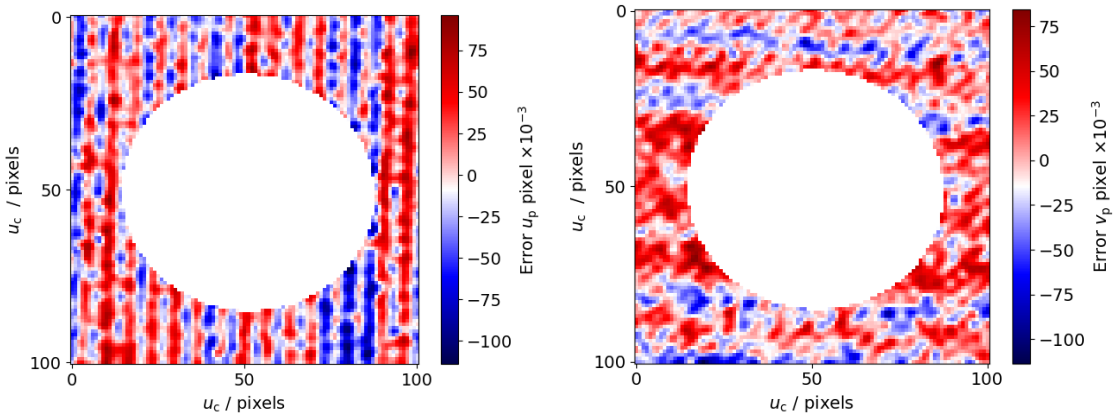

(a) (b)

Figure 6.23 Error in the camera-to-projector mapping of the (a) u-axis and (b) v-axis.

With the transform found, the projector ellipse centres can be found by applying the transform to the elliptical centre points. Uncertainty can be propagated from the elliptical centres, along with the transform, using the propagation of uncertainty given in Section 2.3.

6.8 Eccentricity correction

Consider a circle described by the conic

$$\boldsymbol{x}^\mathrm{T} \boldsymbol{M} \boldsymbol{x} = 0. \tag{6.28}$$

Since $\boldsymbol{M}$ describes a circle or radius r, $\boldsymbol{M}$ is given by

$$\boldsymbol{M} = \begin{bmatrix} r & 0 & 0 \\ 0 & r & 0 \\ 0 & 0 & -r^2 \end{bmatrix}. \tag{6.29}$$

The circle sits at the origin (0,0) without loss of generality. The circle is transformed into an ellipse using a projective transformation $\boldsymbol{H}$,

$$\boldsymbol{H} = \begin{bmatrix} h_{11} & h_{12} & h_{13} \\ h_{12} & h_{22} & h_{23} \\ h_{13} & h_{23} & h_{33} \end{bmatrix}. \tag{6.30}$$

Applying the projective transform on eq. (6.28) gives

$$\boldsymbol{x}^{\mathrm{T}}\boldsymbol{H}^{\mathrm{T}}\boldsymbol{M}\boldsymbol{H}\boldsymbol{x} = 0, \tag{6.31}$$

which is equivalent to redefining the conic $\boldsymbol{M}$ as

$$\boldsymbol{M}' = \boldsymbol{H}^{\mathrm{T}}\boldsymbol{M}\boldsymbol{H} \tag{6.32}$$

$$\boldsymbol{M}' = \begin{bmatrix} m_{11} & m_{12} & m_{13} \\ m_{12} & m_{22} & m_{23} \\ m_{13} & m_{23} & m_{33} \end{bmatrix}.$$

$$\begin{aligned} m_{11} &= h_{11}^2 + h_{21}^2 - h_{31}^2 r \\ m_{12} &= h_{11}h_{12} + h_{21}h_{22} - h_{31}h_{32} r \\ m_{13} &= h_{11}h_{13} + h_{21}h_{23} - h_{31}h_{33} r \\ m_{22} &= h_{12}^2 + h_{22}^2 - h_{32}^2 r \\ m_{23} &= h_{12}h_{13} + h_{22}h_{23} - h_{32}h_{33} r \\ m_{33} &= h_{13}^2 + h_{23}^2 - h_{33}^2 r \end{aligned} \tag{6.33}$$

Note that $\boldsymbol{M}'$ has been divided by r for simplicity, which will have no impact on the properties of $\boldsymbol{M}'$. The centre of the ellipse (x_0, y_0) is found using

$$x_0 = \frac{m_{22}m_{13} - m_{12}m_{23}}{m_{12}^2 - m_{11}m_{22}} \tag{6.34}$$

$$y_0 = \frac{m_{11}m_{23} - m_{12}m_{13}}{m_{12}^2 - m_{11}m_{22}}, \tag{6.35}$$

and the circle centre can be found by applying the projective transformation $\boldsymbol{H}$ on the circle centre

$$\boldsymbol{H}\begin{bmatrix} 0 \\ 0 \\ 1 \end{bmatrix} = \begin{bmatrix} h_{13} \\ h_{23} \\ h_{33} \end{bmatrix} \neq s\begin{bmatrix} y_0 \\ x_0 \\ 1 \end{bmatrix}. \tag{6.36}$$

The centre of the circle, therefore, is not projected onto the centre of the ellipse – every dot localisation will suffer from eccentricity error, requiring correction. The error is displayed graphically in Figure 6.24.

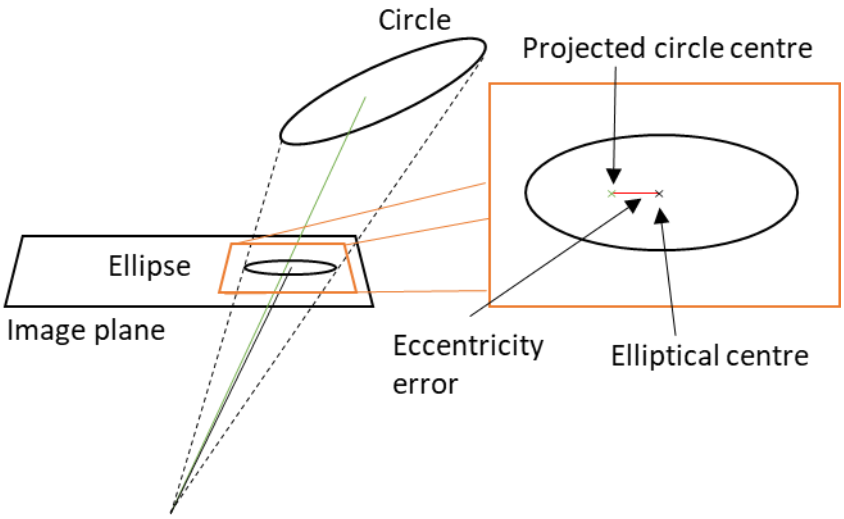

Figure 6.24 Eccentricity error caused by the circle centre not being projected onto the ellipse centre.

The eccentricity error is a function of the projective transform, which itself is a function of the camera intrinsic and feature extrinsic parameters. This is problematic, because the eccentricity error is a function of the parameters estimated during the calibration. Given the function that describes the back propagation onto the camera, the correction can be found by finding the difference between the back propagation of the centre of the dot, and the ellipsis fitting of the back propagated edges of the dot. A similar method can be found in Gong, Liu [221].

6.9 Repeatability test

In this section, the repeatability of the ellipse localisation will be investigated as well as the uncertainty interval of the dot localisation. The repeatability will be defined by the CCD noise, projector jitter, DMD noise and environmental light noise. Additionally, the camera and projector optics are sensitive to internal temperatures. By repeatedly measuring a dot grid, any statistically significant external influencing effects not included in the uncertainty evaluation can be found. The magnitude of the change in dot location can be used as an indicator that the system has reach thermal equilibrium when the mean of each dot locations stop moving across the image and exhibit only Gaussian noise about a central mean location.

Two tests will be completed. The first will place the dot grid in differing positions across the measurement volume to test for consistency across position and orientation, as well as the impact the time in-between measurement has.

The second test will be a longer sustained test using one position only to test the uncertainty interval.

Firstly, after turning on all system components (i.e., starting from “cold”), a 30 minute start-up procedure is completed, to ignore dot location data made when the system is far from thermal equilibrium. Immediately following this, 5 consecutive positions are investigated for several minutes each. The dot grid is placed in unique positions and orientations to test for significant differences in localisation. For each position, the dot grid is measured repeatedly for approximately 10 minutes each. The results are given in Figure 6.25, and the positions in Figure 6.25 are given in Figure 6.26. The coloured spread represents a single standard deviation from the mean (black line) ellipse location of all the points in each camera image. Despite having far higher pixel density, the camera remains far more repeatable as well as having far less drift than the projector. The projector has significant drift for the first 15 min of operations and so the system warm-up time must be set at 45 min. Additionally, in the projector images, the first few sets of images for each position are significantly different from the rest. This indicates that in the small amount of time it takes to set up the new artefact position, the system has fallen somewhat out of equilibrium.

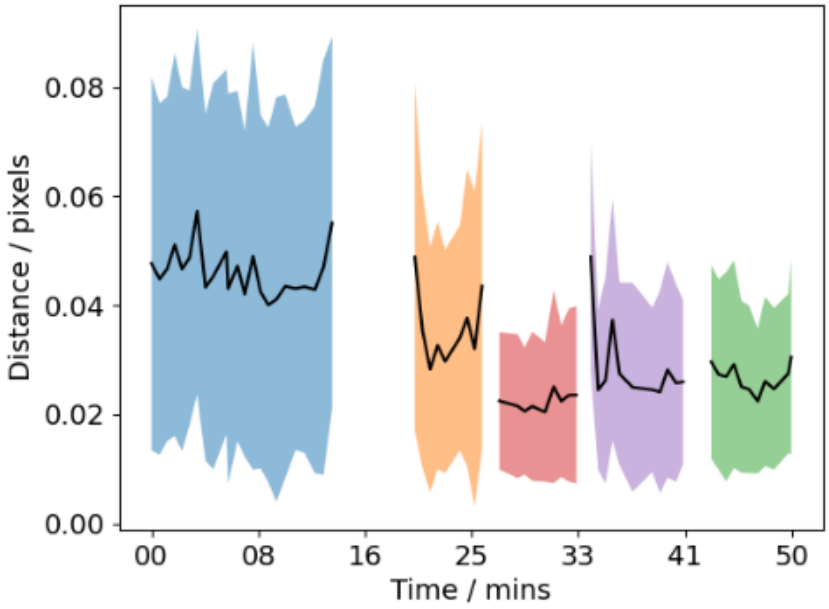

(a)

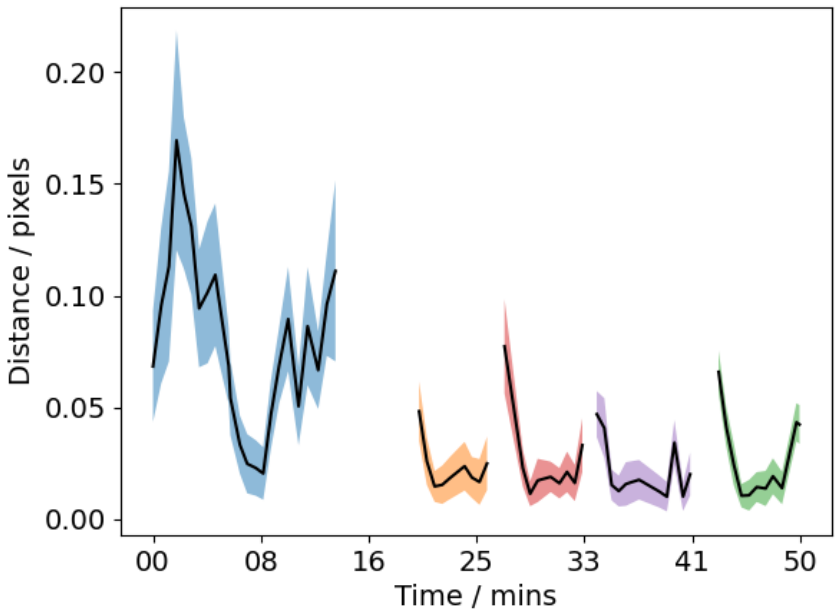

(b)

Figure 6.25 Distance from mean ellipse location taken of artefact in each position against the time of the first measurement. Distance measured on the (a) camera image plane and (b) projector image plane.

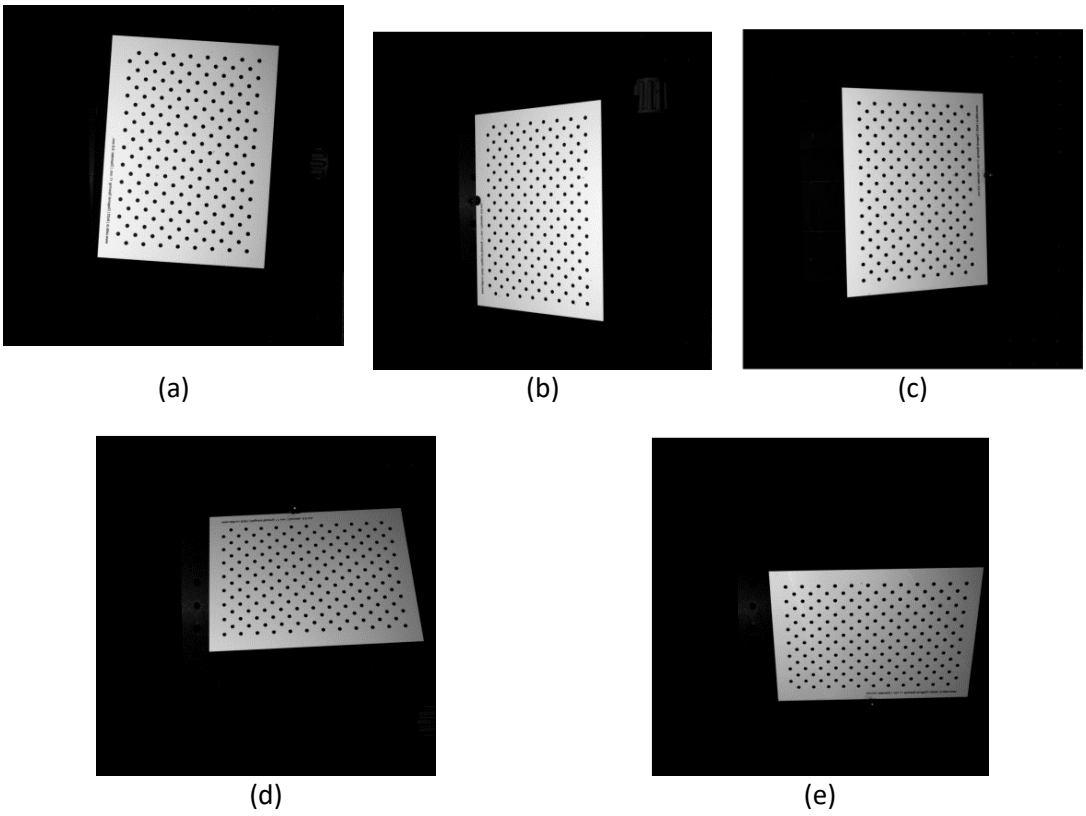

Figure 6.26 (a-e) Position 1-5 of the board during repeatability test as seen by the camera.

In the second test, shown in Figure 6.27, the system is again warmed-up for 30 min before repeating the test, but this time only in one position. Once equilibrium has been reached, i.e., the ellipse locations are no longer trending away from the initial position, the succeeding ellipse locations can be tested using a χ^2 test. The camera does not seem to reach a stable equilibrium, but the range of motion is small enough to be considered for testing.

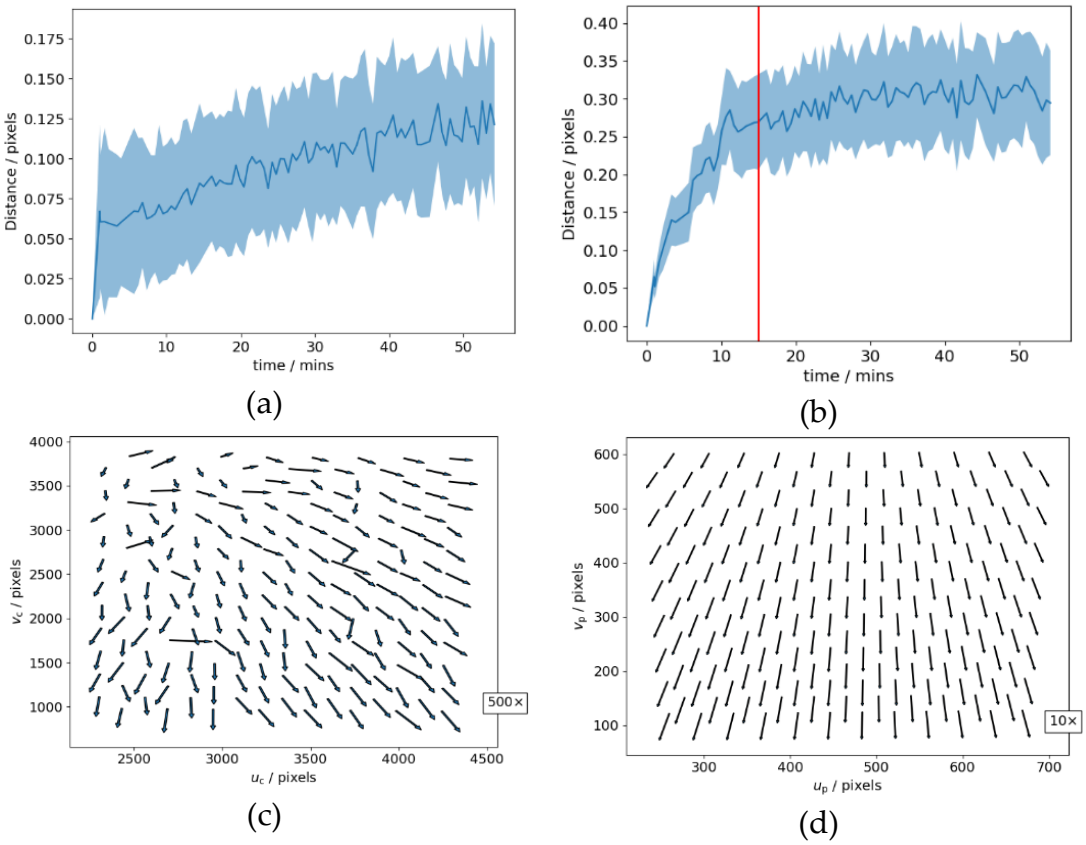

Figure 6.27 Distance from initial ellipse location for the (a,c) camera and (b,d) projector against the time of the first measurement. There is a line drawn at time = 15 min to indicate where thermal equilibrium has been reached for the projector. In (c) and (d), the drift is magnified 500X and 10X respectively for clarity.

The χ^2 test results are given in Table 6.3. The results indicate there are no statistical outliers when considering the repeatability with regards to the uncertainty evaluation.

Table 6.3 Repeatability test results of the camera and projector.

	Test value	p-value
Camera	154	12773
Projector	793	12773

6.10 Summary

This chapter provides a method to obtain feature locations within a camera image of a dot grid artefact, along with an uncertainty evaluation. A dot grid artefact is chosen as the feature artefact for use during calibration for its ease of use in fringe projection calibration. The dot grid artefact is independently

measured using tactile and optical CMS to obtain dot centres and their circularity. The feature localisation method is based upon fitting an ellipse to estimated ellipse boundary points, found using a non-linear regression of a Gaussian curve fitted to 1D lines interpolated from a gradient image. The ellipse parameters are estimated using a weighted total least-square estimator.

The repeatability and validity of the feature localisation method was rigorously tested, where the weighted total least-square estimator was tested in Section 6.6.1, the entire ellipse localisation method was tested on simulated data in Section 6.6.2 and the ellipse localisation method was used repeatedly on real data in Section 6.9. It was found in Section 6.6.1 that the estimator provided accurate ellipse centre determinations as well as valid uncertainties. In Section 6.6.2 proved the uncertainty evaluation tended to be an overestimate. Section 6.9 was used to find the warm-up time of the fringe projection system, i.e., how long it takes for thermal equilibrium to be obtained so system parameters remain constant. A warm-up time of 45 minutes was found to be sufficient.

The feature localisation method presented in this chapter is an improvement over existing feature localisation methods, given this method can provide an evaluation of uncertainty on any localised ellipse. This is the first time an uncertainty has been provided on a feature used in the calibration of fringe projection systems.

Chapter 7 – Calibration of a fringe projection system

In this chapter, the method used to calibrate a fringe projection system along with an uncertainty evaluation is given. Firstly, an overview of current calibration methods is given in Section 7.1. The non-linear calibration method used in this thesis is explicitly defined in Section 7.2, which includes some novel contributions that allow the evaluation of uncertainty alongside the estimation of parameters. In Section 7.3, the outcome of the calibration is given as well as a novel estimation of resolution as well throughout the fringe projection measurement volume, obtained as a by-product of the calibration. In Section 7.4, a series of tests are performed on the calibration method to validate the method.

7.1 Overview of fringe projection calibration

This section will give a brief overview of the calibration process of a fringe projection system. In fringe projection, the act of calibration is the operation that obtains the system parameters that define the relationship between the observed 2D image points and the 3D measurement points. The accuracy in determination of the system parameters will be directly reflected in the accuracy of a fringe projection measurement. System parameters are split into two categories: intrinsic and extrinsic parameters. Intrinsic parameters describe the pinhole models of camera and projector along with its geometric distortion. Extrinsic parameters define the Euclidean transformation between coordinate systems. The complete list of system parameters defining the camera and projector are given in Table 7.1 and Table 7.2 respectively.

Table 7.1 Complete list of camera parameters required to triangulate a point.

Category	Parameter category	Parameter
Intrinsic	Pinhole	Focal length, u-axis
		Focal length, v-axis
		Skew
		Principal point, u-axis
		Principal point, v-axis
	Distortion	Radial coefficient k_1
		Radial coefficient k_2
		Radial coefficient k_3
		Tangential coefficient p_1
		Tangential coefficient p_2
		Distortion centre u_{DC}
		Distortion centre v_{DC}

Table 7.2 Complete list of projector parameters required to triangulate a point.

Category	Parameter category	Parameter
Intrinsic	Pinhole	Focal length, u-axis
		Focal length, v-axis
		Skew
		Principal point, u-axis
		Principal point, v-axis
	Distortion	Radial coefficient k_1
		Radial coefficient k_2
		Radial coefficient k_3
		Tangential coefficient p_1
		Tangential coefficient p_2
		Distortion centre u_{DC}
		Distortion centre v_{DC}
Extrinsic	Rotation	Rotation parameter r_1
		Rotation parameter r_2
		Rotation parameter r_3
	Translation	Translation x
		Translation y
		Translation z

Calibration is carried out by measuring a known artefact and estimating the parameters through regression. In this thesis, the known artefact is chosen to be a dot grid (see Chapter 6). A general calibration model function is of the form

$$\vec{\boldsymbol{y}} = f\left(\vec{\boldsymbol{x}}, \vec{\boldsymbol{\theta}}\right), \tag{7.1}$$

where $\vec{\boldsymbol{y}}$ describes the measurement output, $\vec{\boldsymbol{x}}$ gives the input and $\vec{\boldsymbol{\theta}}$ describes the estimated parameters. Typically, the known artefact points, $\vec{\boldsymbol{x}}$ are propagated to the image plane using the pinhole camera model, (see Section 2.3.1) using $\vec{\boldsymbol{\theta}}$ to produce estimation of image points $\hat{\boldsymbol{y}}$, and the regression minimises the geometric distance

$$\left\|\vec{\boldsymbol{y}} - f\left(\vec{\boldsymbol{x}}, \vec{\boldsymbol{\theta}}\right)\right\|. \tag{7.2}$$

The propagation to the image plane is called forward propagation, and the exact method is given in Section 7.2.3. Alternatively, it is possible to project backwards to the artefact instead of forwards towards the image plane, which provides a more accurate calibration in the presence of large camera distortions [222].

There are two calibration schemes to minimise eq.(7.2), linear and non-linear. Linear calibration is based on a linear regression that requires all calibration points be known in 3D a-priori. Non-linear calibration is based on a non-linear regression; only the relative position of the calibration points are known a-priori and the absolute position is estimated along with the system parameters. Linear calibrations generally require extra equipment compared to non-linear calibrations to provide a-priori information on the position of calibration points. Typically, non-linear calibration is a more robust, accurate and flexible method when compared to alternative linear calibration methods [223]. The advantage of linear calibration methods is their computational simplicity [224]. Bundle adjustment can be considered an extension to the non-linear calibration where the artefact points are also refined during optimisation [225]. Other alternative calibration methods can be based on projective invariants [226]. Given non-linear calibration is very popular for its low set-up cost and high-accuracy, it shall serve as the basis of calibration in this thesis.

7.2 Calibration method

In this section, the calibration method will be explicitly defined, including the steps required to include an estimation of the uncertainty in the parameters in addition to the parameters themselves. In Section 7.1, non-linear calibration was chosen as the calibration method for this thesis for its accuracy and robustness. Non-linear calibration of fringe projection systems is an extension to the non-linear calibration of cameras [201], and was introduced to fringe projection systems in Zhang and Huang [227]. Fundamentally, non-linear calibration is a non-linear regression, the solution to eq. (7.2) is found by making successive linear approximations to eq. (7.2). The function f in eq. (7.2)

can be approximated using a first order Taylor expansion about an epicentre $\vec{\boldsymbol{\theta}}_{\mathrm{e}}$

$$f(\vec{\boldsymbol{x}}, \vec{\boldsymbol{\theta}}) \approx f(\vec{\boldsymbol{x}}, \vec{\boldsymbol{\theta}}_{\mathrm{e}}) + \boldsymbol{\mathcal{J}}(\vec{\boldsymbol{\theta}}_{\mathrm{e}})(\vec{\boldsymbol{\theta}} - \vec{\boldsymbol{\theta}}_{\mathrm{e}}), \tag{7.3}$$

with the Jacobian $\boldsymbol{\mathcal{J}}(\vec{\boldsymbol{\theta}}_{\mathrm{e}})$ defined as the gradient of $\vec{\boldsymbol{y}}$ with respect to $\vec{\boldsymbol{\theta}}$, evaluated at $\vec{\boldsymbol{\theta}} = \vec{\boldsymbol{\theta}}_{\mathrm{e}}$, $\boldsymbol{\mathcal{J}}(\vec{\boldsymbol{\theta}}_{\mathrm{e}}) = \left[\frac{\partial f}{\partial \vec{\boldsymbol{\theta}}}\right]_{\vec{\boldsymbol{\theta}}_{\mathrm{e}}}$, and will be herein shortened to $\boldsymbol{\mathcal{J}}$. The calculation of the Jacobian itself can be challenging, calculation methods are given in Section 7.2.4. From the epicentre $\vec{\boldsymbol{\theta}}_{\mathrm{e}}$, a vector $\vec{\boldsymbol{\delta}} = \vec{\boldsymbol{\theta}} - \vec{\boldsymbol{\theta}}_{\mathrm{e}}$ can be found that minimises eq. (7.2), given by

$$\left(\boldsymbol{\mathcal{J}}^{\mathrm{T}}\boldsymbol{\mathcal{J}} + \lambda \mathrm{diag}(\boldsymbol{\mathcal{J}}^{\mathrm{T}}\boldsymbol{\mathcal{J}})\right)\vec{\boldsymbol{\delta}} = \boldsymbol{\mathcal{J}}^{\mathrm{T}}\vec{\boldsymbol{\epsilon}} = \boldsymbol{\mathcal{J}}^{\mathrm{T}}\left(\vec{\boldsymbol{y}} - f(\vec{\boldsymbol{x}}, \vec{\boldsymbol{\theta}}_{\mathrm{e}})\right). \tag{7.4}$$

Iteratively finding the solution to eq. (7.4) is known as the Levenberg-Marquardt algorithm and is guaranteed to at least find the local minimum [228]. The Levenberg-Marquardt algorithm requires an approximate solution, which can be found analytically, given some assumptions [201]. Heteroscedasticity is problematic in non-linear regression, and typically a requirement for a successful regression is that the errors in the vector $\vec{\boldsymbol{\epsilon}}$ be uncorrelated. This requirement can be removed by instead supplying the correct weighting matrix in the optimisation, altering eq. (7.4) to give

$$\left(\boldsymbol{\mathcal{J}}^{\mathrm{T}}\boldsymbol{W}\boldsymbol{\mathcal{J}} + \lambda \mathrm{diag}(\boldsymbol{\mathcal{J}}^{\mathrm{T}}\boldsymbol{W}\boldsymbol{\mathcal{J}})\right)\vec{\boldsymbol{\delta}} = \boldsymbol{\mathcal{J}}^{\mathrm{T}}\boldsymbol{W}\vec{\boldsymbol{\epsilon}} \tag{7.5}$$

with $\boldsymbol{W} = \boldsymbol{V}_{\epsilon}^{-1}$. It is possible to improve the convergence speed of the Levenberg-Marquardt algorithm by adding an acceleration term [229] – but this is not implemented in this thesis.

The above methodology can be extended to include projectors, by considering the projector as a camera [34, 230]. The projector image is indirectly observed using a suitable correspondence algorithm, see Section 2.4, fully defining both axes by completing the correspondence decoding once for each axis. The camera and projector pinhole parameters and board orientations (in the respective views) can be approximated separately and refined either jointly or separately. Parameters regressed separately will be referred to as serial calibration and parameters regressed jointly will be referred to as parallel calibration in this thesis. Estimating parameters jointly reduces the total degrees of freedom of the regression since the artefact position and orientation must be estimated only once per view. It is expected therefore that a parallel calibration should produce parameter estimates of higher accuracy.

If the linearization eq. (7.3) approximation holds, the region for which the parameter solution exists can be considered linear. For a linear system given by $\vec{\boldsymbol{y}} = \boldsymbol{X}\vec{\boldsymbol{\theta}}$ where the covariance matrix of the observations $\vec{\boldsymbol{y}}$, given as $\boldsymbol{V}_y$ is known, the covariance matrix of the parameters $\vec{\boldsymbol{\theta}}$, given by $\boldsymbol{V}_\theta$, is defined

$$\boldsymbol{V}_\theta = \left(\boldsymbol{X}^{\mathrm{T}}\boldsymbol{V}_y^{-1}\boldsymbol{X}\right)^{-1}. \tag{7.6}$$

During the non-linear regression, the following linear system is solved for $\vec{\boldsymbol{\delta}}$,

$$\boldsymbol{\mathcal{J}}\vec{\boldsymbol{\delta}} = \vec{\boldsymbol{y}} - f\left(\vec{\boldsymbol{x}}, \vec{\boldsymbol{\theta}}_{\mathrm{e}}\right) = \vec{\boldsymbol{\epsilon}}, \tag{7.7}$$

then the parameter covariance matrix $\boldsymbol{V}_\theta$ is given by

$$\boldsymbol{V}_\theta = (\boldsymbol{\mathcal{J}}^{\mathrm{T}}\boldsymbol{V}_\epsilon^{-1}\boldsymbol{\mathcal{J}})^{-1}, \tag{7.8}$$

where $\boldsymbol{V}_\epsilon$ is the covariance matrix of the vector $\vec{\boldsymbol{\epsilon}} = \vec{\boldsymbol{y}} - f\left(\vec{\boldsymbol{x}}, \vec{\boldsymbol{\theta}}_{\mathrm{e}}\right)$.

In eq. (7.5) it was shown the role the weighting matrix (inverse of the covariance matrix $\boldsymbol{V}_\epsilon$) has in a non-linear regression where the input data is correlated or heteroscedastic. In the case of fringe projection:

1. When considering parallel calibration, the projector and camera images have different scales, and since the reprojection error used to regress the uncertainties is calculated on the image plane, the projector and camera image points will have completely different uncertainties.
2. The projector ellipse image locations are inferred from camera ellipse image locations, and are therefore correlated in some way and will have higher errors when compared at the same scale.
3. The same artefact provides repeated measurements, all repeated measurements of the same dot on the dot grid will be correlated in some way.

Therefore, a weighting matrix may be required to perform an optimal non-linear regression for both the serial and parallel calibration methods. This introduces a new issue – the calculation of the weighting matrix. The reprojection error $\vec{\boldsymbol{\epsilon}}$ is a function of both the observation $\vec{\boldsymbol{y}}$ (the ellipse centres), the regressor $\vec{\boldsymbol{x}}$ (the artefact dot positions) and the estimated parameters $\vec{\boldsymbol{\theta}}$. Therefore, so is the covariance matrix $\boldsymbol{V}_\epsilon$ a function of $\vec{\boldsymbol{y}}$, $\vec{\boldsymbol{x}}$ and $\vec{\boldsymbol{\theta}}$. The covariance matrix $\boldsymbol{V}_\epsilon$ can be found by propagating error from the artefact $\vec{\boldsymbol{x}}$, given as $\boldsymbol{V}_x$, by

$$\boldsymbol{V}_\epsilon = \boldsymbol{V}_y + \boldsymbol{\mathcal{J}}\boldsymbol{V}_x\boldsymbol{\mathcal{J}}^{\mathrm{T}}. \tag{7.9}$$

Eq. (7.9) can be solved during each iteration of the Levenberg-Marquardt algorithm or alternatively, using the assumption that $\boldsymbol{V}_\epsilon$ is somewhat constant near the solution locus, an earlier estimation of $\boldsymbol{\mathcal{J}}\boldsymbol{V}_x\boldsymbol{\mathcal{J}}^{\mathrm{T}}$ from a solution of $\vec{\boldsymbol{\theta}}$ that is very close to the solution – which is used in this thesis.

It is typical to use 25 positions within the calibration to ensure there is enough data redundancy. Given there are N_{pos} number of positions, N_{art} number of points on the artefact, and each point has two degrees of freedom and is measured once in the camera and once in the projector, the regression has $N_{\mathrm{pos}} \times N_{\mathrm{art}} \times 2 \times 2$ degrees of freedom. In the case of this thesis, there are 18400 degrees of freedom, so the weighting matrix has the size 18400×18400 – the data density can be memory intensive. Because the dot grid is measurement many different times, consecutive measurements of the same point will be correlated, so $\boldsymbol{V}_\epsilon$ will have significant off-diagonal terms.

The parallel method is based on simplifying the weight matrix $\boldsymbol{W}$ by taking advantage of the matrix sparsity, while the serial method will characterise the camera and projector separately. The parallel method is expected to have a higher accuracy – there are less parameters to estimate. The serial method leaves some degrees of freedom that will be investigated as a validation tool.

The covariance matrix can be reduced by a factor of four by eliminating any correlation between camera and projector points. The covariance matrix is separated into the camera and projector components and inverted separately. The projector points are inferred from the camera points, and the easiest way to remove correlation is to use each dot only once in either the camera or the projector views. Splitting the input dots roughly in half will reduce the computational complexity roughly by a factor of 16.

7.2.1 Serial method

The serial method of characterising both the camera and projector separately – with the explicit aim to reduce computational complexity. Both the camera and the projector will have their own unique estimates of the feature artefact location and orientation. Both artefact estimates are given in coordinate systems that are centered and aligned with the camera and projector "pinhole". Therefore, given N positions, there are N estimates of the camera-projector transformed, otherwise known as the extrinsic. The estimation of $\vec{\boldsymbol{q}}$ and $\vec{\boldsymbol{t}}$ is hereby known as the extrinsic estimation.

The camera-projector transform $\vec{\boldsymbol{q}}$ and $\vec{\boldsymbol{t}}$ relates the camera's artefact estimation, $\boldsymbol{R}_{\mathrm{c}}$ and $\vec{\boldsymbol{t}}_{\mathrm{c}}$, with the projector's artefact transform $\boldsymbol{R}_{\mathrm{p}}$ and $\vec{\boldsymbol{t}}_{\mathrm{p}}$ using

$$\boldsymbol{R}\left(\boldsymbol{R}_{\mathrm{c}}\vec{\boldsymbol{x}}+\vec{\boldsymbol{t}}_{\mathrm{c}}\right)+\boldsymbol{t}=\boldsymbol{R}_{\mathrm{p}}\vec{\boldsymbol{x}}+\vec{\boldsymbol{t}}_{\mathrm{p}}. \tag{7.10}$$

Equating coefficients gives the extrinsic estimation

$$\boldsymbol{R}=\boldsymbol{R}_{\mathrm{p}}\boldsymbol{R}_{\mathrm{c}}^{-\mathbf{1}} \tag{7.11}$$

$$\vec{\boldsymbol{t}}=\vec{\boldsymbol{t}}_{\mathrm{p}}-\boldsymbol{R}_{\mathrm{p}}\boldsymbol{R}_{\mathrm{c}}^{-\mathbf{1}}\vec{\boldsymbol{t}}_{\mathrm{c}}. \tag{7.12}$$

Explicitly, eq.(7.11) and eq. (7.12) are given as

$$\vec{\boldsymbol{q}}=f_{\vec{q}}\left(\vec{\boldsymbol{q}}_{\mathrm{c}},\vec{\boldsymbol{q}}_{\mathrm{p}}\right)=\mathcal{R}\left[\mathcal{R}\left[\vec{\boldsymbol{q}}_{\mathrm{p}}\right]\mathcal{R}[\vec{\boldsymbol{q}}_{\mathrm{c}}]^{-1}\right] \tag{7.13}$$

$$\vec{\boldsymbol{t}}=f_{\vec{t}}\left(\vec{\boldsymbol{q}}_{\mathrm{c}},\vec{\boldsymbol{q}}_{\mathrm{p}}\right)=\vec{\boldsymbol{t}}_{\mathrm{p}}-\mathcal{R}\left[\vec{\boldsymbol{q}}_{\mathrm{p}}\right]\mathcal{R}[\vec{\boldsymbol{q}}_{\mathrm{c}}]^{-1}\vec{\boldsymbol{t}}_{\mathrm{c}}. \tag{7.14}$$

The errors within the feature artefact parameter estimations $\vec{\boldsymbol{q}}_{\mathrm{c}},\vec{\boldsymbol{t}}_{\mathrm{c}},\vec{\boldsymbol{q}}_{\mathrm{p}},\vec{\boldsymbol{t}}_{\mathrm{p}}$ are highly correlated and must be considered in the following evaluation. For the following derivation, individual components of vectors are denoted using a superscript coordinate *j*, with *j* signifying the j^{th} artefact position. For example, $\vec{\boldsymbol{q}}_{\mathrm{c}}^{10}$ is the artefact orientation in the camera coordinate system in the 10^{th} position.

To conserve and propagate correlation between the intrinsic and extrinsic values, the intrinsic values will be include in calculations. The intrinsic values are given as $\vec{\boldsymbol{\theta}}_{\mathrm{c}}$ and $\vec{\boldsymbol{\theta}}_{\mathrm{p}}$ for the camera and projector respectively. The rows and columns of the combined covariance matrix $\boldsymbol{V}_{\mathrm{com}}$ is given by

$$\left[\left(\vec{\boldsymbol{\theta}}_{\mathrm{c}}\right)^{\mathrm{T}}\quad\left(\vec{\boldsymbol{\theta}}_{\mathrm{p}}\right)^{\mathrm{T}}\quad\left(\vec{\boldsymbol{q}}_{\mathrm{c}}^{1}\right)^{\mathrm{T}}\quad\left(\vec{\boldsymbol{t}}_{\mathrm{c}}^{1}\right)^{\mathrm{T}}\quad\left(\vec{\boldsymbol{q}}_{\mathrm{p}}^{1}\right)^{\mathrm{T}}\quad\left(\vec{\boldsymbol{t}}_{\mathrm{p}}^{1}\right)^{\mathrm{T}}\quad\ldots\right]. \tag{7.15}$$

The Jacobian of the j^{th} position, $\boldsymbol{\mathcal{J}}^{j}$, is then given by

$$\boldsymbol{\mathcal{J}}^{j}=\begin{bmatrix}\left[\dfrac{\partial\vec{\boldsymbol{q}}^{j}}{\partial\vec{\boldsymbol{q}}_{\mathrm{c}}^{j}}\right]_{3\times3} & [\mathbf{0}]_{3\times3} & \left[\dfrac{\partial\vec{\boldsymbol{q}}}{\partial\vec{\boldsymbol{q}}_{\mathrm{p}}^{j}}\right]_{3\times3} & [\mathbf{0}]_{3\times3}\\ \left[\dfrac{\partial\vec{\boldsymbol{t}}^{j}}{\partial\vec{\boldsymbol{q}}_{\mathrm{c}}^{j}}\right]_{3\times3} & \left[\dfrac{\partial\vec{\boldsymbol{t}}^{j}}{\partial\vec{\boldsymbol{t}}_{\mathrm{c}}^{j}}\right]_{3\times3} & \left[\dfrac{\partial\vec{\boldsymbol{t}}^{j}}{\partial\vec{\boldsymbol{q}}_{\mathrm{p}}^{j}}\right]_{3\times3} & \left[\dfrac{\partial\vec{\boldsymbol{t}}^{j}}{\partial\vec{\boldsymbol{t}}_{\mathrm{p}}^{j}}\right]_{3\times3}\end{bmatrix}. \tag{7.16}$$

For ease, the Jacobian is defined using the auto-differentiation tools in Tensorflow and the entire Jacobian is defined by

$$\boldsymbol{\mathcal{J}}=\begin{bmatrix}\mathbb{I} & \mathbf{0} & \mathbf{0} & \mathbf{0} & \mathbf{0}\\ \mathbf{0} & \boldsymbol{\mathcal{J}}^{1} & \mathbf{0} & \mathbf{0} & \mathbf{0}\\ \mathbf{0} & \mathbf{0} & \boldsymbol{\mathcal{J}}^{2} & \mathbf{0} & \mathbf{0}\\ \mathbf{0} & \mathbf{0} & \mathbf{0} & \ddots & \mathbf{0}\\ \mathbf{0} & \mathbf{0} & \mathbf{0} & \mathbf{0} & \boldsymbol{\mathcal{J}}^{N}\end{bmatrix}. \tag{7.17}$$

The covariance estimate of all extrinsic estimations $\vec{\boldsymbol{q}}^1, \vec{\boldsymbol{t}}^1 \rightarrow \vec{\boldsymbol{q}}^N, \vec{\boldsymbol{t}}^N$ is given by

$$\boldsymbol{V}_{\text{com}} = \begin{bmatrix} \boldsymbol{V}_{\text{int}} & \cdots \\ \cdots & \boldsymbol{V}_{\text{ext}} \end{bmatrix} = \boldsymbol{\mathcal{J}} \boldsymbol{V}_{\text{com}} \boldsymbol{\mathcal{J}}^{\text{T}}, \tag{7.18}$$

where $\boldsymbol{V}_{\text{com}}$ is split into the intrinsic section $\boldsymbol{V}_{\text{int}}$ and the extrinsic section $\boldsymbol{V}_{\text{ext}}$. Given the covariance matrix of each estimation is known, $\boldsymbol{V}_{\text{ext}}$, the best estimation of camera-projector transform $\vec{\boldsymbol{q}}$ and $\vec{\boldsymbol{t}}$ will minimise the χ^2 value

$$\left(\begin{bmatrix} \vec{\boldsymbol{q}}^1 \\ \vec{\boldsymbol{t}}^1 \\ \vdots \\ \vec{\boldsymbol{q}}^N \\ \vec{\boldsymbol{t}}^N \end{bmatrix} - \begin{bmatrix} \vec{\boldsymbol{q}} \\ \vec{\boldsymbol{t}} \\ \vdots \\ \vec{\boldsymbol{q}} \\ \vec{\boldsymbol{t}} \end{bmatrix} \right)^{\text{T}} \boldsymbol{V}_{\text{ext}}^{-1} \left(\begin{bmatrix} \vec{\boldsymbol{q}}^1 \\ \vec{\boldsymbol{t}}^1 \\ \vdots \\ \vec{\boldsymbol{q}}^N \\ \vec{\boldsymbol{t}}^N \end{bmatrix} - \begin{bmatrix} \vec{\boldsymbol{q}} \\ \vec{\boldsymbol{t}} \\ \vdots \\ \vec{\boldsymbol{q}} \\ \vec{\boldsymbol{t}} \end{bmatrix} \right) \times \frac{1}{6N}. \tag{7.19}$$

Eq. (7.19) can be minimised using a weighted mean over all estimates $\vec{\boldsymbol{q}}^j, \vec{\boldsymbol{t}}^j$, essentially solving the linear system $\vec{\boldsymbol{y}} = \boldsymbol{A}\vec{\boldsymbol{x}}$

$$\begin{bmatrix} \vec{\boldsymbol{q}}^1 \\ \vec{\boldsymbol{t}}^1 \\ \vdots \\ \vec{\boldsymbol{q}}^N \\ \vec{\boldsymbol{t}}^N \end{bmatrix} = \begin{bmatrix} \mathbb{I}_{6\times 6} \\ \vdots \end{bmatrix}_{6N\times 6} \begin{bmatrix} \vec{\boldsymbol{q}} \\ \vec{\boldsymbol{t}} \end{bmatrix}, \tag{7.20}$$

with the solution given by the weighted linear system

$$\begin{bmatrix} \vec{\boldsymbol{q}} \\ \vec{\boldsymbol{t}} \end{bmatrix} = (\boldsymbol{A}^{\text{T}} \boldsymbol{V}_{\text{ext}}^{-1} \boldsymbol{A})^{-1} \boldsymbol{A} \boldsymbol{V}_{\text{ext}}^{-1} \begin{bmatrix} \vec{\boldsymbol{q}}^1 \\ \vec{\boldsymbol{t}}^1 \\ \vdots \\ \vec{\boldsymbol{q}}^N \\ \vec{\boldsymbol{t}}^N \end{bmatrix}. \tag{7.21}$$

Finally, estimating the covariance matrix, $\boldsymbol{V}_\theta$, of the system parameters is found using the law of propagation of uncertainty

$$\boldsymbol{V}_\theta = \begin{bmatrix} \mathbb{I} & \boldsymbol{0} \\ \boldsymbol{0} & (\boldsymbol{A}^{\text{T}} \boldsymbol{V}_{\text{ext}}^{-1} \boldsymbol{A})^{-1} \boldsymbol{A} \boldsymbol{V}_{\text{ext}}^{-1} \end{bmatrix} \boldsymbol{V}_{\text{com}} \begin{bmatrix} \mathbb{I} & \boldsymbol{0} \\ \boldsymbol{0} & (\boldsymbol{A}^{\text{T}} \boldsymbol{V}_{\text{ext}}^{-1} \boldsymbol{A})^{-1} \boldsymbol{A} \boldsymbol{V}_{\text{ext}}^{-1} \end{bmatrix}^{\text{T}} \tag{7.22}$$

The serial method leaves an additional $6N$ degrees of freedom over the parallel method that will inevitably lead to a lower accuracy in estimated parameters $\vec{\boldsymbol{\theta}}$. The eq. (7.19) is not guaranteed to be minimised and the extra degrees of freedom allow the parameter estimates of the camera and projector to be checked against each other. If the parameter estimates agree with each other, eq. (7.19) will be equal or less than 1.

7.2.2 Parallel method

The advantage of the parallel method over the serial method is there are $6N$ less parameters to estimate, that should theoretically increase the accuracy of

the camera and projector parameter estimations. The disadvantage of the parallel method is the added complexity in estimating the input covariance. In the serial method, an input covariance that is incorrect by a scalar multiplication will only produce a parameter estimate covariance that is slightly too high. In the parallel method, the input covariance must now be consistent in regard to the camera and projector. The parallel method makes an alteration to the forward propagation method in Algorithm 7. The new forward propagation method is in Algorithm 6.

Algorithm 6 Forward propagation of the artefact points $\vec{\boldsymbol{x}}$ of the i^{th} position in the parallel method.

Transform into camera coordinate system $\vec{\boldsymbol{x}}_1 = \mathcal{R}(\vec{\boldsymbol{q}}_i)\vec{\boldsymbol{x}} + \vec{\boldsymbol{t}}_i$
Camera:
Transform into homogenous coordinates $\vec{\boldsymbol{x}}_2 = \frac{\vec{\boldsymbol{x}}_1}{[0 \quad 0 \quad 1]\vec{\boldsymbol{x}}_1}$
Apply optical distortion function $\vec{\boldsymbol{x}}_3 = f_{\text{D}}(\vec{\boldsymbol{x}}_2, \vec{\boldsymbol{\tau}}_{\text{c}})$
Apply camera matrix $\vec{\boldsymbol{u}}_{\text{c}} = \boldsymbol{K}_{\text{c}}\vec{\boldsymbol{x}}_3$
Projector:
Transform into projector coordinate system $\vec{\boldsymbol{x}}_4 = \mathcal{R}(\vec{\boldsymbol{q}})\vec{\boldsymbol{x}}_1 + \vec{\boldsymbol{t}}$
Transform into homogenous coordinates $\vec{\boldsymbol{x}}_5 = \frac{\vec{\boldsymbol{x}}_4}{[0 \quad 0 \quad 1]\vec{\boldsymbol{x}}_4}$
Apply optical distortion function $\vec{\boldsymbol{x}}_6 = f_{\text{D}}(\vec{\boldsymbol{x}}_5, \vec{\boldsymbol{\tau}}_{\text{p}})$
Apply camera matrix $\vec{\boldsymbol{u}}_{\text{p}} = \boldsymbol{K}_{\text{p}}\vec{\boldsymbol{x}}_6$

7.2.3 Forward propagation

This section will detail the propagation of light from artefact to image plane, given as function f in eq. (7.1), also called forwards propagation. The rotation convention used here is the Rodrigues rotation formula, otherwise known as the axis-angle representation of rotations. Alternative representations include quaternions [231], Euler angles [232] and rotors [233]. The operator that converts a Rodrigues vector $\vec{\boldsymbol{q}}$ into its corresponding rotation matrix $\boldsymbol{R}$ is given by the Rodrigues operator $\mathcal{R}$

$$\boldsymbol{R} = \mathcal{R}(\vec{\boldsymbol{q}}) \tag{7.23}$$

$$\vec{\boldsymbol{q}} = \mathcal{R}^{-1}(\boldsymbol{R}) \tag{7.24}$$

The algorithms defining the Rodrigues and inverse Rodrigues operator are defined in Appendix C, in Algorithm 12 and Algorithm 13. The function defining the forward propagation is defined as

$$\vec{\boldsymbol{u}} = f\left(\vec{\boldsymbol{x}}, \vec{\boldsymbol{q}}, \vec{\boldsymbol{t}}, \boldsymbol{K}, \vec{\boldsymbol{\tau}}\right), \tag{7.25}$$

where the forward propagation is defined in Algorithm 7 and shown graphically in Figure 7.1.

Algorithm 7 Forward propagation of artefact points $\vec{\boldsymbol{x}}$ in the i^{th} position to the image points $\vec{\boldsymbol{u}}$.

Transform into camera/projector coordinate system $\vec{\boldsymbol{x}} = \mathcal{R}(\vec{\boldsymbol{q}}_i)\vec{\boldsymbol{x}} + \vec{\boldsymbol{t}}_i$
Transform into homogenous coordinates $\vec{\boldsymbol{x}} = {}^{\vec{\boldsymbol{x}}}/_{[0 \quad 0 \quad 1]\vec{\boldsymbol{x}}}$
Apply optical distortion function $\vec{\boldsymbol{x}} = f_{\mathrm{D}}(\vec{\boldsymbol{x}}, \vec{\boldsymbol{\tau}})$
Apply camera matrix $\vec{\boldsymbol{u}} = \boldsymbol{K}\vec{\boldsymbol{x}}$

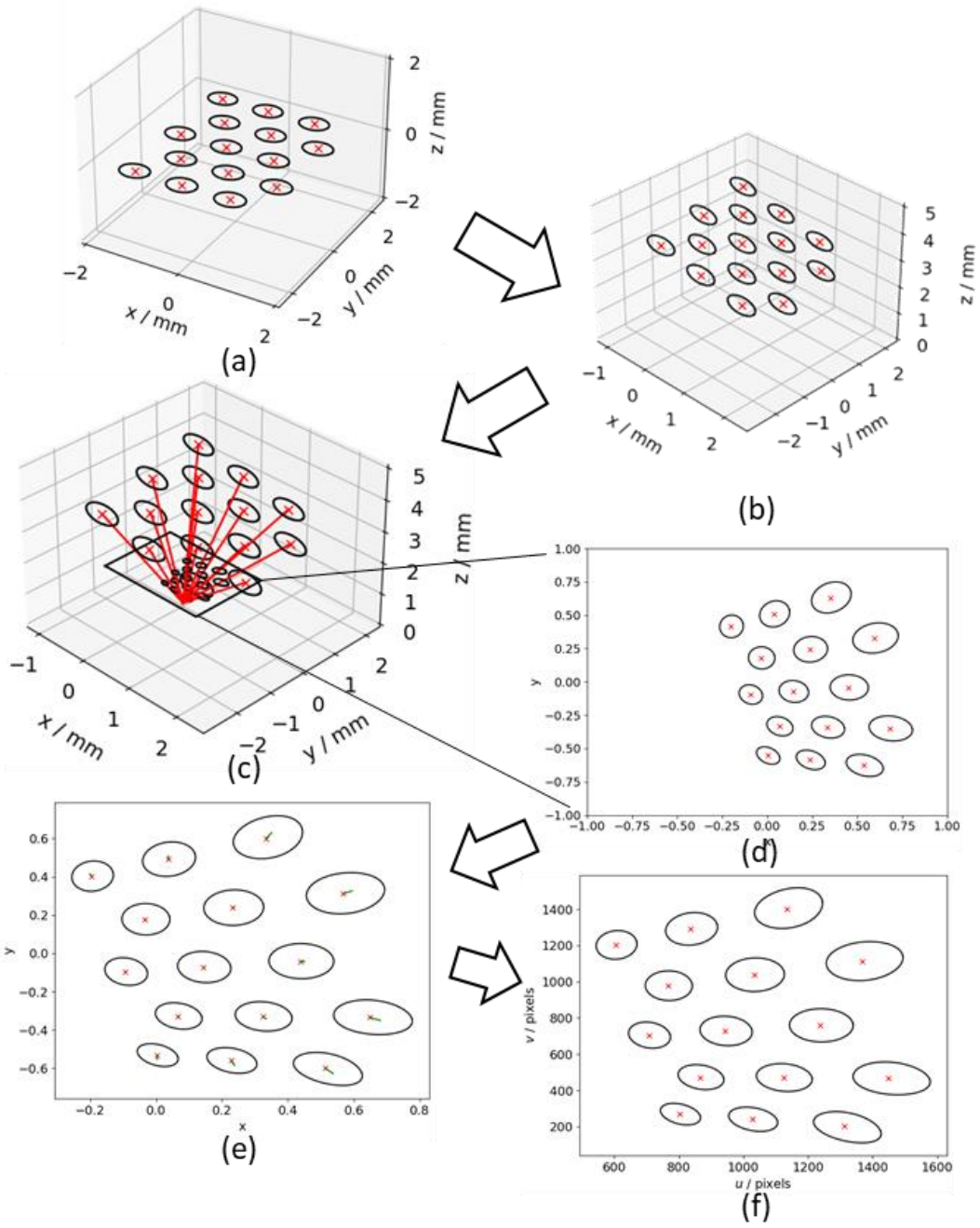

Figure 7.1 Graphical representation of the forward propagation algorithm in Algorithm 7. (a) The board ellipse centres $\vec{x}$ (red x) and dot boundaries (black), (b) a general rotation and translation, (c) conversion to homogeneous coordinates, (d) blown up image of the homogeneous coordinates at $w = 1$, (e) distortion of points (green) and (f) the application of the camera matrix to the distorted points.

7.2.4 Jacobian calculation

The Levenberg-Marquardt algorithm requires a Jacobian to be calculated – or at least a reasonable estimate. An analytical derivative becomes prohibitively complex when considering models that include distortion parameters. Estimation methods can be used to reduce the number of explicit calculations

of the Jacobian, by using Rank-1 Broyden updates [234]. An approximation of the Jacobian can be calculated

$$\boldsymbol{\mathcal{J}} \cong \frac{f\left(\vec{\boldsymbol{x}}, \vec{\boldsymbol{\theta}} + \boldsymbol{\Delta} \times \vec{\mathbf{1}}\right) - f\left(\vec{\boldsymbol{x}}, \vec{\boldsymbol{\theta}} - \boldsymbol{\Delta} \times \vec{\mathbf{1}}\right)}{2\boldsymbol{\Delta}}, \tag{7.26}$$

where $\boldsymbol{\Delta}$ is some small perturbation to $\vec{\boldsymbol{\theta}}$. However, eq. (7.26) is subject to numerical inaccuracies, and the perturbation $\boldsymbol{\Delta}$ must be carefully chosen to avoid numerical issues. Recently, auto-differentiation methods have become popular due to their use in training neural networks. Auto-differentiation tools allow the rapid calculation of almost arbitrarily complex functions. Many auto-differentiation tools are available to researchers, including Theano, PyTorch and Tensorflow. The advantage of auto-differentiation of numerical methods is that they do not suffer from the same magnitude of numerical inaccuracies, whilst having similar computational costs. For this thesis, it was chosen that auto-differentiation tools would be used to eliminate concerns over numerical inaccuracies. Tensorflow was chosen arbitrarily for its auto-differentiation tools.

7.2.5 Conditions

The estimate $\vec{\boldsymbol{\theta}}$ defined during the non-linear regression is only valid under specific conditions. The conditions are given as:

Linearity. The linearisation used to estimate the parameters in the non-linear regression must accurately represent the function over a small interval. A model that is significantly non-linear will not be well approximated by a first-order Taylor approximation, and while the parameter estimate $\vec{\boldsymbol{\theta}}$ may still be correct, the covariance estimate $\boldsymbol{V}_\theta$ given in eq. (7.8) will be invalid.

Normality. The errors introduced in the measurements must follow a Gaussian distribution. If the errors do not follow a Gaussian distribution, then the input uncertainty $\boldsymbol{V}_\epsilon$ is incorrect and there will unaccounted errors propagated to the solution $\vec{\boldsymbol{\theta}}$. Generally given the number of observation used in the calibration, it is assumed that the errors asymptotically follow a normal distribution.

Specificity. Given there are no errors in the regressor vector $\vec{\boldsymbol{x}}$ or the observation vector $\vec{\boldsymbol{y}}$, the function $f\left(\vec{\boldsymbol{x}}, \vec{\boldsymbol{\theta}}\right)$ must accurately predict $\vec{\boldsymbol{y}}$. A model that does not comply with this condition is known as misspecified, and the covariance matrix estimate $\boldsymbol{V}_\theta$ given in eq. (7.8) will be invalid.

Additionally, there is no guarantee the assumptions used in the non-linear regression, specifically linearity and specificity, are not broken. A method is required to test both of these assumptions. The measures of non-linearity used

in this thesis are the parameter-effects curvature T and the intrinsic curvature ϒ found in [235] and the Clarke curvature Γ found in [236]. A function that is highly non-linear will not remain flat around the solution locus, and therefore the covariance matrix $\boldsymbol{V}_\theta$ will not be valid. These test statistics are computed in Section 7.4.The test for model specificity in a non-linear regression is given in White, 1981 [237]. This test is sensitive to heteroscedasticity. White describes a similar test that is not sensitive to heteroscedasticity, and more general test in [238].

7.3 Calibration outcome

This section will detail the outcome of the calibration. The calibration input data is given in Section 7.3.1. The parameters estimated using the serial, weighted serial, parallel and weighed parallel methods are given in Section 7.3.2. A novel metric that can be used to estimate a spatially-dependent resolution metric of the camera is given in Section 7.3.3. A comparison of the uncertainty in the input data caused by the board artefact itself and the ellipse localisation methods is given in Section 7.3.4.

7.3.1 Calibration input data

This section will present the calibration data that will be used in the non-linear regression. A total of twenty-seven unique positions and orientations of the board were imaged to create 2592 camera points and 2376 projector points. Each position is shown in Figure 7.2.

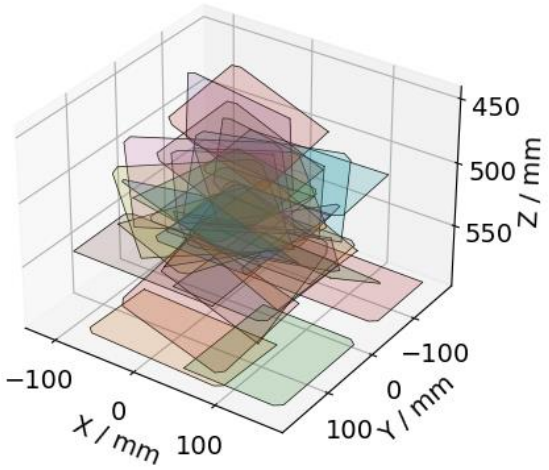

Figure 7.2 Location of the 27 board locations and orientations used for the calibration.

The triangulation method used in this thesis is similar to Zhang's method [34], and is assumed to be similarly robust for measuring points outside of the "calibration volume", i.e., outside the range of points used to calibrate the

system [30]. Nevertheless, a limit is placed on measurements as to only include points measured within the areas of images that have been calibrated. In any future measurement, to ensure any measurements made using the system parameters are not invalidated from measuring outside any calibrated region, both the camera and the projector will remove points outside of a boundary provided by the calibration points. The boundary with the calibration points is shown in Figure 7.3.

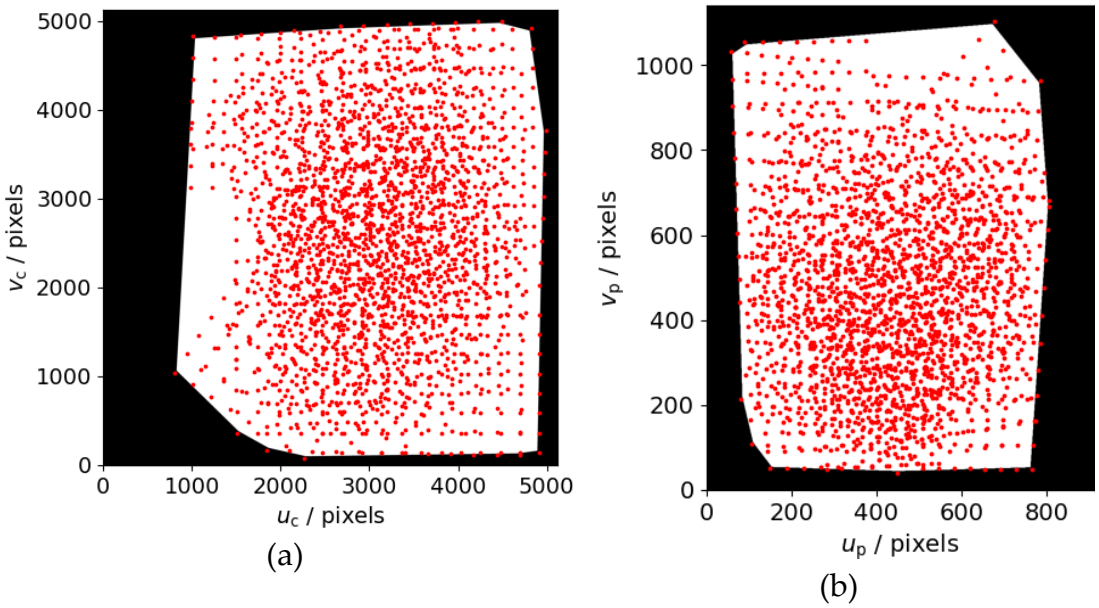

Figure 7.3 Image points used in the calibration for the (a) camera and (b) projector. Upon any future measurement, any points within the black boundary will be discarded.

7.3.2 Parameter estimations

The parameter estimations obtained using the serial, weighted serial, parallel and weighted parallel methods are given in Table 7.3.

Table 7.3 Parameter estimations.

	Unit	Parameter	Serial	Weighted serial	Parallel	Weighted parallel
Camera matrix	pixel	f_x	8520	8536	8510	8534
		f_y	8485	8536	8477	8535
		s	20.00	-0.4431	20.11	-0.4917
		u_0	2674	2676	2674	2675
		v_0	2544	2538	2543	2537
Camera distortion	-	k_1	-0.0158	-0.0339	-0.0173	-0.034
		k_2	-0.0323	0.1264	-0.0263	0.1219
		k_3	0.0541	-0.1619	0.0452	-0.1891
		p_1	-0.0070	-0.0011	-0.0069	-0.0011

		p_2	0.0019	-0.0004	0.0020	0.0004
		u_{dc}	-0.0771	-0.0097	-0.0779	-0.0094
		v_{dc}	0.2730	0.0070	0.2679	0.0060
Projector matrix	pixel	f_x	1123	1121	1121	1121
		f_y	-2247	-2243	-2242	-2242
		s	-0.2423	0.0083	-0.3997	-0.2741
		u_0	443	442	443	443
		v_0	1187	1187	1186	1187
Projector distortion	-	k_1	0.0495	0.0543	0.0579	0.0551
		k_2	-0.1765	-0.1906	-0.2236	-0.1942
		k_3	0.0845	0.0960	0.1461	0.1000
		p_1	0.0006	0.0001	0.0007	0.0001
		p_2	0.0002	0.0002	0.0002	0.0002
		u_{dc}	-0.0033	-0.0042	-0.0062	-0.0048
		v_{dc}	0.0121	0.0167	0.0252	0.0175
Projector extrinsics	-	q_1	0.2659	0.2651	0.2654	0.2651
		q_2	-0.2823	-0.2830	-0.2830	-0.2830
		q_3	1.5706	1.5719	1.5707	1.5719
	mm	t_x	5.7123	5.6859	5.7361	5.6857
		t_y	306.3578	306.3366	306.4418	306.2259
		t_z	-44.3868	-44.4270	-44.2130	-44.4299

The results of both weighted methods are very similar to each other, as are the results of the unweighted methods. Notably the skew parameter is very different across the methods. All methods strongly agree on the focal lengths of the camera, as well as the extrinsic estimates. The correlation matrices are shown in Figure 7.4.

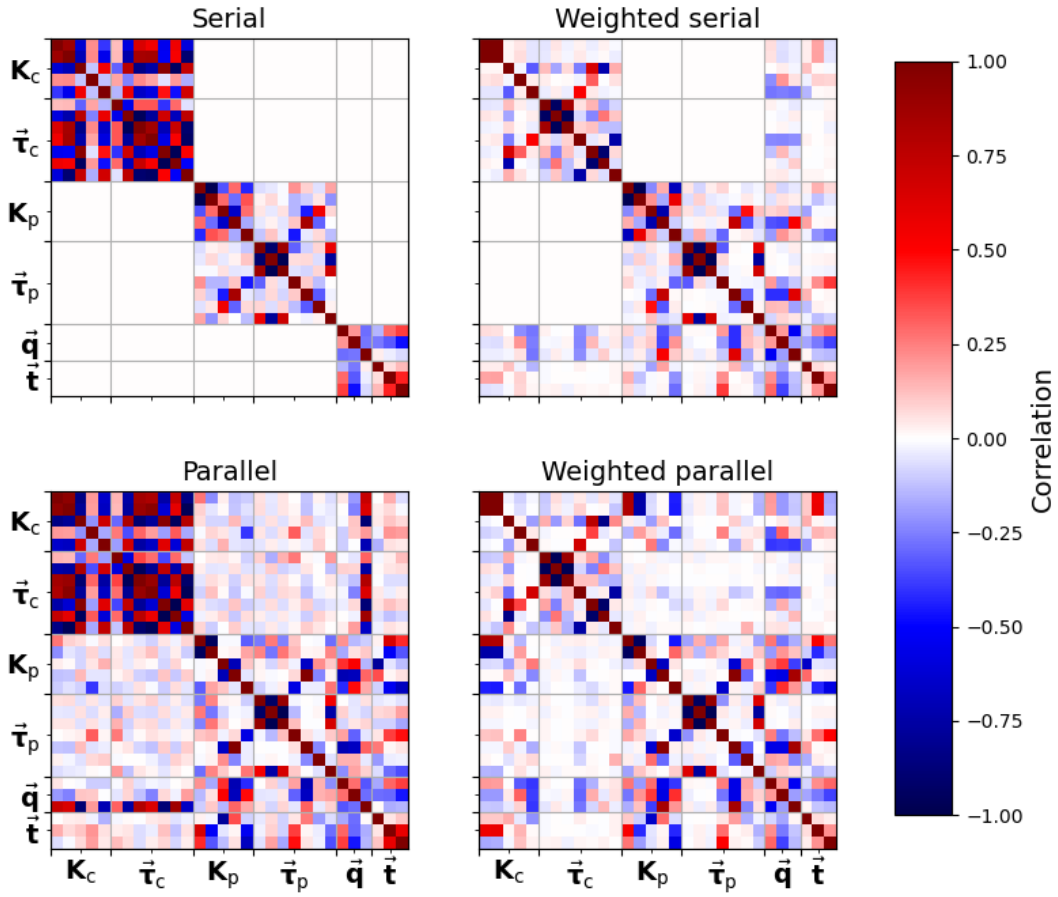

Figure 7.4 Correlation matrix of the parameter estimate from each calibration method.

Similar with the parameter estimate itself, the weighting matrix generally gives a similar correlation matrix for both the weighted serial and weighted parallel method estimates. The serial method gives no correlation between the camera, projector or extrinsic parameters, while the weighted serial methods gives no correlation between the projector and camera parameters. The cause being the serial method does regress camera and projector parameters independently.

The weighted serial and weighted parallel also have similar correlation coefficients for both the extrinsic estimates, $\vec{q}$ and $\vec{t}$, despite both methods deriving each value very differently. The weighting matrix produces large changes in the correlation of most coefficients, that would otherwise be unchanged across serial and parallel methods.

7.3.3 Optical resolution estimate

As a by-product of the ellipse localisation method, an estimate of the camera resolution is made. In Section 6.5.3, ellipse boundaries are determined using a fit of a Gaussian function to a radially-sampled line-spread function. The width

of the Gaussian is related to the resolution of the camera. The line-spread function width is shown in Figure 7.5.

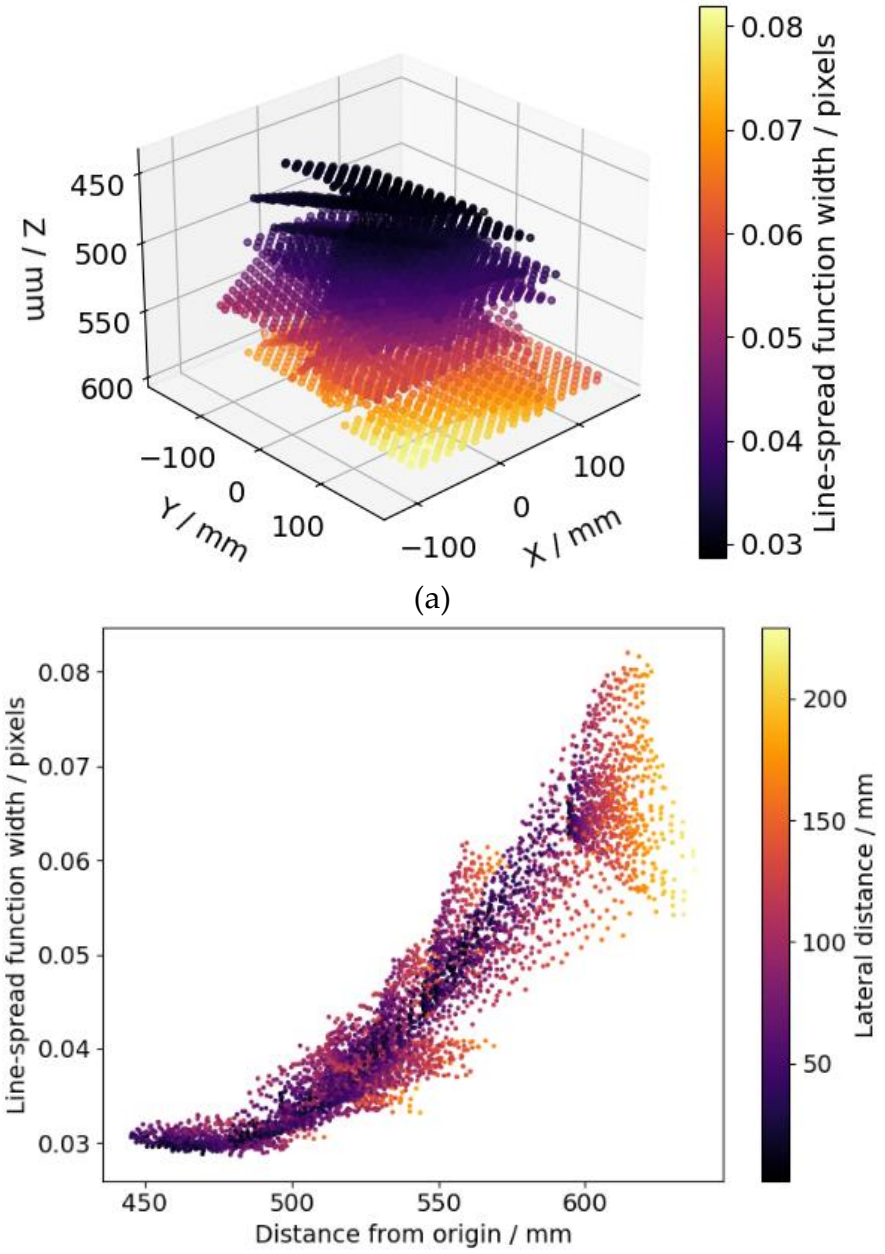

Figure 7.5 The width of the Gaussian line-spread function in (a) 3D and (b) plotted against distance from the camera pinhole origin. The lateral distance is the distance in the XY plane to (0,0).

The point spread function (PSF) describes the response of an imaging system to a point source or point object, and is related to a line-spread function [93]. The line-spread function width found here could possibly be used to estimate a spatially-variant PSF for a camera without requiring any additional data to

be collected. This novel method may be a useful tool in the future in obtaining a full uncertainty evaluation of fringe projection measurements, see Section 9.5.

7.3.4 Input data covariance

This section will show the input uncertainty estimate. The positional uncertainty of each dot in the dot grid is given in Section 6.2. The uncertainty of the board is propagated to the image plane of the camera and projector in Section 7.2. The comparison of the input covariances is given in Figure 7.7.

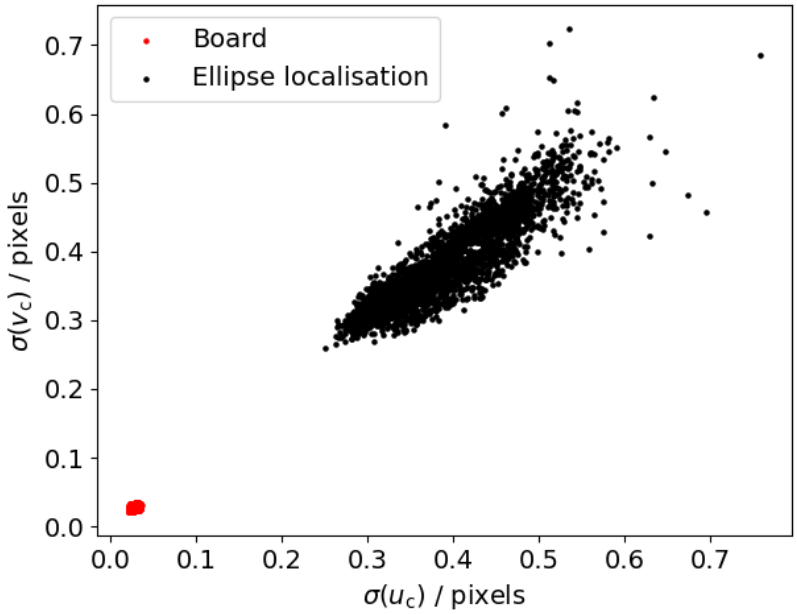

Figure 7.6 Comparison of the uncertainty contributed form the dot grid and the ellipse localisation in the camera image.

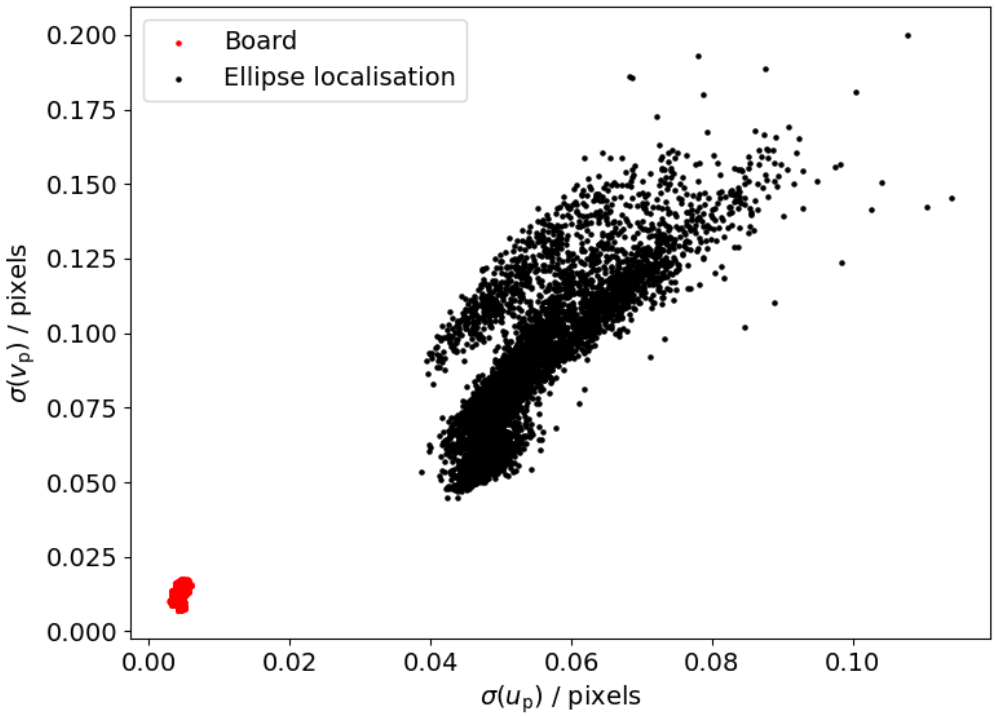

Figure 7.7 Comparison of the uncertainty contributed form the dot grid and the ellipse localisation in the projector image.

The uncertainty of the board is generally very low compared to the uncertainty of the ellipse localisation method for both the camera and the projector. The projector has far higher uncertainty in one axis compared with the other. This is to be expected and is a consequence of triangulation.

7.4 Calibration validation

In this section, several tests are carried out to validate the calibration method defined in this chapter. The tests given in Section 7.4.1, Section 7.4.2 and Section 7.4.3 will validate the conditions given in Section 7.2.5. Section 7.4.3 specifically provides a novel method of testing for parameter stability during the calibration procedure. Section 7.4.4 will test the non-linear regression for convergence to a non-global minimum. Section 7.4.5 will compare the uncertainty of estimated points against the estimated error of each point.

7.4.1 Specificity test

In this subsection, White's specificity test [237] is used to test the specificity of the pinhole model with distortion to fringe projection. Correct specificity is one of the assumptions used in linear regression, and if broken, will render the covariance estimation incorrect. In other words, the specificity test is used to check if the model used in the linear regression is correct up to some additive error. To reject this hypothesis implies there are variables excluded from the

model, and therefore the model is misspecified. The specificity test in White [237] is specifically a specificity test for non-linear regression models For a non-linear regression that, in the final step, computes the Jacobian $\boldsymbol{\mathcal{J}}$ and the residuals $\vec{\boldsymbol{\epsilon}}$ at the solution $\vec{\boldsymbol{\theta}}$, the specificity test is given by finding the solution $\vec{\boldsymbol{\alpha}}$ to

$$\vec{\boldsymbol{\epsilon}}^2 = \alpha_0 \odot \vec{\mathbf{1}} + \boldsymbol{\psi}\vec{\boldsymbol{\alpha}}, \tag{7.27}$$

where

$$\boldsymbol{\psi} = \boldsymbol{\mathcal{J}} \odot \boldsymbol{\mathcal{J}}, \tag{7.28}$$

with $\odot$ being the Hadamard product. The test will fail if there is a solution to eq. (7.27) that has some sufficient statistical power, i.e., if the square residual $\vec{\boldsymbol{\epsilon}}^2$ can be modelled in some way. Given there are N observations and P parameters being estimated in the non-linear regression, the resulting "artificial residual" on $\vec{\boldsymbol{\epsilon}}^2$ is used as a quantity value to test how much structure remains in the residuals $\vec{\boldsymbol{\epsilon}}^2$. The test is completed by computing the constant-adjusted coefficient of determination, R^2, given by

$$R^2 = 1 - \frac{\sum\left(\vec{\boldsymbol{\epsilon}}^2 - \left(\alpha_0 \odot \vec{\mathbf{1}} + \boldsymbol{\psi}\vec{\boldsymbol{\alpha}}\right)\right)^2}{\mathrm{var}(\vec{\boldsymbol{\epsilon}}^2)} \times \frac{n-1}{n-p-1}. \tag{7.29}$$

The coefficient of determination is a measure of statistical power in the solution to eq. (7.27), i.e., how well does the solution $(\alpha_0, \vec{\boldsymbol{\alpha}})$ adequately explain $\vec{\boldsymbol{\epsilon}}^2$. The value $n \times R^2$ is compared against the critical value of the χ^2 distribution at p degrees of freedom. If the value nR^2 exceeds the critical value, the model is misspecified.

In White [237], it was shown that this test will also fail in the presence of heteroscedasticity. In Section 7.2, it was made clear that the image points in the calibration are correlated with one another. However, a method was given in Chapter 6 to estimate the covariance (and by extension the correlation) between image points with covariance matrix $\boldsymbol{V}$. Given a regressor matrix $\boldsymbol{X}$ and observation vector $\vec{\boldsymbol{y}}$, a weighted linear regression can be seen as a transformed linear regression, transformed using the matrix $\boldsymbol{C}\boldsymbol{C}^{\mathrm{T}} = \boldsymbol{V}$, and applying the transform $\boldsymbol{C}$ to the linear regression formula to obtain

$$((\boldsymbol{C}^{-1}\boldsymbol{X})^{\mathrm{T}}\boldsymbol{C}^{-1}\boldsymbol{X})^{-1}(\boldsymbol{C}^{-1}\boldsymbol{X})^{\mathrm{T}}\boldsymbol{C}^{-1}\vec{\boldsymbol{y}} \tag{7.30}$$

$$(\boldsymbol{X}^{\mathrm{T}}\boldsymbol{C}^{-\mathrm{T}}\boldsymbol{C}^{-1}\boldsymbol{X})^{-1}\boldsymbol{X}^{\mathrm{T}}\boldsymbol{C}^{-\mathrm{T}}\boldsymbol{C}^{-1}\vec{\boldsymbol{y}} \tag{7.31}$$

$$(\boldsymbol{X}^{\mathrm{T}}(\boldsymbol{C}\boldsymbol{C}^{\mathrm{T}})^{-1}\boldsymbol{X})^{-1}\boldsymbol{X}^{\mathrm{T}}(\boldsymbol{C}\boldsymbol{C}^{\mathrm{T}})^{-1}\vec{\boldsymbol{y}} \tag{7.32}$$

$$(\boldsymbol{X}^{\mathrm{T}}\boldsymbol{V}^{-1}\boldsymbol{X})^{-1}\boldsymbol{X}^{\mathrm{T}}\boldsymbol{V}^{-1}\vec{\boldsymbol{y}}. \tag{7.33}$$

The weighted least squares regression is therefore a transformed linear regression. Expanding this to non-linear regression, at the solution locus $\vec{\boldsymbol{\theta}}_{\mathrm{e}}$, the solution $\vec{\boldsymbol{\theta}}_{\mathrm{e}} + \boldsymbol{\Delta}\vec{\boldsymbol{\theta}} = \vec{\boldsymbol{\theta}}$ is given using the Jacobian of the solution locus $\boldsymbol{\mathcal{J}}$ as the regressor matrix

$$\boldsymbol{\mathcal{J}}\boldsymbol{\Delta}\vec{\boldsymbol{\theta}} = \vec{\boldsymbol{y}} - f\left(\vec{\boldsymbol{x}}, \vec{\boldsymbol{\theta}}_{\mathrm{e}}\right) = \vec{\boldsymbol{r}} \tag{7.34}$$

$$(\boldsymbol{\mathcal{J}}^{\mathrm{T}}\boldsymbol{V}^{-1}\boldsymbol{\mathcal{J}})^{-1}\boldsymbol{\mathcal{J}}^{\mathrm{T}}\boldsymbol{V}^{-1}\vec{\boldsymbol{r}}. \tag{7.35}$$

The same transform can therefore be applied to eq. (7.27) and eq. (7.28) to remove the heteroscedasticity present in the calibration, giving the updated equations

$$(\boldsymbol{C}^{-1}\vec{\boldsymbol{\epsilon}})^2 = \alpha_0 + \boldsymbol{\psi}\vec{\boldsymbol{\alpha}} \tag{7.36}$$

$$\boldsymbol{\psi} = (\boldsymbol{C}^{-1}\boldsymbol{\mathcal{J}})\odot(\boldsymbol{C}^{-1}\boldsymbol{\mathcal{J}}). \tag{7.37}$$

The test will now fail if the covariance matrix $\boldsymbol{V}$ is incorrect, or if the model is misspecified. The test is insensitive to any scalar multiplicative error in covariance matrix $\boldsymbol{V}$, given the scalar multiplication will cancel in eq. (7.36). In the context of the serial and parallel calibration methods, the serial method is completely insensitive to a scalar multiplicative error in the covariance matrix for the camera and projector regression input. However, the parallel method will be sensitive to a scalar multiplicative error, considering the covariance matrix is a concatenation of the projector and camera regression input covariance matrices. Overestimating or underestimating the uncertainty in the camera or projector matrices in relation to each other will cause this test to fail. The test is performed on the camera and projector regression estimations individually in the serial method and once on the parallel method regression estimation.

In the serial calibration there are 27 positions measured, giving 5 pinhole parameters, 7 distortion parameters 27×6 extrinsic parameters, for a total of 174 parameters.

The critical value of the χ^2 distribution with 174 degrees of freedom is 206, i.e., 95% of values are expected to be below 206. In the parallel calibration, there are now 10 pinhole parameters, 14 distortion parameters and an additional 6

parameters describing the rotation and translation from the camera coordinate system to the projector coordinate system, giving a total of 192 parameters. The critical value of the χ^2 distribution with 174 degrees of freedom is 225.

Table 7.4 Specificity test results for the weighted serial and weighted parallel method.

	Test value	Critical value
Weighted serial (camera)	880	206
Weighted serial (projector)	1116	206
Weighted parallel (all)	5560	225

This specificity test, outlined in White [237], is used in this case to simultaneously test the covariance matrix of inputs used in the calibration, and the model. The specificity test fails for both methods and appears worse in the parallel method. The failure could indicate that the distortion model does not completely explain all observed ellipse locations. The failure could also indicate that the covariance matrix estimation, $\boldsymbol{V}_{\epsilon}$ is poor. Another possible failure mode is the covariance matrices for the camera and projector have a scalar multiplicative error in relation to each other. In the latter, it would be expected that only the parallel method would fail, since the covariance matrices need to be accurate in relation to each other in the parallel method, but not the serial method. Given the higher test score in the parallel method, this could indicate this to be true.

7.4.2 Curvature test

In this section, the non-linearity on the parameter covariance estimate in a non-linear regression will be tested. Given the calibration uses a linear approximation of a non-linear problem, significant non-linearity will invalidate the linear approximations. Significant non-linearity will reduce the efficacy of the covariance estimation.

The measures of nonlinearity used in this thesis are the parameter-effects curvature T, the intrinsic curvature ϒ and the Clarke curvature Γ. The derivation of these measures are beyond the scope of this thesis. The derivation of the parameter-effects curvature, T, and the intrinsic curvature, ϒ, can be found in Bates and Watts [235] and Seber and Wild [239], and the derivation of the Clarke curvature Γ can be found in Clarke [236]. The parameter-effects curvature T depends only on the particular parametrisation used, and can be effectively reduced by choosing the right model. The intrinsic curvature ϒ is a measure of non-linearity of the problem itself, and is invariant of the chosen

model. The Clarke curvature Γ is an extension of the parameter-effects curvature, and can provide a non-linearity measure in individual specific parameters.

The following non-linearity tests require the calculation of the Hessian matrix, which in this case is a three-dimensional tensor, in this subsection only, the standard notation convention used in this thesis will be dropped in favour of tensor notation with the Einstein summation convention. In this subsection only, indices represent coordinates in an arbitrary N-dimensional tensor, where both subscripts and superscripts are used for indices (and superscripts do not infer an exponent). For example, a 2D matrix that was denoted $\boldsymbol{X}$ is now denoted $x_j^i = x_{ij} = x^{ij}$. To denote the exponent k of variable x_j^i, which would otherwise be denoted as $\boldsymbol{X}^k$, is now denoted as $\left[x_j^i\right]^k$. A variable without indices is a scalar. According to this convention, when an index appears twice in a single term and is not otherwise defined, it implies the summation of that term over the index. For example, if the index $i \in \{1,2,3\}$,

$$y = c_i x^i = \sum_{i=1}^{3} c_i \times x^i. \tag{7.38}$$

For consistency, the indices u, v are used exclusively to denote the N observation coordinates, $u, v \in \{1, \dots N\}$ and a, b, c, i, j are used exclusively to denote the P parameter coordinates, $a, b, c, i, j \in \{1, \dots P\}$. The Jacobian and the Hessian are given by

$$\eta_{ij}^u = \frac{\partial^2 f(x_u, \theta)}{\partial \theta_i \partial \theta_j} \tag{7.39}$$

$$\eta_i^u = \frac{\partial f(x_u, \theta)}{\partial \theta_i}. \tag{7.40}$$

The inverse of square of the Jacobian, otherwise given as $(\boldsymbol{\mathcal{J}}^{\mathrm{T}}\boldsymbol{\mathcal{J}})^{-1}$, is given by

$$g^{ij} = \left[\eta_i^n \delta_{nm} \eta_j^m\right]^{-1} \tag{7.41}$$

$$\delta_{uv} = \begin{matrix} 1 \\ 0 \end{matrix} \text{ if } \begin{matrix} u = v \\ \text{otherwise} \end{matrix}. \tag{7.42}$$

The projection matrix, otherwise given as $\boldsymbol{X}(\boldsymbol{X}^{\mathrm{T}}\boldsymbol{X})^{-1}\boldsymbol{X}^{\mathrm{T}}$ for the linear model $\vec{\boldsymbol{y}} = \boldsymbol{X}\vec{\boldsymbol{\beta}}$, is given by

$$P_{uv} = \eta_i^u g_{ij} \eta_j^v. \tag{7.43}$$

The measures of Clarke curvature Γ is defined as

$$\Gamma_{\mathrm{j}} = \left(g^{jj}\right)^{-\frac{3}{2}} g^{ja} g^{jb} g^{jc} \eta_a^u \delta_{uv} \eta_{bc}^v, \tag{7.44}$$

and the non-linear model is considered acceptably linear in the case that $\left|\frac{1}{2}\Gamma sc\right| < .1$. Otherwise, curvature effects are too large to ignore. The parameter-effects curvature T and intrinsic curvature ϒ are calculated along the vector α^i in the P-dimensional parameter space.

$$\mathrm{T} = \frac{\left\|\alpha^i P_{vu} \eta_{ij}^u \alpha^j\right\|}{\left\|\eta_j^u \alpha^j\right\|^2} \tag{7.45}$$

$$\Upsilon = \frac{\left\|\alpha^i ([\mathbb{I} - P]_{vu}) \eta_{ij}^u \alpha^j\right\|}{\left\|\eta_j^u \alpha^j\right\|^2}. \tag{7.46}$$

Given the curvature will depend on the choice of α^i, a good decision would find the maximal value of α^i. Computationally, this is particularly tricky given the size of the tensors involved. The parallel calibration method uses 27 positions, 184 points per position and therefore the Hessian η_{ij}^u has the size $192 \times 192 \times 9936$ – although most entries of the Hessian are 0. A method is presented here that will give a low-cost approximation of α^i. An approximate solution of α^i can be found by estimating the vector α^i that instead maximises

$$\sum_u \alpha^i P_{uv} \eta_{ij}^v \alpha^j, \tag{7.47}$$

which is simply the eigenvector of

$$\sum_u P_{uv} \eta_{ij}^v \tag{7.48}$$

that corresponds to the largest eigenvalue. To evaluate if the measures T and ϒ are within reasonable limits, both measures are scaled

$$\mathrm{T}' = \mathrm{T}\sigma\sqrt{P} \tag{7.49}$$

$$\Upsilon' = \Upsilon\sigma\sqrt{P}, \tag{7.50}$$

where σ in this case is the standard error of the non-linear regression. The combined curvature measures $\sqrt{[\mathrm{T}']^2 + [\Upsilon']^2}$ are compared against the confidence region given by

$$\zeta = \frac{1}{\sqrt{F(P, N; 0.05)}}. \tag{7.51}$$

If $\sqrt{[T']^2 + [Y']^2} > \zeta$, the parameter estimations must be rejected. Otherwise, the curvature can be accepted as low enough so as to still provide a reasonable estimation of the parameters. The results of the Clarke curvatures are given in Figure 7.8 and the parameter-effects and intrinsic curvatures are given in Table 7.5.

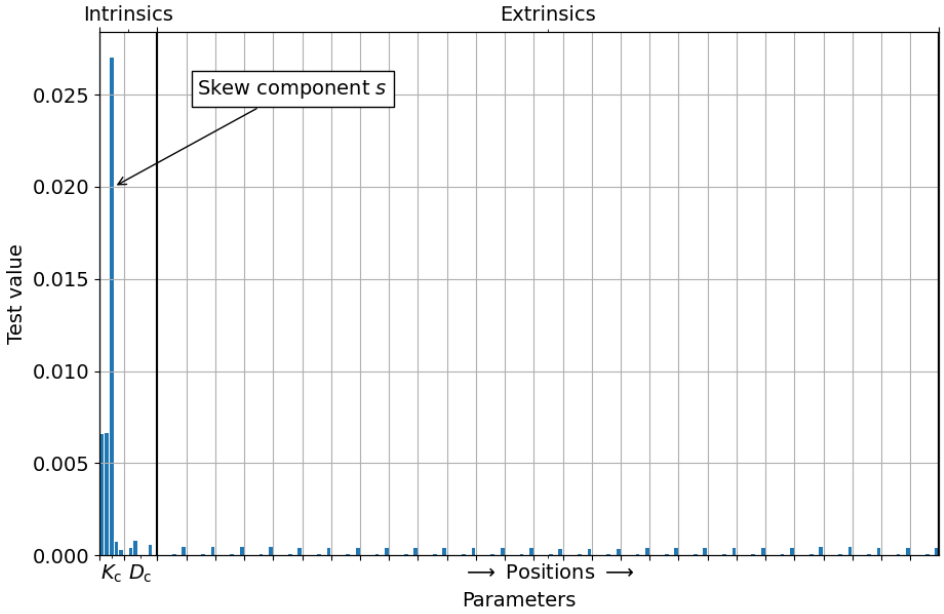
Intrinsics
Extrinsics
Skew component s
0.025
0.020
0.015
0.010
0.005
0.000
Test value
K_c D_c
⟶ Positions ⟶
Parameters

(a)

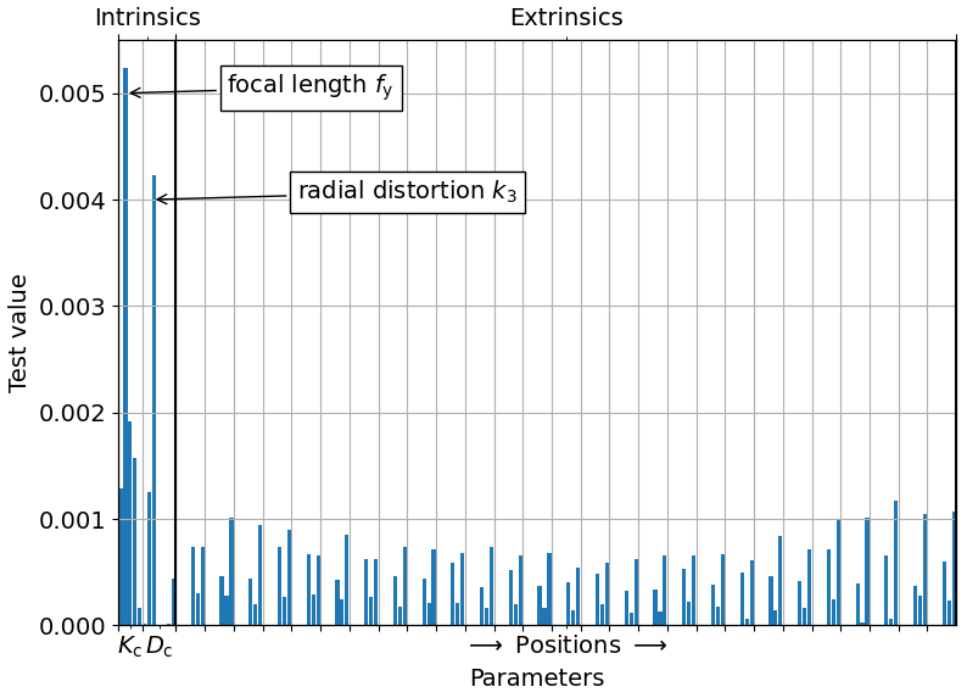
Intrinsics
Extrinsics
focal length f_y
radial distortion k_3
0.005
0.004
0.003
0.002
0.001
0.000
Test value
K_c D_c
⟶ Positions ⟶
Parameters

(b)

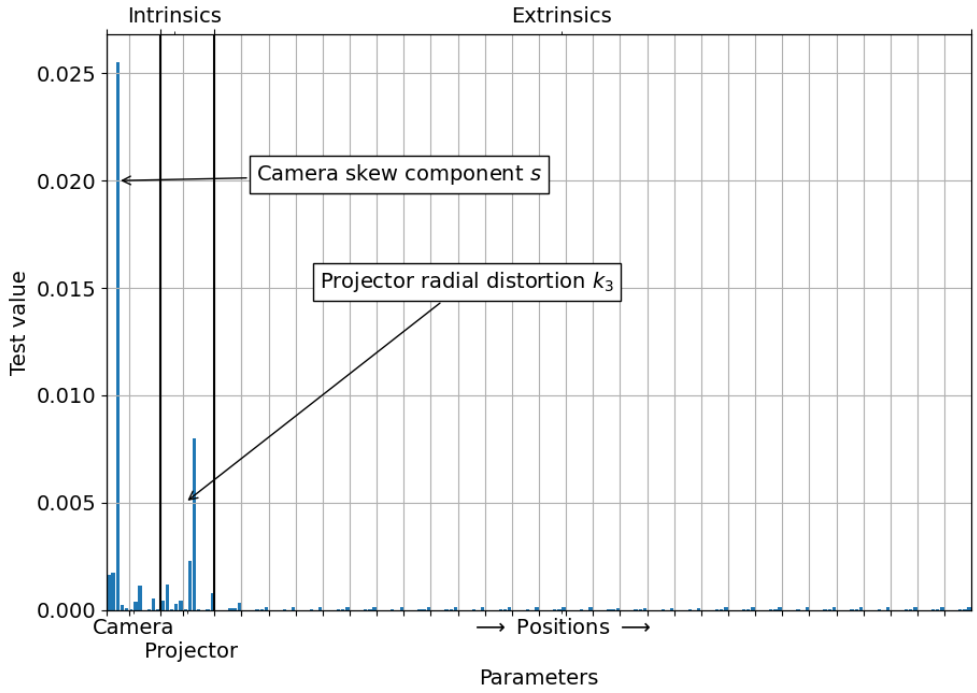

(c)

Figure 7.8 The Clarke curvatures Γ of the system parameters. (a-b). Camera and projector parameters estimated using the serial method. (c) Parameters estimated using the parallel method.

Table 7.5 Parameter-effects and intrinsic curvature measures for the parallel and serial methods.

	Parameter-effects, T′	Intrinsic, Υ′	Combined, $\sqrt{[T']^2 + [\Upsilon']^2}$	Limit, ζ
W. serial (camera)	5×10^{-4}	6×10^{-7}	5×10^{-4}	0.92
W. serial (projector)	3×10^{-4}	8×10^{-8}	3×10^{-4}	0.92
Parallel	4×10^{-4}	5×10^{-7}	4×10^{-4}	0.92

The non-linearity is well within acceptable limits for both methods. The parameter with the highest non-linearity measure is the skew component in the pinhole matrix of the camera. Bates and Watts [235] show that an increase in the number of observations can reduce the non-linearity – in a calibration with fewer observations, it may be prudent to remove the skew component of the pinhole camera matrix. The projector, however, does not show the same behaviour.

7.4.3 Parameter stability test

In Section 3.4, it was made known that optical characteristics are a function of temperature – so must be considered within the calibration. Consider the simple camera pinhole model describing the back propagation

$$u = \frac{f_T(\vec{\boldsymbol{r}}_1^{\mathrm{T}}\vec{\boldsymbol{x}} + t_x)}{(\vec{\boldsymbol{r}}_3^{\mathrm{T}}\vec{\boldsymbol{x}} + t_z)}, \tag{7.52}$$

where $\boldsymbol{R}^{\mathrm{T}} = [\vec{\boldsymbol{r}}_1 \quad \vec{\boldsymbol{r}}_2 \quad \vec{\boldsymbol{r}}_3]$ and $\vec{\boldsymbol{t}}^{\mathrm{T}} = [t_x \quad t_y \quad t_z]$ and the focal length f_T has been explicitly defined as a function of temperature, T. The output u can be kept constant even in the case that f_T is evolving by compensating with the Euclidean transforms $\boldsymbol{R}$ and $\vec{\boldsymbol{t}}$. In the case of many cameras and projectors and with randomly varying optical characteristics, this effect may be cancelled out by estimating all parameters in parallel. In the case of one projector and one camera being calibrated, both will have a time-dependent systematic error if both the camera and projector are not in thermal equilibrium. The internal temperature, therefore, will cause a systematic error in the estimation of the camera and the projector parameters. Furthermore, these systematic errors will not produce a detectable difference in the residual vector $\vec{\boldsymbol{\epsilon}}$, otherwise known as the reprojection error due to the redundancy in eq. (7.52).

This section will define the parameter stability test to detect unstable intrinsic parameters. While the parameter stability test does not guarantee an accurate estimation of parameters, it does prevent the thermal equilibrium condition from failing while being undetected. The test will fail if the linear regression conditions are broken or if the uncertainty matrices are $\boldsymbol{V}_\epsilon$ are poor. The disadvantage of the test is there is no indication of what condition has broken during a failure, and the test can be arbitrarily passed by estimating huge uncertainty in $\boldsymbol{V}_\epsilon$.

The method in Section 7.2.1 gives a weighted estimation of the extrinsic parameters (the Rodrigues rotation vector $\vec{\boldsymbol{q}}$ and translation $\vec{\boldsymbol{t}}$) describing the transform between the camera and the projector, along with an uncertainty. For the unweighted serial method, this is found using an estimate of the parameter covariance matrix, given by the estimator

$$\boldsymbol{V}_\theta = \frac{\|\vec{\boldsymbol{\epsilon}}\|}{N - P}(\boldsymbol{\mathcal{J}}^{\mathrm{T}}\boldsymbol{\mathcal{J}})^{-1}, \tag{7.53}$$

where N equals the number of observations iwthin the regression and P equals the number of parameters obtain from the regression. For the weighted serial method, the parameter covariance matrix is found using the weighted estimator,

$$\boldsymbol{V}_{\text{all}} = (\boldsymbol{\mathcal{J}}^{\mathrm{T}}\boldsymbol{V}_\epsilon^{-1}\boldsymbol{\mathcal{J}})^{-1}. \tag{7.54}$$

With an estimated uncertainty of the parameters $\boldsymbol{V}_{\text{all}}$ obtained, each estimate of the camera-projector transform can be compared for agreement, i.e., if there is

any statistically significant deviation from the final estimate of the camera-projector transform. A χ^2 test can now be completed using

$$\left(\vec{\boldsymbol{\theta}}_{\text{all}} - \vec{\mathbf{1}} \otimes \vec{\boldsymbol{\theta}}_{\text{e}}\right)^{\text{T}} \left(\boldsymbol{V}_{\text{all}} + \boldsymbol{V}_{q,t} \otimes \mathbb{I}\right)^{-1} \left(\boldsymbol{\theta}_{\text{all}} - \vec{\mathbf{1}} \otimes \vec{\boldsymbol{\theta}}_{\text{e}}\right), \tag{7.55}$$

where $\otimes$ is the Kronecker product. A comparison of the camera-projector transforms estimate from each artefact with the final estimate is given in Figure 7.9. With some exceptions, the application of the covariance matrix has reduced the deviation of the quantity values. The critical value of a χ^2 distribution with $26 \times 6 = 162$ degrees of freedom is 192.7, where the unweighted serial method obtained a score of 1691.5, and the weighed serial method obtained a score of 80.4. The parameter stability test will also fail when the covariance matrix $\boldsymbol{V}_{\text{all}}$ is unable to explain the discrepancy in different camera-projector transforms for all artefact positions. The results of the χ^2 cost of each artefact position is given in Figure 7.9.

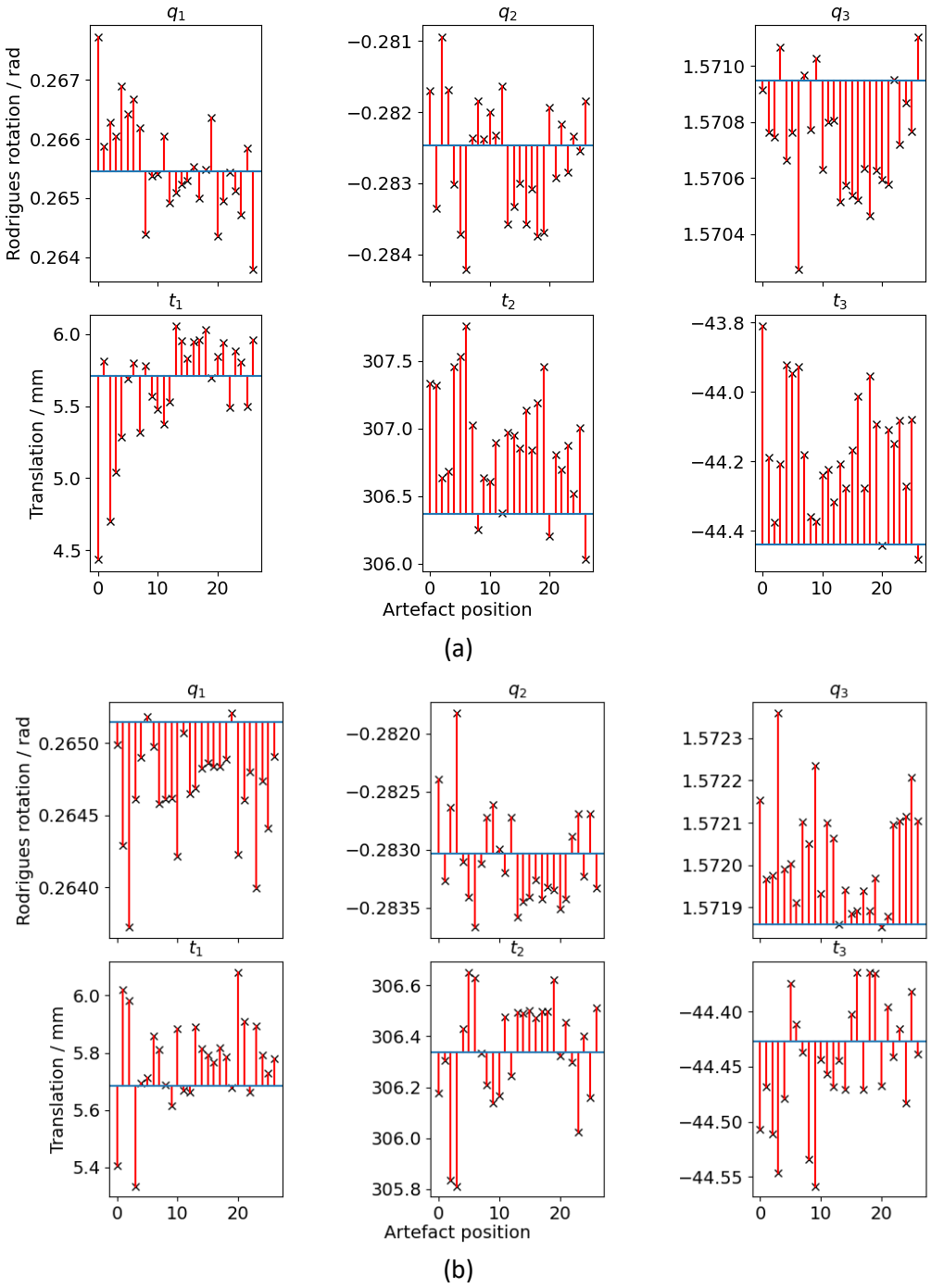

Figure 7.9 Comparison of the twenty-seven estimations of the transform between the camera and projector. Estimation obtained using the (a) serial method and (b) unweighted serial method.

7.4.4 False convergence test

The non-linear regression in the calibration is only guaranteed to find a local minimum, not the global minimum. There is a significant chance that the non-linear regression returns a local minimum that does not correspond with the global minimum. Furthermore, the process is deterministic, i.e., repeating the non-linear regression using the same estimate will lead to the same outcome.

In this section, by randomly varying the input estimate to the non-linear regression by ±5%, the outcome of 200 non-linear regressions will be analysed to estimate how much the non-linear regression provides a non-global minimum. Both the weighed serial and weighted parallel methods will be tested. The first test will look at the reprojection error, since the reprojection error is used to estimate when the non-linear regression is complete, the values of the reprojection error should correspond well with identified minimums. The histogram of reprojection errors across all 200 repeats is given in Figure 7.10.

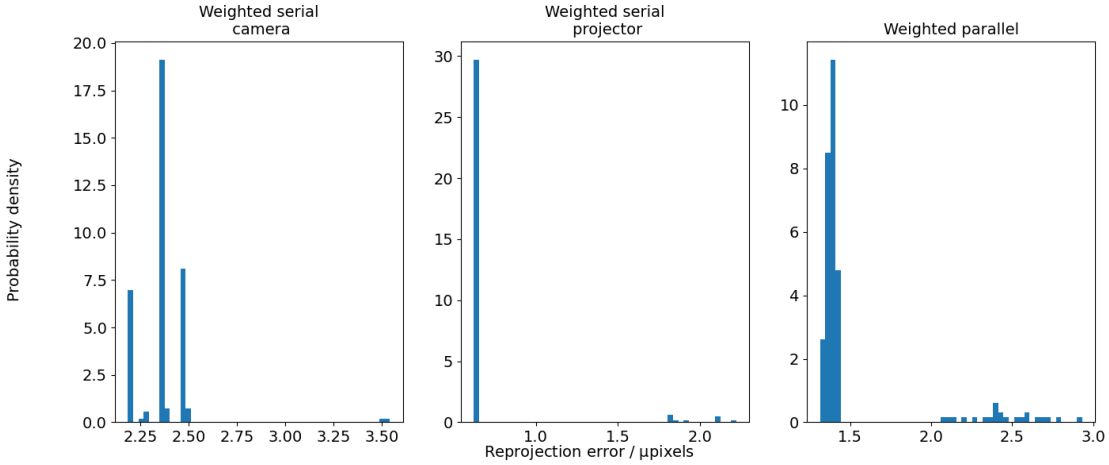

Figure 7.10 Histogram of the reprojection errors of the weighted serial and weighted parallel method across all 200 repeated regressions.

The histogram of reprojection errors show that the regression of camera and projector parameters in the serial method and the parallel method all have a minimum at a reprojection error of 2.18 µpixels, 0.06 µpixels and 1.31 µpixels respectively. In Figure 7.11, the estimations of the camera and projector focal lengths and principal points is given. When comparing to the values of the camera focal length in both the x-axis and the y-axis, there is not such a clear distinction of minima. Except for the projector in the serial method, there are not clear global minimum – the local minimum returned from the non-linear regression are not single points in the P-dimensional parameter space. It is likely caused by the extrinsic and focal length both parameters giving similar effects on the projected point. Both the principal point and focal length values converge to a central location. Although it is difficult to conclusively prove the parameter estimation is the "true" global minimum as the surrounding parameter space must be thoroughly searched, this test gives a good indication that the true minimum has been reached. This test shows that in general, it is necessary to explore some of the local parameter space by repeating the non-

linear regression with different initial estimates, since only ~25% of the serial method camera regression estimates and ~10% of the parallel method regression estimates were close to the minimum.

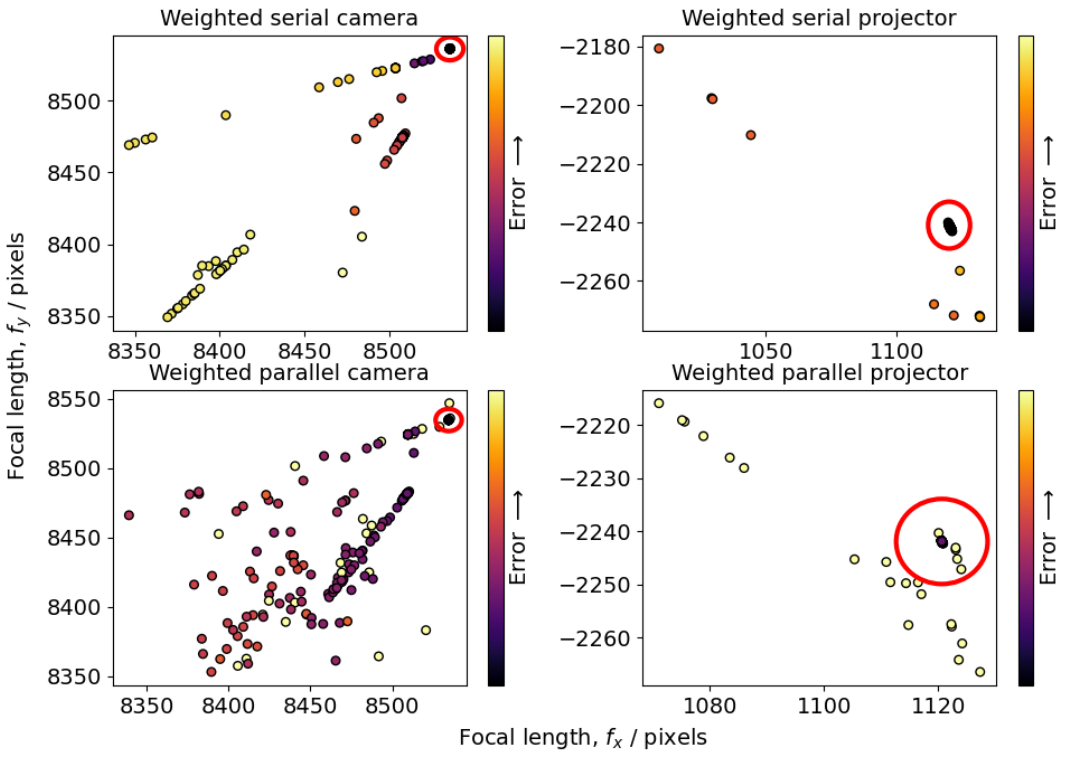

(a)

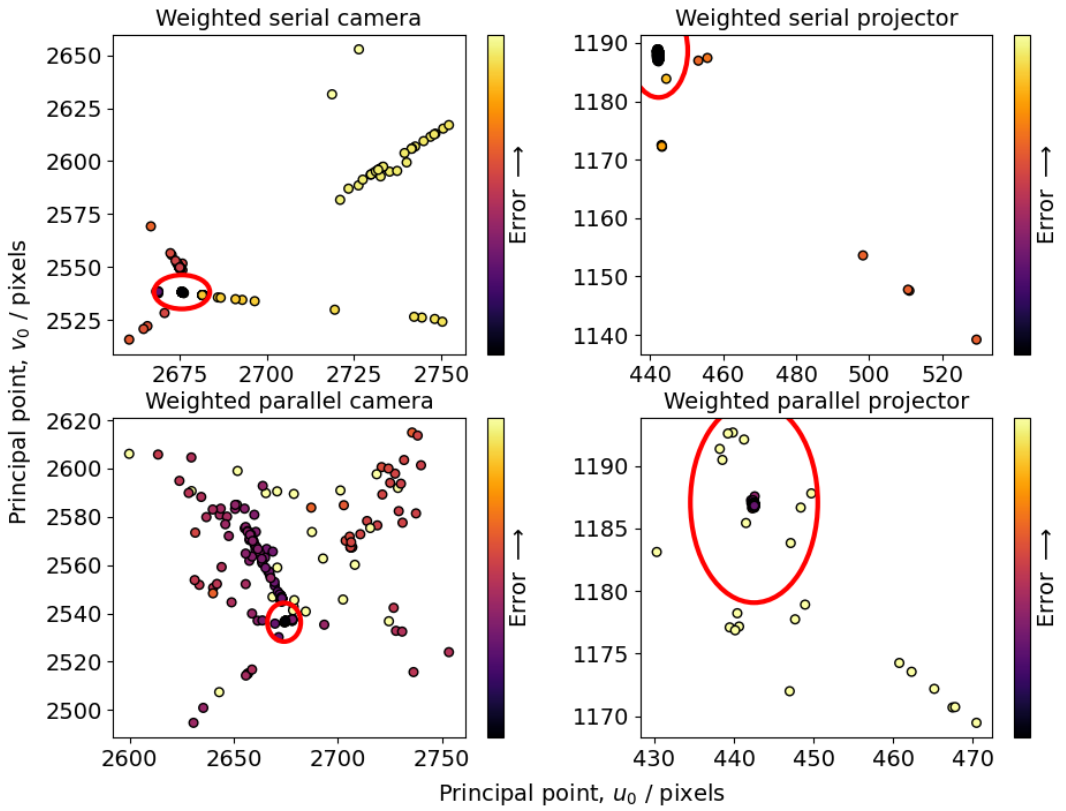

(b)

Figure 7.11 Parameter values of the camera and projector for all repeats of the non-linear regression in the weighted serial and weighted parallel methods. (a) The focal lengths and (b) the principal points.

7.4.5 Reprojection error test

In this section, the covariance of the inputs to the non-linear regression $\boldsymbol{V}_{\epsilon}$ can be tested on the reprojection errors. The test will consist of a reduced χ^2 test on the reprojection errors, given by

$$\vec{\boldsymbol{\epsilon}}^{\mathrm{T}}\boldsymbol{V}_{\epsilon}^{-1}\vec{\boldsymbol{\epsilon}}. \tag{7.56}$$

The test will be conducted on the weighted serial and weighted parallel calibration methods. The weighted serial method gave a reduced χ^2 test score of 0.08 and 0.25 for the camera and projector respectively, while the parallel method gave a reduced χ^2 test score of 0.19. All test scores are below the expected value of approximately 1. Therefore, either the non-linear regression is over-fitting the data or the covariance estimate of the input is overestimated, or both.

7.5 Summary

In this chapter, a calibration method is defined in full detail. The popular non-linear regression method is modified as to allow the evaluation of uncertainty of the estimated parameters. The non-linear regression used in this thesis to obtain the parameter estimates is explicitly defined in Section 7.2, where choices have been made to ensure a high-accuracy regression. The results of the calibration estimates are given in Section 7.3. It was shown that the two weighted methods showed good agreement between estimations. A novel method to obtain a resolution metric without the need to obtain any extra data was given that may be useful when performing a full uncertainty evaluation of a fringe projection measurement. The input data covariance showed the need for increased accuracy of the ellipse localisation. The working conditions for this calibration method to work are given, and tests are undertaken in Section 7.4 to test these conditions are true. Apart from the specificity test, the tests show the calibration was performing within working conditions. The failure of the specificity test indicates that either the covariance matrix of the input quantities was invalid or the pinhole camera model with distortion is not specific enough for fringe projection. Given the success of tests given in Chapter 6, it is likely that the model has poor specificity.

Chapter 8 – Validation

This chapter will validate the parameter estimations and uncertainties obtained in Chapter 7 using measurement artefacts. For each measurement, the parameter uncertainties will be propagated to the final measurement quantity, which will be compared with an independently measured result. The comparison will be completed using the reduced χ^2 test given in Section 4.4. The method of propagation form parameter uncertainty to measurement uncertainty is described in Section 8.1. A validation testis completed on a flatness artefact in Section 8.2 and validation tests completed on sphere-based artefacts is completed in Section 8.3.

8.1 Propagation of uncertainty

This section will define a method that will allow the propagation of uncertainty from the system parameters to the final measurement. Once the uncertainty estimation in the parameters has been obtained, the uncertainty can be propagated to the final measurement point-cloud. Given that more than a million points are being derived from the same set of thirty parameters, the resulting covariance matrix of the point-cloud would contain significant off-diagonal terms.

A covariance of that size is impractically large. A far more memory-efficient solution would be to conduct a Monte-Carlo evaluation of uncertainty based on the covariance matrix on the system parameters $\boldsymbol{V}_{\theta}$. The algorithm is defined in Algorithm 8, and a graphical representation is given in Figure 8.1.

Algorithm 8 Propagation of uncertainty

Find Cholesky decomposition of $\boldsymbol{V}_\theta = \boldsymbol{C}_\theta \boldsymbol{C}_\theta^{\mathrm{T}}$
For 400 repetitions:
    Generate vector of independently and identically distributed random variables, sampled from $\vec{\boldsymbol{\xi}} \sim \mathcal{N}(0, 1)$
    Generate correlations in random parameter perturbation vector, $C_\theta \vec{\boldsymbol{\xi}}$
    Generate a random parameter vector $\vec{\boldsymbol{\vartheta}} = \vec{\boldsymbol{\theta}} + \vec{\boldsymbol{\xi}}$
    Define a virtual point-cloud $\vec{\boldsymbol{\alpha}} = f_\Delta(\vec{\boldsymbol{u}}_\mathrm{c}, \vec{\boldsymbol{u}}_\mathrm{p}, \vec{\boldsymbol{\vartheta}})$
    Conduct measurement processing on virtual point-cloud $\vec{\boldsymbol{\alpha}}$ and store output
End For
Investigate output for its PDF.

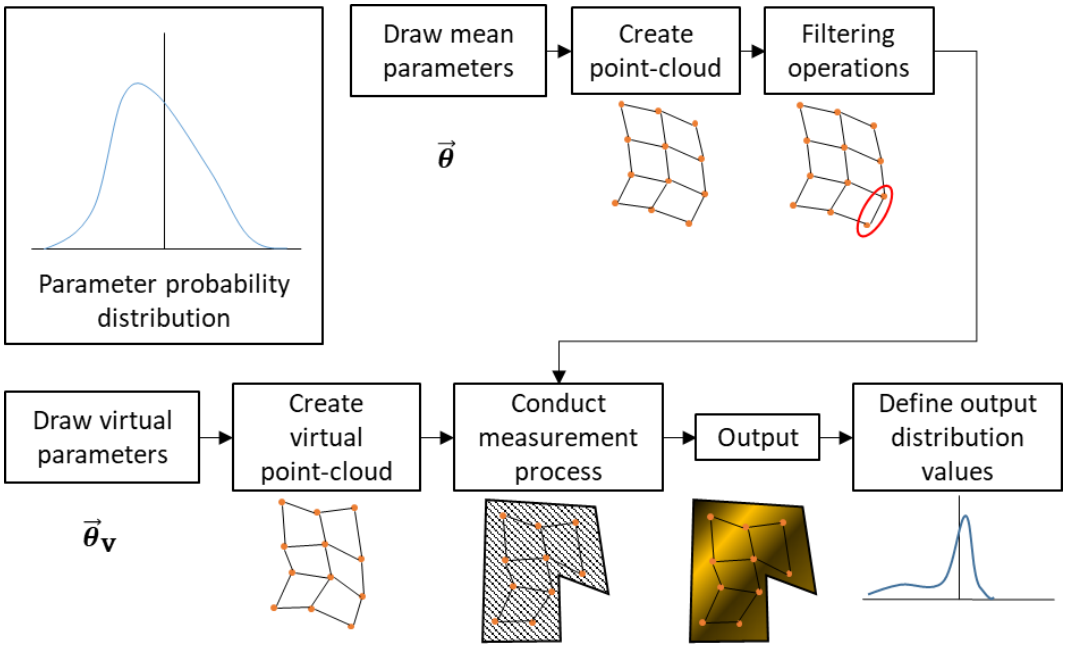

Figure 8.1 Propagation of uncertainty to the final attribute of the point-cloud.

8.2 Flatness artefact

In this section, a measurement of a flatness artefact is made, that will include an uncertainty evaluation using the method provided in Section 8.1 with parameter estimates and uncertainties evaluated using the methods given in Chapter 7 and Chapter 6. The flatness artefact appears in both ISO 10360-13 and VDI/VDE 2634 part 2. A flatness artefact is measured by fitting a plane to the measured point-cloud. The perpendicular distance of each point to the fitted plane is called the flatness deviation. This value can be compared with an

independently measured flatness deviation value, provided by a traceable instrument. A flatness artefact offers many advantages as a measurement artefact for a fringe projection system:

1. The plane is flat so there is no opportunity for long-range multiple reflections.
2. Specular reflection can be avoided by inclining the plane correctly to prevent saturation of CCD pixels.
3. Sub-surface scattering will have little effect on the measurement results, given the lack of high spatial frequencies.
4. The phase map should include no high spatial-frequency components, allowing effective filtering of phase noise from the measurement.
5. The data analysis is simple.

The flat plane artefact has a disadvantage compared to some other measurement artefacts, such as spheres: the measurement result is directly based on the points themselves and not an extracted feature. Any deviation from the best-fit flat plane caused by uncertainty in the system parameters will be additively combined with a phase error that has a higher magnitude than the form error [51, 149]. The correspondence decoding algorithm uses a periodic pattern to establish the link between camera and projector points. It is assumed, therefore, that the range of spatial frequencies in the point-cloud caused by phase error will be limited to approximately the fringe period on the measurement surface. i.e., the form error caused by the system parameters will have much larger spatial frequencies in the measured points compared to the phase error. By averaging over points larger than the fringe period, any phase error should be significantly reduced.

Section 8.2.1 provides information on the flatness artefact itself as well as information on the measurements of the artefact. Section 8.2.2 explicitly defines the evaluation method used to obtain the flatness deviation values. In Section 8.2.3 the accuracy of the parameter estimates is tested. In Section 8.2.4 the validity of the uncertainty of the parameter estimates is tested. Finally, the results of the tests using the flatness artefact are discussed in Section 8.2.5.

8.2.1 Measurement information

The flatness artefact was provided by Trapet. The flat was an aluminium plate with a matte white coating, measured area 308×108 mm, and the deviation from the fitted plane was given as ± 2.6 µm. The area was certified using a total of 121 equally spaced points. The flat plane was measured once in each of the three positions given in Figure 8.2. The relative positions of the flat plane measurements used in the GOM system is shown in Figure 8.3.

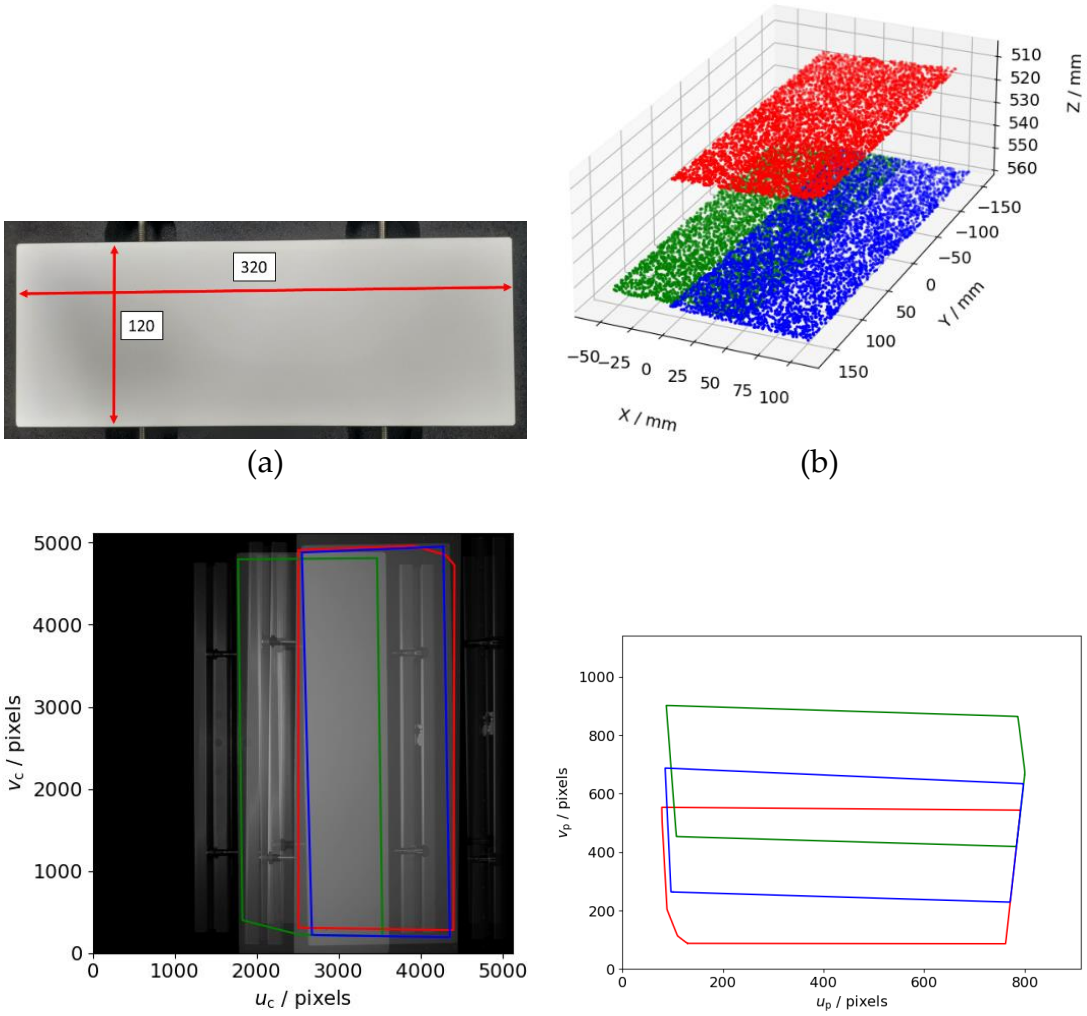

Figure 8.2 Information of the measurements of the flat plane used in the flatness measurements. Measurements are coloured red, green and blue for measurement 1,2 and 3 respectively. (a) The flat plane and its dimensions, (b) the location of each measurement in 3D space, (c-d) the location of each measurement in 2D image space of the camera and projector respectively.

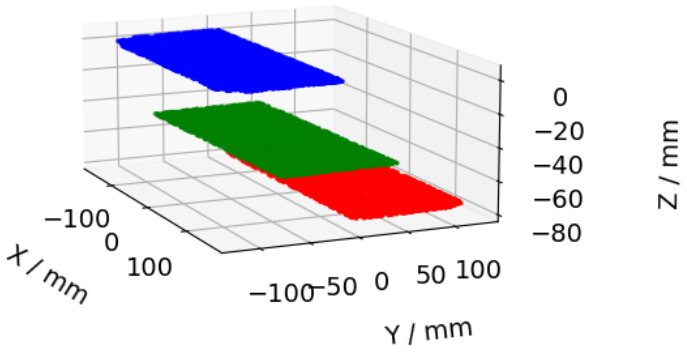

Figure 8.3 Relative locations of the flat plane in the GOM measurements.

8.2.2 Flatness deviation evaluation method

This section will define the method by which the flatness deviation values will obtained when measuring the flatness artefact. Prior to obtaining flatness deviation values, a filtering method is applied that removes high spatial-frequency information and lowers the bandwidth of the measurement. The flat plane is measured within a particular bandwidth of spatial frequencies on a tactile CMS. Fringe projection measurements have higher point density and typically measure a wider bandwidth of spatial frequencies. The flat plane analysis must remove higher spatial frequencies of the measurement to compare with the known measurement of lower bandwidth.

During the measurement, approximately 2×10^6 points were measured of the flatness artefact surface. The clustering method defined here splits the point-cloud into k clusters of points. Each cluster will then be averaged of to produce k pseudo-points that represent the flat plane. In this case, k was chosen to be 1024, which was a compromise between reducing the measurement bandwidth to be comparable with the tactile CMS measurement, and retaining some scale of the form measurement.

For validity, each cluster should be approximately the same size and contain the similar numbers of points. In the measurement of the flatness artefact, the point-cloud points are almost equally spaced. The point-cloud is clustered by repeatedly splitting the point-cloud in half along the two largest principle components to produce successively smaller quarters of the point-cloud. The largest principle component of the point-cloud is found using singular value decomposition (SVD). If the point-cloud is written as

$$\boldsymbol{X}_{N\times 3} = \begin{bmatrix} \vec{\boldsymbol{x}}_1^{\mathrm{T}} \\ \vdots \end{bmatrix} - \bar{\boldsymbol{x}} \tag{8.1}$$

given $\bar{\boldsymbol{x}} = \mathrm{E}(\vec{\boldsymbol{x}}) = \frac{1}{N}\sum \vec{\boldsymbol{x}}_i$. Then $\boldsymbol{X}$ could be decomposed into the form

$$\boldsymbol{U}\boldsymbol{\Sigma}\boldsymbol{V}^{\mathrm{T}} = \boldsymbol{X} \tag{8.2}$$

where both $\boldsymbol{U}$ and $\boldsymbol{V}$ are orthogonal matrices $\boldsymbol{U}^{\mathrm{T}}\boldsymbol{U} = \boldsymbol{V}\boldsymbol{V}^{\mathrm{T}} = \mathbb{I}$ and are orthonormal eigenvectors of $\boldsymbol{C}\boldsymbol{C}^{\mathrm{T}}$ and $\boldsymbol{C}^{\mathrm{T}}\boldsymbol{C}$ [240]. Since $\boldsymbol{C}^{\mathrm{T}}\boldsymbol{C}$ is akin to computing the covariance, the largest eigenvector of $\boldsymbol{C}^{\mathrm{T}}\boldsymbol{C}$ is the vector describing the direction of greatest change – the largest dimension. Given the point-cloud is split using the line $\vec{\boldsymbol{l}} = \lambda\vec{\boldsymbol{\alpha}}$, where $\vec{\boldsymbol{\alpha}}$ is the eigenvector of $\boldsymbol{C}^{\mathrm{T}}\boldsymbol{C}$ corresponding to the largest eigenvalue, each point must be discerned as to which side of the line it lies on, which is found using

$$\text{sign}\left(\frac{x_1 - \alpha_1}{\alpha_2} - \frac{x_2 - \alpha_2}{\alpha_1}\right), \tag{8.3}$$

where the sign operator returns $+1$ if the argument is positive, and -1 if the argument is negative. The SVD clustering algorithm is given in Algorithm 9, and a graphical representation is given in Figure 8.4.

Algorithm 9 SVD-based clustering algorithm used to cluster the flat plane.

Set one cluster to be the full point-cloud $\boldsymbol{X}_0 = \boldsymbol{X}$
For each iteration:
    For each cluster $\boldsymbol{X}_j$:
        If number of points in cluster $\boldsymbol{X}_j$ are less than minimum number:
            Skip this cluster
        End If
        SVD: $\boldsymbol{U\Sigma}\begin{bmatrix}\vec{\boldsymbol{\alpha}}_1 \\ \vec{\boldsymbol{\alpha}}_2\end{bmatrix} = \boldsymbol{X}_j$
        Split $\boldsymbol{X}_j$ into four quadrants using eq. (8.3) and the line equations given by $\vec{\boldsymbol{\alpha}}_1$, $\vec{\boldsymbol{\alpha}}_2$ and the mean of cluster $\boldsymbol{X}_j$, creating four new clusters.
    End For
End For

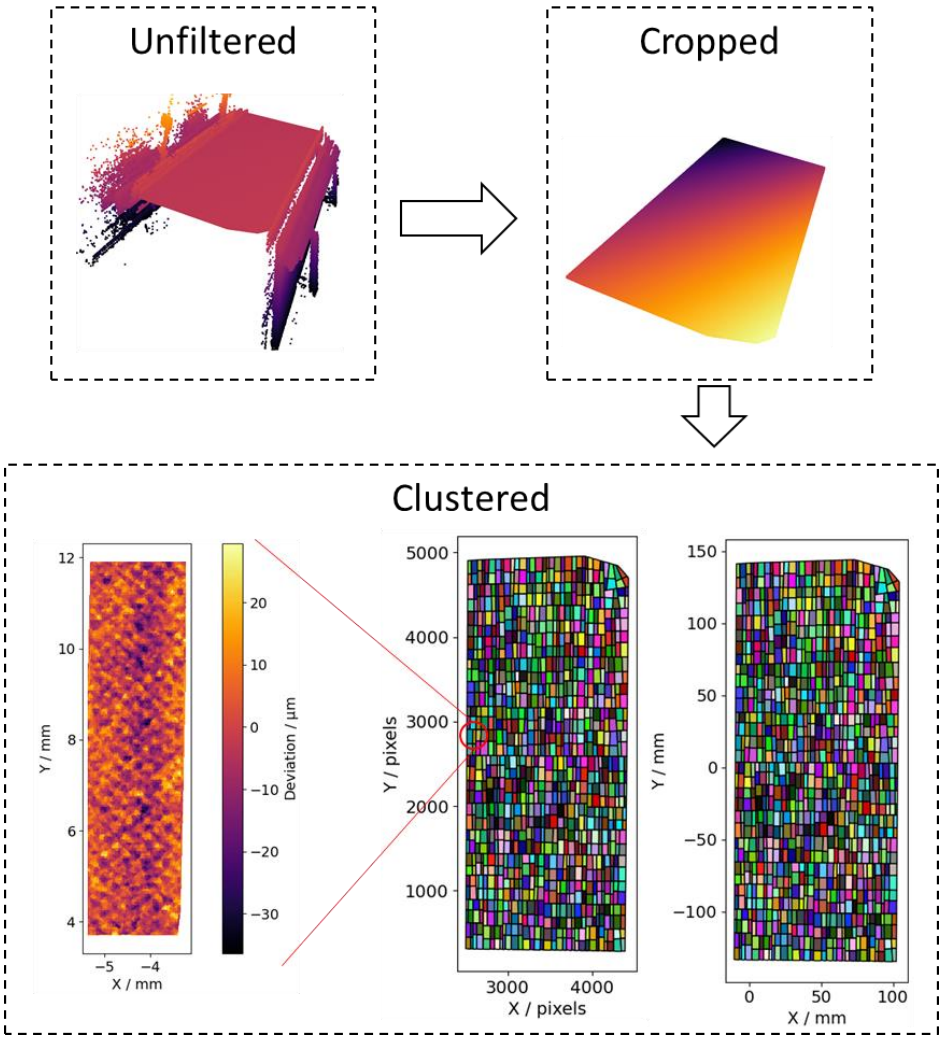

Figure 8.4 Flatness clustering algorithm used to remove phase error noise and lower the bandwidth of the measurement.

8.2.3 Accuracy test

This section will compare the accuracy of a measurement made using parameters obtained from serial, weighted serial, parallel and weighted parallel methods. Additionally, measurements will be compared with a measurement made using parameters obtained using the method stereoCalibrate from OpenCV 4.5.5 [241], and measurements made using the GOM ATOS Core 300. To distinguish between measurements, measurements will be named after the calibration method the system parameters are obtained using. Accuracy will be compared by directly comparing the spread of flatness deviation values obtained. The spread of flatness deviations of each position of the flatness artefact will be shown independently to compare the reproducibility of each measurement. The flatness deviations are shown in Figure 8.5 and Figure 8.6.

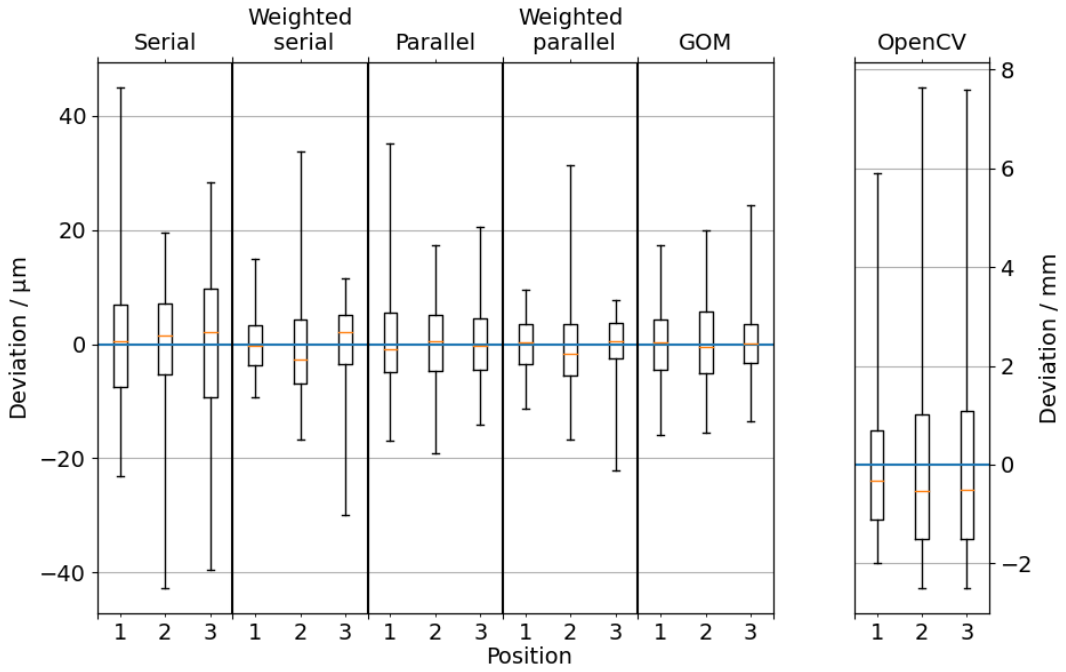

Figure 8.5 Box and whisker plot of the spread of deviations from the fitted plane. The whiskers cover the full range of deviations, while the box shows the interquartile range.

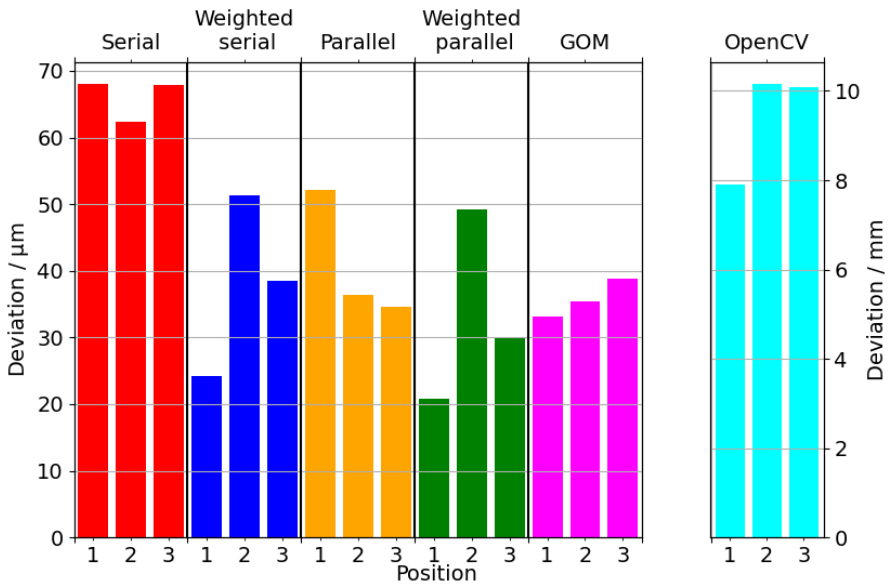

Figure 8.6 Bar plot of the range of deviations from the from the fitted plane.

The weighting matrix has a non-significant effect on the accuracy of the serial calibration method, improving the flatness by two thirds in one case. The weighting brings the serial method to close to the GOM's accuracy. The weighting matrix has a weaker effect on the parallel method, but does improve the flatness deviation by approximately 10 µm in two out of three positions. The accuracy of the weighed parallel method is improved over the GOM in two

instances, but is far less reproducible than the GOM measurements. It is worth noting that unlike the comparison between the serial, weighted serial, parallel, weighted parallel and OpenCV methods, the GOM positions are not the same.

8.2.4 Uncertainty test

This section will test the validity of the estimated parameter values and uncertainties. The propagation of uncertainty will be conducted using 1000 repetitions, which has been chosen as number at which the standard deviation has suitably converged, see Appendix D.

A box and whisker plot of the mean flatness deviation is given in Figure 8.7. The flatness deviations across the flatness artefact are averaged across all repetitions using the two weighted methods and is shown in Figure 8.8. In Figure 8.7, the weighting matrix improves the mean deviation across the measurement volume, reducing the spread of values from the flat plane by approximately a third for two of the positions in both the serial method and the parallel method. Both the serial and weighted serial methods measure the flat plane to a high degree of flatness in one of the three positions.

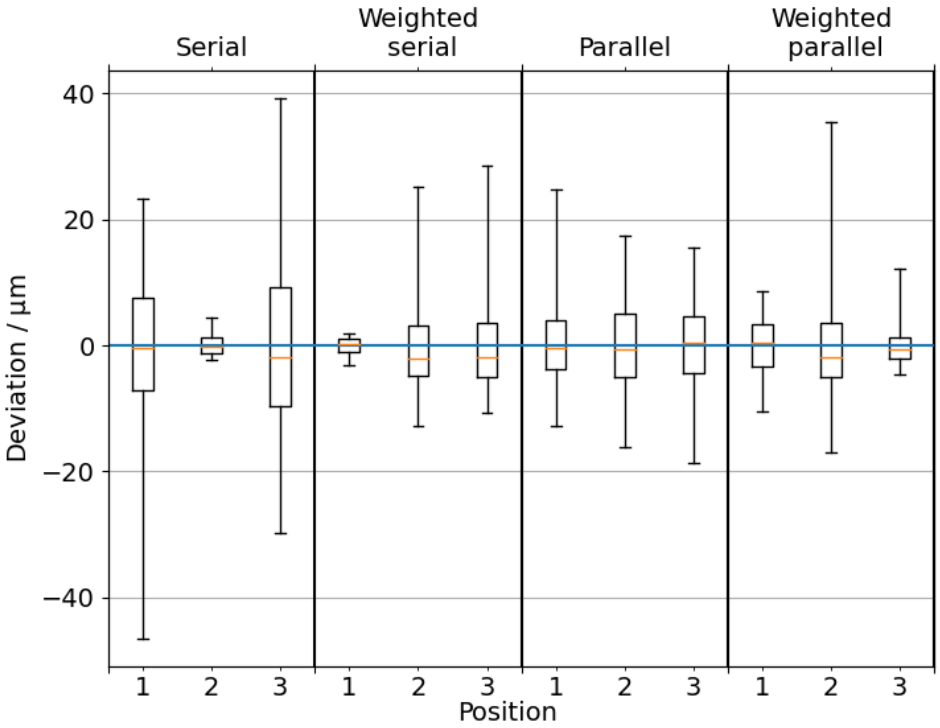

Figure 8.7 Box and whisker of the spread of the mean flatness deviations across all trials.

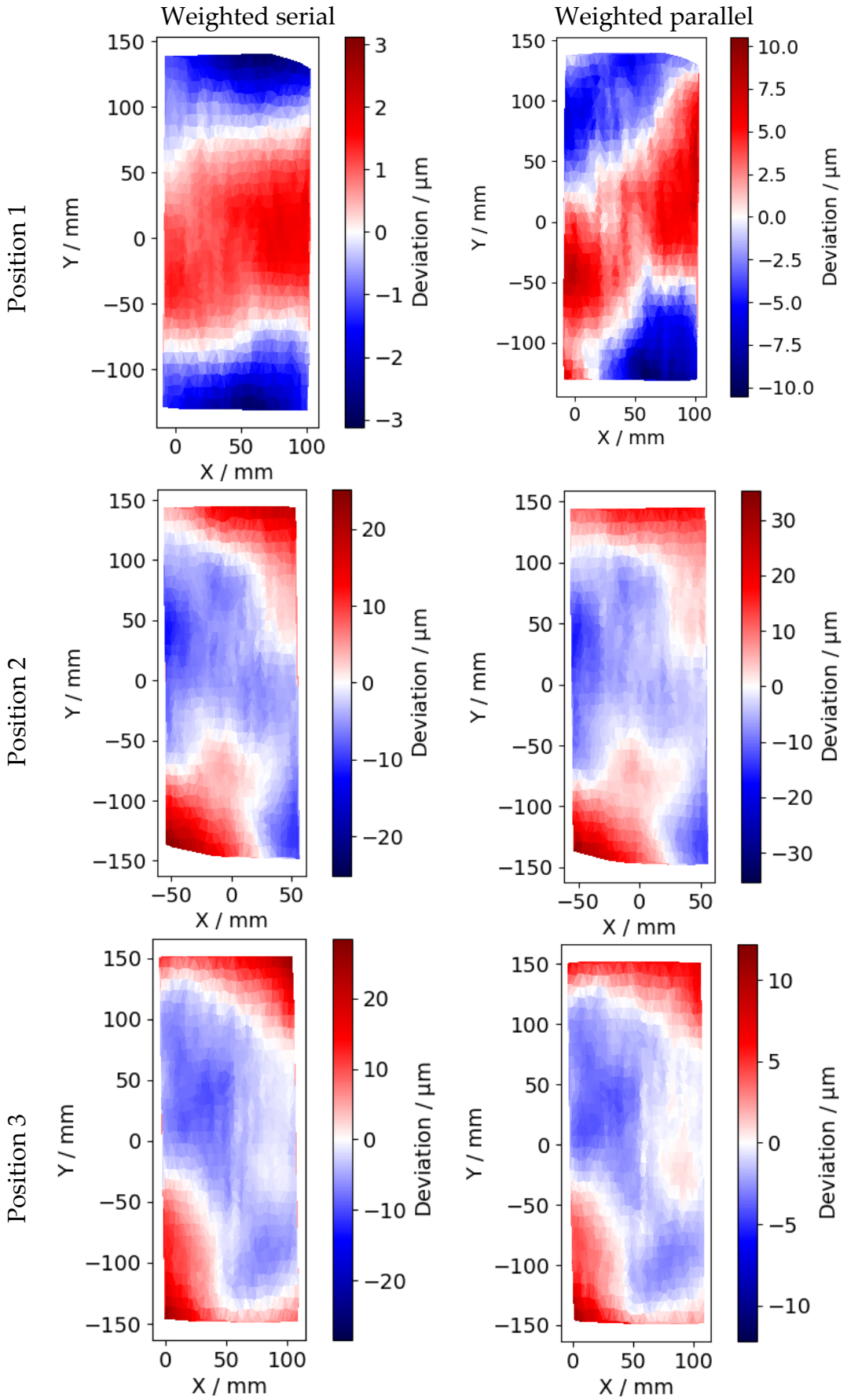

Figure 8.8 Mean deviation of each data point from the substitute best-fit plane across the flat plane from the Monte-Carlo trials.

This next part of this section will display the variability of each pseudo-point across the plane. The distribution of the collective standard distributions of the distance of the pseudo-points from the substitute best-fit plane is given in Figure 8.9. The standard deviation of the distance of each pseudo-point from the substitute best-fit plane is given in Figure 8.10. The uncertainty of the flat plane deviation is unique in each position – given each flat plane measurement covers a unique set of camera-projector coordinates, (u_c, v_c, u_p, v_p). The standard deviation of the distance from the best-fit plane is dependent on the plane position, with no weighted methods sharing a similar uncertainty across the flat plane artefact. Both weighted and unweighted methods share a similar magnitude of uncertainty, but the weighting matrix changes where in the measurement volume the uncertainty is concentrated.

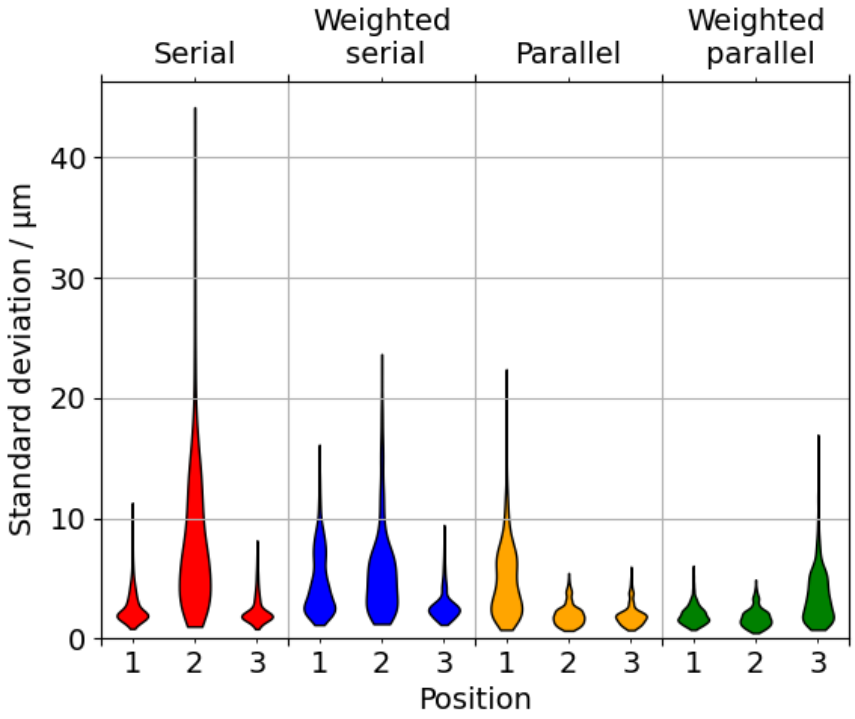

Figure 8.9 Distribution of the standard deviations of the distances of the pseudo-points from the substitute best-fit plane.

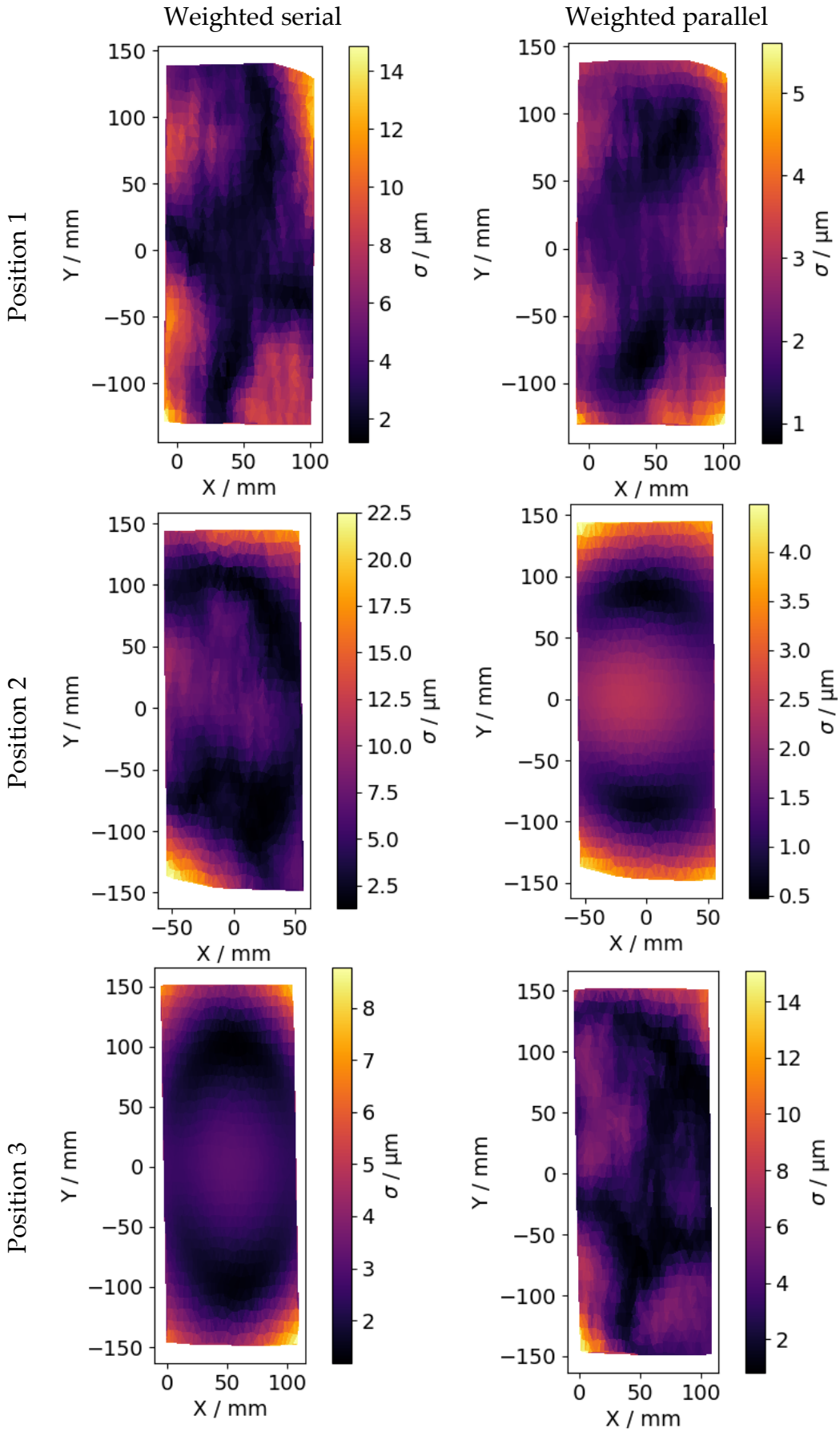

Figure 8.10 Standard deviation of distance of each pseudo-point from the substitute best-fit plane.

The next section tests the validity of the calibration method to provide parameter estimates with uncertainties using the reduced χ^2 test, see Section 4.4. The reduced χ^2 values across the plane are given in Figure 8.12. The collective reduced χ^2 values are given in Figure 8.11. In Figure 8.11, the collective χ^2 results are given for each position and for every position together under "all". The weighted serial method offers the best uncertainty evaluation, given the χ^2 test scores closest to one, or under. The weighting matrix has again improved the uncertainty estimation for both the serial and parallel methods. However, the uncertainty does not satisfactorily cover all positions for any one method.

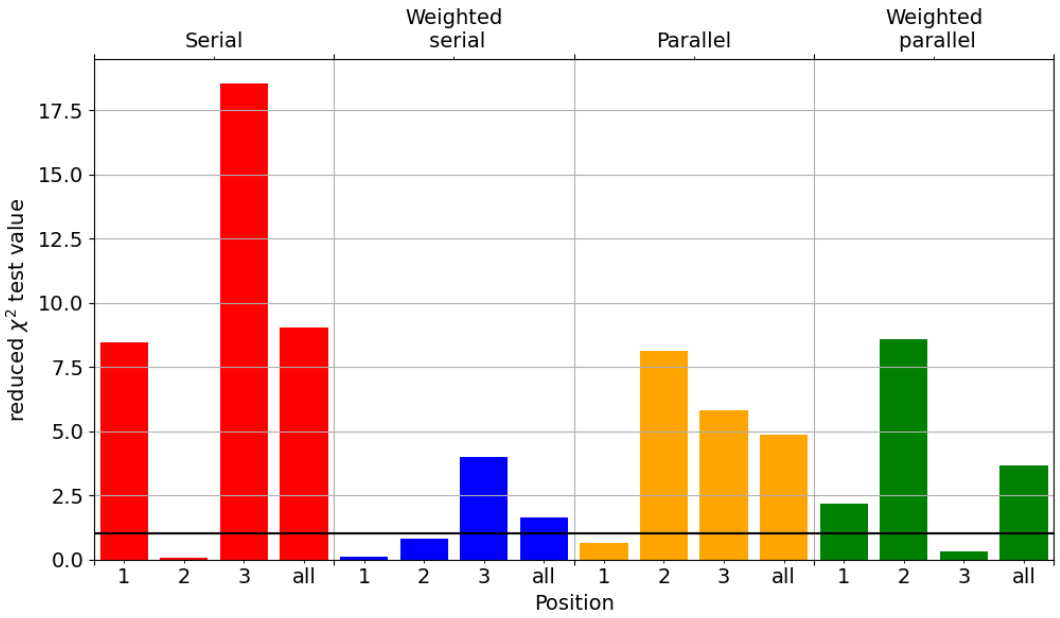

Figure 8.11 Collective reduced χ^2 test results of all pseudo-points.

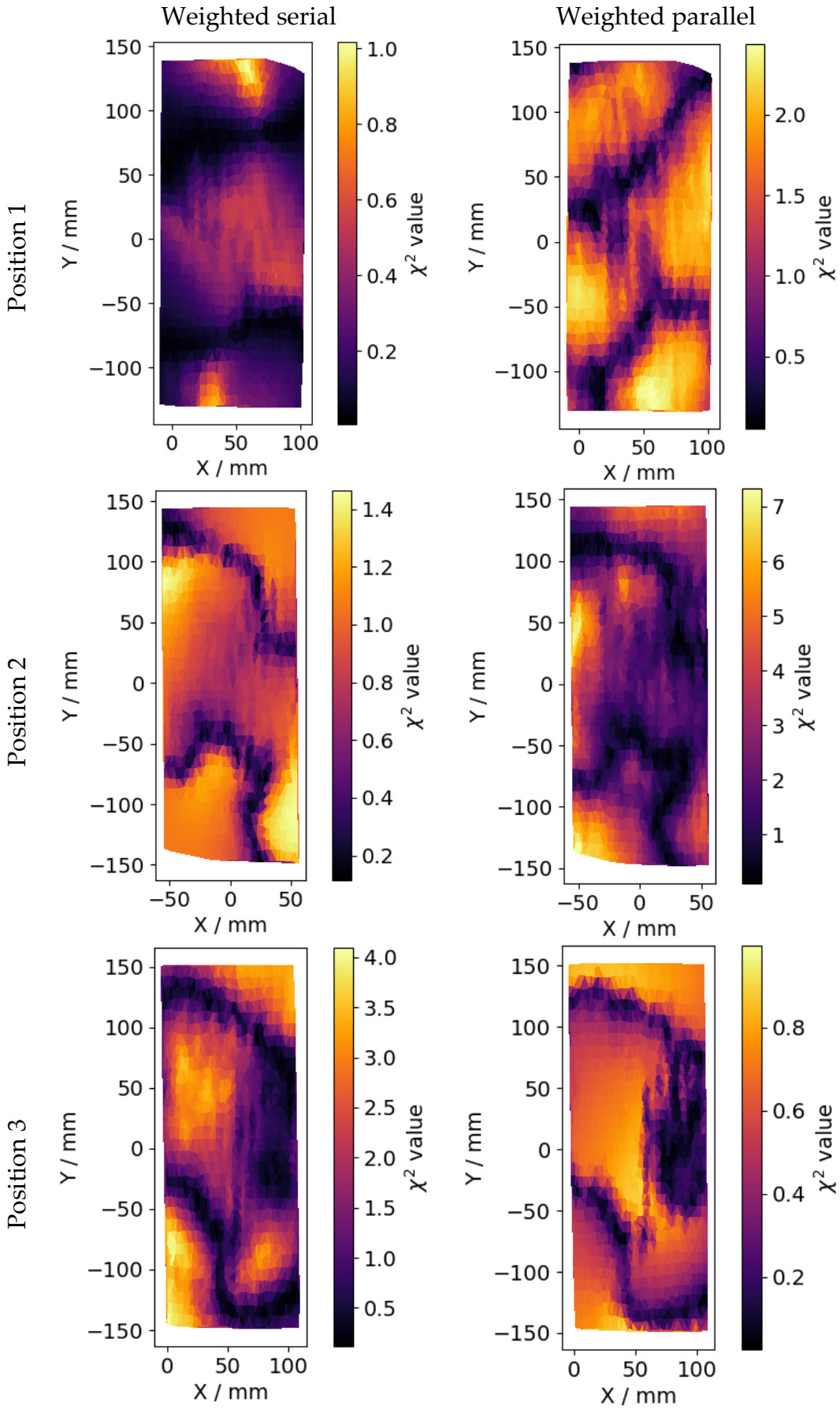

Figure 8.12 Reduced χ^2 test results of each pseudo-point across the plane.

8.2.5 Discussion

The flat plane artefact has failed to validate the parameter estimations and uncertainties obtained using the method of calibration defined in Chapter 7. In Figure 8.6, the accuracy of the parameter estimations are shown to be high: they rival the accuracy of a commercial system, the GOM ATOS Core 300. However, in Figure 8.11 the standard deviation estimated with the calibration method was unable to explain all discrepancies of the measured deviation from flat. Unless the camera and projector are perfectly modelled using the pinhole and distortion models, the models will not be equally applicable across the corresponding image planes. As series of tests were given in Section 7.4 to check the validity of the calibration conditions. Validate conditions included the linearity of local parameter space, stability of parameters and convergence of the problem. However, Section 7.4.5 showed that the weighting matrix overestimated the reprojection errors and in Section 7.4.1 the calibration failed to pass the specificity test given by White [237]. The results of these tests indicate that the pinhole and distortion model is inadequate in modelling a fringe projection system. Therefore, the applicability of the estimated system parameters $\vec{\boldsymbol{\theta}}$ will be dependent on the location of the object in the camera and projector image space, and therefore the position in the measurement volume. In certain portions of the measurement volume, the estimated system parameters correspond well with that location. The weighting matrix has improved the applicability of system parameters across the measurement volume for both methods, but has failed to make the model applicable across the entire measurement volume.

Considering the applicability of the system parameters will differ across the measurement volume (if both the camera and projector is not perfectly described using the pinhole with distortion model), it is possible that many more measurements of the flat plane are necessary to obtain enough statistical significance, and the reduced χ^2 value of every measurement may converge to one. However, if this is true, then this will be in conflict with a basic principle of fringe projection – that a high-density data measurement can be made quickly. In this case, there are fewer reasons to use a fringe projection system over a conventional tactile CMS.

Given the parameter estimates are treated as normally distributed, virtual parameters are sampled symmetrically about the parameter estimate mean value. The differences between the flatness deviation obtained using the mean parameter estimate values (Figure 8.5) and the flatness deviation obtained using the mean of a set of virtual parameter estimate values (Figure 8.7) highlights an asymmetry of the uncertainty problem in fringe projection. The

expected value, i.e., the mean, of flatness deviations is not equal to performing the measurement using the expected values of the parameter estimates. In other words, for measurement outcome $\vec{\boldsymbol{y}}$ and measurement indication $\vec{\boldsymbol{x}}$ with parameters $\vec{\boldsymbol{\theta}}$, the problem is non-linear:

$$\mathbb{E}(\vec{\boldsymbol{y}}) \neq f\left(\vec{\boldsymbol{x}}, \mathbb{E}\left(\vec{\boldsymbol{\theta}}\right)\right). \tag{8.4}$$

8.3 Sphere-based artefacts

Sphere-to-sphere lengths and sphere radii measurements are included in ISO 10360-13 and VDI/VDE 2634 part 2. Unlike flatness artefacts, where the measurement, flatness deviation, is measured from each point to a fitted geometrical shape, sphere measurements are based solely on the fitted geometry. Theoretically, this should provide measurements that are insensitive to phase noise. In this section, two different sphere artefacts will be used. A sphere plate and a sphere dumbbell. The sphere plate consists of 25 spheres fixed to a plate – providing much more information over the sphere dumbbell that consists of only two spheres. However, the sphere plate provides a more difficult measurement scenario and analysis method given the extra information.

Section 8.3.1 and 8.3.2 provide information on the sphere plate and sphere dumbbell artefacts as well as information on the measurements of the artefacts. Section 8.3.3 explicitly defines the evaluation method used to obtain the sphere radii and sphere-to-sphere length values. In Section 8.3.4, the sphere fitting algorithm is tested for bias. In Section 8.3.5 the accuracy of the parameter estimates is tested. In Section 8.3.6 the validity of the uncertainty of the parameter estimates is tested. Finally, the results of the tests using the flatness artefact are discussed in Section 8.3.7.

8.3.1 Sphere plate information

The sphere plate was provided by Taraz metrology and measured in-house. The spheres themselves are polyoxymethylene spheres, each of radius 12.5 mm. The spheres lie in a grid comprised of 40 mm × 40 mm cells. The sphere positions are indicated in Figure 8.13(d). Given there are many spheres and so many possible lengths, a total of twelve sphere-to-sphere distances is given in Figure 8.14, so as not to provide duplicate information.

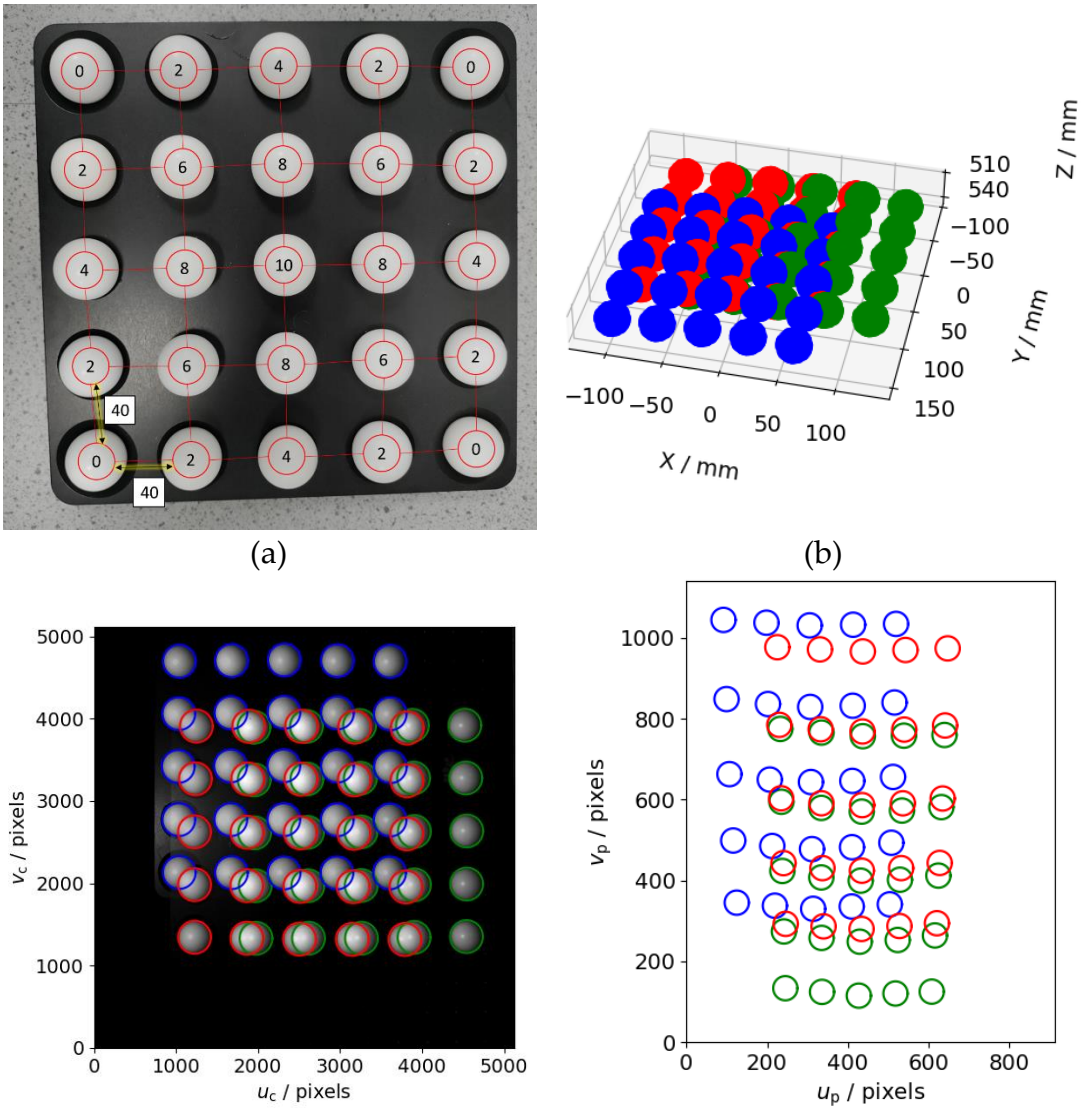

Figure 8.13 Information on the sphere plate used in the sphere-based measurements. (a) An image of the sphere plate, the value within each sphere is its height above the xy plane. (b) The location of the measurements in 3D space. (c-d) The locations of the measurements in the 2D image planes of the camera and projector respectively. Spheres are coloured red, green and blue correspond to the measurements 1,2 and 3 respectively.

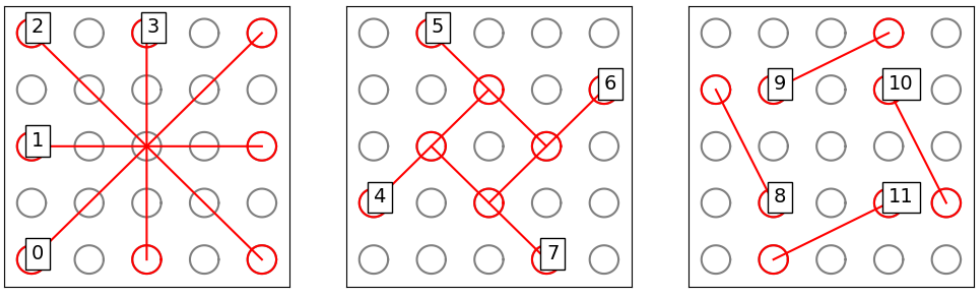

(e)

Figure 8.14 The spheres used for the sphere-to-sphere distances. All sphere radii are 12.5 mm.

8.3.2 Sphere dumbbell information

The dumbbell was provided by Trapet. The sphere-to-sphere distance is 199.946 mm $\pm$ 1 µm and the sphere radii are 10.001 mm and 10.001 mm respectively. The minimum and maximum deviation from the Gaussian substitute sphere is 0.9 µm and 1 µm for the first sphere and 0.6 µm and 0.6 µm for the second sphere. The dumbbell was measured once in each of the six positions shown in Figure 8.15. The relative positions of the dumbbell in the GOM measurements is given in Figure 8.16.

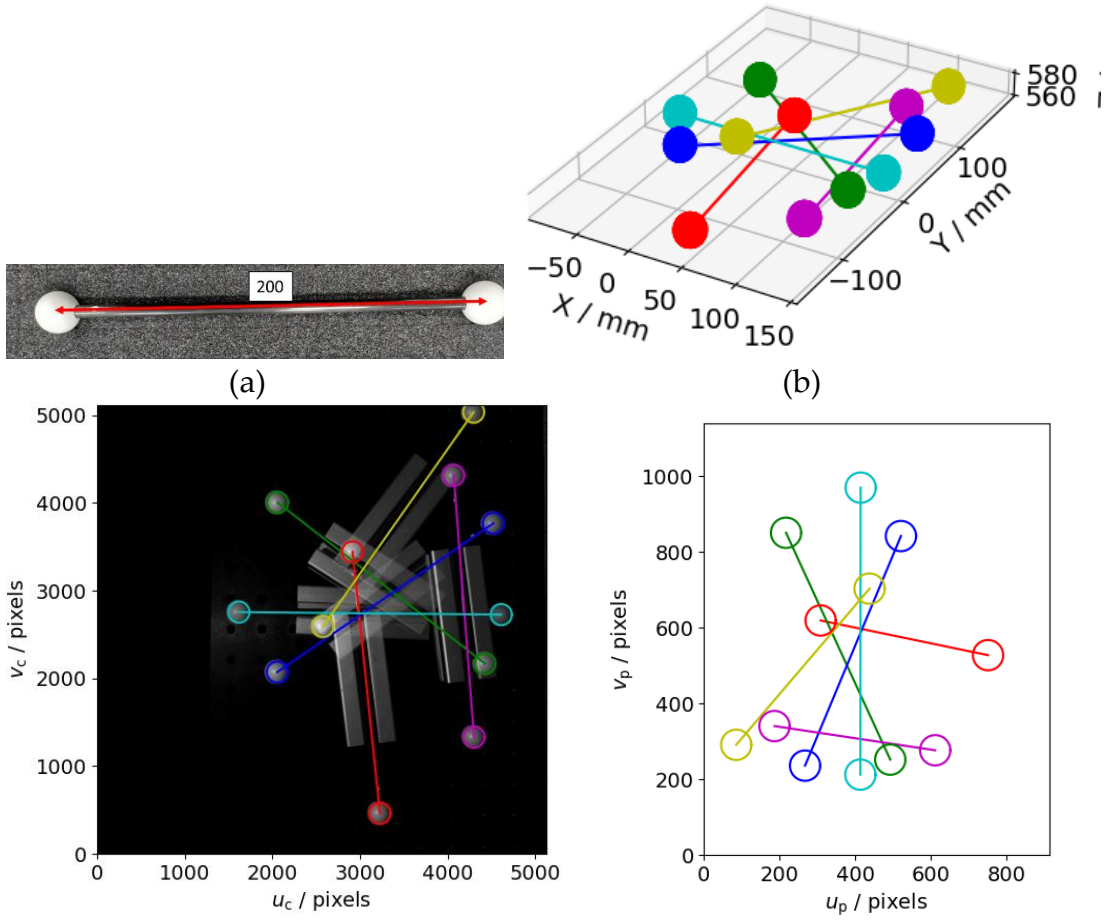

Figure 8.15 Information on the dumbbell measurements. Spheres are coloured red, green, blue, cyan, magenta and yellow correspond to match measurements across the different views. (b) The location of the measurements in 3D space. (c-d) The locations of the measurements in the 2D image planes of the camera and projector respectively.

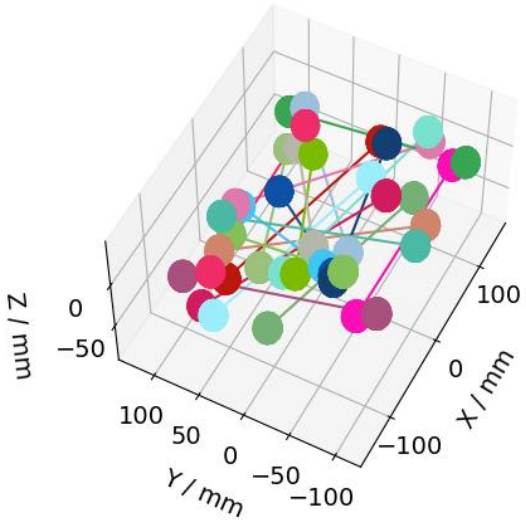

Figure 8.16 Relative positions of the dumbbell in the GOM measurements, with each position given a random colour to show pairs of spheres.

8.3.3 Sphere feature measurement method

This section will detail the sphere feature measurement method completed for sphere-based artefacts. The difference in analysis between the sphere plate and sphere dumbbell is only in the detection and labelling of spheres, which requires more work for the sphere plate given there are many more spheres.

First spheres are identified in the camera image. Sphere identification is based on the contrast difference of the spheres: the spheres themselves are white and the background is dark. The sphere identification is entirely performed on a single globally illuminated image of the spheres. Each sphere will show as a white circle on a black background, and image blob analysis can be used to find all connected pixels within the bright region. The image blob analysis in this thesis is carried out using OpenCV. First, the globally illuminated image is binarized using Otsu's thresholding method [242]. An operator then manually selects an approximate location for each sphere which is used to identify blobs as spheres. All other pixels not belonging to a sphere are removed. Additionally, an operator then labels spheres based on a fiducial that is in the camera image.

Next, using the labelled and cropped sphere pixels, the three-dimensional (3D) points are triangulated. Each sphere is treated as a separate point-cloud and a density-based filtering method [28] is used to select the largest connected group of points – which will define all the points belonging to a specific sphere. Given each point is derived from a single pixel in the camera image, each pixel can be labelled according to what sphere the pixel is viewing, and therefore each virtual point-cloud generated when propagating uncertainty only needs to generate labelled pixels. The graphical representation of the algorithm is in Algorithm 10.

Algorithm 10 Sphere identification, labelling and cleaning.

```
Threshold the image using Otsu's thresholding method
Arrange all the bright pixels into groups of connected bright pixels using blob analysis
Manually select which blobs belong to a sphere
Remove all pixels not belonging to a sphere
For each sphere:
    Triangulate into the corresponding 3D points
    Use density-based filtering to find the largest body of connected points
    Remove all other points
End For
```

Once cleaned and labelled, sphere geometries are fit to the individual sets of point-clouds containing each sphere only. There is a well-known bias in the least-square fitting of spheres. Therefore, the sphere-fitting algorithm given in Al-Sharadqah and Chernov [243] that gives a hyper-accurate fitting will be used. This algorithm is tested in Section 8.3.4.

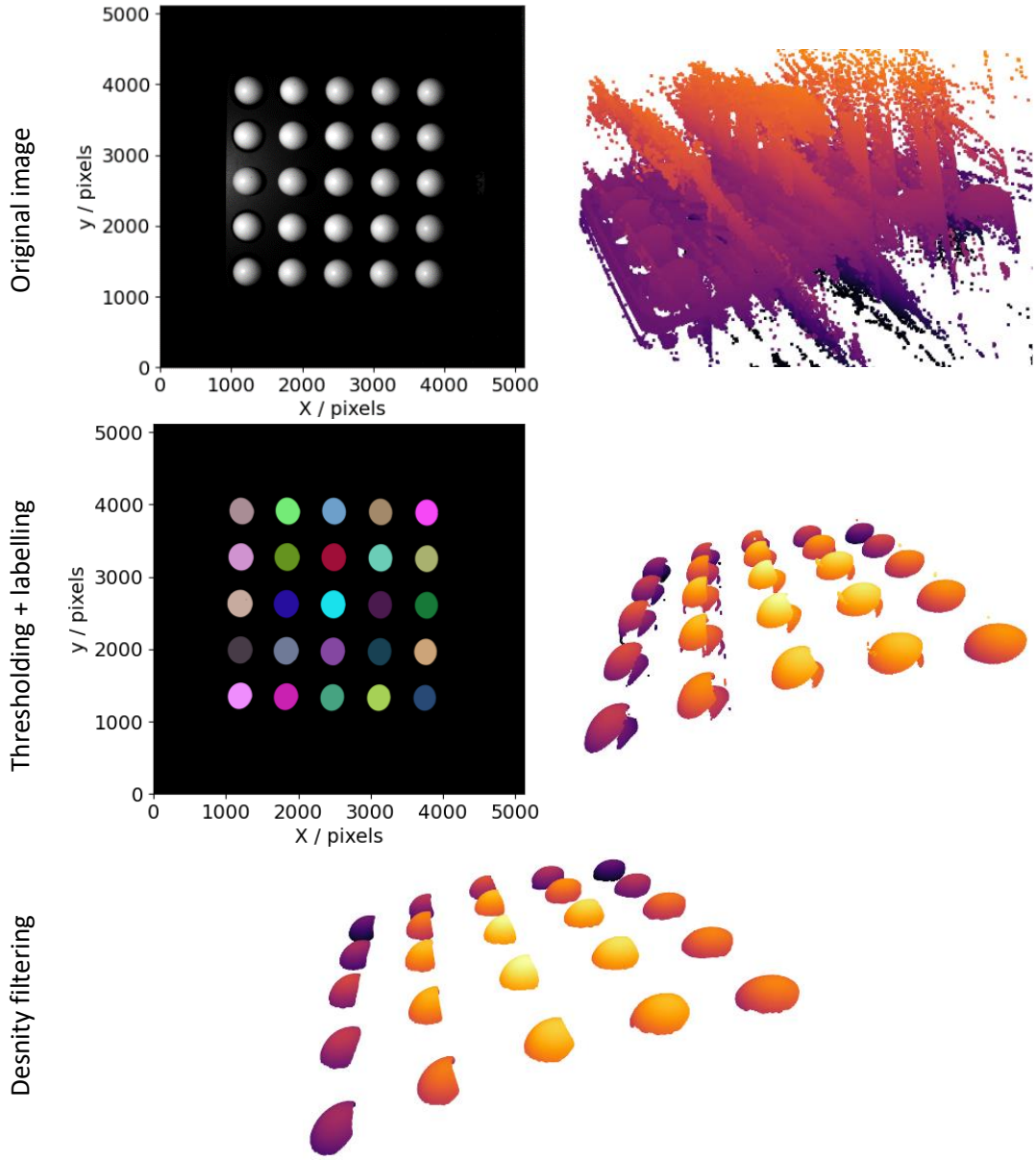

Figure 8.17 Sphere identification and cleaning algorithm used to prepare the sphere for the sphere fitting.

8.3.4 Sphere fitting test

In this section, a test is performed on the sphere-fitting algorithm provided in Al-Sharadqah and Chernov [243] to test for validity. An issue with fringe projection systems is that mapping the entire surface of the sphere in one go is not possible, only the portion of the sphere that is in the line of sight to both the camera and the projector can be measured. Even then, high slope angles must be removed due to the unacceptable noise levels, so practically only approximately 40% of the sphere surface can be mapped.

Additionally, in fringe projection the dominant error is the phase error. The phase error acts along direction of the ray vector of the camera since the phase

error is the error in the correspondence of the projector image. The sphere is particularly ill-defined in the depth axis because there are little points in this axis and therefore the uncertainty is the highest here.

To test the algorithm, a virtual sphere will be generated, where a virtual sphere is just a point-cloud generated from a sphere geometry. The point-cloud is then used in the sphere-fitting algorithm, and the parameters sphere location and radius are compared with known values to test the validity of the sphere fitting method. To simulate a fringe projection measurement, only a portion of the sphere will be generated, which will be referred to as the "sphere cap". For each trial of the test, N points of random sphere cap are created, where the sphere is defined with radius r, sphere cap angle θ and the points are perturbed by some additive Gaussian error defined with a standard deviation σ, shown in Figure 8.18.

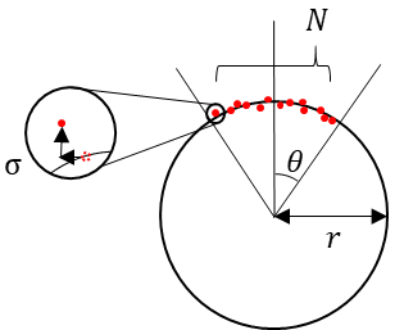

Figure 8.18 Random sphere cap made of N points. Each sphere is defined by its sphere radius r, the measurement area angle θ, and an additive Gaussian error of mean 0 and standard deviation σ.

The values for r, θ, σ, N are drawn from the uniform distributions, given in Table 8.1.

Table 8.1 Distribution of the input values used for the Monte-Carlo testing of the sphere-fitting algorithm.

Value	Distribution
r	$\mathcal{U}(9.5,12.5)$
θ	$\mathcal{U}(0.6,1.4)$
σ	$\mathcal{U}(3 \times 10^5, 7 \times 10^5)$
N	$\mathcal{U}(0.03,0.07)$

The results of the Monte-Carlo trials of the sphere fitting is shown in Figure 8.19.

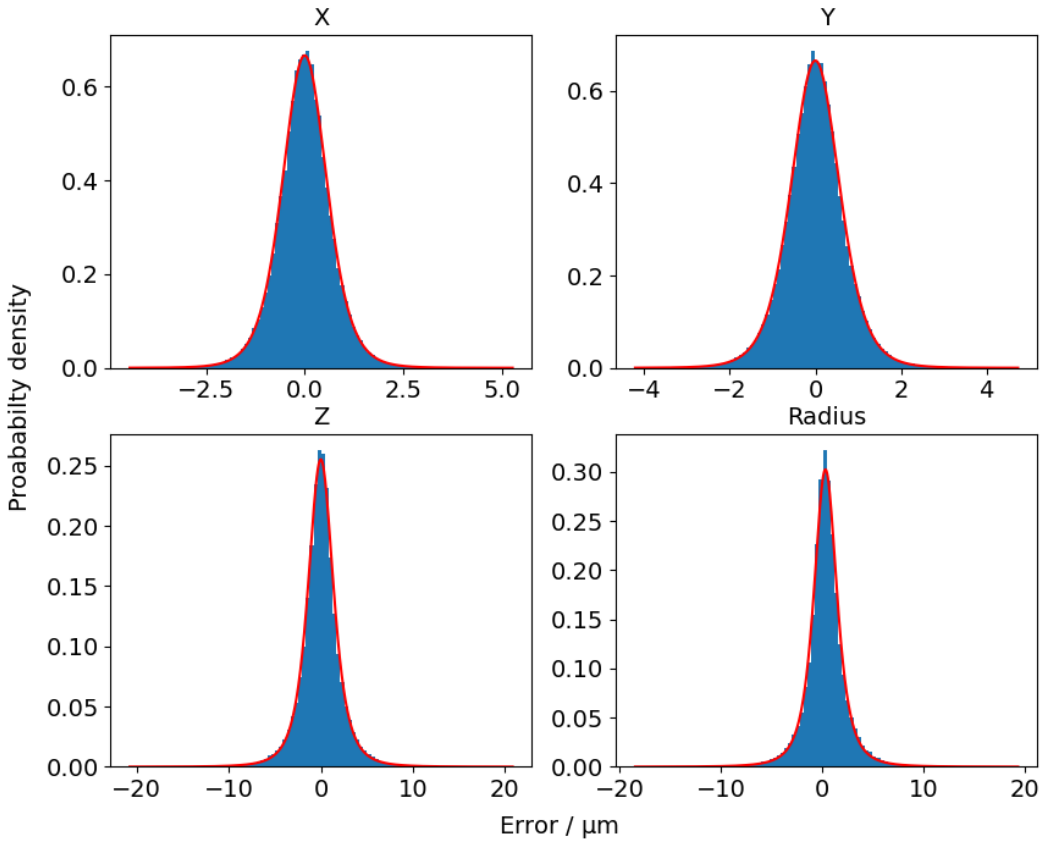

Figure 8.19 Histogram of the errors of the sphere fitting test (blue), with an overlaid fitted Student's t distribution (red).

The sphere fitting test shows significant uncertainty in the position and radius parameters when considering a noisy measurement of a limited portion of a sphere. When considering future measurements of a sphere, the uncertainty in the sphere location caused by the uncertainty in the sphere fitting must be considered. The covariance matrix that will be used within future sphere fitting processes will be

$$\begin{bmatrix} 0.5 & 0 & 0.041 & -0.003 \\ 0 & 0.5 & 0.007 & -0.007 \\ 0.041 & 0.007 & 5 & -4.4 \\ -0.003 & -0.007 & -4.4 & 4 \end{bmatrix}$$

Furthermore, the mean of the errors are -0.002 ± 0.004 µm, -0.001 ± 0.004 µm, 0.001 ± 0.014 µm and -0.36 ± 0.012 µm for the (x, y, z, r), with uncertainties given as the 95% confidence interval found using

$$u(x) = \frac{\sigma}{\sqrt{n}}. \tag{8.5}$$

There is some statistically significant systematic error in the sphere-fitting algorithm given in Al-Sharadqah and Chernov [243] that must be accounted for in any future uncertainty estimations.

8.3.5 Accuracy test

In this section, the accuracy of the estimated parameters will be tested by performing a single measurement using the mean parameter estimate. The sphere radii measurements of the sphere plate are given in Figure 8.20, and the sphere radii measurements of the sphere dumbbell are given in Figure 8.21. Unlike the flatness measurements where every position was treated individually, here the repeated measurements of the sphere radii are treated as a single reproduced measurement. The error bars on Figure 8.20 and Figure 8.21 are a 2σ uncertainty obtained from the spread of values of the reproduced measurements.

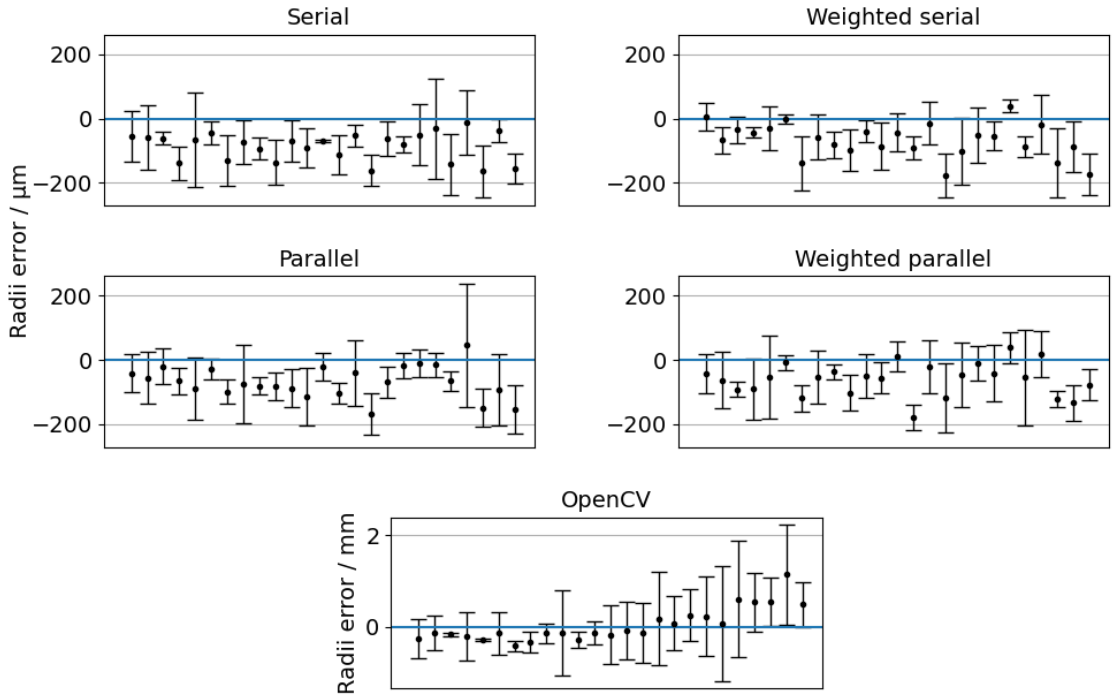

Figure 8.20 Error of the sphere radii measurements for the sphere plate. Each datapoint gives the mean value along with a 95% confidence interval.

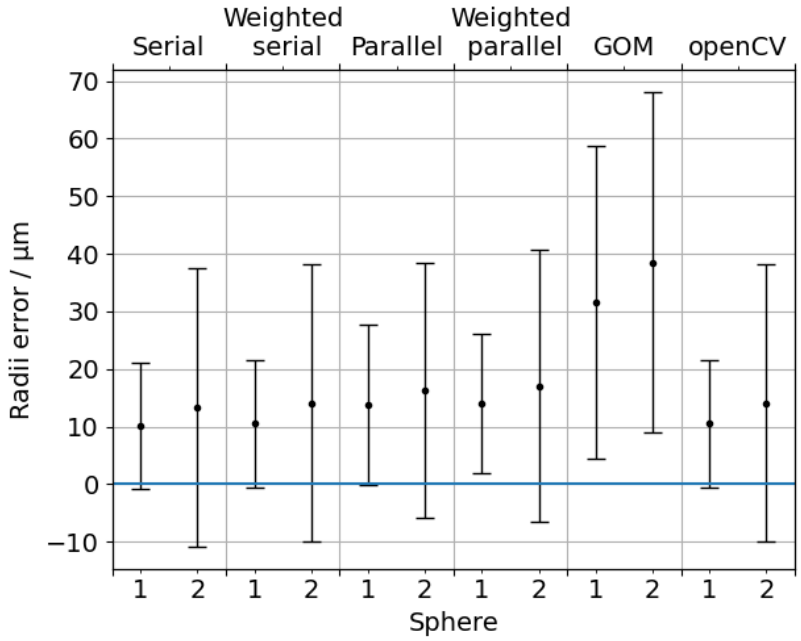

Figure 8.21 Error of the sphere radii measurements for the sphere dumbbells. Each datapoint gives the mean value along with a 95% confidence interval.

The weighting matrix has had very little effect on the measurement of the sphere radii. All methods seem to behave equally poorly when measuring the dumbbells, although the OpenCV parameters have made poor measurements of the sphere plate radii of the sphere plate only.

The sphere-to-sphere lengths of sphere plate and the sphere dumbbell is given in Figure 8.22 and Figure 8.23. The measurements are again treated as reproduced measurements, and the error bars included here are 2σ uncertainty obtained from the reproduced measurement.

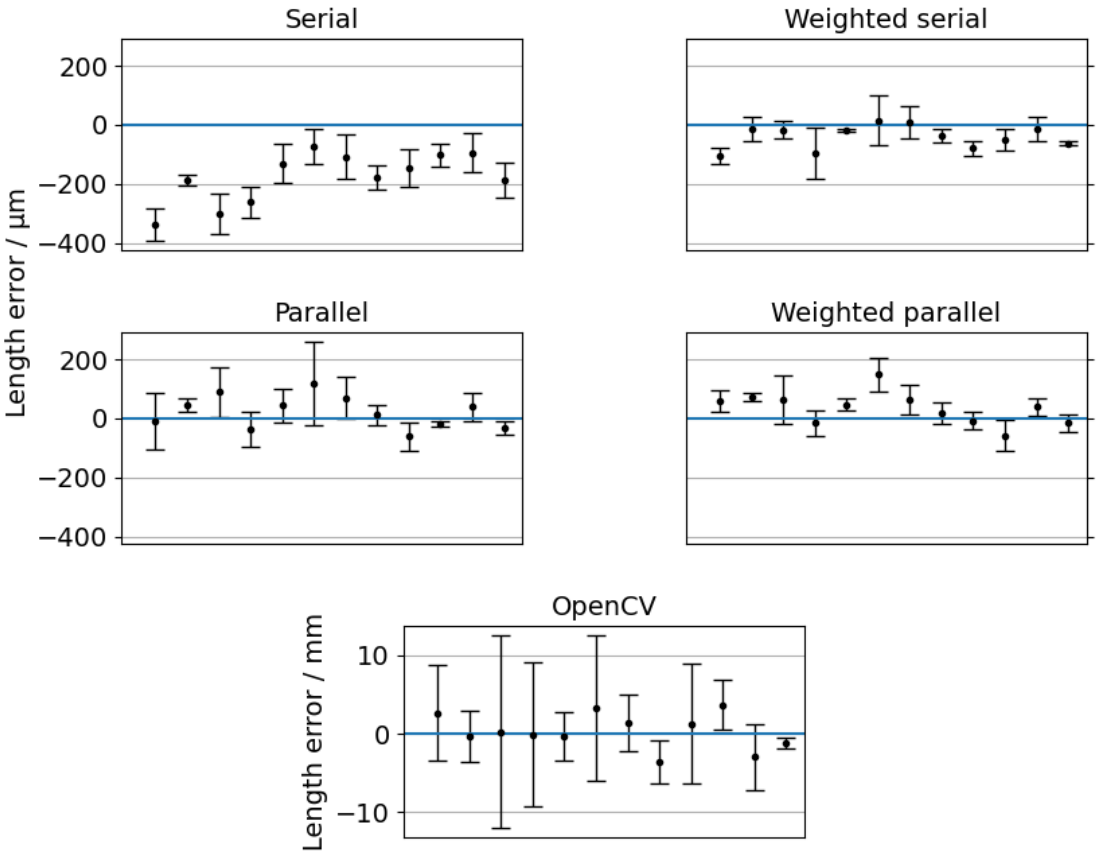

Figure 8.22 Errors in the sphere-to-sphere length measurements of the sphere plate according to the configuration specified in Figure 8.14. The GOM system was unable to measure the sphere plate and so is not included. Each datapoint gives the mean value along with a 95% confidence interval.

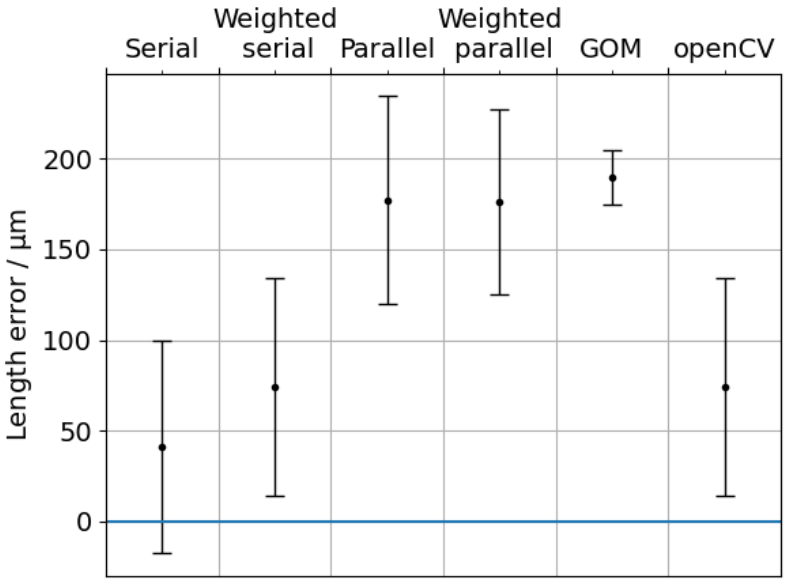

Figure 8.23 Errors in the sphere-to-sphere length measurements of the sphere dumbbell artefact. Each datapoint gives the mean value along with a 95% confidence interval.

The weighting matrix produces no conclusive effect on the measurement result. Concerning the sphere plate, the weighting matrix improves the mean result of the serial method, but reproducing the measurement does not account for the discrepancy in the measurement. The weighting matrix does not improve the parallel method results. The weighting matrix has no discernible impact on the length error for any method. The OpenCV parameters performs very poorly on the sphere plate, but outperforms the parallel method and GOM ATOS Core 300 results – in direct conflict with the results of the sphere plate results and the flat plate results.

8.3.6 Uncertainty test

In this section, the validity of the parameter estimates, and uncertainty will be tested using the sphere-based artefacts. Both the sphere plate and the sphere dumbbells will be used. The test using the sphere plate artefact was completed using 2000 repetitions, and the test using the sphere dumbbell was completed using 1000 repetitions. The sphere plate typically too more repetitions to converge, see Appendix D. Each sphere is treated as a unique sphere if in a unique position. The confidence intervals and mean values shown here are found by propagating uncertainty from the estimated system parameters, see Section 8.1. First the sphere radii error will be shown for both artefacts. Figure 8.24 shows the sphere radii error for the sphere plate artefact, and Figure 8.25 shows the sphere radii error for the sphere dumbbell artefact. In both Figure 8.24 and Figure 8.25, the sphere radii error is shown along with a 95%

confidence interval for each sphere. In Figure 8.24, the mean dot is removed for clarity to see the exact height of the confidence intervals.

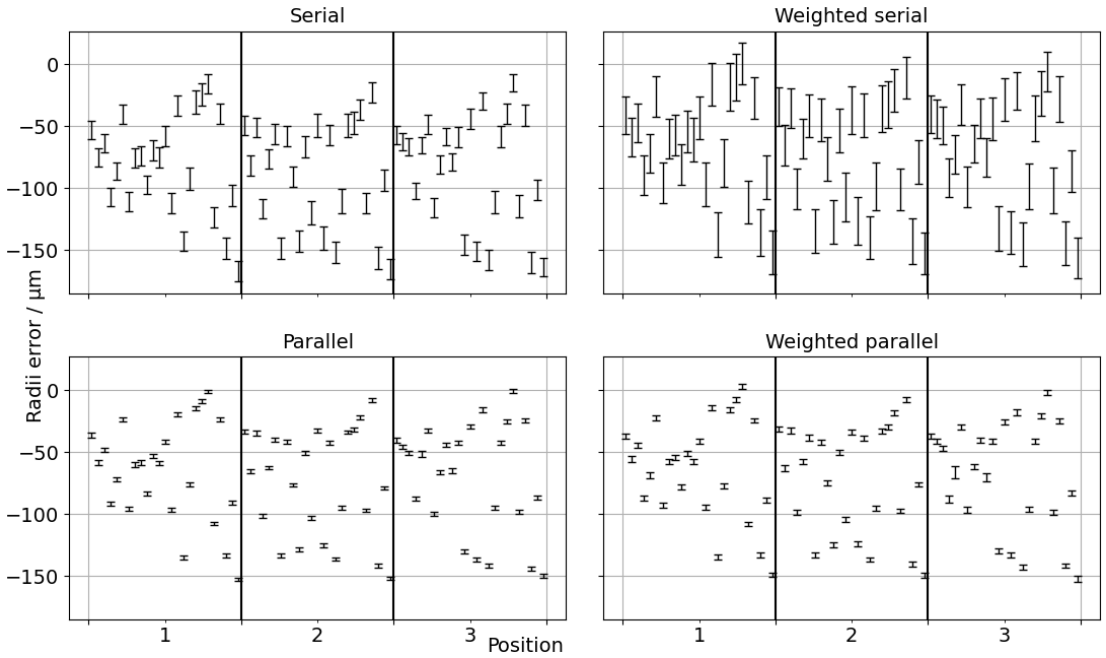

Figure 8.24 Sphere radii error of each unique sphere using the sphere plate artefact along with a 95% confidence interval.

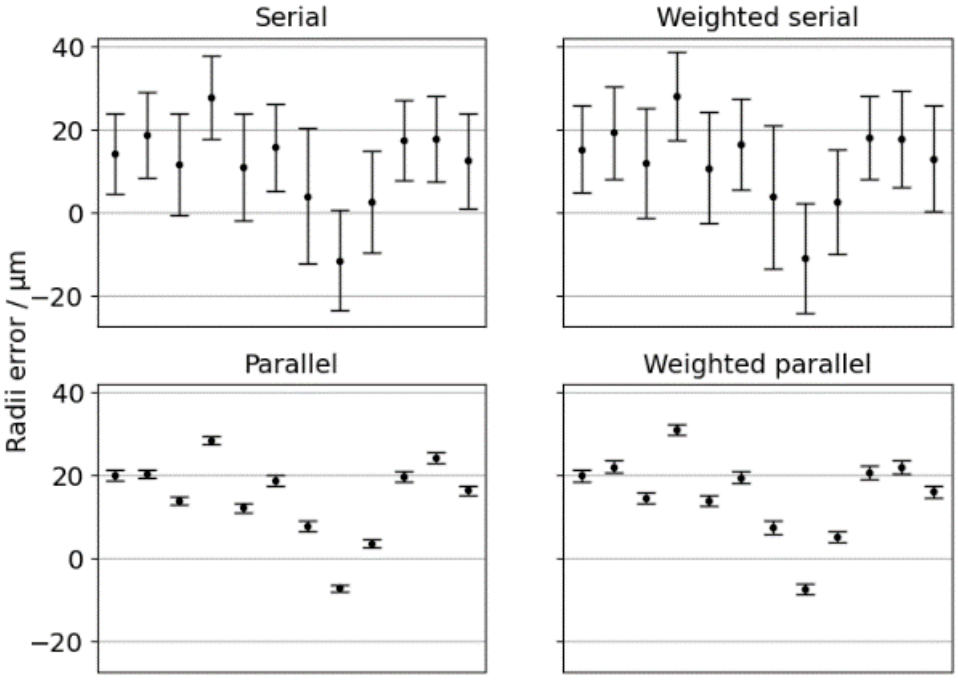

Figure 8.25 Sphere radii error of each unique sphere using the sphere dumbbell artefact along with a 95% confidence interval.

Both tests fail to validate the parameter estimates and their uncertainties. All parameters are consistently underestimating the sphere radii of the sphere plates by a considerable margin, while tending to overestimate the sphere radii or the spheres on the sphere dumbbell artefact. The weighting matrix only seems to change the confidence interval of the serial method. To discern any dependency of sphere radii error to measurement volume position, Figure 8.26 shows the sphere radii error graphically at the position of the sphere in the measurement volume. Figure 8.26 does not show any correlation between sphere radii error and position in the measurement volume.

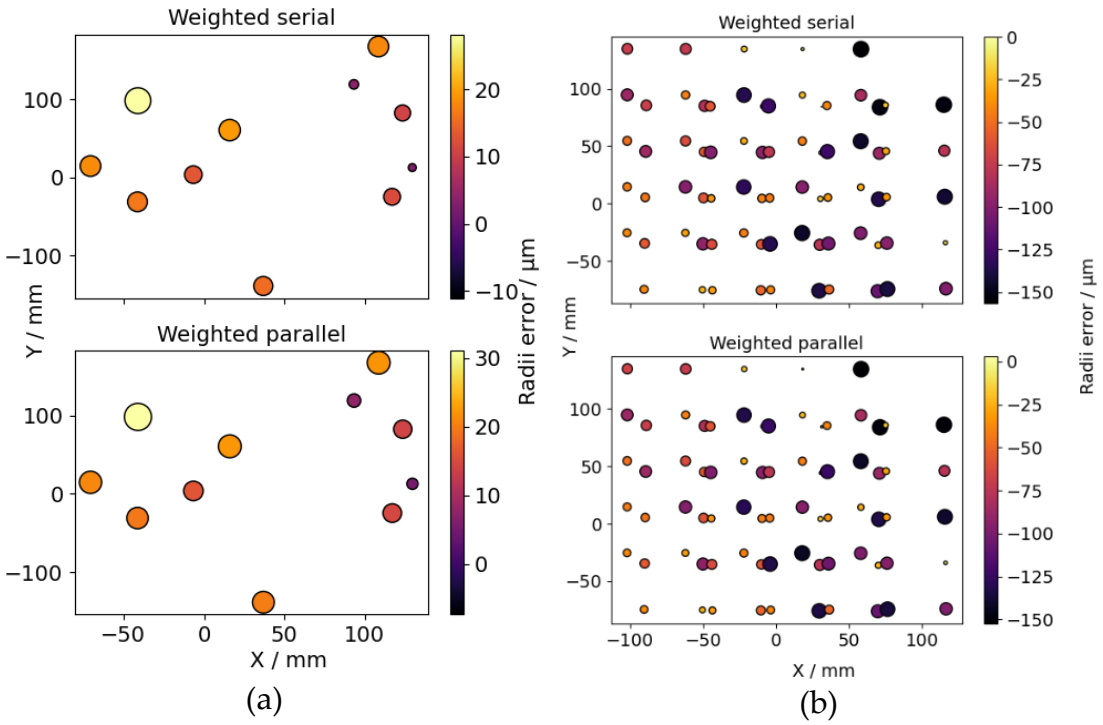

Figure 8.26 The mean sphere radii error obtained from the set of virtual point-clouds shown at its measurement location.(a) The sphere radii error of the sphere dumbbell artefact. (b) The sphere radii error of the sphere plate artefact.

The error in the sphere-to-sphere length along with the positions is given in Figure 8.28(a-b), and the sphere radii error mean with a 95% confidence interval, calculated from the Monte-Carlo trials, is given in Figure 8.28(c-d). Instead of using the prescribed lengths to test the sphere plate measurement, the sphere plate positions will be tested by estimating the position and orientation of the sphere plate.

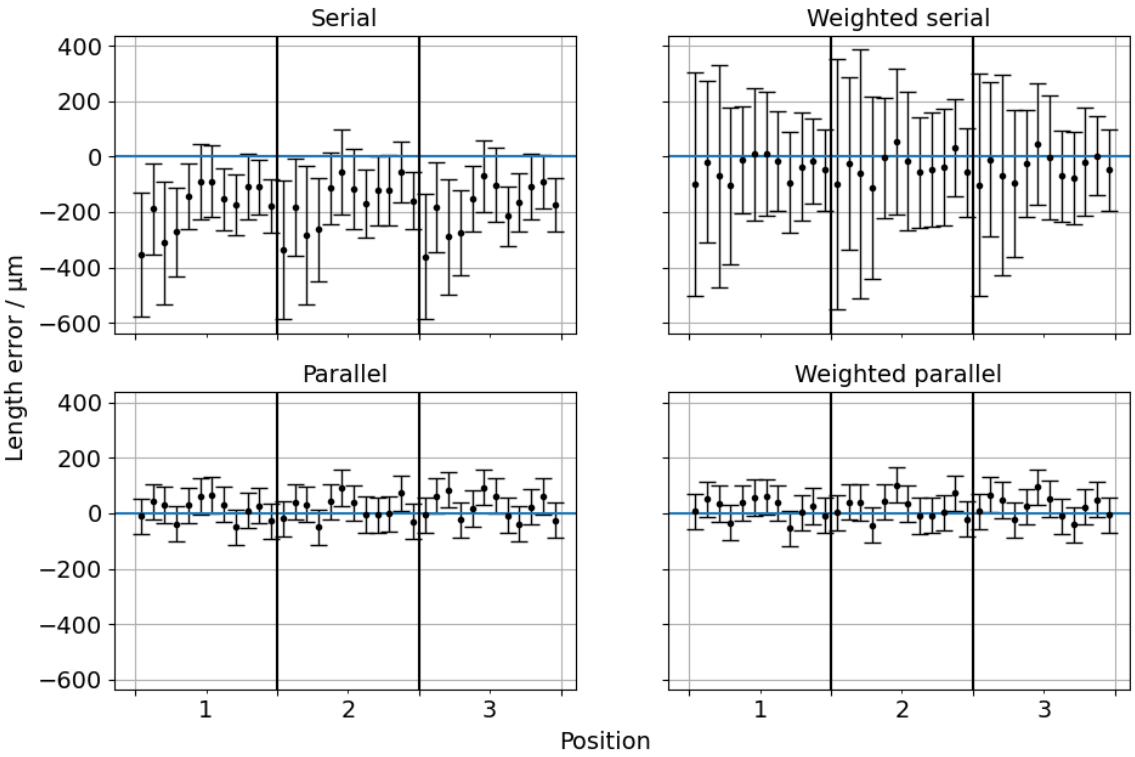

Figure 8.27 The mean sphere-to-sphere lengths of the sphere plate artefact using the configuration given in Figure 8.14. All measurements are given with a 95% confidence interval.

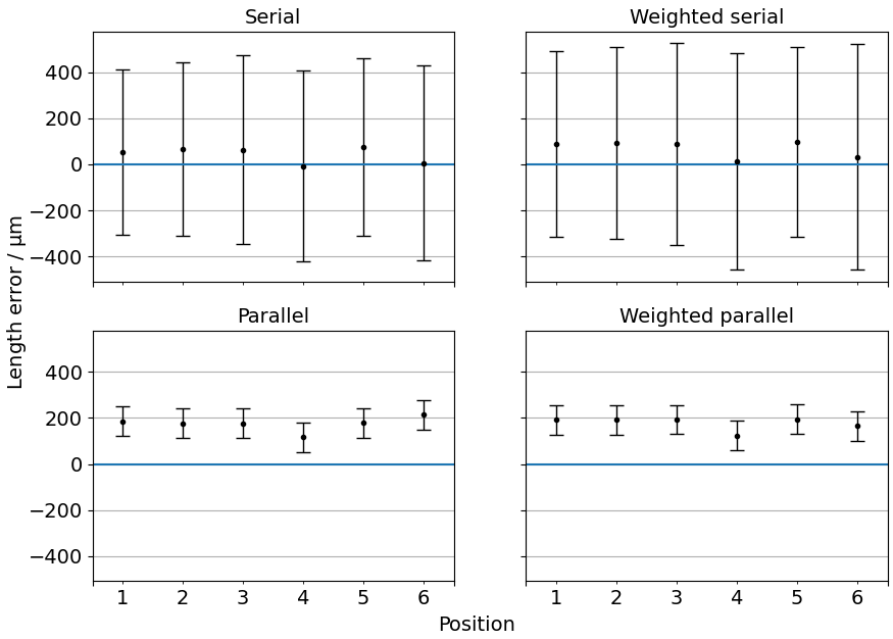

Figure 8.28 The mean sphere-to-sphere lengths of the sphere dumbbell artefact. All measurements are given with a 95% confidence interval.

The variability of the length measurement errors is very high across all measurements. The confidence interval of the weighted serial method covers

the discrepancy in both the sphere plate and sphere dumbbell artefact, but the uncertainty is overestimated. The confidence interval of the parallel methods does not consistently cover the measurement discrepancy. The weighting matrix does improve the serial method measurements for the sphere plate, but this does not agree with measurements of the sphere dumbbell artefact. The weighting matrix has no discernible effect on the measurements of the sphere dumbbell artefact. To identify any dependency on an individual sphere, the mean errors of the position of each sphere in the sphere plate is shown for each measurement in Figure 8.29. Each sphere is shown as distance from nominal, magnified 100× times. A 95% confidence interval is shown in blue. The mean sphere-to-sphere length error of each sphere dumbbell measurement along its position in the measurement volume is shown in Figure 8.30.

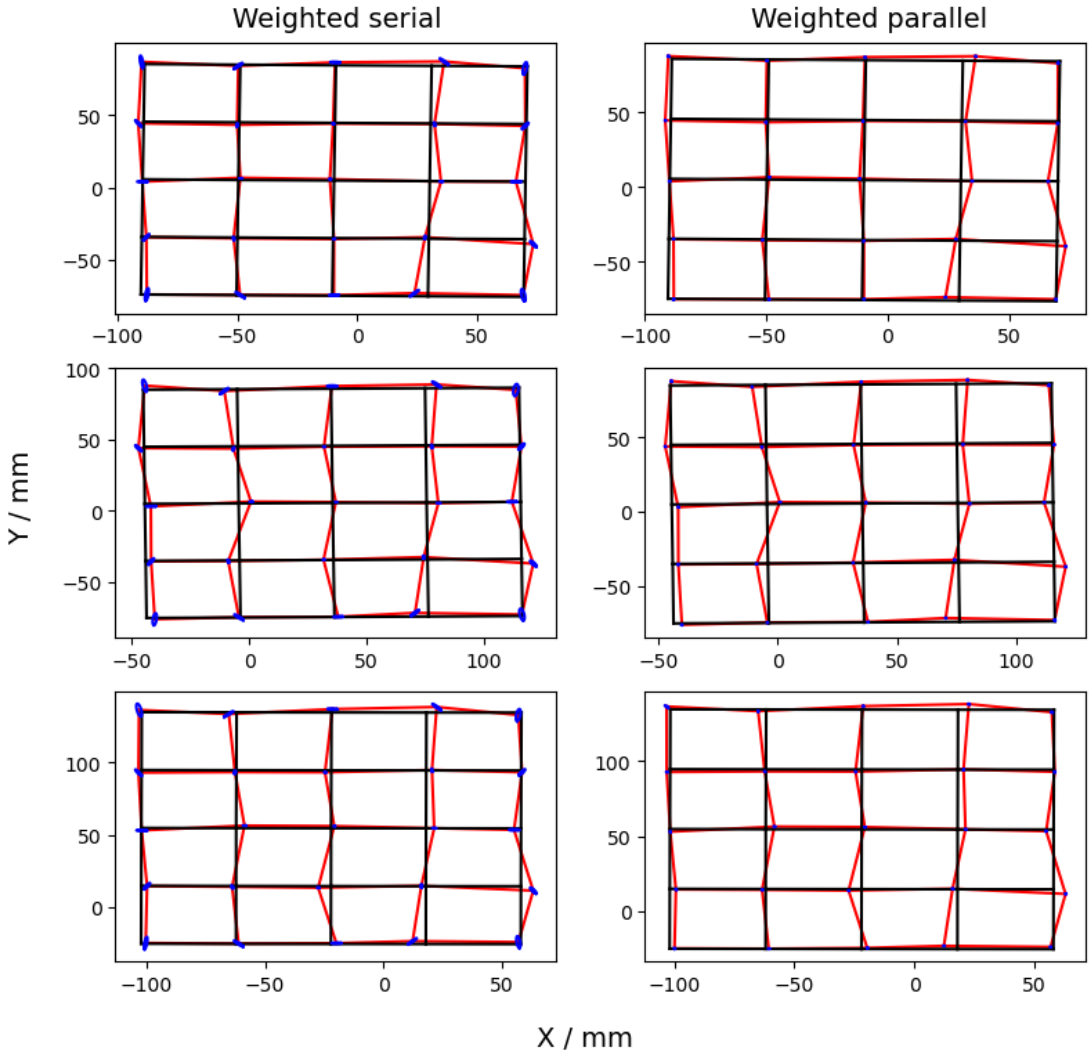

Figure 8.29 The mean position of each sphere (red) in the sphere plate compared to the actual value (black) All measurements are given with a 95% confidence ellipse (blue).

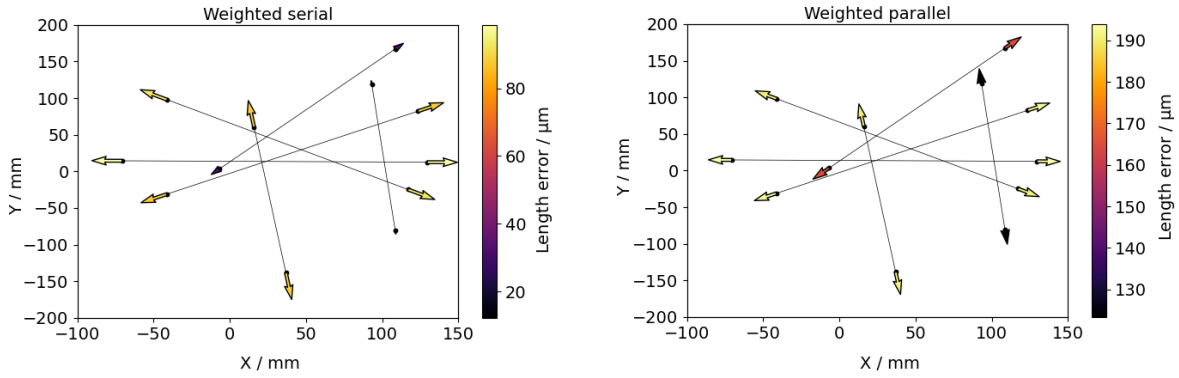

Figure 8.30 The mean sphere-to-sphere length errors shown at the position of measurement.

Figure 8.29 shows there may be some dependency of sphere-to-sphere length error to the sphere itself, given the similar results across methods and positions of the sphere plate. Figure 8.30 shows no indication of dependency on position.

8.3.7 Discussion

Due to the conflicting results of the sphere-based artefacts, it is difficult to obtain a conclusive result on the validity of the parameter estimates. Evidence from the sphere-based measurement indicate that there is some dominating error that is not caused by errors in the system parameters.

The single sphere radii measurement and the mean sphere radii measurement of the sphere plate artefact given in Figure 8.20 and Figure 8.24 show a consistent underestimation. However, the single radii measurement and the mean sphere radii measurements on the sphere dumbbell artefact (Figure 8.21 and Figure 8.25 respectively) show a consistent overestimation. Unlike the flat plane artefact, there is no consistent effect of the weighting matrix. Despite the differences in parameters, that had a measurable effect when measuring the flat plane, there was often little difference when comparing results from weighted methods to results from the same unweighted methods.

The inconsistency in the sphere-based measurements is reflected in the GOM and OpenCV measurements. The GOM measurement of the flat is in good agreement with the weighted methods in Figure 8.6, yet the GOM system was unable to measure the sphere plate artefact and only had good agreement with the parallel methods when measuring the sphere dumbbell artefact. The OpenCV parameters performed poorly in all cases except when measuring the sphere dumbbell artefact.

The dumbbells and sphere plate measurements differ drastically from each other, despite using the same analysis and the spheres being of similar size. It

is well-known that the surface material of measurement artefacts will greatly affect their measurement results [115, 244]. The two spheres are made of different material – which may be the cause of some measurement discrepancy between the two artefacts.

Given the sphere radii is measured across a small portion of the measurement volume, the sphere radii should only be sensitive to changes in system parameters that affect scale. It should be expected therefore that the sphere radii measurements should remain unchanged when measuring it different places across the measurement volume. However, this was shown not to be the case for both the sphere plate and the sphere dumbbell artefact in Figure 8.20 and Figure 8.21. This gives evidence to the fact that a factor other than parameter error is strongly influencing the measurement result.

Furthermore, the length-based measurements are expected to change on similar order to the flatness deviations. The flatness deviation in Figure 8.6 shows approximately a 70 μm change across the flat for the serial method, and approximately 30 μm for other methods and the GOM system. The sphere-to-sphere length measurements showed a change of greater than 100 μm in Figure 8.22 and Figure 8.23, regardless of the choice of parameters. This gives further evidence that parameter error is not the most significant factor influencing measurements of the sphere-based artefacts.

Sphere-based artefacts were chosen for this test because of their use in ISO 10360-13 and VDI/VDE 2634 part 2 and given a measurement result is dependent on tens of thousands of points, it is expected that a sphere would be theoretically insensitive to phase noise. However, unlike the flat, the spheres are small and are not filtered. The spheres are covered by only a few fringes, unlike the flat that is covered by many fringes. A sphere therefore is sensitive to phase errors that span a similar length. Spheres also provide a range of surface normals, a set of which are guaranteed to be produce very erroneous measurements (when surface angle is very high or allows specular reflection). The sphere fitting test in Section 8.3.4 indicated a small systematic error when measuring radii, and a smaller systematic error along the depth coordinate. However, the measured systematic error is considerably larger than the systematic error revealed in Section 8.3.4. The test only included Gaussian noise distribution – however phase noise is not entirely Gaussian and this can be seen in Figure 6.23. Given the limited surface of the sphere that is well measured, it is possible that with the addition of non-Gaussian errors, the systematic error may be larger. While the hyper-renormalisation algorithm used in this thesis is

considered extremely accurate [243], it is possible a weighted non-linear geometric fitting would have been more accurate.

8.4 {Summary

In this chapter, three artefacts, a flatness artefact and two sphere-based artefacts were used to validate the parameter estimates and uncertainties provided by the calibration method given in Chapter 7. The accuracy of the flatness deviation measurements made with the parameter estimates obtained using the weighted methods were comparable to measurements made on a commercial system. The weighting matrix improved the measurements of the flatness artefact. The measurement of the sphere-based artefacts did not show the same effect. Measurements of the two artefacts did not exhibit the same behaviour – despite similar size of the sphere and almost identical measurement processes. Differences in measurements of the two artefacts was attributed to different material composition of the spheres. Additionally, the errors of the sphere measurements showed no positional dependency. The sphere fitting test showed only very minor bias to be expected in the measurements, but evidence showed that the accuracy of the measurements of the spheres was limited by the measurement noise – and not the system parameters. Results from the sphere-based measurements were unable to conclusively validate the system parameter uncertainties.

Results from the flatness measurement showed that the uncertainty obtained using the calibration method defined in Chapter 7 were invalid and unable to explain discrepancies between fringe projection and independent measurements. Tests performed on methods throughout the measurement pipeline indicate that the cause of the invalid uncertainty evaluations is the specificity of the measurement model used for fringe projection. The pinhole and distortion model currently used is not universally applicable – at some scale the terms in the distortion correction are unable to correct the pinhole model. A more comprehensive distortion model is required to measure flatness deviation values beyond 30 μm across the 320×120 mm surface of the flatness artefact.

Chapter 9 – Conclusion

This chapter will conclude the thesis. A summary of the thesis is given in Section 9.1. Section 9.2 summarises the problem of uncertainty in fringe projection investigated in this thesis. Section 9.3 describes the novel contributions made in this thesis. Section 9.4 summarises the results found in this thesis. In Section 9.5, future work based on the findings of this thesis are suggested.

9.1 Thesis summary

The aim of this thesis was to improve the calibration process of fringe projection. Calibration is the process that estimates the quantities (defined system parameters here) that define the functional relationship between a fringe projection indication (a camera image) and the measurement result (a point-cloud). Specifically, this thesis estimated the uncertainty of the system parameters obtained using a popular calibration method. The end goal of this work was to improve understanding of measurement uncertainty in fringe projection and inform future work.

9.2 Problem summary

Currently, a gage R&R study is required to evaluate the uncertainty in a fringe projection measurement. Each study is only applicable to the specific measurement that has been investigated and takes time and resources to complete. Ideally, the uncertainty of a fringe projection system would be found using just one study, and the results would be universally applicable to future measurements made using the system.

The uncertainty problem in fringe projection systems is highlighted in Chapter 3 and Chapter 4. The magnitude of the uncertainty problem was made clear in Chapter 3 – many influence quantities are missing from the measurement model and produce an effect on the measurement result that cannot be analytically derived. It is uncertain whether the effect on the measurement results can be obtained without extensive knowledge of the measurement surface itself, including the surface geometry. The current methods to estimate uncertainty in a fringe projection measurement were explored in Chapter 5.

There exists no unifying measurement model for which to begin a full evaluation of uncertainty of a fringe projection measurement.

9.3 Thesis contributions

The approach to uncertainty used in this thesis, where uncertainty in the measurement results were derived solely from the system parameters, was chosen because it would apply universally to all measurements, it would not require any additional data to be taken and it allows for the separation of uncertainty measurement-specific uncertainty and system-specific uncertainty. An uncertainty evaluation that included surface quantities was considered beyond the scope of this thesis.

This thesis presents several novel contributions to realise this approach to uncertainty. A novel triangulation method derived from the pinhole camera model is defined in Chapter 2. The triangulation method provides similar accuracy over the entire measurement volume as popular methods but achieves the same calculation in far fewer operations. The speed of calculation of the triangulation is useful in propagating uncertainty from the system parameters in Chapter 8, where the triangulation must be completed thousands of times for each measurement. In Chapter 6, a dot localisation algorithm is modified to produce an uncertainty on the centre locations of the dots in camera images. This novel dot localisation algorithm enabled the calculation of an appropriate weighting matrix for the calibration, which in turn led to a novel estimation of the uncertainty of parameter estimations. Chapter 7 explicitly defines the calibration method to estimate both parameters and their uncertainties. Chapter 7 provides two alternative methods to achieve this, the parallel method where all parameters are estimated within one regression, and a serial method were the camera parameters are estimated first followed by the projector parameters. The parallel method was expected to be more accurate, given the reduced degrees of freedom of the problem, the serial method was included as the method is far less computationally intensive.

Many methods proposed in this thesis were tested for validity, notably including the working conditions of the non-linear regression used in the calibration. In a first, both the specificity and non-linearity of the model used in the non-linear regression that estimated the parameters of fringe projection were tested. Additionally, a novel test was proposed to test for stability of the estimated parameters throughout the calibration – which allows operators to determine if thermal instability within the fringe projection system is

problematic. Previously, some thermal instability problems were undetectable when using the reprojection errors as a test metric.

9.4 Thesis results

To test the validity of the parameter and associated uncertainty estimations obtained in this thesis, a flatness artefact, a sphere dumbbell artefact, and a sphere plate artefact were measured in Chapter 8. First, the accuracy of the estimated parameters was compared using the mean system parameters only. The measurements were compared with measurements made using a commercial system and measurements made with parameters obtained using the method stereoCalibrate from OpenCV. The goal was to understand whether the weighting matrix improved the accuracy of the fringe projection system. Then, the uncertainty derived from the system parameters was tested as to whether it could adequately explain the discrepancy between the fringe projection measurements and the independent measurements. If the propagated uncertainty was able to explain all measurement discrepancies, the uncertainty in the system parameters would be found to be valid.

In the flatness measurements made using the mean system parameters, it was found that both the weighted serial and weighted parallel parameters produced measurements that rivalled measurements made by a commercial system, the GOM ATOS Core 300, and far outperformed the measurements made using OpenCV parameters. The sphere-based measurements however were very poor, with no consistent errors found across the two artefacts. The propagated uncertainty of the system parameters was unable to explain all measurement discrepancies in all three of the artefacts used – but was considerably worse for the sphere-based measurements.

All fringe projection systems, GOM included, performed poorly on the sphere-based measurements. Given measurements made with different parameters from the different calibration methods gave very similar measurements (unlike the flat plane measurements), it was concluded that the uncertainty in the sphere parameter estimates were dominated by phase error, and not error in the system parameters. The uncertainty in the sphere fitting process found in Section 8.3.4 was ~15 μm lower than the unexplained discrepancy in the parallel calibration method, and ~170 μm lower than the discrepancy in the GOM measurements. It was determined that the sphere fitting test in Section 8.3.4 did not fully eliminate the phase error which led to unaccounted effects on the sphere fit. The sphere plate artefact produced very different results to the dumbbell artefact, despite near identical measurements and analysis. It was

established that the material of the spheres in the sphere plate artefact was the cause of this issue. The results of the sphere-based measurements in this thesis lead to the question of the validity of using sphere-based measurements to empirically test the performance of fringe projection systems. While the flatness artefact presents a very simple measurement scenario, the sphere-based measurements present a challenging measurement scenario. Unlike the flatness measurements, the sphere-based measurements provide limited information on the nature of system-specific errors as the measurements are dominated by measurement-specific errors.

The flatness measured using system parameters obtained from either the serial or parallel calibration methods can obtain a flatness value of ~30 μm. However, the uncertainty of the estimated parameters fails to account for the entire range of values in the flatness measurement – despite the weighting matrix being potentially overestimated. It was concluded that while the weighting matrix could be improved, the pinhole with the Brown-Conrady distortion model used to define fringe projection systems is inadequate for producing a flatness beyond ~30 μm of a 300 mm × 140 mm flatness measurement. The distortion model generally defines the distortion found in a camera well, but at a certain scale, this model will fail – and this thesis shows the limit to this model has been reached.

9.5 Future work

This thesis identifies two key areas of improvement that could be made to improve the accuracy of a fringe projection measurement as well as the uncertainty evaluation of a fringe projection measurement, in relation to the system parameters.

Firstly, the input covariance estimates to the non-linear regression derived in this thesis could be improved. It was made clear in this thesis that the covariance estimates typically overestimated errors, and in the case that this error is not a scalar multiplicative error, will lead to an incorrect regression covariance estimate. In the case that this error is a scalar multiplicative error, the errors will be overestimated.

The failure of the sphere-based measurements indicates a better choice of artefact could have been chosen. An artefact that presents a lower range of surface normal vectors, no surface geometrical or contrast discontinuities, and spans a larger volume, would allow for more robust averaging methods to be utilised. If these conditions are followed, even material that presented sub-surface scattering would not be problematic. Unfortunately, it is unlikely a

prismatic shape (that is not a flat plane) would fit this description – a freeform surface may be the only solution.

The failure of the distortion model indicates a more sophisticated model is required for higher accuracy measurements as those obtained in this thesis. Each pixel is considered as a direction sensor, where the direction of each pixel is dictated by the pinhole matrix and the distortion parameters. Increasing the orders in the distortion model will give diminishing returns on accuracy, not all distortion (especially very low-level distortion) is guaranteed to be well-described the Brown-Conrady model. Alternative distortion models, such as a non-parametric distortion model, i.e., a Gaussian process model, may enable a more accurate measurement by not relying on specificity of any single distortion model.

References

1. BIPM, *The international vocabulary of metrology - basic and general concepts and associated terms (VIM)*. 2012: France.
2. Korpela, M., et al., *Additive Manufacturing—Past, Present, and the Future*, in *Technical, Economic and Societal Effects of Manufacturing 4.0: Automation, Adaption and Manufacturing in Finland and Beyond*, M. Collan and K.-E. Michelsen, Editors. 2020, Springer International Publishing: Cham. p. 17-41.
3. Gogolinskiy, K. and V. Syasko, *Prospects and challenges of the Fourth Industrial Revolution for instrument engineering and metrology in the field of non-destructive testing and condition monitoring.* Insight-Non-Destructive Testing and Condition Monitoring, 2019. **61**(8): p. 434-440.
4. ISO, *Geometrical product specifications (GPS) - Geometrical tolerancing*, in *Tolerances of form, orientation, location and run-out*. 2017.
5. Morse, E., *Specification of Design Intent, Introduction to Dimensioning and Tolerancing*, in *Coordinate Measuring Machines and Systems*, R. Hocken and P. Pereira, Editors. 2017, CRC press. p. 41-56.
6. Hocken, R. and J. Bosch, *Evolution of measurement*, in *Coordinate Measuring Machines and Systems*, R. Hocken and P. Pereira, Editors. 2017, CRC press. p. 1-30.
7. Pereira, P., *Cartesian Coordinate Measuring Machines*, in *Coordinate Measuring Machines and Systems*, R. Hocken and P. Pereira, Editors. 2017, CRC press. p. 57-80.
8. Mohan, P., J. Shah, and J.K. Davidson. *A library of feature fitting algorithms for GD&T verification of planar and cylindrical features*. in *International Design Engineering Technical Conferences and Computers and Information in Engineering Conference*. 2013. American Society of Mechanical Engineers.
9. Williams, R.M. and H.T. Ilieş, *Practical shape analysis and segmentation methods for point cloud models.* Computer Aided Geometric Design, 2018. **67**: p. 97-120.
10. Zhang, G., *Non-Cartesian Coordinate Measuring Machines*, in *Coordinate Measuring Machines and Systems*, R. Hocken and P. Pereira, Editors. 2017, CRC press. p. 467-514.
11. Hinz, L., et al., *Fringe projection profilometry in production metrology: A multi-scale comparison in sheet-bulk metal forming.* Sensors, 2021. **21**(7): p. 2389.

12. Broadley, L.H., A.F. Chrimes, and A. Mitchell, *Fringe analysis approach for imaging surface undulations on technical surfaces.* Optics Express, 2021. **29**(21): p. 33067-33076.
13. Shang, H., C. Liu, and R. Wang, *Measurement methods of 3D shape of large-scale complex surfaces based on computer vision: A review.* Measurement, 2022: p. 111302.
14. Kulkarni, R., E. Banoth, and P. Pal, *Automated surface feature detection using fringe projection: An autoregressive modeling-based approach.* Optics and Lasers in Engineering, 2019. **121**: p. 506-511 , ISSN = 0143-8166.
15. Nogales, S.O., et al., *Shape defect measurement by fringe projection profilometry and phase-shifting algorithms.* Optical Engineering, 2020. **59**(1): p. 014107 , ISSN = 0091-3286.
16. Ding, Y., et al., *Development of a novel mobile robotic system for large-scale manufacturing.* Proceedings of the Institution of Mechanical Engineers, Part B: Journal of Engineering Manufacture, 2021. **235**(14): p. 2300-2309.
17. Xia, R., et al., *Detection method of manufacturing defects on aircraft surface based on fringe projection.* Optik, 2020. **208**: p. 164332 , ISSN = 0030-4026.
18. Catalucci, S., et al., *Optical metrology for digital manufacturing: a review.* The International Journal of Advanced Manufacturing Technology, 2022: p. 1-20.
19. Grasso, M.L.G., et al., *In-situ measurement and monitoring methods for metal powder bed fusion–an updated review.* Measurement Science and Technology, 2021.
20. Zhang, B., *In Situ Fringe Projection Profilometry for Laser Power Bed Fusion Process*. 2017, The University of North Carolina at Charlotte.
21. Southon, N., et al., *In-process measurement and monitoring of a polymer laser sintering powder bed with fringe projection.* Materials & Design, 2018. **157**: p. 227-234 , ISSN = 0264-1275.
22. Dickins, A., et al., *Multi-view fringe projection system for surface topography measurement during metal powder bed fusion.* JOSA A, 2020. **37**(9): p. B93-B105.
23. Christoph, R. and H. Joachim Neumann, *Multisensor Coordinate Metrology*, in *Coordinate Measuring Machines and Systems*, R. Hocken and P. Pereira, Editors. 2017, CRC press. p. 125-153.
24. 100, J., *Evaluation of measurement data - Guide to the expression of uncertainty in measurement*. 2008: France.
25. ISO, *Geometrical product specifications (GPS) - Coordinate measuring machines (CMM): Technique for determining the uncertainty of measurement*, in *Use of calibrated workpieces or measurement standards*. 2011.
26. Hartley, R.I. and P. Sturm, *Triangulation.* Computer vision and image understanding, 1997. **68**(2): p. 146-157.

27. Zhang, S., *Temporal phase unwrapping for digital fringe proejction systems*, in *High-speed 3D imaging with digital fringe projection techniques*. 2016, CRC Press. p. 45-71.
28. Ester, M., et al. *A density-based algorithm for discovering clusters in large spatial databases with noise*. in *Knowledge Discovery and Data Mining*. 1996.
29. Chen, R., J. Xu, and S. Zhang, *Digital fringe projection profilometry*, in *Advances in Optical Form and Coordinate Metrology*, R.K. Leach, Editor. 2020, IOP Publishing. p. 115-143.
30. Feng, S., et al., *Calibration of fringe projection profilometry: A comparative review.* Optics and Lasers in Engineering, 2021. **143**: p. 106622.
31. Xu, J. and S. Zhang, *Status, challenges, and future perspectives of fringe projection profilometry.* Optics and Lasers in Engineering, 2020. **135**: p. 106193.
32. Kühmstedt, P., et al. *3D shape measurement with phase correlation based fringe projection*. in *Optical Measurement Systems for Industrial Inspection V*. 2007. International Society for Optics and Photonics.
33. Juarez-Salazar, R., et al., *Key concepts for phase-to-coordinate conversion in fringe projection systems.* Applied optics, 2019. **58**(18): p. 4828-4834.
34. Zhang, S. and P.S. Huang, *Novel method for structured light system calibration.* Optical Engineering, 2006. **45**(8): p. 083601.
35. Zhang, S., *High-speed 3D imaging with digital fringe projection techniques*. 2016: CRC Press.
36. Jia, P., J. Kofman, and C.E. English, *Comparison of linear and nonlinear calibration methods for phase-measuring profilometry.* Optical Engineering, 2007. **46**(4): p. 043601.
37. Liu, H., et al., *Calibration-based phase-shifting projected fringe profilometry for accurate absolute 3D surface profile measurement.* Optics communications, 2003. **216**(1-3): p. 65-80.
38. Zhang, R. and H. Guo, *Depth recovering method immune to projector errors in fringe projection profilometry by use of cross-ratio invariance.* Optics Express, 2017. **25**(23): p. 29272-29286.
39. Lv, S., et al., *Projector distortion correction in 3D shape measurement using a structured-light system by deep neural networks.* Optics Letters, 2020. **45**(1): p. 204-207.
40. Zheng, Y., et al., *Fringe projection profilometry by conducting deep learning from its digital twin.* Optics Express, 2020. **28**(24): p. 36568-36583.
41. Fan, S., et al., *Unsupervised deep learning for 3D reconstruction with dual-frequency fringe projection profilometry.* Optics Express, 2021. **29**(20): p. 32547-32567.
42. Tang, Z., et al., *A precision analysis of camera distortion models.* IEEE Transactions on Image Processing, 2017. **26**(6): p. 2694-2704.
43. Ma, L., Y. Chen, and K.L. Moore, *A family of simplified geometric distortion models for camera calibration.* arXiv, 2003.

44. Vo, M., et al., *Hyper-accurate flexible calibration technique for fringe-projection-based three-dimensional imaging.* Optics Express, 2012. **20**(15): p. 16926-16941.
45. Brown, D.C., *Decentering distortion of lenses.* Photogrammetric Engineering and Remote Sensing, 1966.
46. Ronda, J.I. and A. Valdés, *Geometrical analysis of polynomial lens distortion models.* Journal of Mathematical Imaging and Vision, 2019. **61**(3): p. 252-268.
47. Ranganathan, P. and E. Olson. *Gaussian process for lens distortion modeling*. in *2012 IEEE/RSJ International Conference on Intelligent Robots and Systems*. 2012. IEEE.
48. Wang, J., et al., *A new calibration model of camera lens distortion.* Pattern Recognition, 2008. **41**(2): p. 607-615.
49. Sun, W. and J.R. Cooperstock, *An empirical evaluation of factors influencing camera calibration accuracy using three publicly available techniques.* Machine Vision and Applications, 2006. **17**(1): p. 51-67.
50. Vargas, R., et al., *Camera-projector calibration methods with compensation of geometric distortions in fringe projection profilometry: A comparative study.* Optica Pura y Aplicada, 2018. **51**(3): p. 1-10.
51. Wang, J., et al., *Predistorting Projected Fringes for High-Accuracy 3-D Phase Mapping in Fringe Projection Profilometry.* IEEE Transactions on Instrumentation and Measurement, 2021. **70**: p. 1-9.
52. Li, K., J. Bu, and D. Zhang, *Lens distortion elimination for improving measurement accuracy of fringe projection profilometry.* Optics and Lasers in Engineering, 2016. **85**: p. 53-64.
53. Yang, S., et al., *Projector distortion residual compensation in fringe projection system.* Optics and Lasers in Engineering, 2019. **114**: p. 104-110.
54. Drap, P. and J. Lefèvre, *An exact formula for calculating inverse radial lens distortions.* Sensors, 2016. **16**(6): p. 807.
55. De Villiers, J.P., F.W. Leuschner, and R. Geldenhuys. *Centi-pixel accurate real-time inverse distortion correction*. in *Optomechatronic Technologies 2008*. 2008. International Society for Optics and Photonics.
56. Bradski, G., *The openCV library.* Dr. Dobb's Journal: Software Tools for the Professional Programmer, 2000. **25**(11): p. 120-123.
57. Zheng, D. and F. Da, *Absolute phase retrieval for defocused fringe projection three-dimensional measurement.* Optics Communications, 2014. **312**: p. 302-311.
58. Garnica, G., M. Padilla, and M. Servin, *Dual-sensitivity profilometry with defocused projection of binary fringes.* Applied optics, 2017. **56**(28): p. 7985-7989.
59. Zuo, C., et al., *Phase shifting algorithms for fringe projection profilometry: A review.* Optics and Lasers in Engineering, 2018. **109**: p. 23-59.

60. He, X. and Q. Kemao, *A comparison of n-ary simple code and n-ary gray code phase unwrapping in high-speed fringe projection profilometry.* Optics and Lasers in Engineering, 2020. **128**: p. 106046.
61. Zhang, S., *Practical considerations for system development*, in *High-speed 3D imaging with digital fringe projection techniques*. 2016, CRC Press. p. 143-155.
62. Ri, S., et al., *Spatiotemporal phase-shifting method for accurate phase analysis of fringe pattern.* Journal of Optics, 2019. **21**(9): p. 095702.
63. Zhang, S., *Spatial phase-unwrapping algorithm for real time applications*, in *High-speed 3D imaging with digital fringe projection techniques*. 2016, CRC Press. p. 71-84.
64. Ma, S., et al., *A fast and accurate gamma correction based on Fourier spectrum analysis for digital fringe projection profilometry.* Optics Communications, 2012. **285**(5): p. 533-538.
65. Zhang, Z., et al., *Comparison of Fourier transform, windowed Fourier transform, and wavelet transform methods for phase calculation at discontinuities in fringe projection profilometry.* Optics and Lasers in Engineering, 2012. **50**(8): p. 1152-1160.
66. Huang, L., et al., *Comparison of Fourier transform, windowed Fourier transform, and wavelet transform methods for phase extraction from a single fringe pattern in fringe projection profilometry.* Optics and Lasers in Engineering, 2010. **48**(2): p. 141-148.
67. Gai, S., F. Da, and X. Dai, *Novel 3D measurement system based on speckle and fringe pattern projection.* Optics express, 2016. **24**(16): p. 17686-17697.
68. An, Y., J.-S. Hyun, and S. Zhang, *Pixel-wise absolute phase unwrapping using geometric constraints of structured light system.* Optics express, 2016. **24**(16): p. 18445-18459.
69. An, Y., Z. Liu, and S. Zhang, *Evaluation of pixel-wise geometric constraint-based phase-unwrapping method for low signal-to-noise-ratio (SNR) phase.* Advanced Optical Technologies, 2016. **5**(5-6): p. 423-432.
70. Zhang, S., *Absolute phase retrieval methods for digital fringe projection profilometry: A review.* Optics and Lasers in Engineering, 2018. **107**: p. 28-37.
71. Zuo, C., et al., *Temporal phase unwrapping algorithms for fringe projection profilometry: A comparative review.* Optics and Lasers in Engineering, 2016. **85**: p. 84-103.
72. He, X. and Q. Kemao, *A comparative study on temporal phase unwrapping methods in high-speed fringe projection profilometry.* Optics and Lasers in Engineering, 2021. **142**: p. 106613.
73. Xiao, Z., O. Chee, and A. Asundi, *An accurate 3D inspection system using heterodyne multiple frequency phase-shifting algorithm.* Physics Procedia, 2011. **19**: p. 115-121.

74. Zhang, J., et al., *Error analysis in the absolute phase maps recovered by fringe patterns with three different wavelengths.* Journal of Modern Optics, 2018. **65**(3): p. 237-245.
75. Cho, C.S. and J. Han, *Phase error reduction for multi-frequency fringe projection profilometry using adaptive compensation.* Current Optics and Photonics, 2018. **2**(4): p. 332-339.
76. Yin, W., et al., *High-speed three-dimensional shape measurement using geometry-constraint-based number-theoretical phase unwrapping.* Optics and Lasers in Engineering, 2019. **115**: p. 21-31.
77. Hu, W., et al., *A Fringe Phase Extraction Method Based on Neural Network.* Sensors, 2021. **21**(5): p. 1664.
78. Yu, H., et al., *Untrained deep learning-based fringe projection profilometry.* APL Photonics, 2022. **7**(1): p. 016102.
79. Tian, J., X. Peng, and X. Zhao, *A generalized temporal phase unwrapping algorithm for three-dimensional profilometry.* Optics and Lasers in Engineering, 2008. **46**(4): p. 336-342.
80. Lai, J., et al., *A robust and effective phase-shift fringe projection profilometry method for the extreme intensity.* Optik, 2019. **179**: p. 810-818.
81. Wang, Z., D.A. Nguyen, and J.C. Barnes, *Some practical considerations in fringe projection profilometry.* Optics and Lasers in Engineering, 2010. **48**(2): p. 218-225.
82. Zhang, S. *Active versus passive projector nonlinear gamma compensation method for high-quality fringe pattern generation*. in *Dimensional Optical Metrology and Inspection for Practical Applications III*. 2014. SPIE.
83. Babaei, A., M. Saadatseresht, and J. Kofman, *Exponential fringe pattern projection approach to gamma-independent phase computation without calibration for gamma nonlinearity in 3D optical metrology.* Optics express, 2017. **25**(21): p. 24927-24938.
84. Zhang, S., *Digital fringe generation technique*, in *High-speed 3D imaging with digital fringe projection techniques*. 2016, CRC Press. p. 29-45.
85. Petković, T., et al. *Software synchronization of projector and camera for structured light 3D body scanning*. in *Proceedings of the 7th International Conference on 3D Body Scanning Technologies*. 2016.
86. Atif, M. and S. Lee, *FPGA based adaptive rate and manifold pattern projection for structured light 3D camera system.* Sensors, 2018. **18**(4): p. 1139.
87. Yu, Y., et al., *Dual-projector structured light 3D shape measurement.* Applied Optics, 2020. **59**(4): p. 964-974.
88. Atif, M. and S. Lee, *FPGA based pattern generation and synchonization for high speed structured light 3D camera.* Telkomnika, 2017. **15**(2): p. 926.
89. Shaheen, A., et al., *Characterisation of a multi-view fringe projection system based on the stereo matching of rectified phase maps.* Measurement Science and Technology, 2021. **32**(4): p. 045006.

90. Zhang, R., et al. *Rapid matching of stereo vision based on fringe projection profilometry*. in *8th International Symposium on Advanced Optical Manufacturing and Testing Technologies: Optical Test, Measurement Technology, and Equipment*. 2016. International Society for Optics and Photonics.
91. Yong, L., *A correspondence finding method based on space conversion in 3D shape measurement using fringe projection.* Optics Express, 2015. **23**(11): p. 14188-14202.
92. Brus, Z., et al., *Real-Time FPGA Accelerated Stereo Matching for Temporal Statistical Pattern Projector Systems.* Sensors, 2021. **21**(19): p. 6435.
93. Hecht, E., *Optics, 5e*. 2002: Pearson Education India.
94. Brakhage, P., G. Notni, and R. Kowarschik, *Image aberrations in optical three-dimensional measurement systems with fringe projection.* Applied Optics, 2004. **43**(16): p. 3217-3223.
95. Miks, A. and J. Novak, *Dependence of camera lens induced radial distortion and circle of confusion on object position.* Optics & Laser Technology, 2012. **44**(4): p. 1043-1049.
96. Blostein, S.D. and T.S. Huang, *Error analysis in stereo determination of 3-D point positions.* IEEE Transactions on Pattern Analysis and Machine Intelligence, 1987. **9**(6): p. 752-765.
97. Streibl, N., *Three-dimensional imaging by a microscope.* JOSA A, 1985. **2**(2): p. 121-127.
98. Berssenbrügge, P., et al., *Characterization of the 3D resolution of topometric sensors based on fringe and speckle pattern projection by a 3D transfer function.* Optics and Lasers in Engineering, 2012. **50**(3): p. 465-472.
99. Zhang, B., et al., *Validity of the instrument transfer function for fringe projection metrology.* Applied Optics, 2018. **57**(11): p. 2795-2803.
100. Drouin, M.-A., G. Godin, and F. Blais, *Efficient representation of the variant PSF of structured light system*, in *International Conference on Image Processing*. 2010, IEEE: Hong Kong, China. p. 1693-1696.
101. Rao, L. and F. Da, *Local blur analysis and phase error correction method for fringe projection profilometry systems.* Applied optics, 2018. **57**(15): p. 4267-4276.
102. Guidi, G., et al., *Performance evaluation of triangulation based range sensors.* Sensors, 2010. **10**(8): p. 7192-7215.
103. Notni, G.H. and G. Notni, *Digital fringe projection in 3D shape measurement: an error analysis*, in *Optical Measurement Systems for Industrial Inspection III*. 2003, International Society for Optics and Photonics: Munich, Germany. p. 372–380.
104. Zhang, L. and S. Nayar, *Projection defocus analysis for scene capture and image display.* ACM Transactions on Graphics, 2006. **25**(3): p. 907-915.
105. Park, J. and B.-U. Lee, *Defocus and geometric distortion correction for projected images on a curved surface.* Applied optics, 2016. **55**(4): p. 896-902.

106. Pan, B., et al., *Phase error analysis and compensation for nonsinusoidal waveforms in phase-shifting digital fringe projection profilometry.* Optics Letters, 2009. **34**(4): p. 416-418.
107. Ma, S., et al., *Investigation of phase error correction for digital sinusoidal phase-shifting fringe projection profilometry.* Optics and Lasers in Engineering, 2012. **50**(8): p. 1107-1118.
108. Padilla, M., M. Servin, and G. Garnica, *Fourier analysis of RGB fringe-projection profilometry and robust phase-demodulation methods against crosstalk distortion.* Optics express, 2016. **24**(14): p. 15417-15428.
109. Chen, C. and B. Pan, *Correcting lateral chromatic aberration using orthogonal fringe patterns.* Applied Optics, 2020. **59**(22): p. 6517-6525.
110. Li, D. and J. Kofman, *Adaptive fringe-pattern projection for image saturation avoidance in 3D surface-shape measurement.* Optics express, 2014. **22**(8): p. 9887-9901.
111. Waddington, C. and J. Kofman, *Analysis of measurement sensitivity to illuminance and fringe-pattern gray levels for fringe-pattern projection adaptive to ambient lighting.* Optics and Lasers in Engineering, 2010. **48**(2): p. 251-256.
112. Chen, C., Y. Wan, and Y. Cao, *Instability of projection light source and real-time phase error correction method for phase-shifting profilometry.* Optics express, 2018. **26**(4): p. 4258-4270.
113. Irie, K., et al., *A technique for evaluation of CCD video-camera noise.* IEEE Transactions on Circuits and Systems for Video Technology, 2008. **18**(2): p. 280-284.
114. Fischer, M., M. Petz, and R. Tutsch, *Statistical characterization of evaluation strategies for fringe projection systems by means of a model-based noise prediction.* Journal of Sensors and Sensor Systems, 2017. **6**(1): p. 145.
115. Hodgson, J.R., et al., *Novel metrics and methodology for the characterisation of 3D imaging systems.* Optics and Lasers in Engineering, 2017. **91**: p. 169-177.
116. Kühmstedt, P., C. Bräuer-Burchardt, and G. Notni. *Measurement accuracy of fringe projection depending on surface normal direction*. in *Optical Inspection and Metrology for Non-Optics Industries*. 2009. San Diego, US: International Society for Optics and Photonics.
117. Xu, Y., et al., *High-accuracy 3D shape measurement of translucent objects by fringe projection profilometry.* Optics express, 2019. **27**(13): p. 18421-18434.
118. Chen, H., et al., *Suppression of the nonlinear phase error in phase shifting profilometry: considering non-smooth reflectivity and fractional period.* Optics express, 2018. **26**(10): p. 13489-13505.
119. Yue, H., et al., *Reduction of systematic errors in structured light metrology at discontinuities in surface reflectivity.* Optics and Lasers in Engineering, 2019. **112**: p. 68-76.

120. Gu, J., et al. *Multiplexed illumination for scene recovery in the presence of global illumination*. in *International Conference on Computer Vision*. 2011. Barcelona, Spain: Institute of Electrical and Electronics Engineers.
121. Gupta, M., et al., *A practical approach to 3D scanning in the presence of interreflections, subsurface scattering and defocus.* International Journal of Computer Vision, 2013. **102**(1-3): p. 33-55.
122. Adamczyk, M., P. Liberadzki, and R. Sitnik, *Temperature compensation method for digital cameras in 2D and 3D measurement applications.* Sensors, 2018. **18**(11): p. 3685.
123. Adamczyk, M., P. Liberadzki, and R. Sitnik, *Temperature compensation method for mechanical base of 3D-structured light scanners.* Sensors, 2020. **20**(2): p. 362.
124. Yu, Q., et al., *The effects of temperature variation on videometric measurement and a compensation method.* Image and Vision Computing, 2014. **32**(12): p. 1021-1029.
125. Smith, M. and E. Cope, *The effects of temperature variation on single-lens-reflex digital camera calibration parameters.* International Archives of Photogrammetry, Remote Sensing and Spatial Information Sciences, 2010. **38**(5): p. 554-559.
126. Miller, A., et al., *Positional uncertainty in optical-based metrology systems in large volume manufacturing.* Acta IMEKO, 2018. **7**(2).
127. Bointon, P., et al., *The effects of vibration on fringe projection systems*, in *International Conference of the European Society for Precision Engineering and Nanotechnology*. 2018: Venice, Italy. p. 119-120.
128. Yao, J., et al., *Phase error elimination considering gamma nonlinearity, system vibration, and noise for fringe projection profilometry.* Optical Engineering, 2014. **53**(9).
129. Li, F., D. Stoddart, and I. Zwierzak, *A performance test for a fringe projection scanner in various ambient light conditions.* Procedia CIRP, 2017. **62**: p. 400-404.
130. Haitjema, H., *Measurement uncertainty*, in *Basics of Precision Engineering*, R.K. Leach and S. Smith, Editors. 2018, CRC Press. p. 413-448.
131. Arras, K.O., *An introduction to error propagation: derivation, meaning and examples of equation CY= FX CX FXT*. 1998, École Polytechnique Fédérale de Lausanne.
132. Cox, M. and P. Harris, *Uncertainty evaluation*, in *Software Support for Metrology Best Practice Guide no. 6*. 2010, National Physics Laboratory.
133. Harris, P. and M. Cox, *On a Monte Carlo method for measurement uncertainty evaluation and its implementation.* Metrologia, 2014. **51**(4): p. S176.
134. Von Neumann, J., *Various techniques used in connection with random digits.* Applied Math Series, 1951. **12**(36-38): p. 5.

135. Benoit, C., *Note sur une méthode de résolution des équations normales provenant de l'application de la méthode des moindres carrés à un système d'équations linéaires en nombre inférieur à celui des inconnues (Procédé du Commandant Cholesky).* Bulletin géodésique, 1924. **2**(1): p. 67-77.
136. Morel, S., *Methods for measuring a lens focal length*. 2011.
137. Wang, F., et al., *Distortion measurement of optical system using phase diffractive beam splitter.* Optics express, 2019. **27**(21): p. 29803-29816.
138. Zhang, Z., D. Zhang, and X. Peng, *Performance analysis of a 3D full-field sensor based on fringe projection.* Optics and lasers in engineering, 2004. **42**(3): p. 341-353.
139. Liu, J. and Y. Li. *Performance analysis of 3-D shape measurement projector-camera system with short baseline arrangement*. in *International Conference on Robotics and Biomimetics*. 2013. Shenzhen, China: Institute of Electrical and Electronics Engineers.
140. Busca, G. and E. Zappa, *Sensitivity analysis applied to an improved Fourier-transform profilometry.* Optics and Lasers in Engineering, 2011. **49**(2): p. 210-221.
141. Xiao, S., W. Tao, and H. Zhao, *A flexible fringe projection vision system with extended mathematical model for accurate three-dimensional measurement.* Sensors, 2016. **16**(5): p. 612.
142. Moylan, S.P. and G.W. Vogl. *Uncertainty analysis of a simple fringe projection system*. in *American Society for Precision Engineering*. 2009. Peoria, US.
143. Kanatani, K., et al. *Renormalization returns: Hyper-renormalization and its applications*. in *European Conference on Computer Vision*. 2012. Springer.
144. Zhang, Z. and J. Dai, *Error analysis of a 3D imaging system based on fringe projection technique*, in *International Conference on Optical Instruments and Technology: Optical Systems and Modern Optoelectronic Instruments*. 2013, International Society for Optics and Photonics: Beijing, China. p. 90420M.
145. Huang, J., et al., *Calibration of a camera–projector measurement system and error impact analysis.* Measurement Science and Technology, 2012. **23**(12): p. 125402.
146. Schreve, K., *How accurate can a stereovision measurement be?*, in *International Workshop on Research and Education in Mechatronics*. 2014, Institute of Electrical and Electronics Engineers: El Gouna, Egypt. p. 1-7.
147. Li, Y., J. Zhang, and J. Tian. *Error analysis in stereo vision for location measurement of 3D point*. in *MIPPR 2015: Pattern Recognition and Computer Vision*. 2015. International Society for Optics and Photonics.
148. Fooladgar, F., et al., *Geometrical analysis of localization error in stereo vision systems.* IEEE Sensors Journal, 2013. **13**(11): p. 4236-4246.

149. Molimard, J. and L. Navarro, *Uncertainty on fringe projection technique: a Monte-Carlo-based approach.* Optics and Lasers in Engineering, 2013. **51**(7): p. 840-847.
150. 101, J., *Evaluation of measurement data - Supplement 1 to the guide to the expression of uncertainty in measurement - Propagation of distributions using a Monte Carlo method*. 2008.
151. O'Dowd, N.M., A.J. Wachtor, and M.D. Todd, *A model for describing phase-converted image intensity noise in digital fringe projection techniques.* Optics and Lasers in Engineering, 2020. **134**: p. 106293.
152. Semeniuta, O., *Analysis of camera calibration with respect to measurement accuracy.* Procedia Cirp, 2016. **41**: p. 765-770.
153. Caja, J., E. Gómez, and P. Maresca, *Optical measuring equipments. Part I: Calibration model and uncertainty estimation.* Precision Engineering, 2015. **40**: p. 298-304.
154. Sankowski, W., et al., *Estimation of measurement uncertainty in stereo vision system.* Image and Vision Computing, 2017. **61**: p. 70-81.
155. Yang, L., et al., *Analysis on location accuracy for the binocular stereo vision system.* IEEE Photonics Journal, 2017. **10**(1): p. 1-16.
156. ISO, *Geometrical Product Specifications (GPS) - Acceptance and reverification tests for coordinate measuring machines (CMM)*, in *Optical 3D CMS*. 2005.
157. VDI/VDE, *Optical 3D measuring systems*, in *Multiple view systems based on area scanning*. 2008.
158. Wei, Y., et al. *Experimental study for the influence of surface characteristics on the fringe patterns*. in *Optical Metrology and Inspection for Industrial Applications III*. 2014. SPIE.
159. Jemt, T. and L. Hjalmarsson, *In vitro measurements of precision of fit of implant-supported frameworks. A comparison between "virtual" and "physical" assessments of fit using two different techniques of measurements.* Clinical implant dentistry and related research, 2012. **14**: p. e175-e182.
160. Senin, N., et al., *Statistical point cloud model to investigate measurement uncertainty in coordinate metrology.* Precision Engineering, 2021. **70**: p. 44-62.
161. Fei, L., et al., *Calibration and uncertainty estimation of non-contact coordinate measurement systems based on Kriging models.* Precision Engineering, 2019. **57**: p. 16-29.
162. Ranganathan, P. and E. Olson. *Locally-weighted homographies for calibration of imaging systems*. in *2014 IEEE/RSJ International Conference on Intelligent Robots and Systems*. 2014. IEEE.
163. Gayton, G., et al. *Evaluating and propagating uncertainty in digital fringe projection systems*. in *Optical Measurement Systems for Industrial Inspection XII*. 2021. International Society for Optics and Photonics.
164. Srinivasan, B.V., R. Duraiswami, and R. Murtugudde. *Efficient kriging for real-time spatio-temporal interpolation*. in *Proceedings of the 20th Conference*

on Probability and Statistics in the Atmospheric Sciences. 2010. American Meteorological Society Atlanta GA.
165. Matthews, A.G.d.G., et al., *GPflow: A Gaussian Process Library using TensorFlow.* J. Mach. Learn. Res., 2017. **18**(40): p. 1-6.
166. van der Wilk, M., et al., *A framework for interdomain and multioutput Gaussian processes.* arXiv preprint arXiv:2003.01115, 2020.
167. Titsias, M. *Variational learning of inducing variables in sparse Gaussian processes*. in *Artificial intelligence and statistics*. 2009. PMLR.
168. Baumann, M., C. Koch, and S. Staudacher, *Application of Neural Networks and Transfer Learning to Turbomachinery Heat Transfer.* Aerospace, 2022. **9**(2): p. 49.
169. Ketzler, B., et al., *Digital twins for cities: A state of the art review.* Built Environment, 2020. **46**(4): p. 547-573.
170. Varshney, A., et al., *Challenges in sensors technology for industry 4.0 for futuristic metrological applications.* MAPAN, 2021. **36**(2): p. 215-226.
171. Gohari, H., C. Berry, and A. Barari, *A digital twin for integrated inspection system in digital manufacturing.* IFAC-PapersOnLine, 2019. **52**(10): p. 182-187.
172. Stojadinovic, S.M., V.D. Majstorovic, and N.M. Durakbasa, *An approach to development of the digital inspection twin based on CMM.* Measurement: Sensors, 2021. **18**: p. 100300.
173. Gaha, R., A. Durupt, and B. Eynard, *Towards the implementation of the Digital Twin in CMM inspection process: opportunities, challenges and proposals.* Procedia Manufacturing, 2021. **54**: p. 216-221.
174. Rasmussen, K., et al., *Novel mathematical and statistical approaches to uncertainty evaluation: best practice guide to uncertainty evaluation for computationally expensive models.* Brunswick, Germany: Euramet, 2015.
175. Jakubiec, W. and W. Płowucha, *First coordinate measurements uncertainty evaluation software fully consistent with the GPS philosophy.* Procedia CIRP, 2013. **10**: p. 317-322.
176. Balsamo, A., et al., *Evaluation of CMM Uncertainty Through Monte Carlo Simulations.* CIRP Annals - Manufacturing Technology, 1999. **48**(1): p. 425-428.
177. Gąska, A., et al., *Virtual CMM-based model for uncertainty estimation of coordinate measurements performed in industrial conditions.* Measurement, 2017. **98**: p. 361-371.
178. Vlaeyen, M., H. Haitjema, and W. Dewulf, *Digital Twin of an Optical Measurement System.* Sensors, 2021. **21**(19): p. 6638.
179. Wright, L. and S. Davidson, *How to tell the difference between a model and a digital twin.* Advanced Modeling and Simulation in Engineering Sciences, 2020. **7**(1): p. 1-13.
180. Agrawal, A., M. Fischer, and V. Singh, *Digital Twin: From Concept to Practice.* arXiv preprint arXiv:2201.06912, 2022.

181. Rajoub, B., et al., *A new model for measuring object shape using non-collimated fringe-pattern projections.* Journal of Optics, 2007. **9**(6): p. S66.
182. Al-Hamdan, S.F. and M.A. Bawaneh, *Simulation of intensity based triangular fringe projection technique for surface shape measurements*, in *International Conference on Electrical and Computing Technologies and Applications*. 2017, Institute of Electrical and Electronics Engineers: Aurak, UAE. p. 1-5.
183. Veach, E. and L.J. Guibas. *Metropolis light transport*. in *Proceedings of the 24th annual conference on Computer graphics and interactive techniques*. 1997. ACM Press/Addison-Wesley Publishing Co.
184. Haskamp, K., et al., *Estimation of measurement uncertainties using virtual fringe projection technique.* Applied optics, 2012. **51**(10): p. 1516-1520.
185. Zhou, D., et al., *Virtual fringe projection system with nonparallel illumination based on iteration.* Measurement Science and Technology, 2017. **28**(6): p. 1-9.
186. Li, W., S. Fang, and S. Duan, *Accurate and efficient algorithm for simulation of fringe projection system.* Optik: International Journal for Light and Electron Optics, 2013. **124**(18): p. 3542-3548.
187. Guarnera, D., et al., *BRDF representation and acquisition.* Computer Graphics Forum, 2016. **35**(2): p. 625-650.
188. von Enzberg, S., E. Lilienblum, and B. Michaelis, *A physical simulation approach for active photogrammetric 3D measurement systems*, in *International Instrumentation and Measurement Technology Conference*. 2011, Institute of Electrical and Electronics Engineers: Binjiang, China. p. 1-5.
189. Medeiros, E., et al., *Using physically based rendering to benchmark structured light scanners.* Computer Graphics Forum, 2014. **33**(7): p. 71-80.
190. Ortuño, J.E., et al., *3D surface acquisition for FMT using high-accuracy fringe projection profilometry*, in *IEEE Nuclear Science Symposium and Medical Imaging Conference*. 2009, Institute of Electrical and Electronics Engineers: Orlando, US. p. 4009-4012.
191. Weckenmann, A., W. Hartmann, and J. Weickmann. *Model and simulation of fringe projection measurements as part of an assistance system for multi-component fringe projection sensors*. in *Optical Fabrication, Testing, and Metrology III*. 2008. SPIE.
192. Barone, S., et al., *3D acquisition and stereo-camera calibration by active devices: A unique structured light encoding framework.* Optics and Lasers in Engineering, 2020. **127**: p. 105989.
193. Schmalz, C., F. Forster, and E. Angelopoulou, *Camera calibration: active versus passive targets.* Optical Engineering, 2011. **50**(11): p. 113601.
194. Wang, Y., et al., *Accurate feature detection for out-of-focus camera calibration.* Applied optics, 2016. **55**(28): p. 7964-7971.

195. Huang, L., Q. Zhang, and A. Asundi, *Camera calibration with active phase target: improvement on feature detection and optimization.* Optics letters, 2013. **38**(9): p. 1446-1448.
196. Strobl, K.H. and G. Hirzinger. *More accurate pinhole camera calibration with imperfect planar target*. in *2011 IEEE International Conference on Computer Vision Workshops (ICCV Workshops)*. 2011. IEEE.
197. Huang, L., Q. Zhang, and A. Asundi, *Flexible camera calibration using not-measured imperfect target.* Applied optics, 2013. **52**(25): p. 6278-6286.
198. Zhou, F., et al., *Accurate and robust estimation of camera parameters using RANSAC.* Optics and Lasers in Engineering, 2013. **51**(3): p. 197-212.
199. Yu, S., et al. *Effect of checkerboard on the accuracy of camera calibration*. in *Pacific Rim Conference on Multimedia*. 2018. Springer.
200. Vo, M., et al., *Flexible calibration technique for fringe-projection-based three-dimensional imaging.* Optics letters, 2010. **35**(19): p. 3192-3194.
201. Zhang, Z., *A flexible new technique for camera calibration.* IEEE Transactions on pattern analysis and machine intelligence, 2000. **22**.
202. Duda, A. and U. Frese. *Accurate Detection and Localization of Checkerboard Corners for Calibration*. in *BMVC*. 2018.
203. Zhang, S., *Digital fringe projection system calibration*, in *High-speed 3D imaging with digital fringe projection techniques*. 2016, CRC Press. p. 103-128.
204. Fiala, M. and C. Shu, *Self-identifying patterns for plane-based camera calibration.* Machine Vision and Applications, 2008. **19**(4): p. 209-216.
205. Mateos, G.G. *A camera calibration technique using targets of circular features*. in *5th Ibero-America Symposium On Pattern Recognition (SIARP)*. 2000. Citeseer.
206. Li, B., N. Karpinsky, and S. Zhang, *Novel calibration method for structured-light system with an out-of-focus projector.* Applied optics, 2014. **53**(16): p. 3415-3426.
207. Chen, R., et al., *Accurate calibration method for camera and projector in fringe patterns measurement system.* Applied optics, 2016. **55**(16): p. 4293-4300.
208. Daemi, B., *Enhanced image analysis, a tool for precision metrology in the micro and macro world*. 2017, KTH Royal Institute of Technology.
209. Yang, X. and S. Fang, *Eccentricity error compensation for geometric camera calibration based on circular features.* Measurement Science and Technology, 2014. **25**(2): p. 025007.
210. Matsuoka, R. and S. Maruyama, *Eccentricity on an image caused by projection of a circle and a sphere.* ISPRS Annals of the Photogrammetry, Remote Sensing and Spatial Information Sciences, 2016. **3**: p. 19.
211. Yang, L., J.-M. Normand, and G. Moreau. *Practical and precise projector-camera calibration*. in *2016 IEEE International Symposium on Mixed and Augmented Reality (ISMAR)*. 2016. IEEE.

212. Li, B., et al. *A multiple-camera system calibration toolbox using a feature descriptor-based calibration pattern*. in *2013 IEEE/RSJ International Conference on Intelligent Robots and Systems*. 2013. IEEE.
213. Ouellet, J.-N. and P. Hébert. *A simple operator for very precise estimation of ellipses*. in *Fourth Canadian Conference on Computer and Robot Vision (CRV'07)*. 2007. IEEE.
214. Chou, C.-C., *A closed-form general solution for the distance of point-to-ellipse in two dimensions.* Journal of Interdisciplinary Mathematics, 2019. **22**(3): p. 337-351.
215. Amiri-Simkooei, A. and S. Jazaeri, *Weighted total least squares formulated by standard least squares theory.* Journal of geodetic science, 2012. **2**(2): p. 113-124.
216. Fitzgibbon, A.W., M. Pilu, and R.B. Fisher. *Direct least squares fitting of ellipses*. in *Proceedings of 13th International Conference on Pattern Recognition*. 1996. IEEE.
217. Amiri-Simkooei, A., F. Zangeneh-Nejad, and J. Asgari, *On the covariance matrix of weighted total least-squares estimates.* Journal of surveying engineering, 2016. **142**(3): p. 04015014.
218. Fang, X., et al., *On total least squares for quadratic form estimation.* Studia geophysica et geodaetica, 2015. **59**(3): p. 366-379.
219. Kanatani, K., Y. Sugaya, and Y. Kanazawa, *Ellipse fitting for computer vision: implementation and applications.* Synthesis Lectures on Computer Vision, 2016. **6**(1): p. 1-141.
220. Silverman, B.W., *Density estimation for statistics and data analysis*. 1986: Routledge.
221. Gong, Z., Z. Liu, and G. Zhang, *Flexible global calibration of multiple cameras with nonoverlapping fields of view using circular targets.* Applied optics, 2017. **56**(11): p. 3122-3131.
222. Gu, F., et al., *Camera calibration based on the back projection process.* Measurement Science and Technology, 2015. **26**(12): p. 125004.
223. Salvi, J., X. Armangué, and J. Batlle, *A comparative review of camera calibrating methods with accuracy evaluation.* Pattern recognition, 2002. **35**(7): p. 1617-1635.
224. Huang, L., P.S. Chua, and A. Asundi, *Least-squares calibration method for fringe projection profilometry considering camera lens distortion.* Applied optics, 2010. **49**(9): p. 1539-1548.
225. Yin, Y., et al., *Calibration of fringe projection profilometry with bundle adjustment strategy.* Optics letters, 2012. **37**(4): p. 542-544.
226. Zhang, W., et al., *Sub-pixel projector calibration method for fringe projection profilometry.* Optics express, 2017. **25**(16): p. 19158-19169.
227. Zhang, S. and P.S. Huang, *Novel method for structured light system calibration.* Optical Engineering, 2006. **45**(8): p. 083601 , ISSN = 0091-3286.

228. Ranganathan, A., *The levenberg-marquardt algorithm.* Tutoral on LM algorithm, 2004. **11**(1): p. 101-110.
229. Transtrum, M.K. and J.P. Sethna, *Improvements to the Levenberg-Marquardt algorithm for nonlinear least-squares minimization.* arXiv preprint arXiv:1201.5885, 2012.
230. Xing, S. and H. Guo, *Iterative calibration method for measurement system having lens distortions in fringe projection profilometry.* Optics Express, 2020. **28**(2): p. 1177-1196.
231. Altmann, S.L., *Rotations, quaternions, and double groups*. 2005: Courier Corporation.
232. Diebel, J., *Representing attitude: Euler angles, unit quaternions, and rotation vectors.* Matrix, 2006. **58**(15-16): p. 1-35.
233. Hestenes, D. and G. Sobczyk, *Clifford algebra to geometric calculus: a unified language for mathematics and physics*. Vol. 5. 2012: Springer Science & Business Media.
234. Broyden, C., *On the discovery of the "good Broyden" method.* Mathematical programming, 2000. **87**(2): p. 209-213.
235. Bates, D.M. and D.G. Watts, *Relative Curvature Measures of Nonlinearity.* Journal of the Royal Statistical Society. Series B (Methodological), 1980. **42**(1): p. 1-25.
236. Clarke, G.P.Y., *Marginal Curvatures and Their Usefulness in the Analysis of Nonlinear Regression Models.* Journal of the American Statistical Association, 1987. **82**(399): p. 844-850.
237. White, H., *Consequences and detection of misspecified nonlinear regression models.* Journal of the American Statistical Association, 1981. **76**(374): p. 419-433.
238. White, H. and I. Domowitz, *Nonlinear Regression with Dependent Observations.* Econometrica, 1984. **52**(1): p. 143-161.
239. Seber, G. and C. Wild, *Measures of Curvature and Nonlinearity*, in *Nonlinear regression*, G.A.F. Seber and C.J. Wild, Editors. 1989, Wiley, New York. p. 127-190.
240. Golub, G.H. and C. Reinsch, *Singular value decomposition and least squares solutions*, in *Linear algebra*. 1971, Springer. p. 134-151.
241. *OpenCV*. https://github.com/opencv/opencv: Github.
242. Otsu, N., *A threshold selection method from gray-level histograms.* IEEE transactions on systems, man, and cybernetics, 1979. **9**(1): p. 62-66.
243. Al-Sharadqah, A. and N. Chernov, *Error analysis for circle fitting algorithms.* Electronic Journal of Statistics, 2009. **3**: p. 886-911.
244. Phillips, S., et al., *Dimensional measurement traceability of 3D imaging data*, in *Three-Dimensional Imaging Metrology*. 2009, International Society for Optics and Photonics: San Jose, US. p. 72390E.

Appendix A – Gaussian fitting

This appendix will detail the exact method used to fit the Gaussian function to the P line-spread functions. With P line-spread functions per dot there are $1 + 2P$ parameters to be estimated. Each line-spread function is normalised so both its abscissa and ordinate range is [0,1) to prevent one line-spread function from having too much influence on the Gaussian fitting. The method is based on the Levenberg-Marquardt algorithm, the basics of which is detailed in Section 6.5. The i^{th} value of the j^{th} line-spread function is given by y_{ij} at location x_{ij}. The Gaussian function therefore is given by

$$y_{ij} = A_j e^{-\frac{(x_{ij}-\mu_j)^2}{2\sigma^2}}. \tag{A.1}$$

With each line-spread function containing M points each, stacking each line-function gives $\vec{\boldsymbol{y}} = \{y_{ij}\}$, with each component found using the subscript $M \times (j-1) + i$. The list of parameters is defined as $\vec{\boldsymbol{\psi}} = [\sigma \quad \mu_0 \quad A_0 \quad \dots \quad \mu_P \quad A_P]^{\mathrm{T}}$. The linear form is then given by

$$\vec{\boldsymbol{y}} = \boldsymbol{\mathcal{J}}\vec{\boldsymbol{\psi}}, \tag{A.2}$$

with the Jacobian $\boldsymbol{\mathcal{J}}$ size $Mj \times (1 + 2P)$ given with

$$\boldsymbol{\mathcal{J}}_{Mj\times(1+2P)} = \begin{bmatrix} \frac{\partial y_{0,0}}{\partial \sigma} & \frac{\partial y_{0,0}}{\partial \mu_0} & \frac{\partial y_{0,0}}{\partial A_0} & 0 & 0 & 0 & 0 & \cdots & 0 & 0 \\ \vdots & \vdots & \vdots & \vdots & \vdots & \vdots & \vdots & \ddots & \vdots & \vdots \\ \frac{\partial y_{0,1}}{\partial \sigma} & 0 & 0 & \frac{\partial y_{0,1}}{\partial \mu_1} & \frac{\partial y_{0,1}}{\partial A_1} & 0 & 0 & \cdots & 0 & 0 \\ \vdots & \vdots & \vdots & \vdots & \vdots & \vdots & \vdots & \ddots & \vdots & \vdots \\ \frac{\partial y_{M,P}}{\partial \sigma} & 0 & 0 & 0 & 0 & 0 & 0 & \cdots & \frac{\partial y_{M,P}}{\partial \mu_P} & \frac{\partial y_{M,P}}{\partial A_P} \end{bmatrix}. \tag{A.3}$$

The components of the Jacobian $\boldsymbol{\mathcal{J}}$ can be derived from eq.(A.1). The subscripts have been dropped from the following equations for generality and clarity.

$$\frac{\partial y}{\partial \sigma} = \frac{A(x-\mu)^2}{\sigma^3} e^{-\frac{(x-\mu)^2}{2\sigma^2}} \tag{A.4}$$

$$\frac{\partial y}{\partial \mu} = \frac{A(x-\mu)}{\sigma^2} e^{-\frac{(x-\mu)^2}{2\sigma^2}} \tag{A.5}$$

$$\frac{\partial y}{\partial A} = e^{-\frac{(x-\mu)^2}{2\sigma^2}} \tag{A.6}$$

This naturally leads to the method of estimating an uncertainty from a least-squares estimate

$$V_{\text{fit}} = \sigma^2(\boldsymbol{J}^T\boldsymbol{J})^{-1}, \tag{A.7}$$

$$\sigma^2 = (\boldsymbol{y} - \hat{\boldsymbol{y}})^{\top}(\boldsymbol{y} - \hat{\boldsymbol{y}})\frac{1}{N' - (1+2P)}, \tag{A.8}$$

where N' gives the number of points that define the Gaussian peak. Since points far from the peak centre offer no information when defining the peak, the total N' is made of points that exist only within $\pm 3\sigma$. Eq. (A.2) would require the regression follow all the regular assumptions of a least squares regression. However, errors will exhibit some autocorrelation due to spatial frequency limitations. The line-spread function is also assumed to be a Gaussian function and there is no guarantee of this validity. The uncertainty will be estimated using a combination of the least-squares estimate and a resolution limit defined by the full-width at half-maximum (FWHM) of the Gaussian peak

$$\boldsymbol{V}_{\psi} = \boldsymbol{V}_{\text{fit}} + \boldsymbol{V}_{\text{res}}. \tag{A.9}$$

The matrix $\boldsymbol{V}_{\text{fit}}$ defines the uncertainty from the fitting procedure given by the least squares estimate of eq. (4.60) and eq. (4.61), while the matrix $\boldsymbol{V}_{\text{res}}$ defines the uncertainty to defining the ellipse boundary. The least-squares estimate defines the goodness-of-fit. For example, an ellipse completely corrupted with specular reflections will not fit a Gaussian function well, and this will be reflected in $\boldsymbol{V}_{\text{fit}}$. The FWHM is given by

$$FWHM = 2\sqrt{2\,ln\,2}\,\sigma \cong 2.355\sigma, \tag{A.10}$$

and determines a uniform confidence interval of $\pm\sqrt{2\ln 2}\,\sigma$, and can be adjust to a "normal" interval, as described in GUM [24], with

$$\boldsymbol{V}_{res} = \mathbb{I}_{1+2P} \times \frac{2\,ln\,2}{3}\sigma^2. \tag{A.11}$$

Appendix B – Ellipse fitting

The least squares method used in this work is taken from Fitzgibbon, Pilu [216], chosen for its simplicity. The ellipse equation, eq. (6.18),

$$\vec{\boldsymbol{x}}^{\mathrm{T}}\boldsymbol{M}\vec{\boldsymbol{x}} = 0, \tag{6.18}$$

can be rewritten as:

$$\begin{bmatrix} x^2 & xy & y^2 & x & y \\ \vdots & \vdots & \vdots & \vdots & \vdots \end{bmatrix} \begin{bmatrix} A' \\ B' \\ C' \\ D' \\ E' \end{bmatrix} = \vec{\mathbf{1}} \tag{B.1}$$

$$\boldsymbol{X}\vec{\boldsymbol{m}}' = \vec{\mathbf{1}} \tag{B.2}$$

and the coefficients $\vec{\boldsymbol{m}}'$ can be found in the least-squares manner

$$\vec{\boldsymbol{m}}' = (\boldsymbol{X}^{\mathrm{T}}\boldsymbol{X})\boldsymbol{X}^{\mathrm{T}}\vec{\mathbf{1}} \tag{B.3}$$

The coefficients $\vec{\boldsymbol{m}}'$ can be converted to $\vec{\boldsymbol{\alpha}}' = \{x_0, y_0, a, b, \phi\}$ using

$$\phi = \frac{1}{2}\arctan\left(\frac{-B'}{C' - A'}\right) \tag{B.4}$$

$$\begin{gathered} A'' = A'\cos^2\phi + B'\cos\phi\sin\phi + C'\sin^2\phi \\ C'' = A'\sin^2\phi\, 2 - B'\cos\phi\sin\phi + C'\cos^2\phi \\ D'' = D'\cos\phi + E'\sin\phi \\ E'' = -D'\sin\phi + E'\cos\phi \\ F'' = 1 + \frac{D'^2}{4A'} + \frac{E'^2}{4C'} \end{gathered} \tag{B.5}$$

$$x_0 = -\frac{D''}{2A''}\cos\phi + \frac{E''}{2C'}\sin\phi \tag{B.6}$$

$$y_0 = -\frac{D''}{2A''}\sin\phi - \frac{E''}{2C''}\cos\phi \tag{B.7}$$

$$a = \sqrt{\frac{F''}{A''}} \tag{B.8}$$

$$b = \sqrt{\frac{F''}{C''}} \tag{B.9}$$

The issue with this approach is it does not consider errors in the regressors $\boldsymbol{X}$, and many of the regressor are correlated, so will be biased in some way. One method to deal with this is to estimate the error the regressors have on $\vec{\mathbf{1}}$ and iteratively reweight. To relax the assumption homoscedasticity without an a priori estimation of errors in the regressors, the coefficients $\vec{\boldsymbol{m}}'$ can be found by weighting each point

$$\vec{\boldsymbol{m}}' = (\boldsymbol{X}^{\mathrm{T}}\boldsymbol{W}\boldsymbol{X})\boldsymbol{X}^{\mathrm{T}}\boldsymbol{W}\vec{\mathbf{1}}. \tag{B.10}$$

The weighting matrix can be estimated from a previous fitting. The full algorithm is given in Algorithm 11 .

Algorithm 11 Iterative least-squares estimation of ellipse parameters.

Set $\boldsymbol{W} = \mathbb{I}$.
Set $\delta = 1 \times 10^{-3}$.
For 3 repetitions:
    Find $\vec{\boldsymbol{m}}'$ through least squares.
    Update the weight matrix using $\boldsymbol{W} = \mathbb{I} \times \frac{1}{\max(\delta, \vec{\mathbf{1}} - \boldsymbol{X}\vec{\boldsymbol{m}}')}$.
End For
Find covariance matrix $\boldsymbol{V}_m = (\boldsymbol{X}^{\mathrm{T}}\boldsymbol{W}\boldsymbol{X})^{-1}$.

The variable $\vec{\mathbf{1}}$ is a constant, the error in $\vec{\mathbf{1}}$ does not carry much physical meaning. Additionally, the regressor matrix is derived from only two variables, x and y – clearly the regressor matrix will be highly correlated. Thanks to the square terms in the regressor $\boldsymbol{X}$, the errors will be dominated by any significant outliers, this method is not particularly robust. A natural extension to this method is the weighted total least-squares method.

Appendix C – Rodrigues operator

The algorithms for the Rodrigues operator and inverse Rodrigues operator are given below.

Algorithm 12 Rodrigues operator to define rotation matrix from Rodrigues vector.

Find theta $\theta = \|\vec{\boldsymbol{q}}\|$
Normalise $\vec{q}' = \frac{\vec{q}}{\theta}$
Split vector into component parts $\vec{q}' = \begin{bmatrix} q_1' \\ q_2' \\ q_3' \end{bmatrix}$
Create matrix $Q = \begin{bmatrix} 0 & -q_3' & q_2' \\ q_3' & 0 & q_1' \\ -q_2' & -q_1' & 0 \end{bmatrix}$
Create the rotation matrix $R = \mathbb{I}_{3\times3} + \sin(\theta)\, K + \cos(\theta)\, KK$

Algorithm 13 Inverse Rodrigues operator to define Rodrigues vector from rotation matrix.

Find the rotation angle $\theta = \arccos\left(\frac{(R_{11}+R_{22}+R_{33}-1)}{2}\right)$
Find the first component $q_1' = R_{32} - R_{23}$
Find the second component $q_2' = R_{13} - R_{31}$
Find the third component $q_3' = R_{21} - R_{12}$
Assemble $\vec{\boldsymbol{q}}' = \begin{bmatrix} \mathrm{q}_1' \\ \mathrm{q}_2' \\ \mathrm{q}_3' \end{bmatrix}$
Normalise and incorporate theta $\vec{\boldsymbol{q}} = \frac{\vec{\boldsymbol{q}}'}{\|\vec{\boldsymbol{q}}'\|}\theta$

Appendix D – Convergence

In this section, it will be shown that the Monte-Carlo trial results have converged enough as to estimate the effectiveness of each calibration method. In supplement one to the GUM, an adaptive Monte-Carlo procedure is given defined off the numerical tolerance of the standard uncertainty. The purpose of this study is to test the system parameters and their associated uncertainties. For this purpose, it was decided that a $\pm 5\%$ difference in standard deviation was acceptable. For a set of values $\vec{\boldsymbol{x}} = \{x_i\}$, the standard deviation, σ, is given by

$$\sigma^2 = \sum_{i=1}^{n} (x_i - \bar{x}), \tag{D.1}$$

with $\bar{x}$ being the mean value of $\vec{\boldsymbol{x}} = \{x_i\}$. Each addition of a new data point x_i will make successively smaller contributions to the computed standard deviation. Therefore it can be safely assumed that the standard deviation will always converge to a final value, and changes in the standard deviation after Monte-Carlo trial i will be less than the changes at Monte-Carlo trial i. Therefore, once a standard deviation has stabilised to $\pm 5\%$ for 50 trials, the Monte-Carlo trial is considered complete. The convergence plots showing stabilisation of the standard deviation to within $\pm 5\%$ are shown for the flat plane, sphere plate and dumbbells in Figure 9.1, Figure 9.2 and Figure 9.3. The solid lines in each graph show the min-max range of percentage changes of every data point of the artefact. The lines becomes red when all points of that particular measurement are within $\pm 5\%$ range of the final value.

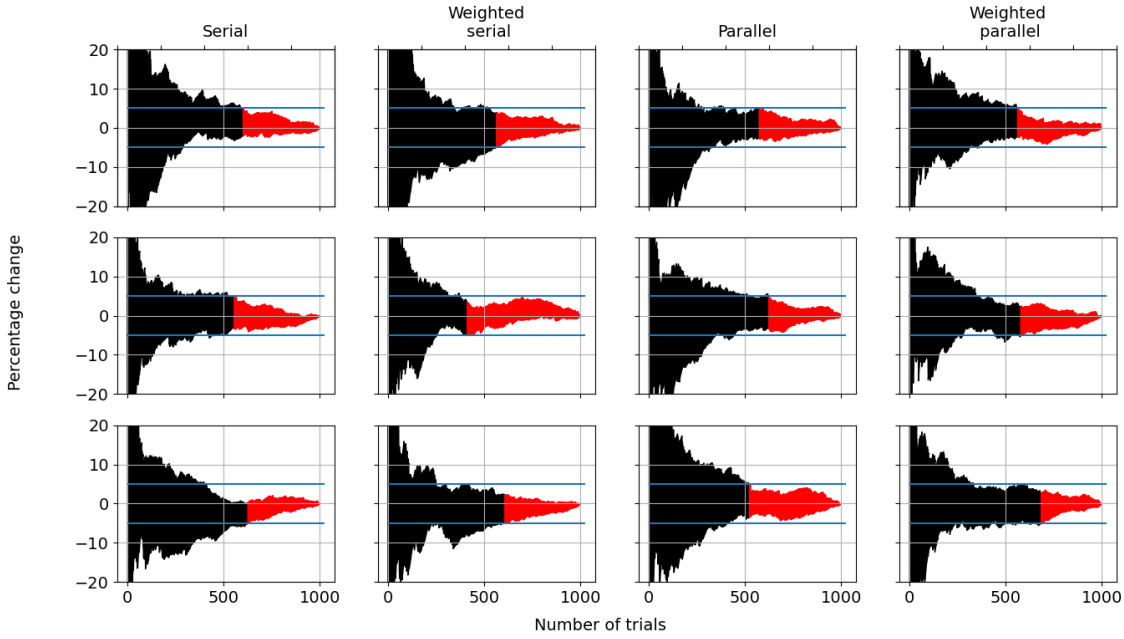

Figure 9.1 Convergence of deviation from flatness values to their final value in each Monte-Carlo trial.

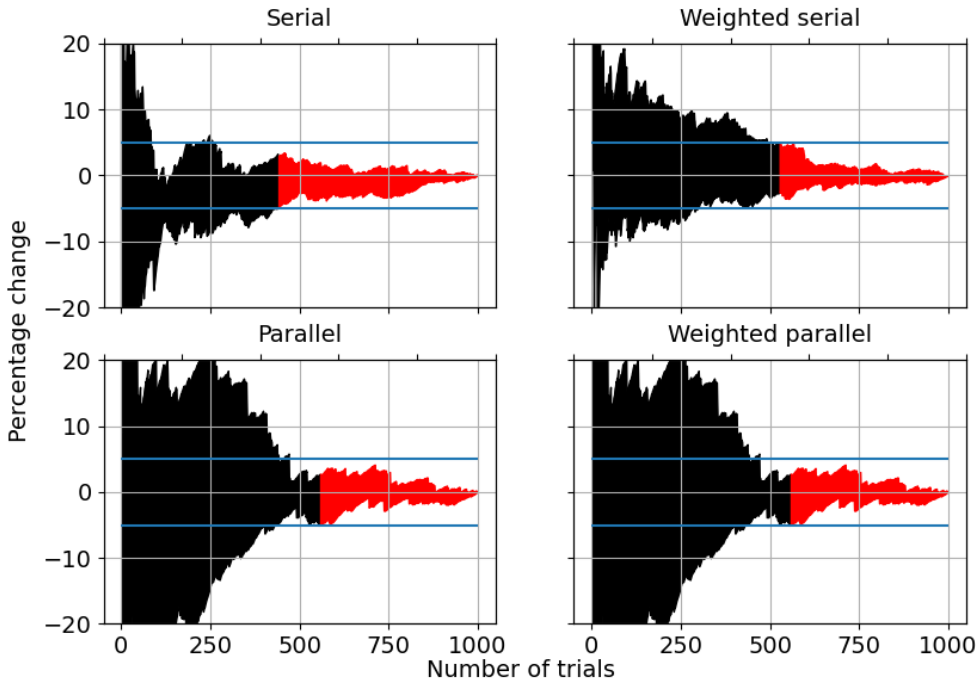

(a)

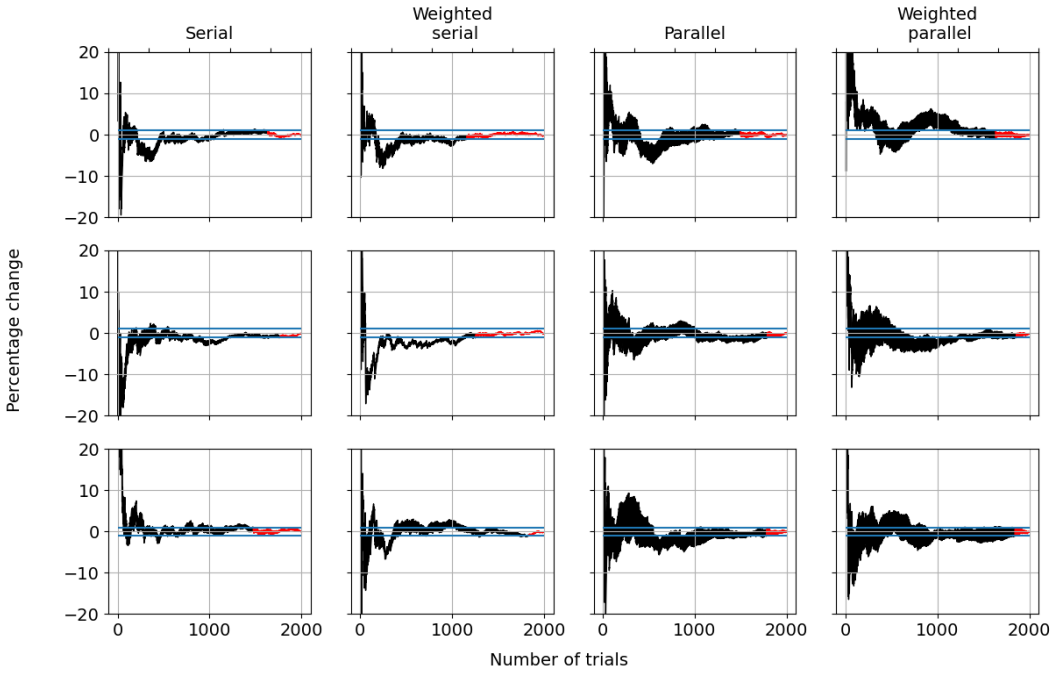

(b)

Figure 9.2 Convergence of error of sphere radii values to their final value in each Monte-Carlo trial for (a) dumbbell and (b) sphere plate.

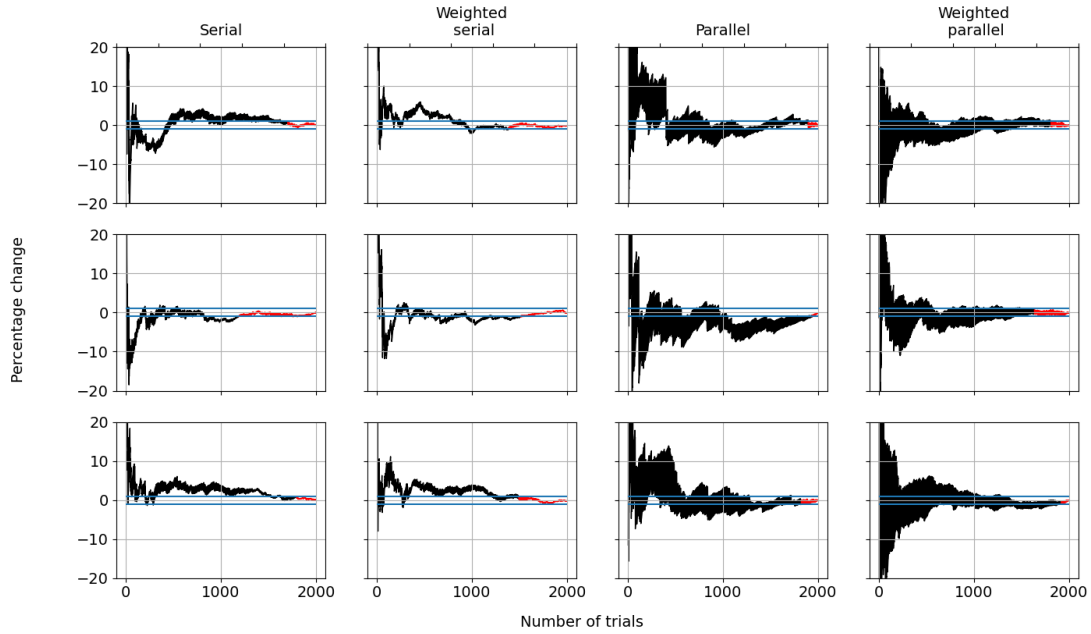

(a)

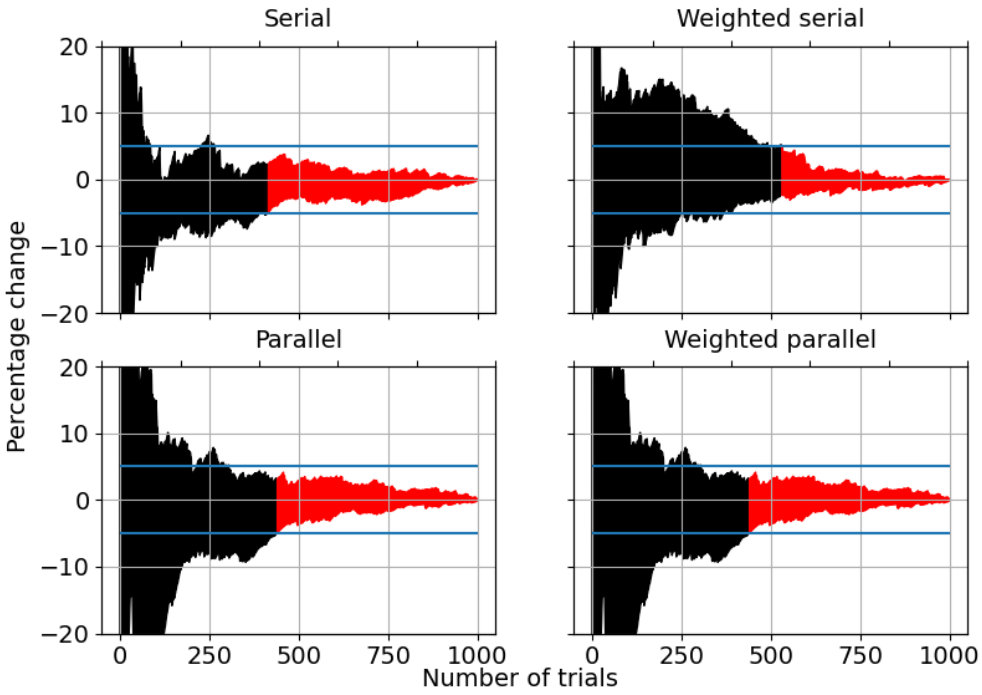

(b)

Figure 9.3 Convergence of error of sphere-to-sphere length values to their final value in each Monte-Carlo trial for (a) dumbbell and (b) sphere plate.

While the sphere plate measurements required more trials to stabilise, all the trials stabilised within a reasonable rage of values – allowing the comparison of the calibration methods. For a real measurement, the number of trails would likely have to be higher.s